DESIGN AND ASSESSMENT OF FABRY-PEROT QUANTUM WELL ELECTROABSORPTION OPTICAL MODULATORS

A thesis by

Paraskevi Zouganeli

submitted to the University of London for the degree of Ph.D.

Department of Electronic and Electrical Engineering
University College London

September 1992

to my mother Maria my father Petro
and my sister Popi

ABSTRACT

The optical properties of multiple quantum well (MQW) material can be modified by application of an electric field across the wells. Hence, by locating the wells in the intrinsic region of a p-i-n diode, an optical beam incident on the diode may be modulated. The incorporation of such a diode in an integrated Fabry-Perot (FP) cavity yields an enhancement of the modulation characteristics. This thesis deals with the assessment and optimisation of Fabry-Perot reflection modulators in the GaAs/AlGaAs material system, where the electroabsorption effects in quantum wells are employed to attain voltage-controlled optical intensity modulation.

The work is primarily concerned with the asymmetric Fabry-Perot modulator (AFPM) where the front mirror of the FP cavity is of lower reflectivity than that of the back. Although the achievable very high on:off reflectivity ratios make this type of device very attractive, its ultimate implementation imposes a number of other requirements. Firstly, the operation needs to be compatible with existing electronics required to drive the modulator. Secondly, the performance must be tolerant to fluctuations of a number of parameters associated both with the epitaxial growth and with the operational conditions including ambient temperature. Our optimisation aims, therefore, both to improve the modulation characteristics and to maximise the tolerance of the structure. To do this, we examine theoretically and experimentally the parameters that affect the performance, addressing both the quantum well effects and the microresonator design. We develop a comprehensive design method, demonstrate modulators with improved characteristics, proceed to a thorough evaluation of the performance ultimately attainable by AFPMs, and finally produce optimised designs to meet predefined specifications.

Another quantum well electroabsorption-based device, the symmetric cavity electroabsorption modulator (SCEM), is fully investigated and its relative merits are critically examined. In this case the front and back mirrors are equal and the device offers certain advantages in the normally-off mode, thereby lending itself to optically bistable operation. We demonstrate switching using SCEMs in the symmetric self-electro-optic-effect device (S-SEED) configuration.

Finally, we examine the microresonator devices in terms of their potential for versatile functionality within optoelectronic systems, and propose integrated configurations and new composite devices.

LIST OF CONTENTS

Chapter 1: INTRODUCTION

Chapter 2: THE INTEGRATED FABRY-PEROT MODULATOR: OPERATION, DEVICE FABRICATION, EXPERIMENTAL METHOD, AND OPTIMISATION OBJECTIVES

Chapter 3: MODELLING OF FABRY-PEROT ELECTROABSORPTION DEVICES

Chapter 4: THE TEMPERATURE TOLERANCE OF THE ASYMMETRIC FABRY-PEROT MODULATOR

Chapter 5: TOLERANCES OF THE ASYMMETRIC FABRY-PEROT MODULATOR

Chapter 6: TRADE-OFFS INVOLVED IN THE AFPM PERFORMANCE IMPOSED BY THE MIRROR DESIGN

Chapter 7: ASYMMETRIC FABRY-PEROT MODULATOR DESIGNS

Chapter 8: THE SYMMETRIC CAVITY ELECTROABSORPTION MODULATOR

Chapter 9: APPLICATIONS OF THE FABRY-PEROT MODULATOR AT THE CHIP LEVEL

CHAPTER 1: INTRODUCTION

1.1 HISTORICAL DEVELOPMENT

The invention of the transistor in 1948 signifies the starting-point of the contemporary technology oriented period that has earned the title: information era. Since the 50's, there has been a steady exponential advancement in electronics predominantly due to the fast-paced progress in semiconductor technology and in particular the integration of thousands of different components in light, compact, small-area chips. Indeed, the most valued craft of the last quarter of the century has been miniaturisation. The impact of these advancements has been tremendous in an intriguing range of ways, indeed it can be said that most of the progress in other sciences, from medicine to astrophysics, has by and large been a bi-product of the vast and diverse achievements in the electronics industry that facilitated better diagnostics and accurate instrumentation. Information exchange and processing are in intimate relation with the very fabric of the current social-economic structures. The increasing demand for high speed large throughput information technology has so far been met by an increase of component density and a simultaneous enlargement of chip area. It has, however, been realised that there are some fundamental limits to the performance that can be attained by electronics, as they are limited by propagation delays on the capacitive connectors. Additionally, the area of telecommunications has suffered substantial limitations due to high transmission losses and restricted bandwidth availability, which have been alleviated by the implementation of the optical fibre.

The invention of the fibre by Kao and Hockman and Werts in 1966, and the demonstration of laser emission from GaAs in 1963 can be viewed as the two events that permitted the birth of modern optics. The very early boost in optical communications was largely thanks to the military industry, the interest of which was driven by the immunity of fibre to electromagnetic interference and crosstalk. Today, however, and as envisaged by the early researchers in the field, the striking majority of applications are commercial. Fibre offers broadband low-loss transmission with the currently achieved cost/performance figures establishing its dominance in telecommunications. Indeed, fibres are now extensively used in sub-marine systems and are generally the preferred medium for long-haul communications. Furthermore, the development of Er^+ doped fibre amplifiers has resulted in virtually lossless transmission links. This has encouraged further demands for broadband services.

As the technologies mature and at the same time it becomes clear that optics is here to stay, it is evident that there may be a much more substantial role optics can play. Optics offers a vast available bandwidth, massive parallelism, and high speeds, and hence it may prove a viable solution to problems encountered in information technology in the broad sense, i.e. be it telecommunications or connections between modules in a data processor. Optical interconnects can be used within processing systems to alleviate the speed and capacity limitations in VLSI. As this has been broadly investigated, new issues have been revealed where a certain degree of functionality of the optical node, other than that of a mere interface element, appears possibly advantageous. Additionally, as transmission becomes less of an issue, problems encountered at the switching end of fibre communications promote the notion of switching being performed in the optical domain. Thus, progressively, optics is being considered for possible implementation higher up the hierarchy of data manipulation. The degree to which this may materialise is in many areas still open to debate.

The role of III-V compound semiconductors within this framework is more than essential in that the their development has actually influenced the very perspective optical implementations are viewed upon. Compound semiconductors have been a field of intense investigation predominantly because, unlike Si, the direct band-gaps of such materials allow the realisation of active optical devices, i.e. light sources. Moreover, the realisation of electrically-pumped laser action in semiconductor diodes has established their usability. A decisive factor with respect to the further deployment of optics in data processing, is its compatibility with existing technology. This has been the prime rationale that has fuelled the extensive interest in semiconductor technologies for optical applications. GaAs is the most advanced material among III-Vs and by far the most mature technology where both electronic and optical devices have been realised [Haigh and Everard]. Good quality epitaxial growth was first achieved in GaAs and most of the novel optical and electronic devices in III-Vs have been first demonstrated in this material system. Moreover, its almost perfect lattice match to $Al_xGa_{1-x}As$ permits the realisation of heterostructures that yield a considerable performance improvement specifically in transistor and laser structures. A special class of optoelectronic material, the quantum well material, that uses short-period heterostructures acquires characteristic qualities that result in the realisation of a range of very efficient optoelectronic devices which compare favourably to these in bulk material. Such devices in GaAs are strong candidates for several applications in optical interconnection and switching networks. On the other hand, InP based material is used in long-haul communications in order to exploit the low-loss window of the optical fibre (≈1.55μm).

This thesis is concerned with a class of GaAs multiple quantum well optoelectronic devices where the reflected optical intensity is controlled by the electrical signal applied to the terminals of the device. Specifically, we are concerned with Fabry-Perot quantum well electroabsorption modulators in the GaAs material system. When this work was started such modulators, namely the asymmetric Fabry-Perot modulator, had just been demonstrated [Whitehead *et al.*, 1989b; Yan *et al.*, 1989] with modulator characteristics that clearly outperformed other semiconductor such devices. The aim of this work was to study such devices in greater detail and optimise their performance. Such optical modulators may become important elements at the interface between optics and electronics that lend themselves to a variety of functions in optoelectronic systems. It was decided that the direction of this work would be towards a realistic evaluation of the potential for implementation of this type of modulator in a real system and thus its performance ought to be studied and optimised with real conditions and systems requirements in mind.

In the following we give a brief account of optoelectronic systems considering in particular areas where the reflection modulator may be incorporated. Subsequently, after an introduction to quantum well effects, we present the main types of modulators that may be realised using quantum well material and which can be used as building blocks in more complex composite structures. Finally, we introduce briefly the implementation of composite quantum well devices in optoelectronic logic.

1.2 OPTOELECTRONIC SYSTEMS

A wide range of optoelectronic systems has been developed for communications, interconnection, optical computing, neural networks, as well as for applications in industries not directly associated with information technology. From these, the systems at the communications end of the range are at the most advanced stage as their implementation is imminent. A discussion of optoelectronic systems in general is certainly beyond the scope of this introduction. In this section we give, therefore, a brief account of systems from the perspective of potential applications for a semiconductor reflection modulator.

Optical interconnects in VLSI

Faster processing of ever larger amounts of data has been achieved by scaling down the device features in ICs and a simultaneous scaling up of the chip-size. Consequently, the density of devices per unit chip area is increased, the power dissipation per device is decreased and so is the switching delay of each gate. The interconnect RC time, however, remains unchanged [Goodman,1984], when at the same time the enlarged chip size results in a larger number of elements per block and thus more and more interconnects between blocks. Furthermore, as clock speeds increase, clock skews are caused by the different path delays along varying path lengths [Midwinter, 1988]. The situation has thus reached the stage where the performance is in fact in many cases Input/Output (I/O) bound rather than processing bound. To take this argument a bit further, current electronic technologies are certainly poor in supporting the necessary I/O density and bandwidth required for large amounts of data and parallel computing [Feldman, 1990; Guha *et al.*,1990]. In the course of various developments in optics there has been a certain advancement in the performance of electronics in recent years. An attempt to minimise the interconnection lengths and achieve better overall chip-topography has been the implementation of multi-layered chips where many levels of interconnections are stacked together in the vertical direction with point connections joining layer to layer [Topham, 1991]. However, these circuits suffer severe heat dissipation problems.

Optical interconnects offer the potential to overcome the limitations encountered in VLSI implementations and yield faster point-to-point communications with a reduction of the necessary electrical pins per chip. This can result in designs that consume less power, and operate at higher speeds. Additionally, the footprint area corresponding to the "optical pads" is reduced as compared to electrical pads that normally occupy ≈25% of the chip area. The 'break-even' length when comparing optical and electrical interconnects in terms of power consumption has been estimated to a couple of mm beyond which optics is more efficient than electronics. This is, nevertheless, very much dependent upon the specific components as well as the application [Farhadiroushan *et al.*, 1991]. Also one can argue that power consumption is only one of the points to be considered.

Optical interconnections may be implemented in local-area networks (LANs), module-to-module, board-to-board and chip-to-chip communications. In such short distance systems, GaAs based material could be favoured as stemming from its superior performance. The approaches towards optical interconnects in VLSI may be classified in two types: guided and free-space interconnects. The former could be implemented using for example polymer waveguides in the backplane [Guha *et al.*, 1990] or other waveguides and optical fibres [Goodman, 1984] for connections between various levels. Free space interconnections of VLSI implementations allow for direct access to various locations on the chip and are inherently flexible to ultimately offer the possibility of dynamic reconfiguration of the connecting routes between elements.

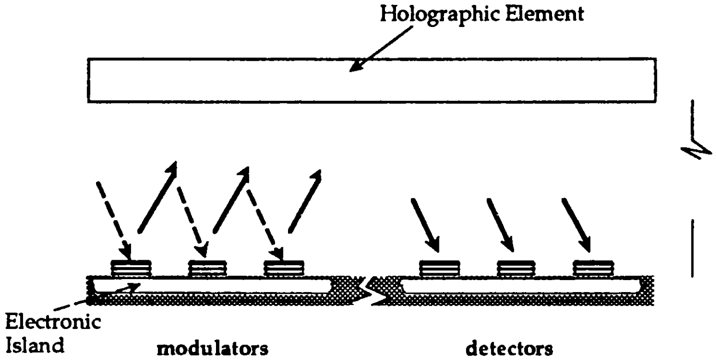

Fig.1.2.1 *A schematic diagram illustrating the use of reflection modulators as optical pads performing the connections between islands of electronics in VLSI. Diagram not to scale.*

Holographic elements may be used to facilitate complex connectivity. These would be preferably computer generated as it would be uneconomical to realise an optically generated hologram in cases where dense complex routing is required [Facanha *et al.*, 1989].

The transmitter element may be either a laser diode or a modulator. In the case of free-space interconnections, modulators seemed at the start of this work to be the most viable candidate since the performance of surface emitting diodes was simply inadequate. However, the advancements in surface emitting laser diodes in the last five years [see for example Yoo *et al.*, 1990; Orenstein *et al.*, 1991] have promoted them to serious candidates for 2-D arrays of transmitting elements in these implementations. However, there are two major disadvantages encompassed with the use of lasers for this task [Midwinter, 1987]. One is that lasers are very much more power consumptive devices and this would inhibit the realisation of high-density networks with optical modules integrated in close proximity to the electronic ones. A second disadvantage is that lasers are devices critically dependent upon the epitaxial material quality and the operational conditions. Therefore, for example, it would be quite difficult to realise reliable lasers in GaAs monolithically integrated on Si electronics

(Chapter 9). In addition to the above arguments, the use of modulators offers the advantage that the optical source is located away from the active chip and thus not only dissipates its heat elsewhere but also facilitates better timing and control of the elements [Midwinter, 1987]. Finally, and very importantly, a modulator can comprise the main element of both the transmitter and the receiver end of the link. The created bi-directional paths can offer additional connectivity, flexibility, and ultimately dynamic reconfigurability. Thus one could envisage arrays of reflection modulators acting as the interconnecting pads between electronic islands or between boards in free-space links (Fig.1.2.1) [see Parker, 1991].

Optical switching

At present transmission rates in fibre optic packet switching systems routing decisions can be made electronically, thus hybrid architectures are used where the transmission is done optically and the switching electronically. However, as the transmission rates increase electronic processing will find it increasingly difficult to perform the required routing functions. The electronic switch suffers from relatively low transmission bandwidths while also the optoelectronic (O/E) interfaces associated with the hybrid architectures prevent the full exploitation of the large bandwidth-distance product of the optical fibre. To fully exploit the advantages of optics, it would be desirable to generate, transmit, process, and detect broadband high frequency optical signals in the optical domain and interface these to external, probably Si based, integrated circuits operating at the same speed. Thus the possible data flow bottleneck created at the electronic switch would be overcome.

Switches may be realised using either logic devices or using passive devices that respond to some routing instruction, be it in the time or the wavelength domain [Midwinter, 1988]. The latter (i.e. relational switches) would have the additional advantage of a versatile bandwidth provided by the "transparent" switched optical path. That is, unlike an electronic switch which operates for a certain type of data format, an optical switch may be able to cope with any optical signal provided of course this lies within a certain wavelength range. Thus in total, the use of optical switching would realise systems that take full advantage of the endemic qualities of optics: parallelism, broad bandwidth, and high speed. From a historical perspective, switching has always followed the format of transmission [Nussbaum, 1988], and transmission is now being performed increasingly in the optical domain. There is, however, a series of practical difficulties that must be bypassed before optical switching is actually implemented.

Several technologies are applicable to the realisation optical switching such as $LiNbO_3$ waveguides, photorefractive materials, semiconductor waveguide switches making use of absorption or phase techniques, all-optical bistable devices, semiconductor optoelectronic logic. A review of semiconductor-based switches has been presented by Ikegami [1988], while several approaches have been realised in the laboratory since then [see for example Lindgeren *et al.*, 1990; Shimomura *et al.*, 1992; Hamamoto *et al.*, 1992]. Self-routing switches, i.e. switches that can decide upon the function to apply at the input signal as this is dictated by a header instruction preceding the signal, have received much interest [Ballance *et al.*, 1990]. Such switches perform the switching action without needing to know the inputs to the other ports to the network, thereby resulting in faster processing. Self-routing electronic switching networks are mainly limited by I/O capacity. Hence optics could be used in conjunction with electronic switching in a less ambitious manner, to constitute the I/O element between islands of electronic logic (J.E. Midwinter, private communications).

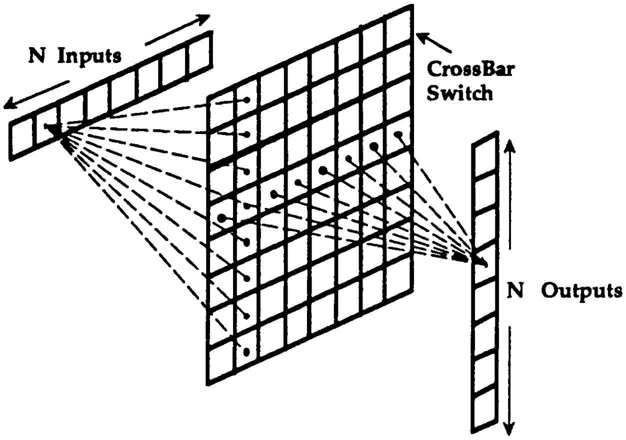

Fig.1.2.2 *A schematic diagram showing the connection of N inputs to N outputs using a crossbar switch. A matrix of NxN elements is required.*

The role of optical switching may also be envisaged in data processing as the implementation of optical interconnection might favour the addition of a certain level of intelligence in the elements that perform the connection. In the simplest form of a switching net the pixels act merely as shutters that may or may not transmit the optical signal. In more complex arrays, each pixel may perform both detection and transmission and, moreover, apply some logic function before transmitting. These so called "smart-pixels" [see for example Kurokawa *et al.*, 1992; Midwinter, 1988] could assist in achieving such levels of versatility and complex functionality that fundamentally new routes in signal processing and data manipulation could be opened. Electronic components would be part of the intelligence. The extent to which these would be incorporated within the node is another issue to be addressed, as functionality may start decreasing again after a certain level of electronics have been incorporated in the node.

Interconnections are an inseparable part of switching networks. Bus, crossbar, and (possibly 3-D) multistage architectures can be utilised [Kiamilev *et al.*, 1991]. The two former have a limited I/O capacity while, in the case of a 3-D multistage network (such as a shuffle or butterfly net), the exploitation of the second dimension in the input and the output plane allows large amounts of data to be manipulated [Taylor and Midwinter, 1991]. For communications applications a crossbar network connecting N=128 or 256 inputs to an identical number of outputs (and hence requiring a NxN number of nodes) is the type of switch that could be implemented in the near future [Midwinter, 1987]. On the other hand, in non-communications applications, in the case of a parallel computer eg., multistage networks could be preferred in some cases as they provide efficient performance using a reasonable number of switches [Guha *et al.*, 1990; Matsuda and Shibata, 1991].

1.3 QUANTUM WELLS

1.3.1 Quantum well effects.

The term quantum well material refers to a class of semiconductor material where two semiconductors of different bandgaps are sandwiched together so that electrons and holes experience a potential well in the conduction and the valence band respectively in the direction perpendicular to the plane of the layers. When the width of the well is less than ≈200Å, confined states are created for the carriers in the semiconductor with the lower bandgap energy (well) (Fig.1.3.1). The situation is a bit more complicated in the valence band where the confinement lifts the degeneracy at the centre of the band since the effects are dependent upon the mass of the particle involved (Appendix). This leads thus to separate hole-bands at k=0, i.e. the light hole and the heavy hole (Chapter 3). Transitions may take place between the discrete levels created in the conduction and the valence band with the lowest transition occurring at an energy higher than the corresponding band-gap.

The reduced (quasi 2-D) dimensionality in quantum wells has a profound effect on the density of states which changes from a parabolic function of energy in 3-

D to a step function in the case of quantum wells (Fig.1.3.2). The steps correspond to the n=1,2,... levels. At the same time the confinement of the carriers within the well results in tighter-bound excitons, i.e. hydrogen-like bound electron-hole pairs. Thus, unlike bulk, the excitons in quantum wells are not ionised at room temperature as their binding energy is now greater. Excitonic features are observed in the absorption spectra as sharp peaks at an energy equal to the sub-band energy minus the binding energy of the pair. In total, the absorption spectra of quantum wells exhibit a step-like shape with the excitonic features superimposed at the edge of each step and the same features are thus observed in the photocurrent spectra obtained from a p-i-n such structure (Fig.1.3.2). These features not only increase the absorption coefficient compared with that of bulk material, but also give rise to pronounced electroabsorptive and electrorefractive effects that lend themselves to efficient voltage-induced modulation. We discuss this later in this section.

The advancement in epitaxial growth technology has allowed the realisation of GaAs/AlGaAs quantum wells. The first observation of quantisation effects was by Dingle and co-workers in 1974 at liquid helium temperatures (4K). Further rapid improvement in epitaxial growth techniques has permitted the achievement of smooth interfaces and of good control of the layer thicknesses [Herman *et al.*, 1991] so that

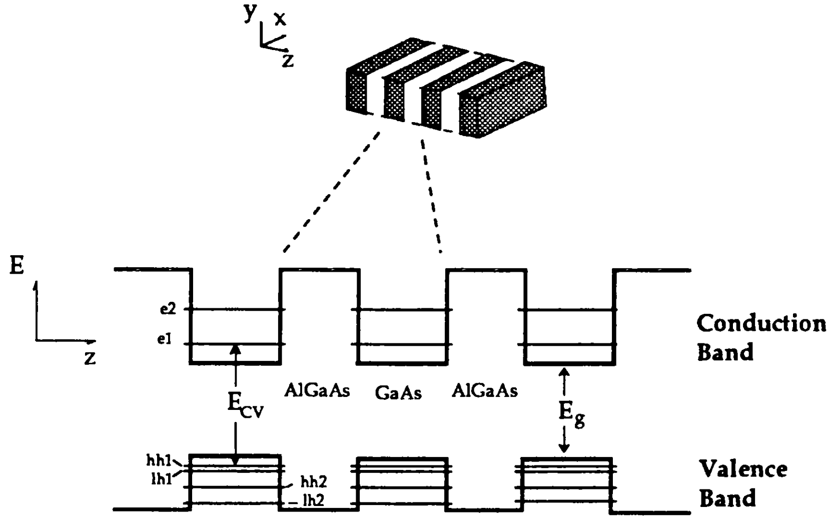

Fig.1.3.1 *Quantum wells are formed when alternating layers of typically ≈100Å GaAs and AlGaAs are sandwiched together. These are formed perpendicular to the growth direction (z). Confined states (n=1,2 shown) for the electron (en) and for the heavy- and light-hole (hhn and lhn) occur within the well (type I). The fundamental transition corresponds to* E_{CV} *as opposed to the smaller band-gap energy* E_g.

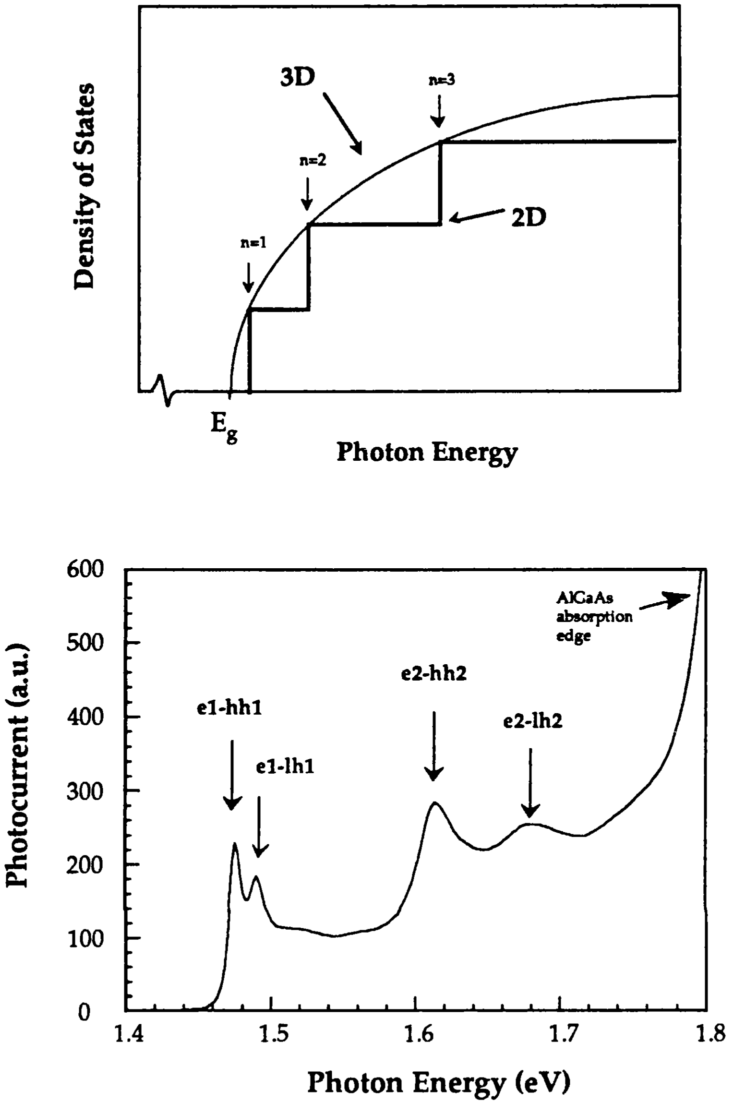

Fig.1.3.2 *The top graph is a schematic of the parabolic density of states corresponding to the 3D bulk case, and the step like DOS corresponding to the 2D case (infinite wells). The bottom plot shows experimental photocurrent data with clear quantisation effects. These have been obtained from a 95Å well p-i-n diode at zero Volts (Built-in field).*

clear quantisation effects are now routinely observed at room temperature (Chapters 3 and 5).

Quantum confined Stark effect (QCSE)

The probability of an optical transition occurring between two discrete levels is proportional to the overlap of the wavefunctions of the two particles (electrons and holes), and this holds both with and without field. In the infinite well approximation and for zero field, the wavefunctions are orthogonal and thus only transitions with Δn=0 can take place. In a real quantum well system, the barrier-height is finite leading to a deviation of the wavefunctions from simple sines and cosines and a considerable penetration into the barrier. This causes a partial break down of the selection rules even in the zero field case discussed above, but nevertheless in that case only transitions with Δn=0 result in pronounced features (Fig.1.3.2). Upon the application of a field perpendicular to the plane of the wells, the shape of the well changes and as a result the energy levels within the well are altered. The transitions occur at smaller energies and thus the excitonic features red-shift. The application of a field causes the

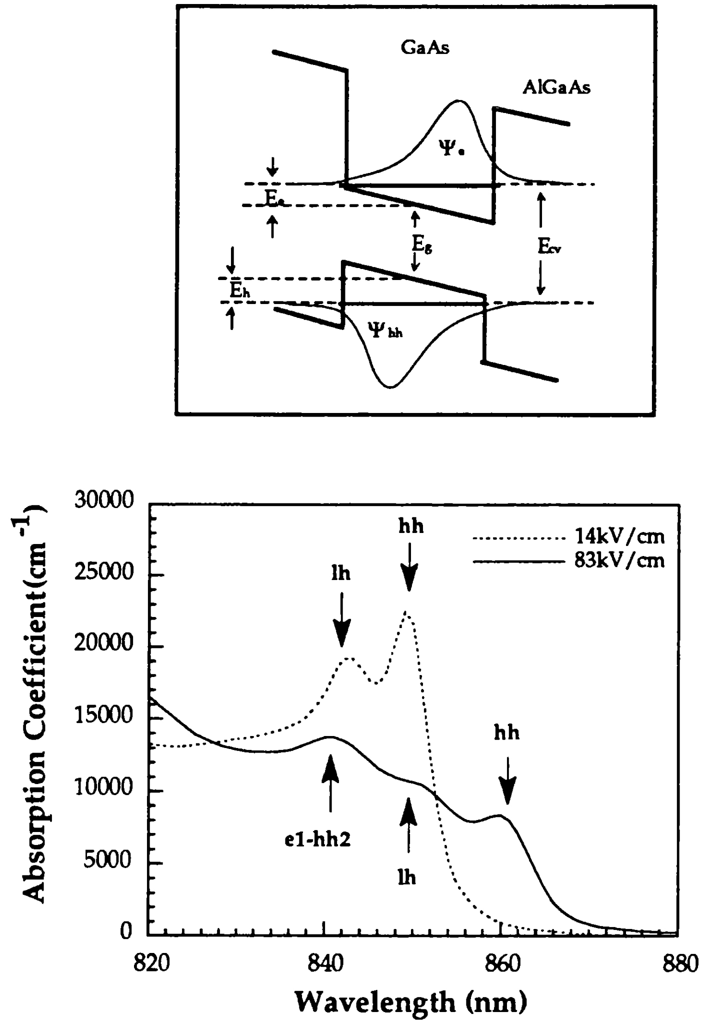

Fig.1.3.3. *Upon the application of an electric field perpendicular to the plane of the wells, the well is tilted and the energy levels shift to longer wavelengths. This is manifested in the experimental absorption spectra of a 95Å. The e1-hh1 (hh) and e1-lh1 (lh) transitions subside with field, while the "forbidden" e1-hh2 is gradually enhanced with field.*

selection rules to break completely as the symmetry along the middle of the well is destroyed and the wavefunctions lose their parity. At the same time, the two carriers are pushed to opposite sides of the well as a result of the opposite electrical forces they experience. These two effects lead to a reduction of the overlap between the two wavefunctions for an "allowed" transition and an increase for several previously "forbidden" transitions. In total, the main excitonic features in the absorption spectra red-shift with the application of a field, at the same time gradually losing their strength as the field is increased (Fig.1.3.3). We discuss this in some detail in Chapter 3. The QCSE was quantified and explained by D.A.B. Miller [1984], while the first people to observe the QCSE-associated red-shift of the spectra were Chemla and co-workers [1983]. A neat way to make use of the effect is to incorporate the wells in the intrinsic region of a p-i-n diode, as was first done by Wood and co-workers [1984]. All the above observations were first made in GaAs while now different material systems have been successfully realised. Finally, it is important to note that the electroabsorptive effects are simultaneously accompanied by strongly wavelength dependent electrorefractive effects as the two parameters (i.e. the absorption and the real index) are intimately interrelated (Chapter 2).

Quantum wells have become a topic of intense investigation and indeed many stimulating results have been generated by numerous groups worldwide. The confinement has been demonstrated to have beneficial effects on the operation characteristics of lasers and a wide range of devices can be realised using quantum wells. Quantum wells are, by definition, structures where the wavefunctions in each well are not influenced by the presence of the adjacent wells. When the well and the barrier are sufficiently narrow one refers to superlattice material which is ascribed distinct characteristic effects, such as the Wannier-Stark localisation effect [Voisin, 1989]. Also various other arrangements have emerged in recent years, the realisation of some having been the result of the refinement of growth techniques. Thus coupled quantum well systems [Atkinson *et al.*, 1990], asymmetric coupled [Lee *et al.*, 1988], parabolic [Ishikawa *et al.*, 1990], triangular [Kopf, 1992] and other more complex well structures have been realised each of them offering specific advantages or occasionally simply ground experimentation and deeper understanding. Finally, there has been a lot of incentive and effort in further reduced dimensionality, i.e. the realisation of quantum wires (1-D) [Ismail *et al.*, 1991] and quantum dots (0-D) [Fukui *et al.*, 1991].

1.3.2. Quantum well modulators.

The worldwide research in QWs has yielded a large range of optical as well as electronic devices that incorporate this type of material. The optical devices may be classified in two main categories: passive elements, i.e modulators and detectors, and active elements, i.e. lasers light-emitting diodes and optical amplifiers. The performance of these devices is more than often superior to those of bulk devices. However, the prime advantages of quantum well material lie firstly with its versatility in terms of the large diverse range of devices that may be fabricated and which are, more often than not, mutually integrable on the same wafer, and secondly with the vast scope for bandgap engineering that yields tailored operation within a large range of wavelengths. In the following we discuss quantum well modulators.

Modulators

The strong electroabsorptive and electrorefractive effects in QWs (Fig.1.3.3) can be exploited to realise voltage-controlled optical modulation. Modulators fall in two classes according to the direction of propagation of the optical beam with respect to the plane of the well, referred to as waveguide and transverse structures (Fig.1.3.4).

Waveguide modulators: Here the light propagates parallel to the plane of the wells and the absorption-length product (αd) is determined by adjusting the length of the waveguide. Thus incorporation of a small number of wells in the intrinsic region results in low voltages for a given electric field while the modulation depth is determined by the length of the device. There is, however, a trade-off between the operating voltage and the operating speed of the devices as their capacitance is increased for increasing guide length and decreasing intrinsic width. Waveguides are polarisation sensitive devices as the heavy-hole transition is not an allowed transition for the TM mode [Weisbuch and Vinter]. The results of Wood *et al.* [1985] that achieved 10dB contrast at 15 V with an insertion loss of 7.2dB are typical for an electroabsorption-based device in the GaAs system. In general, good contrast ratios may be attained at relatively low voltages with such modulators provided the quality of the quantum well medium is sufficiently high. High speed phase modulators have also been intensely investigated [Mendoza-Alvarez *et al.*, 1988]. Effects other than the electroabsorption and electrorefraction may also be utilised to obtain modulation. For example, Zucker *et al.* [1990] have achieved modulation by use of a current injection bandfilling mechanism where the carriers are stored in a (doped) barrier reservoir. Finally, Moretti *et al.* [1992] have demonstrated 22dB contrast at 2.5V using a superlattice. The insertion loss was, however, 13dB.

Waveguides have received a lot of attention because they are directly integrable with conventional lasers and ultimately also with fibres Their impact in photonic circuits to realise integrated receivers incorporating wavelength- and time-division multiplexing is expected to be very large, although not necessarily solely in the form of quantum well devices [Walker, 1991]. For these applications, InP based material will have to be used to exploit the low-loss optical window in fibres (≈1.55μm) [Pütz, 1991].

Transverse modulators: Both in optical switching and in interconnections applications, it may be necessary to fabricate large two-dimensional arrays of devices in order to achieve bigger pin density. This makes transverse devices most desirable as they allow free-space direct communication, random placement on a chip, easy access for optical accessories, and flexibility in connection routes. These may be found in the transmission or the reflection mode.

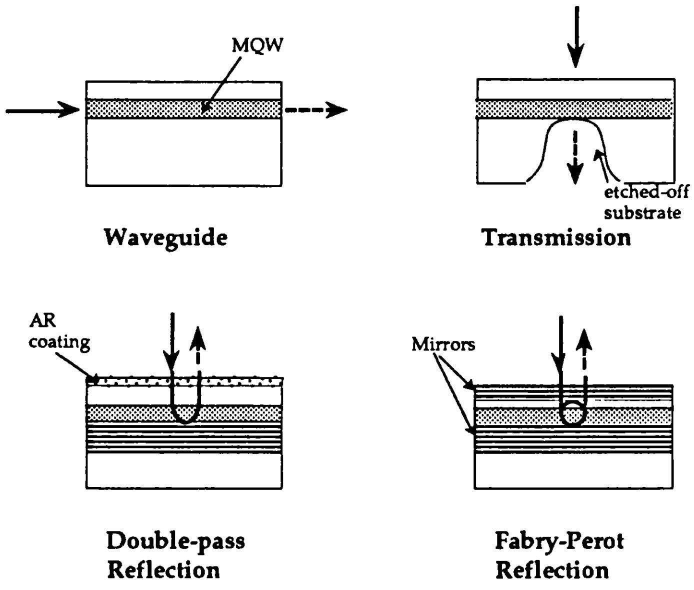

Fig.1.3.4 *Various quantum well modulator configurations.*

i. Transmission modulators: Unlike waveguide structures, here better contrast or transmission changes can only be achieved at the expense of the operating voltage as the intrinsic region width is also the interaction length between the optical beam and the absorbing medium. A 10dB contrast has also been attained by such an arrangement in GaAs but at a large voltage of ≈20V and with very large insertion loss (13dB), while obviously the exhibited transmission-change is indeed limited [Hsu *et* *al.*, 1988]. A serious disadvantage of transmission modulators in the GaAs system is that the substrate has to be etched off as it is absorbing at the wavelengths of interest. This, apart from complicating the processing, results in brittle devices. In certain systems the transmission mode may be beneficial and in particular in the InP system where the substrate is transparent [Barnes N, 1990a,b]. In general, however, reflection modulators are preferable as they offer better flexibility in positioning and addressing on a chip. Additionally, they acquire a better potential for vertical integration with electronics as well as with other optoelectronic devices.

ii. Reflection modulators: a)Double-pass reflection: With a Bragg reflector at the back and an anti-reflection coating at the front, a double-pass reflection modulator can be realised. The voltages of operation are half those of the transmission modulator for a given intensity change/contrast. A contrast of 9dB has been attained at 18V with an insertion loss of 5.7dBfrom such a structure [Boyd *et al.*, 1987]. Recently, Amano *et al.* [1991] have demonstrated a double-pass reflection modulator with >20dB contrast. This was achieved by a dramatic reduction of the background doping in the intrinsic region to $<10^{14}$cm^{-3} and the incorporation of 220 wells. Consequently, the operating voltage of that device is very high at 30V. b)Electrorefraction-based Fabry-Perot modulator (Symmetric Fabry-Perot modulator, SFPM): Such modulators are realised with a front and back reflector so that a Fabry-Perot cavity is formed. The resonance of that cavity is set at a wavelength far away (to longer wavelengths) from the zero bias exciton peak to attain a large ratio $\Delta n/\Delta\alpha$, where n is the real part of the refractive index and α is the absorption coefficient. The device is operated at its unbiased resonance and is not reflecting at zero bias whereas with a reverse bias applied the change of the index induces a shift of the resonant position. Consequently, a rise of the reflectivity at the position of the initial resonance is accomplished with bias. In theory such devices may achieve high contrasts. In practice, however, the combined effect of the high finesse and the required good matching between the reflectivities of the grown mirrors severely limits the modulation performance, and in particular the obtained contrast. Moreover, the operating voltages are inherently high because the operating wavelength is at a large separation from the exciton. Such devices inherently suffer from relatively high insertion losses. Contrast of 9dB has been exhibited at 25V with an insertion loss of 5.8dB [Simes *et al.*, 1988]. The low optical bandwidth and the slim tolerances of the SFPM are big disadvantages. c)Electroabsorption-based Fabry-Perot modulator: Here the electroabsorptive effects serve to reduce the effective back mirror and thus modulate the overall reflectivity at the resonant wavelength. Such a structure incorporating unequal (asymmetric) mirrors was first proposed and demonstrated by Whitehead *et al.* [1989b] and independently by Yan *et al.* [1989].

This asymmetric FP modulator (AFPM) exhibited a record contrast in excess of 20dB at 9V with an insertion loss of 3.5dB. Moreover, the wavelength range over which contrast in excess of 10dB is achieved is ≈6nm. This device performance was a major improvement over previously achieved performances. It is this type of modulators that we are concerned with in this thesis. Since the introduction of the AFPM in 1989, the operating voltage of such devices has been reduced to as low as 3V, in parallel with, and as a result, of the work presented in this thesis, making the device attractive for many of the applications discussed earlier in this introduction.

1.4 QUANTUM WELL MODULATORS IN OPTOELECTRONIC LOGIC

In order to perform optical logic it is required to either obtain bistability or a transfer characteristic with two hard limits so as to unambiguously encode the two logic levels. Various optical logic functions may then be performed using combinations of such devices. Ideally the devices should acquire non-critical biasing, input/output isolation, logic level restoration, and multiple functionality. Additionally, high speed operation at low optical power inputs, cascadability, and fan-out are vital for digital logic implementations.

There are several technologies that could be used in this respect [Midwinter, 1988]. Liquid crystal devices show bistable operation [Lloyd, 1987] but they have the disadvantage of slow speeds (ns). Bistability that relies on non-linear phenomena in semiconductors (and indeed as a rule in most materials) requires large input powers [Sfez *et al.*, 1990] which in principle does not favour such devices. A class of devices that seem to offer many of the previously mentioned required characteristics, utilise a combination of electroabsorptive effects and electrical feedback. Thus these devices are not purely optical in nature, although the inputs and the outputs are all in the optical domain, because electrical transport is endemic to their operation. Quantum wells are incorporated in such structures in most cases but some non-quantum well devices have also been demonstrated. We refer to these below.

Self-Electro-optic-Effect-Device (SEED)

The first SEED was demonstrated using a modulator connected in series with a resistor (R-SEED) [Miller D A B *et al.*, 1984]. However, a later version that uses two identical modulators connected in series, the symmetric-SEED (S-SEED), is far superior [Lentine *et al.*, 1988] and thus we will mainly discuss the S-SEED. This device may be realised when the individual modulators show negative differential resistance (NDR), i.e. a decrease of the current with biasing voltage. NDR is obtained for MQW modulators when operating at the vicinity at the zero bias heavy-hole exciton peak (Fig.1.3.3). When the two modulators are connected in series, Kirchoff's laws imply that an increase in the power absorbed on D1 (Fig.1.4.1) with respect to that absorbed in D2 is projected as a decrease of the voltage that is applied across D1 and vice versa. Moreover, as a result of the NDR, positive feedback is applied that causes the device with the least power-input to be it its least absorbing state. The operation is best understood by observing the load lines. A a more detailed account of the exact mechanism is given in Chapter 8 of this thesis. For a certain pair of inputs, there are two stable modes of operation provided the two powers are sufficiently different. One of the diodes is it its absorbing state with very little voltage at its terminals, and the other is it its least absorbing state with virtually all the biasing voltage applied to it. With the power on one of the diodes fixed at one level, switching of the composite device from one state to the other occurs at two different powers incident on the second diode depending on whether its power is being ramped up or down. Thus, within a range of input power, the composite device is bistable in the ratio of the input

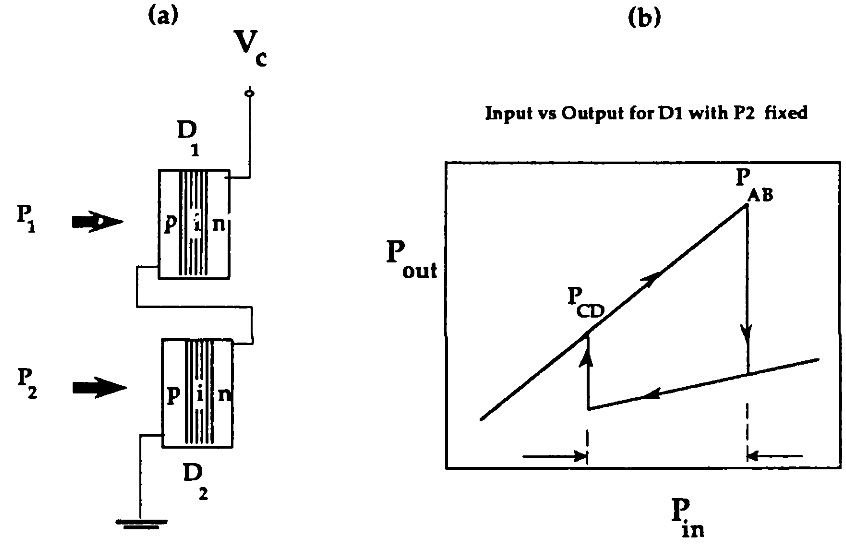

Fig.1.4.1 *A schematic showing the connection of two modulators in the S-SEED configuration (a). The performance is symmetrical for the two diodes. With a fixed amount of power incident on one of the diodes, the input-output characteristic of the other exhibits bistability (b).*

powers incident on the diodes. This may be implemented to produce various logic functions using combinations of devices [Lentine *et al.*, 1990b]. Eight-kbit arrays of devices have been fabricated [Chirovsky *et al.*, 1991] and various implementations of SEEDs have been demonstrated in the laboratory, such as the parallel interconnection between two 64x32 arrays of such devices [McCormick *et al.*, 1991]. The potential for 10Gbit operation has also been demonstrated [Boyd et al., 1990] and faster operation is potentially achievable [Feldman *et al.*, 1991]. The realisation of differential logic by the S-SEED implies that its operation is not critically dependent upon the optical power level although power requirements do affect the speed of operation (Chapter 8). As the device holds its state due to the finite time required for discharging the capacitors, time-sequential logic can be implemented which provides input-output isolation as well as the potential for the control of a high power beam by low input beams. These characteristics of the S-SEED, as well as further functionality [Grindle and Midwinter, 1991] are indeed valuable for real implementations. Also the S-SEED may be used as an exchange-bypass transparent switch, with the advantages discussed in section 1.2, or possibly in a combination of the relational and the logic mode to obtain self-routed switching [Grindle and Midwinter, 1992].

A similar to the S-SEED device has been reported [Kurata *et al.*, 1990] where a transmission modulator is connected with a current controlled negative resistance realised by a modified resonant tunnelling diode. For this device, the modulator is not required to exhibit NDR and thus may operate at wavelengths longer than the zero-bias exciton peak where good modulation characteristics are obtained. However, the results from that device are not particularly impressive. A variation of the S-SEED is the heterojunction bipolar transistor (HBT) SEED (T-SEED) [Wheatley *et al.*, 1987] where the two elements are a phototransistor and a modulator. This arrangement integrates a gain element which increases the cascadability of the resulting devices. The principle is the same as above [Taylor, 1990] but the device is not bistable. An integrated version of this structure has been recently demonstrated using FETs (F-SEED) [Woodward *et al.*, 1992]. Bistability may be obtained by connecting two T-SEEDs back -to-back. [Taylor, 1990]. Kurokawa *et al.* [1992a] have recently demonstrated bistability and various logic operations and optical memory functions [1992b], using a device that they name exciton-absorptive-reflection-switch (EARS). In reality, this is nothing else but a T-SEED where an AR coated reflection modulator is vertically integrated with a heterojunction phototransistor (HPT). Hara *et al.* [1990] have demonstrated an optical switch that is realised by the series connection of two parallel-connected pnpn heterostructures with a resistor. This structure does not incorporate quantum wells. On the other hand, Goswami *et al.* [1991] use HBT structures that incorporate QWs in their intrinsic region connected in parallel to obtain logic and memory functions.

Finally, logic devices may also be fabricated using active optical devices such as lasers and LEDs. The principle of operation is largely similar to that above in that electronic feedback is employed. For example, Chan *et al.* have used a laser diode to create a switch [1991] and Ogura *et al.* have demonstrated vertical-cavity vertical-to-surface-transmission-electrophotonic devices (VC-VSTEP) switching operation [1991]. Beyette *et al.* [1992] have realised a logic gate using two HPTs as the input and a third HPT in series with an LED for the ouput. These switches exhibit real optical gain. In general, gain is desirable in systems where cascades of stages are required to compensate for the losses and to allow for high powers at all inputs thus achieving higher speeds. It is not clear, however, whether an optical source needs to be incorporated and this systems-decision will largely depend upon the specific application. The arguments against a source element are identical to these listed when encountered with the analogous problem in interconnection applications. The use of transistors to provide the required gain, combined with arrangements where a fresh high power clock beam is applied at the passive optical output element (modulator), may be sufficient thereby avoiding the incorporation of optical sources.

1.5 INTRODUCTION TO THE THESIS

Progress in III-V compound semiconductors has allowed the fabrication of low-dimensional structures such as quantum wells which produce distinct effects thereby lending themselves to practical exploitation. The technology has reached the stage where a range of discrete devices have been realised and small-scale integration of these has been implemented. A reflection modulator is a versatile device that comprises the main building block in many applications such as optical interconnections in VLSI and switching matrices in communications and data processing. The parallel effort at both the systems and the device design level has produced a series of concrete conclusions in some areas while, on the other hand, there are aspects of the technology that are still under debate. At this stage of development it is imperative that any component design makes use of the insights gained with regard to systems requirements and addresses practical issues with which an implementation of the component would be confronted.

This thesis deals with multiple quantum well electroabsorption Fabry-Perot modulators. The aim of this work is to develop a comprehensive design method for this type of device, evaluate the obtainable performance after a thorough optimisation, and assess its potential performance under real conditions. This would facilitate a realistic view of its implementation at the systems level. The work is restricted to the GaAs system but both the method and the general conclusions may be extended to other material systems.

We start with an introduction (Chapter 2) to the operation of the asymmetric Fabry-Perot modulator (AFPM), bringing up various aspects of the integrated device such as the speed of operation. In that Chapter, we determine the optimisation aims with respect to different applications and set the target performance characteristics for the design to follow. The design is based upon modelled reflectivity spectra the derivation of which is presented in Chapter 3.

The next Chapter is a description of the experimental study of the temperature tolerance of the AFPM, which is of paramount practical importance. The insights gained from that work are subsequently employed in the study of the overall tolerances in Chapter 5. There we address the tolerances to lateral non-uniformity across the epitaxial wafer and calibration accuracy and refer to expected progress in that direction. A method for the evaluation of the combined tolerances of the modulator is developed, where we identify a measure of the tolerances and thus devise means of optimisation in that respect. This is supported by experimental results from a device where such optimisation has been applied. Furthermore, we assess the requirements for optical addressing and alignment, including the effect of incidence off the normal. In Chapter 6 we present experimental results from two modulator designs that achieve a substantial improvement of the modulator characteristics, compared to the original AFPM, but at the same time achieve the same degree of tolerance. Moreover, these results confirm the validity of several optimisation techniques that we have considered theoretically. Subsequently, the conclusions from the study in Chapters 4-6 are implemented in Chapter 7 where modelling facilitates a comprehensive evaluation of the achievable performance from structures that incorporate different well widths. This is done after optimisation has been applied to the designs and finally produces a quantitative study of the trade-offs as well as optimisation with respect to well width. We then proceed to some example designs of structures that are optimised to meet specific performance requirements.

In Chapter 8 we discuss configurations that exhibit negative differential resistance (NDR). We present a novel configuration where the electroabsorptive effects yield modulation in a symmetric Fabry-Perot cavity (SCEM), including theoretical analysis and experimental data. This configuration results in an improvement of modulation depth as compared to other NDR-exhibiting devices and may thus be exploited in SEEDs. Indeed, SEED operation is experimentally demonstrated using SCEMs. In order to compare the SCEM and the bias-reflecting (hence NDR-exhibiting) AFPM, we evaluate the best performance attainable by such AFPMs after optimisation is implemented.

Next, having analysed various aspects of the performance of the devices thus far in the thesis, we return to their implementation in Chapter 9. There we discuss the manufacture of 2D arrays and the integration of the reflection modulator with other optoelectronic devices as well as with electronic circuitry. The discussion is extended to the multiple functionality of this type of structure and shows how this is reflected on useful implementations. In the same Chapter we also present a set of novel ideas where the FP reflection modulator is incorporated in composite configurations to produce a range of functions. Finally, a brief overall summary concludes the thesis.

CHAPTER 2: THE INTEGRATED FABRY-PEROT MODULATOR: OPERATION, DEVICE FABRICATION, EXPERIMENTAL METHOD, AND OPTIMISATION OBJECTIVES

2.1 INTRODUCTION

In this Chapter we introduce the operation of electroabsorption-based Fabry-Perot modulators that are the subject of this thesis. The base-line of this work has been the demonstration of the asymmetric Fabry-Perot modulator (AFPM) by Whitehead *et al.* [1989b], and independently by Yan *et al.* [1989]. The principle of operation of the AFPM is described. We give a detailed account of the impact of the electroabsorptive effects on the performance of the modulator, discuss the operation of Bragg stacks that comprise an essential part of the integrated device, and we raise the issues involved in determining the speed of the device. Additionally, we discuss the epitaxial growth and the device fabrication process, and describe the experimental method and apparatus that has been employed in the practical part of this study. Finally, we proceed to a discussion of the optimisation objectives and the target performance characteristics of the modulator.

2.2 THE FABRY-PEROT EFFECTS

Two parallel mirrors of reflectivities R_f and R_b separated by a medium of index n_m and thickness L, form a Fabry-Perot cavity. Multiple reflections between the two mirrors give rise to interferometric effects that depend upon the corresponding optical length $L_{opt} = L \cdot n_m \cdot \cos\vartheta/\lambda$, where λ is the optical wavelength and θ is the angle with respect to the normal within the cavity medium (Fig.2.2.1). The reflectivity R is thus given by [Whitehead *et al.*, 1989a]

$$R = \frac{\left[R_f \cdot \left(1-\sqrt{R_b/R_f}\right)^2 \Big/ \left(1-\sqrt{R_f \cdot R_b}\right)^2\right] + F \cdot \sin^2\varphi}{1+F \cdot \sin^2\varphi} \qquad 2.2.1$$

$$\varphi = 2\pi n_m L/\lambda \quad \cdot \cos\vartheta$$

where F is the coefficient of finesse given by $F = 4\sqrt{R_f R_b}\Big/\left(1-\sqrt{R_f R_b}\right)^2$, and ϕ is the

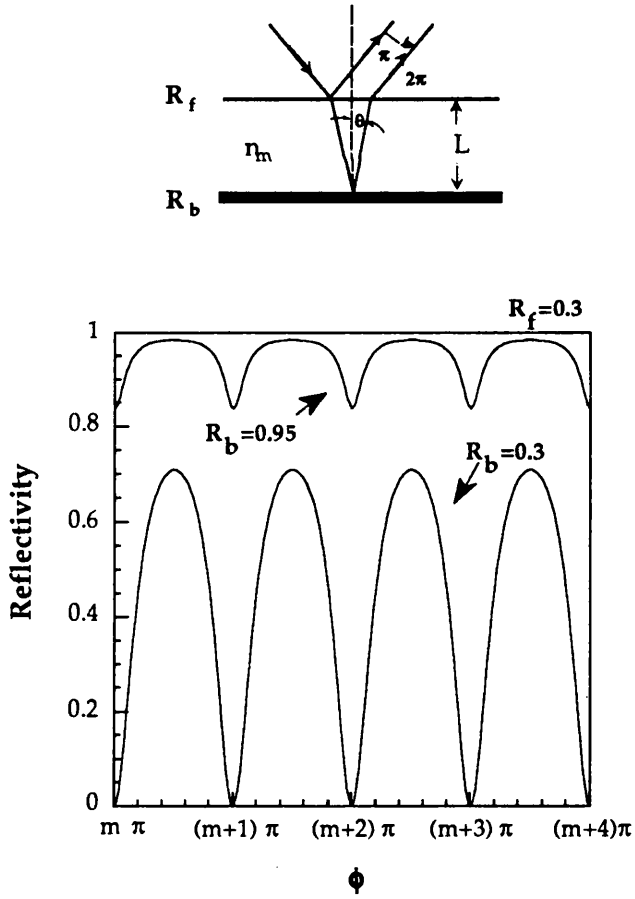

Fig.2.2.1 *Interference in a Fabry-Perot cavity results in the known fringes shown here in the reflectivity against the phase-change plot.*

(one-way) phase-change through the cavity medium. Destructive interference at the front surface occurs when the multiply reflected beams are in-phase but they are in antiphase with the beam that is directly reflected at the front surface (Fig.2.2.1). Therefore, reflection minima correspond to transmission maxima and occur at equally spaced (2π) intervals of double-trip phase-change through the cavity. The reflectivity of monochromatic light incident on such a cavity, is minimum at integral multiples of a certain mirror separation, or of angle of incidence, and, for the same underlying reason, the spectra of the reflected intensity from a certain fixed cavity exhibit evenly spaced minima (transmission maxima) (Fig.2.2.1). Complete cancellation of the reflected light at a resonant position can only be attained if the reflectivities of the two mirrors are equal ($R_f=R_b$). Indeed, only under that condition, are both the phases and the individual amplitudes such that the sum of the complex amplitudes of the multiply reflected beams is equal in amplitude to that of the directly reflected one.

With absorption in the cavity, the effective back reflectivity R_b^{eff} is reduced to

$$R_b^{eff} = R_b \cdot e^{-2\alpha d} \qquad 2.2.2$$

where α is the absorption coefficient and d the thickness of the absorbing material. The reflectivity of such a cavity at a *resonant* wavelength is given by

$$R = \frac{R_f \cdot (1 - R_\alpha / R_f)^2}{(1 - R_\alpha)^2}$$

$$\qquad 2.2.3$$

$$R_\alpha = \sqrt{R_f \cdot R_b} \cdot e^{-\alpha d}$$

The higher the reflectivity of the mirrors the sharper the FP resonances and this is described by the cavity finesse

$$\mathcal{F} = \frac{\pi\sqrt{F}}{2} \qquad 2.2.4$$

where now, with absorption in the cavity, the coefficient of finesse is given by the equivalent $F = \frac{4R_\alpha}{(1-R_\alpha)^2}$, i.e. R_b has been replaced by R_b^{eff} in the previous expression.

2.3. THE INTEGRATED FABRY-PEROT MODULATOR

2.3.1. Principles of operation.

FP cavities can be implemented to enhance the manifestation of electroabsorptive effects in QWs. The QWs are then employed as a field-dependent absorber (quantum confined Stark effect, Fig.2.3.1) that determines the effective reflectivity of the back mirror R_b^{eff} (eqn.2.2.2). The reflected optical signal of monochromatic light of a wavelength coinciding with one of the FP resonances, can be controlled in this manner by an electrical signal, thereby realising voltage-controlled optoelectronic modulation.

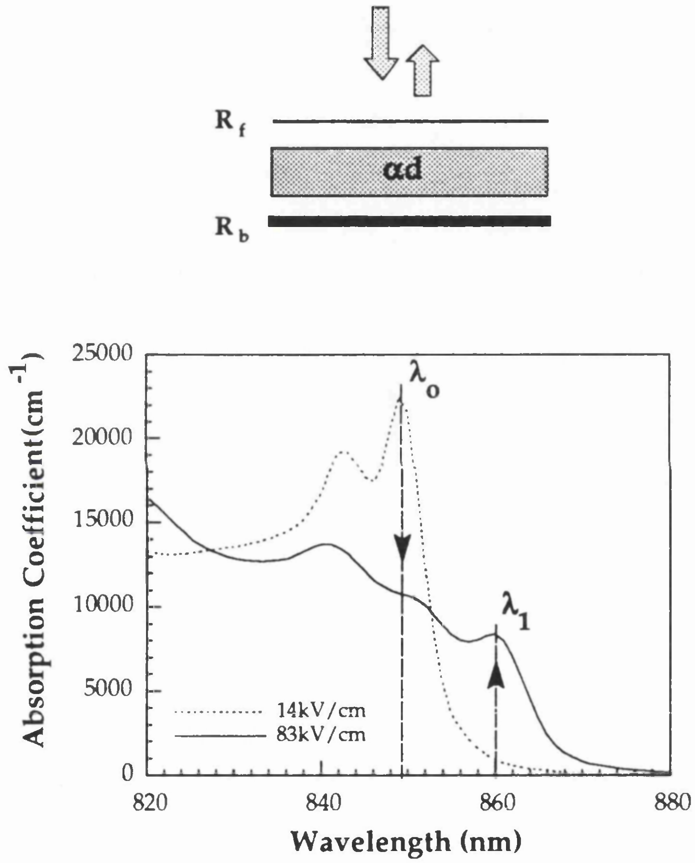

Fig.2.3.1 *The field-induced modulation of the absorption coefficient of quantum wells can be employed to attain a modulation of the reflectivity of a Fabry-Perot cavity. Normally-on operation is obtained at* λ_1 *and normally-off at* λ_o.

The Asymmetric Fabry-Perot Modulator (AFPM) is such a device the operation of which relies upon the electroabsorption effects in QWs. These are incorporated in a FP cavity with asymmetric (unequal) mirrors such that $R_f<R_b$ and with an optical length that leads to a resonance at a (pre-) designed wavelength. The operation is set at that resonance, i.e. at a reflection minimum. For such an arrangement, with little or no absorption in the cavity, the front and effective back mirrors are unequal so that complete cancellation of the interfering beams cannot be accomplished and therefore the device is reflecting part of the incident intensity. We will refer to this as the on-state (positive logic). If a sufficient amount of absorbing medium is introduced in the cavity so that $R_f=R_b^{eff}$, the device switches to its off-state the total reflectivity being zero. The quantum well absorption serves to reduce the back mirror and attain this action. The critical amount of absorber $[\alpha d]_c$ required to accomplish zero off-state reflectivity is given by

$$[\alpha d]_c = \ln\sqrt{\frac{R_b}{R_f}} \qquad 2.3.1$$

When the FP wavelength λ_{FP} is set at a wavelength longer than the zero-bias heavy-hole exciton peak, then at zero bias there is minimal absorption at the resonant position brought about by the absorption tails of the QWs. Thus the device is at its reflecting state with no bias applied. With the appropriate bias applied across the wells, the absorption coefficient is increased at the resonance causing the device to switch to its off-state (non-reflecting). The above would be a so called *'normally-on'* or bias-absorbing device. The operating wavelength would correspond typically to λ_1 in Fig. 2.3.1. By contrast, with the resonant wavelength set at the vicinity of the zero-bias exciton peak, the situation is reversed in that the amount of absorber that is present at

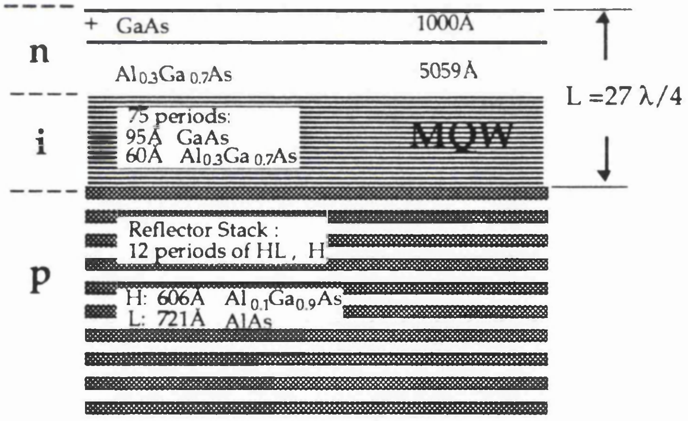

Fig.2.3.2 *The epitaxial structure of CB145 AFPM that was grown by MOCVD at the University of Sheffield.*

the resonance drops with field. The device is so called *'normally-off'* or bias-reflecting. Such a device would be operating at λ_0 in Fig.2.3.1. The latter configuration exhibits negative differential resistance (not because of the FP effect but certainly enhanced by it) which is a necessary condition for optical bistability [Miller D A B *et al.*, 1989].

It follows from the above that in order to realise an integrated AFPM the structure has to be electrically a p-i-n diode so that bias can be applied across the wells, and optically a FP cavity. The epitaxial structure of the first AFPM designed by M. Whitehead [1989b] is shown in Fig.2.3.2. The MQWs are incorporated in the intrinsic region of the diode, while the FP cavity is formed between the natural front air-semiconductor interface that is ≈31% reflecting and an integrated back mirror that has a reflectivity of ≈95% in this case. This back reflector is a multilayer Bragg stack consisting of alternating quarter wave layers of high (H) and low (L) refractive index materials, namely $Al_{0.1}Ga_{0.9}As$ and AlAs respectively. A brief section on the operation of the Bragg reflector stacks follows later on in this Chapter (section 2.4) and so does information on the growth, device fabrication and experimental testing techniques.

2.3.2. Experimental performance.

Operation as a modulator

Field-dependent reflectivity spectra from a device that was fabricated from the structure in Fig.2.3.2, are shown in Fig.2.3.3. The excitonic features may be seen clearly in the zero-bias spectra (heavy-hole at ≈851nm) with the resonant position at a longer wavelength (≈862nm). The QCSE-induced shift of the heavy-hole exciton yields a reduction of the resonant reflectivity that falls to zero at 9V reverse bias. Higher voltages cause the exciton to shift further from the resonant position and thus lead to an increase of the reflectivity at the resonant (operating) wavelength. The position of the resonance may be seen to be voltage dependent. This is caused by the QW electrorefractive effects that are discussed in the next section. Operation at around 862nm and at 9V reverse bias exhibits contrast (R_{on}/R_{off}) in excess of 20dB (contrast ratio >100:1) with an insertion loss of ≈3.5dB (insertion loss = $10\log(R_{on})$) as shown in Fig.2.3.4. It is also evident from the same figure that contrast in excess of 10dB is exhibited within a wide wavelength range of ≈5.5nm. This broad resonance of the AFPM is a result of the low finesse of this configuration with the additional characteristic that in the off-state, which is the one that effectively determines the contrast, the cavity is equivalent to one with front and back mirrors equal to R_f (R_b^{eff} = R_f=0.3), resulting in a low finesse of just 2.45 at that state. The wide resonance does not only lead to a large optical BW but it also reflects the general tolerances of the structure, as will be discussed in Chapter 5.

Maximum reflection-change ΔR_{max}=48% is obtained at ≈864nm, i.e. at a longer wavelength than that where maximum contrast is achieved. The two maxima do not coincide because whereas the wavelength of maximum contrast is determined by the position where the off-state reflectivity is minimum, the reflection-change is equally governed by both the on- and off-state spectra (subtraction).

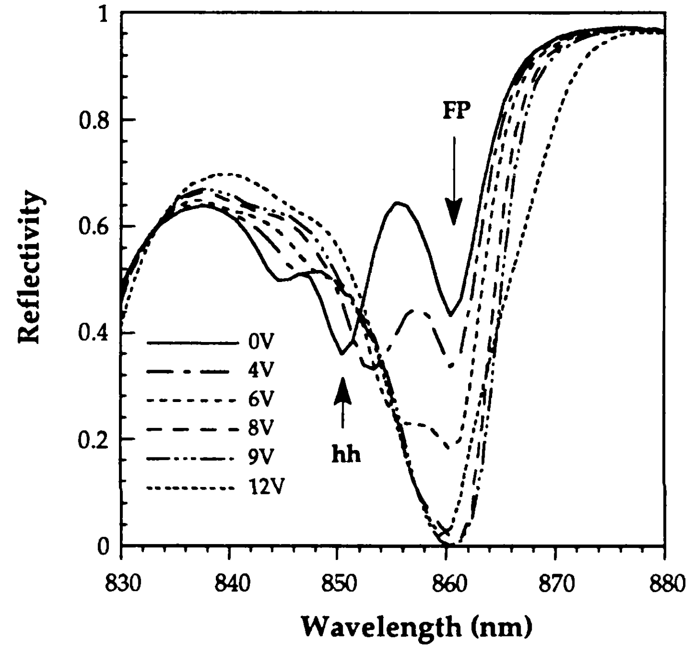

Fig.2.3.3 *Reflectivity spectra for CB145 AFPM, the epitaxial structure of which is shown in the previous Fig.2.3.2. Data by M. Whitehead.*

The AFPM by far outperforms any other vertical modulator in terms of contrast, reflection-change, and operating voltage. Transmission and double-pass reflection modulators (Chapter 1) are limited mainly by the fact that the improvement of the achieved modulation depth with increasing number of wells levels off due to broadening of the absorption spectra when the number of wells becomes too large [Stevens, 1989]. Recently, well after the AFPM had been introduced, very good quality MQWs with very low background dopings of <10^{14}cm^{-3} (compared to the common 10^{15}cm^{-3}) have been reported [Amano *et al.*, 1991]. The above mentioned tradeoff is

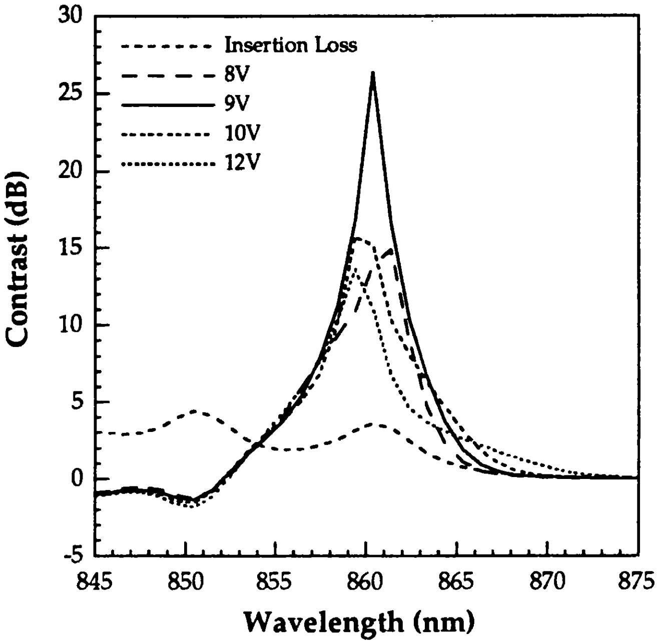

Fig.2.3.4 *Bias dependent contrast ratio curves and insertion loss obtained from the data in Fig.2.3.3.*

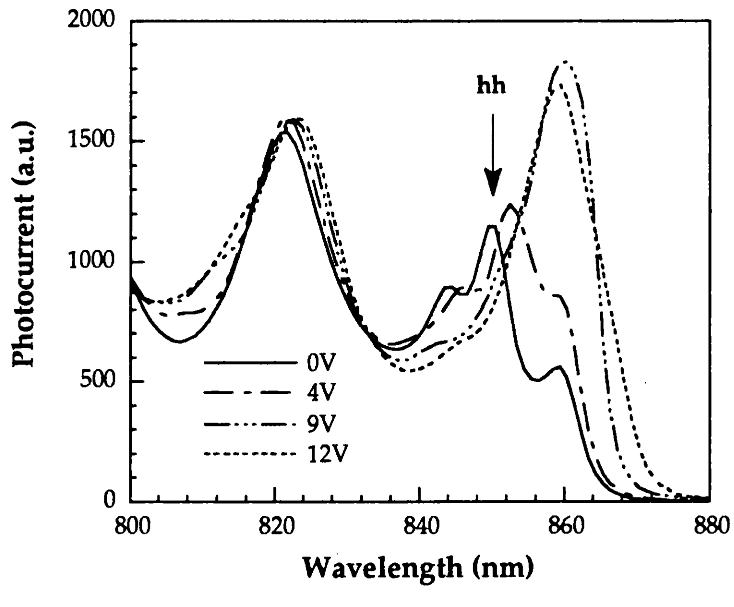

Fig.2.3.5 *Photocurrent spectra for the same device as in Fig.2.3.3. Data by M. Whitehead.*

then bypassed and large contrasts (>20dB) may be obtained by non-resonant structures. The operating voltages are, however, prohibitively high (≈30V) for most major applications (section 2.5). Symmetric Fabry-Perot modulators (Chapter 1) that make use of the electrorefractive effects [Simes *et al.*, 1988; Yan *et al.*, 1989b] are highly intolerant structures that may yield large reflection-changes but at considerably high voltages (25V). Finally, we ought to mention that waveguide modulators attain large changes at very low voltages, but they are planar structures with the advantages and disadvantages this encompasses (Chapter 1). The AFPM comprises thus a small scale breakthrough as far as modulator characteristics are concerned.

Operation as a detector

In Fig.2.3.5 we present photocurrent spectra for the same device as above. The spectra are scaled at ≈750nm to account for the voltage-dependent quantum efficiency. In this way, although the spectra do not correspond to absorptance (A) directly (Chapter 3), the change of photocurrent at each wavelength does correspond to the modulation of the absorptance. The choice of 750nm is somewhat arbitrary but can be justified as follows. Firstly, this wavelength is shorter than the wavelengths associated with both the light-hole exciton and the e1-hh2 forbidden transition but at a longer wavelength than the second order transitions, which has been confirmed by photocurrent spectra of simple p-i-n samples of the same well width. The implication therefore is that this part of the absorption spectrum is, to a large extent, not dependent upon the applied field. Moreover, this was further supported by the fact that upon the application of a field the reflectivity spectra at this wavelength did not show a notable change.

The presence of the Fabry-Perot cavity has a profound effect on the absorptance (A) that is given by

$$A = \frac{\left(1-e^{-\alpha d}\right)\cdot\left(1-R_f\right)\cdot\left(1+R_b\cdot e^{-\alpha d}\right)}{\left(1-R_\alpha\right)^2} \qquad 2.3.2$$

The features in the photocurrent spectra correspond directly to those in the reflectivity spectra. The maximum absorption, that occurs at the resonant position at 9V, is estimated from calculations to be ≈99%. The AFPM configuration can act, therefore, as a very efficient detector within a wavelength range of ≈5.5nm. This dual functionality of the AFPM adds another positive point to a long list of advantages over alternative structures. A discussion concerning the multiple functionality and large versatility of the AFPM is included in Chapter 9.

2.3.3 The electrorefractive effects.

A change of the absorption spectrum is simultaneously accompanied by a change of the (real) refractive index spectrum, as those two characteristic parameters of materials are intimately linked. This is expressed by the Kramers-Krönig relation.

$$\Delta n(E) = \frac{hc}{\pi} \cdot \mathcal{P} \int_{0}^{\infty} \frac{\Delta\alpha(E')}{E'^2 - E^2} \cdot dE' \qquad 2.3.3$$

where E and E' are photon energies and $\mathcal{P}$ denotes the principal Cauchy integral. As a consequence, the electroabsorptive effects in quantum wells give rise to

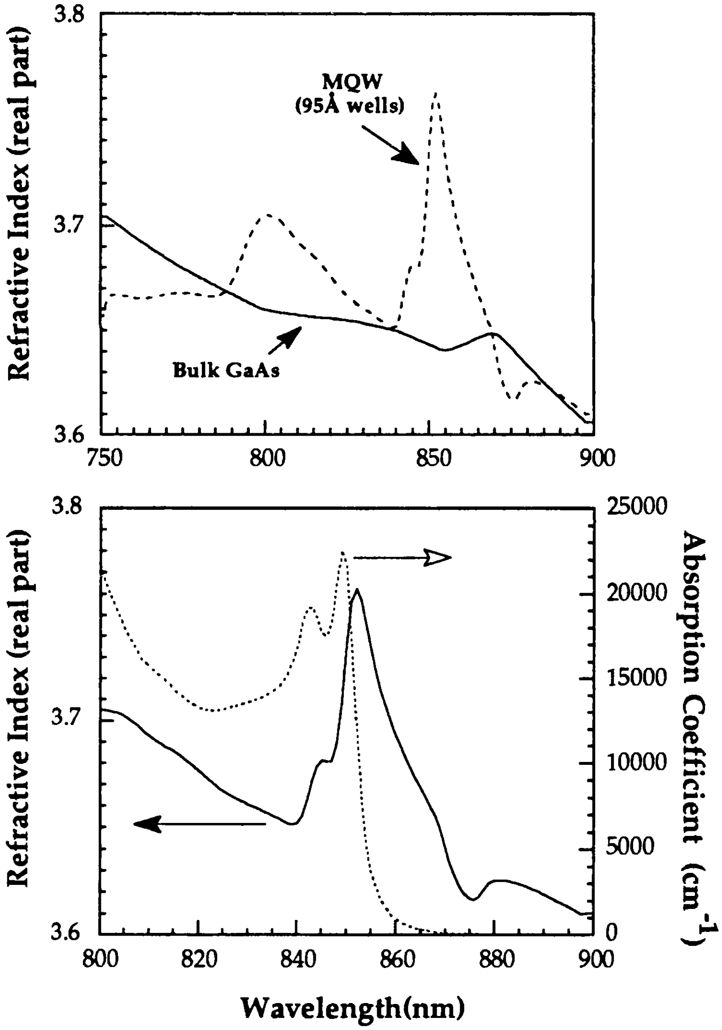

Fig.2.3.6 *The excitonic features in quantum wells cause a modification of the index with respect to that of bulk GaAs. The latter is reproduced from Sell et al. [1974]. Absorption spectrum for 95Å wells (0V) as in Fig.2.3.7.*

electrorefractive effects. Thus upon the application of a field the index of the MQW material may change substantially at a certain wavelength and therefore the Fabry-Perot resonances may experience a QCSE-induced shift.

The refractive index of bulk material is, in general, a decreasing function of wavelength. The experimentally obtained index spectrum of lightly p-doped bulk GaAs is shown in Fig.2.3.6, as reported by Sell *et al.* [1974]. The index of GaAs wells will be modified with respect to that of bulk, because of the excitonic features in the QW absorption spectrum. We may calculate the index spectrum of, for example, 95Å wells from that of bulk GaAs by means of eqn.2.3.3. For this purpose, the absorption spectra of both bulk and quantum wells are required over a large range of wavelengths. We use the absorption spectrum of bulk GaAs from Sturge [1962] and

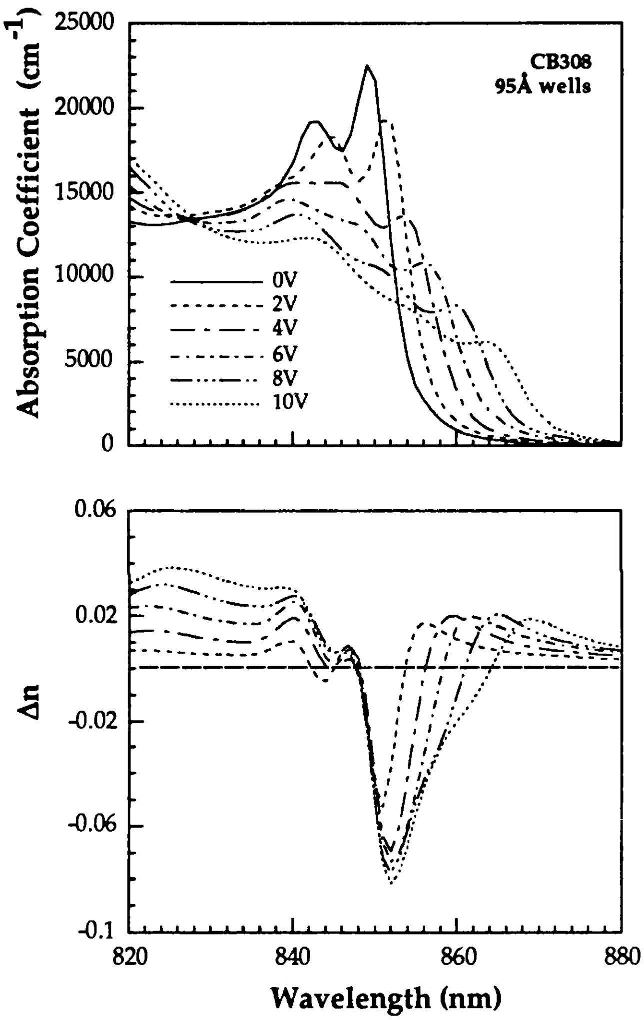

Fig.2.3.7 *The change in absorption induced by the QCSE is simultaneously accompanied by a field-dependent change Δn in the index of the well material.*

our experimental absorption spectra for 95Å wells obtained when no bias is applied across them. The absorption coefficient corresponds to the well material only. The derived quantum well index spectrum is shown in Fig.2.3.6 with the unbiased absorption spectrum being also shown to facilitate the identification of the observed features. Note that the required integration to yield the index-change spectra (eqn.2.3.3) was performed over the 750-900nm wavelength range.

Upon the application of a field, the QCSE-induced red-shift of the excitons causes a modification of the QW absorption spectrum and therefore leads to an alteration of the corresponding index spectrum. Experimental bias dependent absorption spectra for the 95Å wells and the corresponding changes of the index spectra are shown in Fig.2.3.7. The integration has again been performed over the 750-900nm range. The final index spectrum at a reverse bias V_o is given by the sum $n(V_o)=n(0V)+\Delta n(V_o)$ at each wavelength, where the zero bias index spectrum n(0V) for the well is shown in Fig.2.3.6.

It follows from the above that the position of the Fabry-Perot resonance, where the modulator would operate, is dependent upon the applied electric field. It is clear, however, that these index changes are restricted to the well material only and therefore the manifestation in the reflectivity spectra depends upon the proportion of well material within the total cavity medium. Around the 862nm wavelength, where the device in Fig.2.3.3 operates, the electrorefractive effects are relatively weak. In general for normally-on modulators that operate at wavelengths longer than the exciton peak, the performance is predominantly governed by the electroabsorptive effects. By contrast, the electrorefractive effects may be quite significant at the vicinity of the exciton peak and thus in the case of normally-off modulators. Work by Livescu *et al.* [1992] and Boyd and Livescu [1992] also supported this view. Notwithstanding, the electrorefractive effects are readily manifested in the spectra of Fig.2.3.3 and Fig.2.3.5, albeit without any major effect upon the performance of the device. Indeed, the resonance can be seen to shift to shorter wavelengths upon an increase of the voltage from 8V to 10V in agreement to expectations based on the data in Fig.2.3.7.

2.3.4 The multilayer reflector stack.

In order to realise an integrated resonant vertical structure, it is required to be able to construct high quality epitaxial mirrors of controllable reflectivity. The back mirror needs to be as highly reflective as possible in order to obtain an optimisation of the performance, as will be discussed in Chapters 6, while also front mirrors need to be used so as to reduce the operating voltage (Chapters 6 and 7). Thus the Bragg reflector stack comprises an essential part of the modulator.

The operation of the multilayer stack is illustrated in Fig.2.3.8. A quarter wave layer (thickness equal to $\lambda_o/4n$, where n the refractive index of the material)

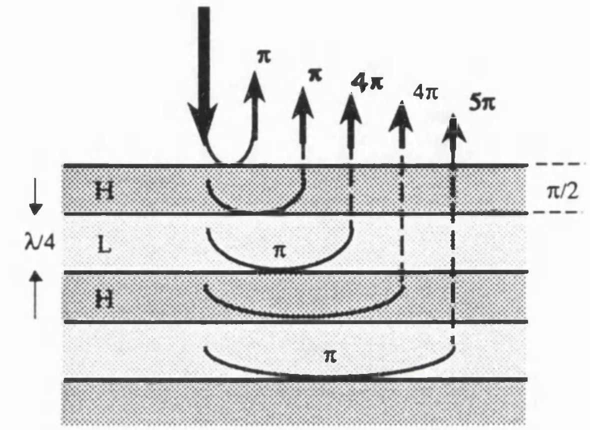

Fig.2.3.8 *A schematic diagram illustrating the operation of a Bragg reflector stack formed by alternating quarter-wave layers of high (H) and low (L) refractive index materials.*

introduces a double-pass phase-change of π. The directly reflected beam and the 1st, 3rd, 5th etc. order multiply reflected beams within each layer (not shown in Fig.2.3.8) are in phase at the top surface of the stack leading to a reflection maximum at λ_o. The reflection from one of those layers is very low and thus alternating layers of high (H) and low (L) refractive index materials are employed to contribute to the overall constructive interference and yield large reflectivities. Note that there is a phase change of π on reflection from a low to a higher index medium. The reflectivity R_s of such a multilayer reflector stack (MRS) is dependent upon the ratio n_H/n_L of the high and low indices respectively, and upon the number N of pairs employed in the stack as depicted by

$$R_s = \left[\frac{\frac{n_{in}}{n_s} - \left(\frac{n_H}{n_L}\right)^{2N}}{\frac{n_{in}}{n_s} + \left(\frac{n_H}{n_L}\right)^{2N}} \right]^2 \qquad 2.3.4$$

where n_{in} is the refractive index of the medium of incidence (in this case the mean value for the MQW region) and n_s that of the exit medium which in this case is the substrate.

The absorption in the reflectors obviously has to be minimal at the operating wavelength. Therefore, for a device that incorporates ≈100Å GaAs wells and $Al_{0.3}Ga_{0.7}As$ barriers, the stack must be non-absorbing at wavelengths longer than ≈850nm (to allow for normally-off operation as well) and consequently the aluminium content of the layers comprising the stack has to be greater than 10%. When the objective is a large mirror reflectivity it is also important to use large values of n_H/n_L as follows from eqn.2.3.1. As a result, $Al_{0.1}Ga_{0.9}As$ (H) and AlAs (L) are used in that case. Calculated spectra of such a MRS with a high-reflectivity band centred at 860nm are shown in Fig.2.3.9 for different periods of HL pairs. The spectrum is a band-pass with a FWHM of

$$\Delta\lambda = \frac{2\lambda_o}{\pi}\cdot\sin^{-1}\left[\frac{n_H-n_L}{n_H+n_L}\right] \tag{2.3.5}$$

where λ_o is the centre wavelength in nm. When smaller wells are used, specifically below ≈70Å, higher concentrations of Al have to be used for the high index layer. This imposes the need for a larger number of periods in the stack in order to obtain a certain reflectivity as follows from eqn.2.3.4. Additionally, the consequent reduction of the ratio n_H/n_L leads to a narrowing of the high-reflection band of the stack according to eqn.2.3.5.

The experimental values for the bandwidths of the Bragg stacks used in this

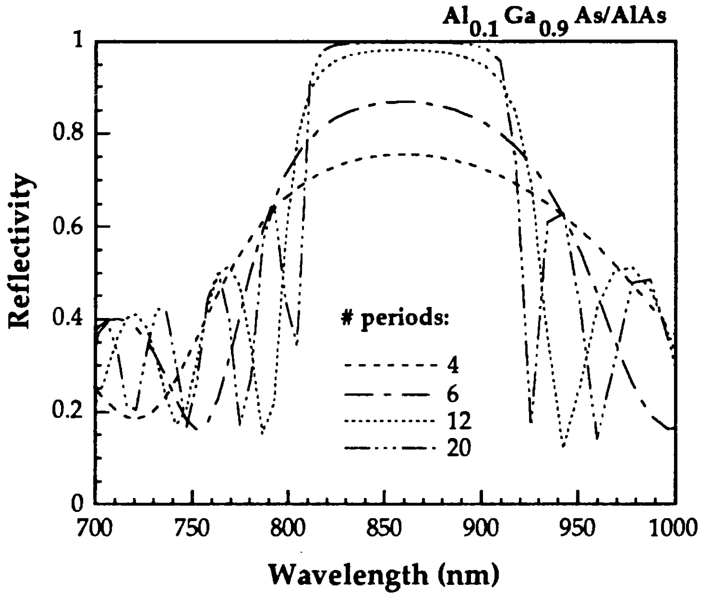

Fig.2.3.9 *The high reflection band of a $Al_{0.1}Ga_{0.9}As/AlAs$ quarter wave stack centred at 860nm (n_H=3.54, n_L=2.98).*

work, deviate slightly from the theoretically estimated values. Specifically, the bands are found to have a FWHM of ≈90nm as opposed to the calculated ≈110nm. This may be caused by a few reasons, or, most likely, by a combination of these. In general, the FWHM of the stack is restricted when the optical lengths of the two layers in the pair do not correspond to the same central wavelength. This can be brought about by erroneous Al-concentrations in the AlGaAs (H) layer, that will affect the refractive index and possibly the thickness (Chapter 5) and will thus have the dual effect of both reducing n_H/n_L (eqn.2.3.5) and causing the optical length of that layer to deviate from the intended. The thickness of the AlAs may also be different from that intended and not necessarily by the same proportion as that of the AlGaAs layer. This latter point would by itself cause the band-pass of the stack to become narrower since then the corresponding centre wavelengths would differ for the two layers within the period.

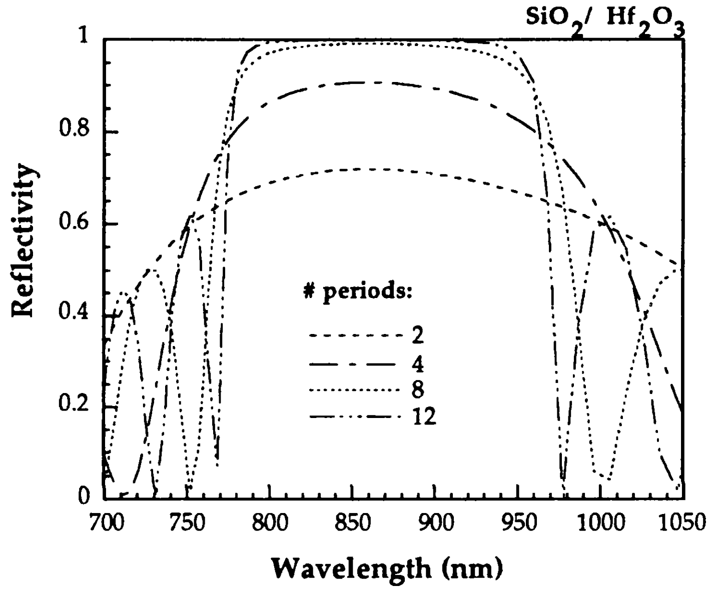

Fig.2.3.10 *The high reflection band of a* SiO_2/Hf_2O_3 *quarter wave dielectric Bragg stack centred at 860nm* (n_H=2.0, n_L=1.5).

The recent advances in surface emitting semiconductor lasers have fuelled an increased interest in various high quality stacks. Interestingly, a lot of work on those structures was carried out a few decades ago when optical filters were developed for completely different applications. Alternative stacks that can be used as front mirrors, and can be deposited on the front surface after the device fabrication has taken place, are dielectric stacks using materials such as SiO_2, TiO_2, Hf_2O_3. Calculated spectra for a dielectric stack are shown in Fig.2.3.10. The high-reflectivity bands of those stacks are broader as follows from the lower indices of both the materials in comparison to these of AlAs and $Al_xGa_{1-x}As$ (eqn.2.3.5). The low indices of these materials allow large reflectivities to be attained with a small number of periods. By the same token, however, the reflectivities that may be obtained from a certain pair are restricted. This is offset by the availability of a large range of materials that are readily deposited in the same machine, as we mention in Chapter 5.

Bayler *et al.* [1991] have demonstrated the fabrication of air/AlGaAs stacks, the motivation having been that the number of layers that are needed to attain a large reflectivity is indeed reduced in this case where the ratio of n_H/n_L is increased to 3.4, when the corresponding value for an $Al_{0.1}Ga_{0.9}As$/AlAs stack is 1.2. The manufacture difficulties imposed by such a stack, however, and the implied inflexibily upon the integration of different components, by far outweighs the advantages.

Finally, we ought to point out that the design of the Fabry-Perot cavity, in particular the required cavity-length, is modified as caused by the incorporation of Bragg reflector stacks. Thus, for a cavity where the front mirror consists of an even number of periods starting with a high-index material (HLHL...HL) and the back mirror starts with a high-index material as well, a resonance is obtained where the optical length corresponds to an odd number of quarter wavelengths. By contrast, if the front mirror consists of an odd number of periods starting with a high-index material (HLHL...H), the separating cavity medium has to be an odd number of half-wavelengths for a resonance to occur at a given wavelength. This follows straightforwardly when the phase-changeson transmission through the mirror are taken into account.

2.3.5. Epitaxial growth and device fabrication.

The devices described in this work are grown by atmospheric pressure MOVPE (metal-organic vapour phase epitaxy) [Roberts *et al.*, 1988] at the University of Sheffield. Excellent well width uniformity is acquired by this growth technique, both across the 2" wafer as is evident from the negligible variation of the exciton peak wavelength, and parallel to the growth direction as has been measured by X-ray diffraction microscopy. Depth non-uniformity would result in poor electroabsorption effects due to the consequent broadening of the exciton [Stevens *et al.*, 1989]. Good well width control and uniformity are achieved by the very low growth rates introduced when growing the QW layers. The state-of-the-art with respect to the lateral uniformity of these resonant structures, where control of the cavity thickness is decisive for successful operation, is discussed in Chapter 5. Typical doping levels are $1\times10^{17}cm^{-3}$ for the n-region where the dopant used is Si, and $2\times10^{17}cm^{-3}$ for the p-region which is doped with Zn. The doping levels differ between the two materials that comprise the stacks, being higher for the material with larger Al concentrations. The intrinsic region has a p-type background doping of typically $5\times10^{15}cm^{-3}$, as obtained by various Capacitance-Voltage measurements. This background doping depends upon the proportion of well and barrier material in the intrinsic region, i.e.

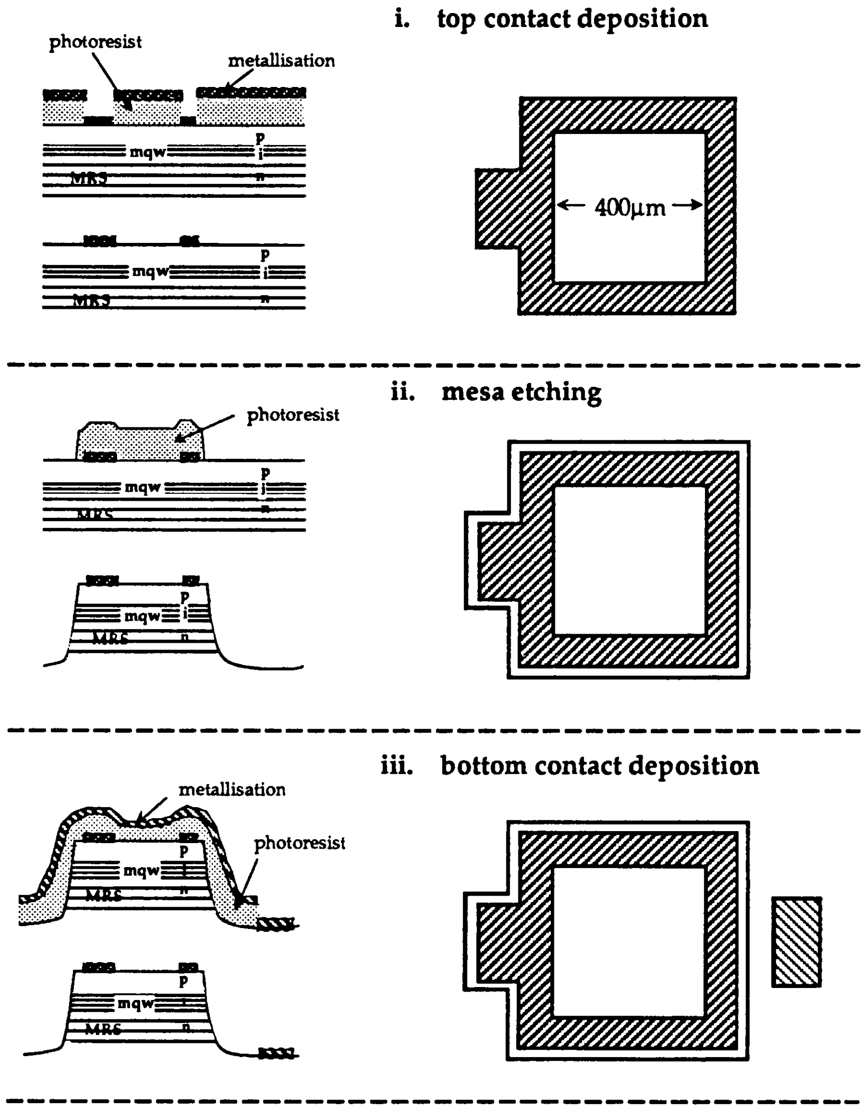

Fig.2.3.11 *A schematic diagram illustrating the processing steps that are followed in order to fabricate a diode. The cross-section is shown on the left and the planar view on the right of the figure.*

upon the average Al concentration, since the dopant originates mainly from the Al source (John Roberts, private communications).

One common feature of the epitaxial design, that should be mentioned here, is the p^+ GaAs top capping layer which is used for contacting purposes. This layer absorbs at the wavelengths of operation and since it is not a field-controlled absorber its thickness should be kept minimum; a 50Å layer suffices. Also it is interesting to note that in early p-i-n structures large GaAs buffer layers had been grown on top of the substrate to ensure a smooth growth at the main parts of the devices. The good growth quality attained in recent years, combined with the fact that thicker modulator designs are required for resonant structures as a result of the incorporation of the multilayer stacks, have resulted in a substantial reduction of the thickness of the buffer layer. Another point worth mentioning, is the intentionally undoped layer which is normally grown just before the quantum well layers to act as a doping buffer. In all of the structures I designed this intrinsic-buffer (i-buffer) is kept to the minimum safe value estimated by John Roberts (private communications) to be ≈200Å. This is always part of the top layer of the reflector stack. In some of the structures, in addition to the i-buffer layer underneath the quantum wells, there is one such buffer on top of the MQW layers which serves to eliminate any diffusion of dopants from the top doped layers to the QWs.

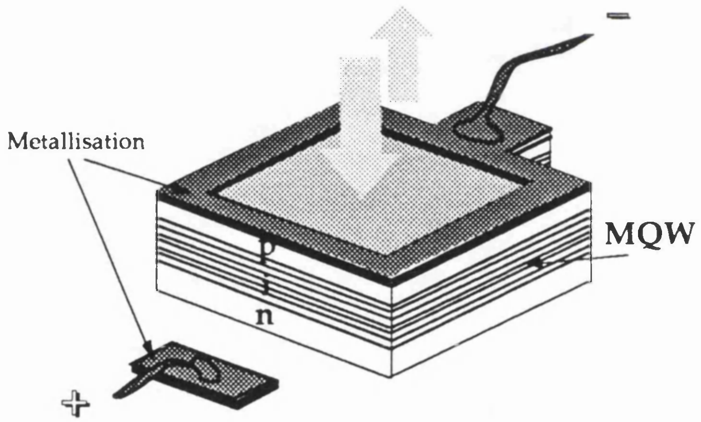

Fig.2.3.12 *A schematic of the final modulator device.*

The devices used in this work are 400μmx400μm optical window mesa devices fabricated by standard photolithographic techniques. An exception are the 4x4 arrays of devices where much smaller mesas are used; those are mentioned in Chapter 9. Briefly, the processing (Fig.2.3.11) involves photolithography to define the top contact followed by metallisation of that contact in a standard evaporator unit where Cr:Au is deposited for a p-type contact and Sn:Au for an n-type contact (note that the devices may be p-i-n or n-i-p). A second photolithographic step results in definition of the mesas that are etched down through the back stack to the GaAs buffer using a H_3PO_4;H_2O_2;H_2O solution. The purpose of the mesa formation is electrical isolation between devices. A last photolithographic step followed by another metallisation forms the bottom contacts. These are deposited on the GaAs buffer layer and thus carriers have to travel through the bottom reflector stack on their way to that electrode. This could limit the speed of a practical device since it leads to increased contact resistances as we discuss in section 2.3.6 and in Chapter 6. Our experiments have not been directed towards the demonstration of high speed modulation, however, and therefore the relatively large mesa devices and the general processing more than suffices for our purposes. Finally, the fabricated devices are mounted on a TO5 header and wire-bonded using an ultrasonic wedge bonder.

2.3.6 Device speed.

One of the important performance characteristics of an optoelectronic device is the speed at which it can be operated. The main limitation to the speed of the quantum well modulator is the RC time constant associated with the electronic circuit with which the modulator is affiliated. The equivalent circuit is shown in Fig.2.3.13. The shunt resistance R_{sh} is the resistance of the reverse biased p-i-n diode and therefore it is of the order of MΩ. There is also a resistance at the metal contacts with the p and n layers of the diode. This is increased in the case of resonant structures due to the presence of the reflector stacks as the flow of the carriers is inhibited by band 'spikes' at the hetero-interfaces [Wang *et al.*, 1992]. This resistance may be reduced if graded interfaces are employed in the stack [Sugimoto *et al.*, 1992], and may be overall eliminated if the contacts are made such that the stacks are bypassed [Barron *et al.*, 1992], i.e. on top of the bottom and below the front reflector stack. Alternatively, instead of the latter, dielectric front mirrors may be used that would be deposited after metallisation. In any case, the contact resistances may be of the order of a couple of Ohms to some tens of Ohms. Further, as the device comprises two doped parallel plates separated by an undoped region, a parallel plate capacitor is formed with C given by

$$C = \varepsilon \cdot \frac{S}{d}$$

where d is the width of the intrinsic region and S is the mesa area. The RC time constant associated with the circuit in Fig.2.3.13. is given by

$$RC = (R_i // R_{sh} + R_o) \cdot C \approx (R_i + R_o) \cdot C$$

For high speed operation, this RC time-constant must be minimised. Appropriately designed electronic driving circuitry is required to yield low values of the output resistance R_i and, furthermore, matched to the input of the modulator (effectively R_o). For example, operation at 10GHz requires that the capacitance of the modulator is of the order of 1pF if we assume that the total R is ≈100Ohms. The mesa dimensions have to be decreased, therefore, for high speed and this imposes stringent requirements upon the device fabrication and upon the optical alignment. Moreover, there may be a trade-off between the mesa area and the achieved contrast when the optical windows are reduced to very small dimensions, caused by the highly convergent beam that is incident on the device in this case (Chapter 5). As the operating voltage is inversely proportional to the thickness of the intrinsic region, there is also a trade-off between the voltage and the speed of the device (Chapter 7).

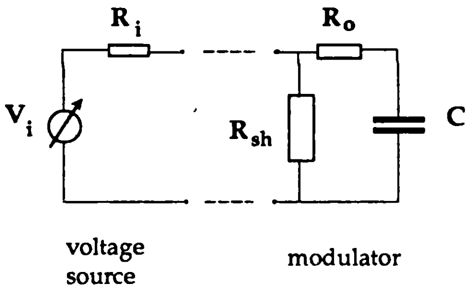

Fig.2.3.13 *The equivalent circuit of the modulator when it is driven by a voltage source.*

Finally, it is important to clarify two points with regard to the speed of operation. One is concerned with the effect of the time required for vertical transport of the carriers out of the wells. This is mainly manifested in the saturation intensities of the device that are reduced when this process becomes slower (Chapter 8) [Fox *et al.*, 1991]. Additionally, the operation of the device as a detector is affected by the carrier sweep-out stemming from the dependence of the quantum efficiency on carrier effects. However, it is important to point out that the speed of the carrier sweep-out process is not directly relevant to the speed at which the modulator may be operated. The second point to draw our attention is concerned with the effect of the resonant nature of the device upon speed. The time-delay introduced by the cavity can be estimated as follows. The finesse (eqn.2.2.4) of the cavity expresses the number of multiple reflections that are required until the FP action is effectively attained. Thus, as an example, for a cavity with a finesse of 5 (which corresponds to mirrors $R_f=R_b=0.77$) the time delay may be evaluated as the time needed for the 5-times internally reflected beam to come out from the front surface and contribute to the overall reflectivity. Assuming a cavity length of 1μm, we find that 15fs are required for that action to take place which is an indeed negligible time constant. In total the Fabry-Perot action imposes no limitation upon the speed in practice.

2.4. EXPERIMENTAL TESTING APPARATUS

Optical Multichannel Analyser System

The optical testing of the devices includes photocurrent and reflectivity measurements. The reflectivity spectra of such resonant devices varies significantly across the wafer at

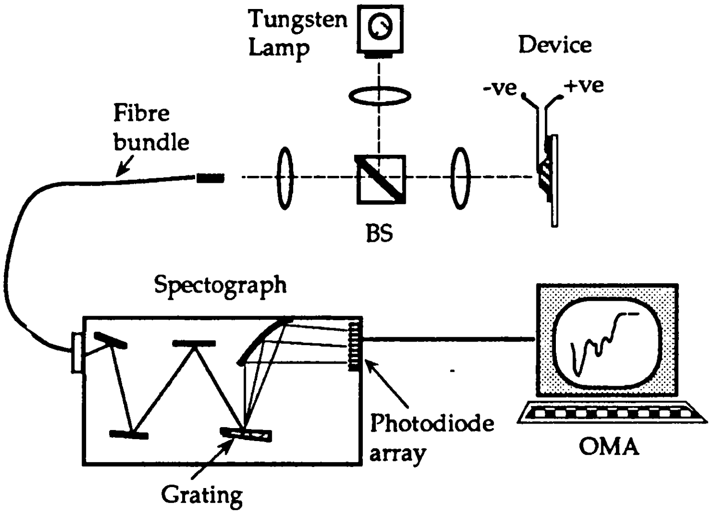

Fig.2.4.1 *A schematic diagram of the optical multichannel analyser system, that may be used to obtain bias-dependent reflectivity spectra as well as wafer uniformity plots.*

present, as we discuss in Chapter 5 on uniformity. This is not surprising since the growth equipment is not optimised for good lateral uniformity. It it very important for that reason to be able to test the wafer prior to device processing in order to ensure that it has been grown as specified, and if so, to choose a part of that wafer where optimum performance can be achieved. An optical spectrometer linked to a multichannel analyser system (OMA) has been used for that purpose where real-time reflectivity spectra can be obtained. The wafer that is being tested is held on a x-y-z positioner and light from a Tungsten (W) white source is focused at normal incidence (Fig.2.4.1). The reflected light is sent back in a fibre bundle that carries it to an EG&G spectrometer. The spectrometer has a grating blazed at ≈850nm and the analysed spectrum is incident on an array of 1024 Si photodetectors so that each one of them picks a small fraction of the spectrum. The outputs are parallel-to-series-converted and subsequently directly fed into the multichannel analyser processor. Real-time spectra with a typical sampling cycle time of 300ms are seen on a screen. The resolution of that system is determined by the choice of grating for a fixed photodetector array and is ≈0.5nm currently, when the total observed optical spectrum is ≈330nm. After the chosen samples are processed, the devices with acceptable electrical performance are optically tested on the OMA system and the best of those are further tested. Biased data of bonded devices can also be obtained on the same system.

Monochromator System

Since the contrast is a very important performance characteristic for these devices, it is mandatory to obtain very accurate reflectivity measurements and, moreover, where the reflectivities involved may be extremely low, as is the case when the device is at its off-state. Accurate measurements involve a careful focusing of the light in a tight spot at the centre of the optical window to avoid any reflections off the contacts which would obviously be unmodulated and would degrade the apparent contrast. Additionally, good alignment of the optics is needed so that stray beams are not collected. A standard monochromator system was used for accurate reflectivity measurements and for photocurrent measurements. This system is illustrated in Fig. 2.4.2. The devices are again held at right angles to the optical plane. The wavelength of the output of the monochromator is determined by the position of a grating which is rotated by a stepper motor. Photocurrent spectra are collected from the voltage across a resistor (typically 100kΩ) that is connected in series with the device, and reflectivity spectra are collected at the Si photodetector. Prior to entering the monochromator, the light is optically chopped and lock-in amplifiers are employed for signal extraction. An LCZ meter is used as a programmable voltage source and the whole process is controlled by a BBC microcomputer. The resolution of this system is estimated to be

0.5nm with the slits open at 50μm.

When reflectivity measurements are taken, the lock-in reading is zeroed around the wavelength of maximum contrast with a black opaque paper behind of the microscope objective, the reflectivity of which has to be zero. The spectra are then normalised to that of a freshly deposited Au reflector.

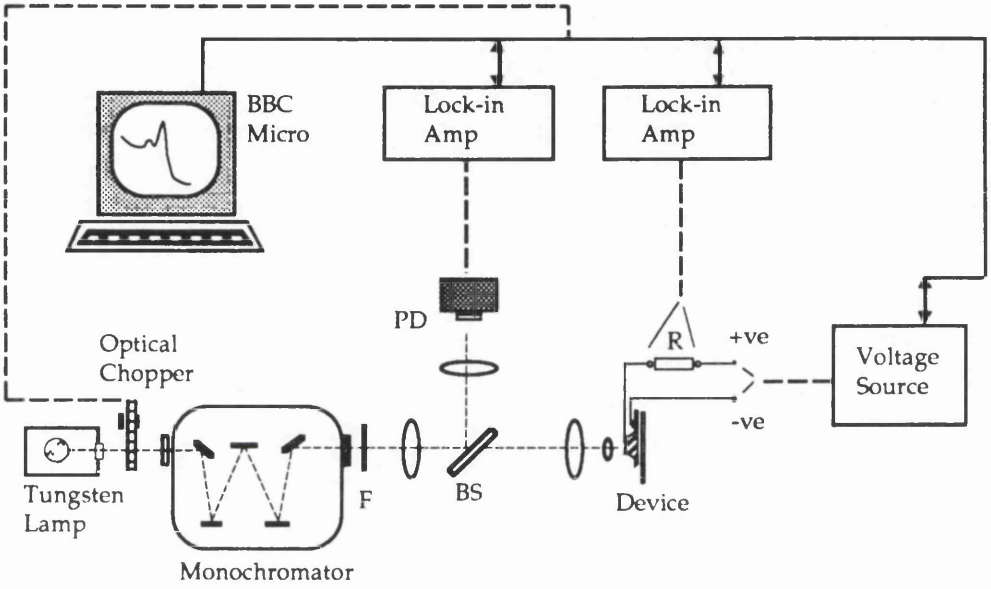

Fig.2.4.2 *A schematic diagram of the monochromator system where bias-dependent reflectivity and photocurrent spectra may be obtained.*

2.5 OPTIMISATION OBJECTIVES AND TARGET PERFORMANCE CHARACTERISTICS

In this thesis we are concerned with Fabry-Perot reflection modulators in the GaAs material system which are applicable primarily to optical interconnections in VLSI, optical data processing, and switching networks in short-haul communication links (Chapter 1). The optimisation objectives with regard to the modulator characteristics are very much dependent upon the application. In this section we will raise the issues involved and subsequently we will identify target performance characteristics for the investigation to follow.

A common denominator that applies to all systems applications is that the tolerance of the device must comply with real conditions. The specific requirements with respect to tolerances are, however, application dependent. For example, when large arrays of devices are implemented, as is the case for optical data processing and switching networks, the uniformity of the performance in the lateral direction across the array becomes particularly important. By contrast, in optical interconnection applications the array sizes may be relatively small while local area temperature variations and the consequent effect upon the device performance may become the prime consideration. Similarly, the difficulties involved in the optical addressing of the modulator will vary greatly depending on the systems geometry. It is certainly beyond the scope of this section, and indeed of this thesis, to yield a comprehensive study of the required tolerances at a systems level. Nevertheless, it is imperative that the effect of variations of the operational conditions as well as that of the fabrication accuracy on the performance of the device are well understood. Furthermore, it is desirable that ways to minimise the impact of these upon the eventual performance are possibly established. We examine the modulator in this respect in Chapters 4 and 5.

As far as the actual modulation characteristics are concerned, i.e. with regard to the exhibited contrast ratio and reflection-change, the insertion loss, and the operating voltage, the required performance will be determined by the system the modulator is affiliated to. We address different applications separately below:-

Table 2.5.A *The relative significance of various modulator performance characteristics with respect to applications. This refers to VLSI interconnections, SEED applications, and switching networks where modulators are utilised (not in SEED configurations). The speed refers to the RC-associated time-constant and therefore does not apply directly to SEEDs.*

	Contrast Ratio	Reflection Change	Insertion Loss	Voltage	Speed
Interconnects	●	●●●	●●	●●●	●●
SEEDs	●●	●●●	●●	●●	—
Switching Nets	●●●	●	●●	●●	●●

In *optical interconnections*, the modulator will act as the transmitting and receiving element in the created free-space links (Chapter 1). Here, although a high contrast ratio is desirable as it leads to low noise at the receiver plane, the parameter to optimise is the attained reflection-change. Indeed, it is the difference between the on-and off- levels that is of prime importance in this case. Also, since the modulator acts as an information-exchange element between electronic modules, it is necessary that its operation is compatible with the driving electronic circuitry. This reflects certain requirements on the speed of the device, which has to be sufficiently higher than that of the electronic clock, and also on the operating voltage, as we discuss later in this section. The *self-electro-optic effect device* (SEED) has been introduced in Chapter 1 and we refer to this type of device, and the respective optimisation objectives, in greater detail in Chapter 8. As we discuss there, the switching power and switching speed of such composite devices depends greatly upon the reflection-change attained by the modulators that comprise the SEED. Large reflection-change, low insertion loss, and low operating voltage are the decisive characteristics of the modulator that result in fast, low-power switching and increased cascadability (Chapter 1). Finally, in implementations of the modulator in 2D *switching networks*, such as the cross-bar switch (Chapter 1), the maximum array size depends on the contrast achieved by individual devices. This determines, therefore, the capacity of the network. The above are summarised in Table 2.5.A.

The optoelectronic devices will need to be integrated with electronic circuitry which we discuss in Chapter 9. In the case of optical interconnections in VLSI the electronics are certainly going to be Si-based while in certain other applications there is the possibility that the whole circuit is realised in III-V material (Chapter 9). The main candidates for the electronic circuitry in VLSI are CMOS, ECL and possibly BiMOS technologies [Sedra and Smith]. The low-power, high input-impedance, and wide noise-margins of CMOS circuitry have established its dominance in electronics industry. On the other hand, ECL is the fastest logic circuit family while the less established BiMOS combines some of the advantages of the two. As CMOS outputs are below 5V and ECL much lower, it is apparent that voltages of operation lower than the 9V of the device presented in section 2.3 will need to be attained.

Based on the above discussion we may set target performance characteristics for the optimisation of the modulator to follow. These are listed in Table 2.5.B.

Table 2.5.B *Target modulator characteristics for the optimisation carried out in the rest of the thesis. Either high contrast ratio or large reflection change devices are the aim, depending on the application.*

Contrast Ratio	>10dB
Reflection-Change	>50%
Operating Voltage	<5V
Insertion Loss	<3dB

CHAPTER 3. MODELLING OF FABRY-PEROT MQW ELECTROABSORPTION DEVICES

3.1 INTRODUCTION

As we have seen in the previous Chapter, Fabry-Perot (FP) multiple quantum well (MQW) devices are multi-layered semiconductor structures, the optoelectronic performance of which relies upon a combination of FP interference and MQW electroabsorption effects. Modelling such structures is essential for a study of the trade-offs involved in the design, the subsequent optimisation, and the final design of efficient modulators.

In this Chapter we present briefly the logistics of the model employed in this work. This is based upon a standard transfer matrix method to evaluate the reflectivity, absorptance and transmittance of an assembly of multiple layers. Firstly, we describe the transfer matrix method and thereafter we present the theoretical evaluation of the field-dependent MQW absorption spectra that are a prerequisite for the final simulation of the operation of a device with and without bias. The absorption spectra calculations are based on the theory developed by P.J. Stevens [1988] with a modification that was required in the case of resonant devices. The final absorption coefficient values are obtained by an empirical fit to experimental data. As a result, our calculations are restricted to GaAs/$Al_{0.3}Ga_{0.7}As$ (well/barrier) since extensive experimental absorption data for a number of well widths exist for this material system [Jelley *et al.*, 1989].

A comparison between calculated and experimental spectra is made at the end of the Chapter so as to test the validity of the overall model in the case of resonant devices. Finally, we discuss the model's limitations.

3.2 MODELLING OF A MULTILAYER DEVICE

The reflectivity R, transmittance T and absorptance A of an assembly of N layers can be evaluated in the steady state (time-independent) by means of the standard transfer matrix method [Macleod]. This technique involves basically the representation of an assembly of layers by a matrix that contains all the information on the effect the assembly has on light of a given optical wavelength incident on the layers at a certain angle. The relations originate from Maxwell's equations. These govern the modifications imposed upon the transverse and tangential components of the electric field E and the magnetic field H of electromagnetic waves at an interface between two materials, depending upon the dielectric properties of those materials. Interference effects are implicit in this kind of analysis making it applicable to FP-based devices.

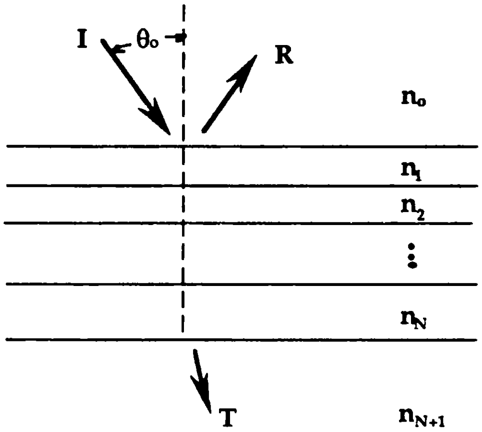

Fig. 3.2.1 *A schematic of a multilayer structure.*

In order to apply this technique, the refractive indices (RI) n_0 of the incoming and n_{N+1} of the exit medium are required (Fig.3.2.1). Also required is a full (optical) description of the N layers, i.e. a knowledge of the complex RI and the thickness of each layer. In the cases studied, the incoming medium is air (n_0=1). The exit medium is meant to be semi-infinite. However, here the exit medium is in effect the substrate which may be considered of (semi-) infinite thickness in comparison to the total vertical extent of the device.

A brief outline of the transfer matrix method is given in the following.

Characteristic matrix of one layer

Let us consider the situation depicted in Fig.3.2.2 where monochromatic light of optical wavelength λ is incident at an angle θ_0 on a layer of thickness d_r and complex refractive index $N_r=n_r-ik_r$, n_r being the real RI and k_r the extinction coefficient of the medium comprising the layer. The single layer can be regarded as a mere interface between the semi-infinite media 0 and r+1, only if its effect on the incident light is contained within the transfer function of that interface. The appropriate transfer

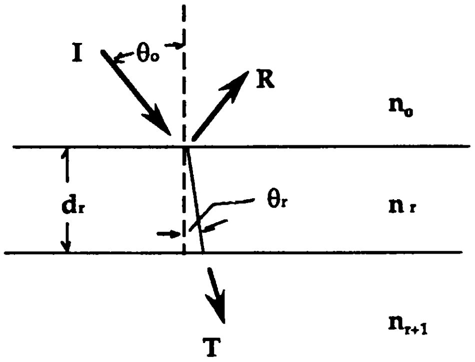

Fig.3.2.2 *Schematic of a single layer r between two media 0 and r+1 with monochromatic light incident at an angle* θ_0.

function is the characteristic matrix of the layer given by

$$M_r = \begin{bmatrix} \cos\delta_r & i\cdot\cos\delta_r / y_r \\ i\cdot\sin\delta_r \cdot y_r & \cos\delta_r \end{bmatrix} \qquad 3.2.1$$

where $\delta_r = \dfrac{2\pi N_r d_r \cos\theta_r}{\lambda}$ is a complex phase factor, and $y_r=N_r\cos\theta_0$ for TE (s) and $y_r=N_r/\cos\theta_0$ for TM (p) modes is the so-called characteristic admittance of the medium. That is in fact the effective complex refractive index seen by the particular optical wave incident at that angle. The complex phase factor δ_r describes the effect upon (one-way) propagation through the medium. If we assume that the (intensity) amplitude just after the interface with medium 0 is I_r, then after propagation through layer r the complex amplitude will be modified to

$$I_r \cdot e^{-i2\delta_r} = I_r \cdot e^{-i\frac{4\pi n_r d_r \cos\theta_r}{\lambda}} \cdot e^{-\frac{4\pi k_r d_r \cos\theta_r}{\lambda}} \qquad 3.2.2$$

The last term in the above expression is a decaying real exponential which expresses the attenuation through the layer. This way, the matrix in eqn.3.2.1 accounts for both phase-change and attenuation through the medium.

The tangential components of E and H at the bottom interface in Fig.3.2.2 are related to those at the top via the characteristic matrix of the intermediate layer. The reflectivity from layer r may then be evaluated. Prior to presenting the expressions involved in that calculation, we will extend the analysis to the multiple layer case.

The multilayer structure

The transfer function of an assembly of N layers is another matrix, M_t evaluated simply by the product of the individual characteristic matrices taken in the correct order, i.e.

$$M_t = \prod_{r=1}^{N} M_r \qquad 3.2.3$$

The whole multiple layer case in Fig.3.2.3a can be simplified to its equivalent in Fig.3.2.3b where the assembly of the N layers together with the exit medium have been replaced by a fictitious medium of characteristic admittance Y. The final transfer matrix of that medium is

$$\begin{bmatrix} B \\ C \end{bmatrix} = M_t \cdot \begin{bmatrix} I \\ y_{N+1} \end{bmatrix} \qquad 3.2.4$$

and the admittance is given by Y=C/B.

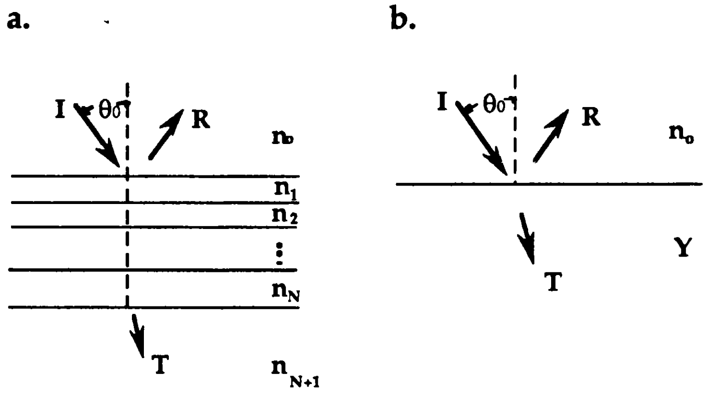

Fig.3.2.3 *The multilayer structure together with the substrate may be replaced by a fictitious medium of an appropriate effective refractive index Y.*

The total reflectivity R, absorptance A and transmittance T may now be evaluated very simply as

$$
\begin{aligned}
R &= \frac{(y_0B - C)\cdot(y_0B - C)^*}{(y_0B + C)\cdot(y_0B + C)^*} \\
A &= (I - R)\cdot\left[I - \frac{y_{N+1}}{\mathrm{RealPart}(BC)^*}\right] \\
T &= \frac{4\cdot y_{N+1}\cdot y_0}{(y_0B + C)\cdot(y_0B + C)^*}
\end{aligned}
\qquad 3.2.5
$$

where y_o and y_{N+1} are the characteristic admittances (i.e. the effective refractive indices) of the input and the exit medium respectively (eqn.3.2.1).

The MQW layer

The final aim is to model the bias-dependent operation of an MQW structure, hence the electric-field dependent characteristic matrix of the MQW region needs to be evaluated. This region is a multilayer structure itself. However, the changes from well to barrier and vice versa are not 'seen' by the light propagating through since the period of such changes is very small in comparison to the optical wavelength.

Hence, in our calculations, the MQW layer may be treated as a single homogeneous layer having the total thickness of the MQW region and its complex refractive index being the average between those of the well and barrier material comprising the quantum well layers. The expressions giving the real part of the refractive index are straightforward. As for the extinction coefficient k, this is directly associated with the absorption coefficient α via

$$
k = \frac{\alpha\lambda}{4\pi} \qquad 3.2.6
$$

at a certain wavelength λ. The value $k(\lambda,V)$ of the wavelength and voltage (V) dependent extinction coefficient for the well material can be evaluated by means of eqn.3.2.6 from the field dependent absorption spectra. At the wavelengths of interest (near the band-edge) the absorption coefficient of the barrier material is zero, hence an average $k(\lambda,V)$ for the composite MQW layer is readily obtained. The evaluation of the characteristic matrix of the MQW layer implies thus a calculation of the absorption spectra; this is discussed in the next section.

3.3 MODELLING OF THE MQW ABSORPTION SPECTRA

A prerequisite to the evaluation of the full MQW absorption spectra is the determination of the subband energy levels within the wells, both in the conduction and in the valence band, and thereafter the evaluation of the corresponding wavefunctions. Subsequently, the overlap integrals between the e- and h-wavefunctions can be determined; these have been associated [Miller D A B *et al.*, 1986] with the oscillator strength of a transition resulting in the formation of an exciton, i.e. a bound e-h pair.

The subband energy levels and corresponding wavefunctions may be determined by several methods. In this work the above evaluations have been 'inherited' directly from a former Ph.D. student, P.J. Stevens, who uses the transmission resonance technique [1988] also used by other workers [Miller D A B *et al.*, 1985a]. An outline of the technique is presented in the following section. The calculation of the absorption spectra is subsequently described. This is based upon the theory used by Stevens *et al.* [1988], with a modification on the thermal lineshapes that proved to be essential for a realistic model of FP devices.

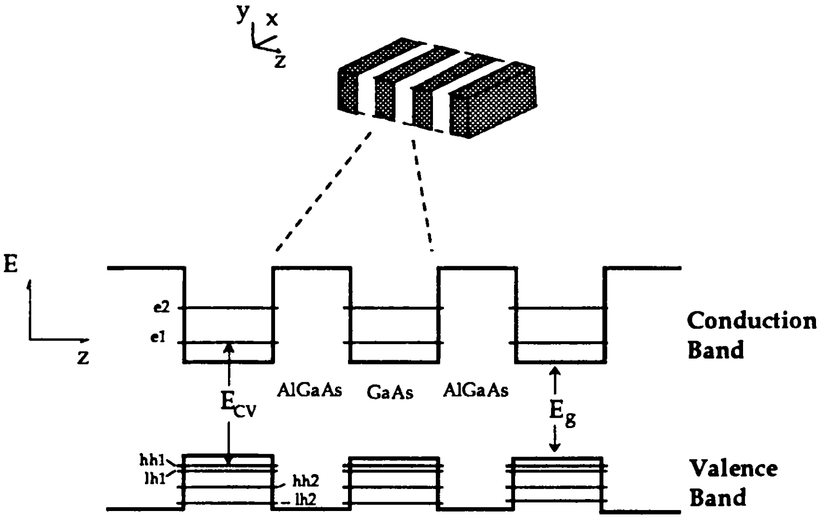

Fig.3.3.1. *The conduction and valence bands of alternating GaAs and AlGaAs layers form potential wells in the growth direction. Discrete energy levels are formed for the electron in the conduction band (en, n=1,2...), and the holes in the valence band (heavy-hole hh,and light hole lh). The diagram is not to scale.*

3.3.1 The Tunnelling Resonance technique.

The conduction and valence bands of MQW material form potential wells in the direction perpendicular to the layers, as a result of the difference in the bandgap energies between the barrier and the well materials (Fig.3.3.1). These are not treated as a periodic potential when calculating the energy levels, wavefunctions etc, since by convention quantum well material employs sufficiently wide barriers to ensure no coupling occurs between neighbouring wells. Each well may thus be treated independently so that at zero field one is met with the situation of a finite square potential well as in Fig.3.3.2. The eigenvalues of the corresponding time-independent Schrödinger's equation and the consequent wavefunctions may be evaluated in the standard manner employed in quantum mechanics [Schiff]. However, upon application of an electric field, the situation becomes more complex, the wells now being tilted (Fig.3.3.4). In order to use a unified method for both the biased and the unbiased case, the well and barrier region are divided into 'layers' (Fig.3.3.3) where each 'layer', or step, is a flat potential region with unequal potential steps at the interfaces either side. Following the standard quantum mechanical treatment of such problems, a solution within each step may be found assuming an envelope function that is a combination of a forward and a backward travelling wave 'reflected' and 'transmitted' through the potential steps accordingly. The wavefunction ψ and the particle current density are required to be continuous at each of the interfaces and physically permissible within each of the steps, thus boundary conditions are imposed

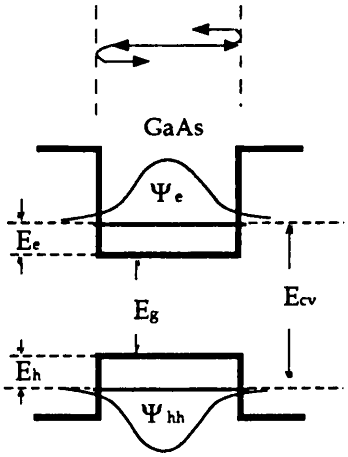

Fig.3.3.2 *Schematic diagram of the zero-field case, showing the sub-band energy levels and wavefunctions* Ψ_e *of the 1s electron in the conduction band, and* Ψ_{hh} *of the heavy-hole in the valence band. (Diagram not to scale).*

and the physical problem is at this point fully described in mathematical terms.

The calculation of the overall wavefunction is performed in a manner analogous to that described in section 3.2 for the evaluation of the transmission and reflection through a multilayer structure. The wavefunction and its (space-)derivative at one interface are expressed as functions of these at the previous interface. Eventually, an overall wavefunction compatible with all the subconditions is obtained by means of this series-like process. The masses used are the effective masses of the particles in the direction of interest, i.e. perpendicular to the layers [Chemla *et al.*, 1985; Miller R C *et al.*, 1984]. Band non-parabolicity is included in the expressions giving the effective masses. Details are given in the Appendix.

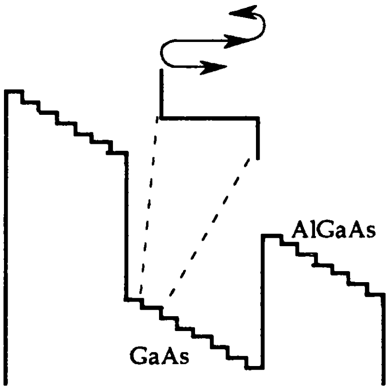

Fig.3.3.3 *The well and barrier regions are divided in 'steps'.*

At a given field perpendicular to the wells, an excitonic transition resulting in an electron at sub-level i in the conduction band bound to a hole at sub-level j in the valence band, occurs at an energy given by

$$E_{ex}^{ij} = E_{cv}^{ij} - E_{b}^{ij}$$
$$E_{cv}^{ij} = E_g + E_e^i + E_h^j \qquad 3.3.1$$

where E_{cv}^{ij} is the subband energy, E_g is the bandgap energy of the well (GaAs), E_e^i is the electron subband level, E_h^j is the hole subband level and E_b^{ij} is the binding energy of the resulting exciton. With the exception of E_g and E_b, the terms in eqn.3.3.1 are field dependent. The binding energy is assumed to be dependent only upon the well width; values of E_b as a function of well width are obtained by a polynomial fit to those reported by Ekenberg and Altarelli [1987] (see the Appendix). In reality, E_b does depend on field as a result of the reduced confinement upon the application of a field perpendicular to the wells. However, calculations estimate the corresponding shift of E_b to be an order of magnitude smaller than the overall subband field-induced shift [Miller D A B *et al.*, 1985a; Stevens, 1989] so that the induced inaccuracy is negligible.

Following the evaluation of the transition energies, the determination of the associated probability of occurrence of these transitions is carried out. The oscillator strength of a transition expresses the relative likelihood of that transition taking place and manifests itself in the relative height of the various exciton-associated peaks in the absorption spectrum. The oscillator strength has been associated [Miller D A B *et al.*, 1986] with the square of the e- and h- wavefunctions overlap integral extended over the well and surrounding barriers. Hence, transitions that are forbidden at zero field because the corresponding wavefunctions are orthogonal (overlap-integral =0), become allowed with a field applied when the e- and h- wavefunctions localise to different sides of the well as caused by the opposite forces experienced by the two particles (Fig.3.3.4). As a consequence, 'allowed' transitions subside with field while the oscillator strength of 'forbidden' transitions increases (Fig.3.3.4) (sum rule [Miller D A B *et al.*, 1986]). In our simulation, this drop in oscillator strength is the main means of accounting for the field-induced reduction of the exciton absorption. This stems from the following assumptions: a) that the binding energy is field-independent, and - more importantly- b) that relative to the continuum-level the area of the excitonic transition is field-independent. The latter assumption is discussed in a later section.

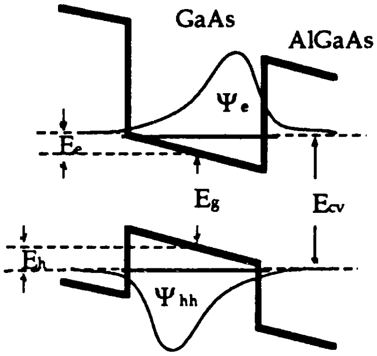

Fig.3.3.4 *Electron and heavy-hole sub-band energy levels and wavefunctions in the case of an electric field being applied perpendicular to the quantum well layers.*

Summarising this section, the transmission resonance method determines the field-dependent subband levels in both the conduction and the valence band as well as the overlap integrals of the transitions between these levels and hence the associated probabilities of the transitions. These lend themselves to the calculation of the absorption spectra as discussed in the next section.

3.3.2 Scaling to experimental absorption spectra.

Since we are concerned with modulation at wavelengths longer than the zero bias heavy-hole exciton peak, the modelling of the absorption spectra may be restricted to two transitions, the e1-hh1 between the 1s electron and the heavy-hole and the e1-lh1 between the 1s electron and the light-hole. For this purpose, the model developed by P.J. Stevens [1988], has been reproduced and modified in order to meet the particular requirements imposed by this work.

Henceforth we refer to the absorption spectrum of the well material only as opposed to that of the composite MQW. This spectrum is assumed to originate from two distinguishable contributions: one from exciton transitions between discrete energy levels just below the subband gap energy (by an amount equal to the binding energy), and one from a continuum of free-particle states at energies greater than the subband energy. All transitions considered are therefore interband transitions between the valence and the conduction band.

The heavy-hole and light-hole associated transitions are treated independently. The two resulting spectra are subsequently simply added together. The first step to a fit to experimental spectra is the determination of the relative contributions to the final continuum level from the light-hole and the heavy-hole associated continua (the continuum level is taken as the absorption coefficient seen directly behind the light hole peak in the spectra). The relative contribution of the two holes is dependent upon the polarisation of the light. When the electric field E of the optical wave is perpendicular to the plane of the wells there is no interaction that results in a heavy-hole exciton formation, whereas when the E-field is parallel to the plane of the wells the ratio between the heavy-hole and the light-hole contribution is 3:1 [Asada *et al.*, 1984; Yamanishi and Suemune, 1984]. The devices concerned here are

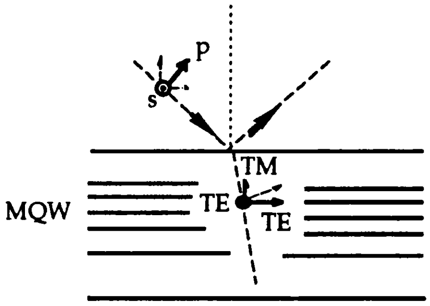

Fig.3.3.5. *Optical wave at oblique incidence on a multiple quantum well structure and the corresponding modes of propagation within the layers.(The little arrows denote the electric-field vectors).*

transverse so when light is incident at right angles from air, the E-field is always parallel to the layers since only TEM modes are supported in free space. However, oblique incidence results in a TM component (E perpendicular to the layers) propagating within the device, for which the heavy-hole is suppressed (Fig.3.3.5). We will restrict our analysis here to the case of normal incidence, and revisit this issue in Chapter 5 where we address the sensitivity of the modulator's operation to angle of incidence.

Having determined the relative contributions of the two hole-associated spectra we need to evaluate two scaling factors in order to calculate the final spectra: the continuum level and the area of the exciton relative to the continuum-level.

Continuum level

The continuum level is theoretically expected to be well width dependent [Matsumoto *et al.*, 1985] stemming from the increased dimensionality (tending to 3D) related to the excitonic confinement as the well width increases. As mentioned previously, the heavy-hole continuum level α_∞ is three quarters of the experimental value of the zero-field absorption coefficient directly behind (i.e. to higher energies of) the light-hole exciton peak. A division by the Sommerfeld factor corresponding to that point (≈1.9) is further required. The Sommerfeld factor is introduced in the next section.

An extensive range of absorption spectra has been obtained by Jelley *et al.*

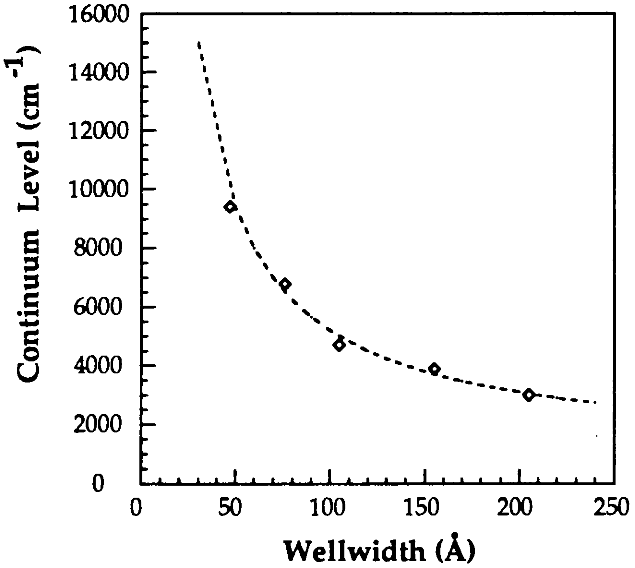

Fig.3.3.6 *Heavy-hole continuum level obtained from a fit to experimental absorption data by Jelley et al [1989]. The dashed line is a fit to the derived points (eqn.3.3.2).*

[1989] at different well widths for the GaAs/$Al_{0.33}Ga_{0.67}As$ system. The continuum level is derived from these and is indeed found to be well width dependent (Fig.3.3.6), in agreement with theoretical expectations. An empirical fit to the data is given by

$$\alpha_{\infty} = 1000 + 4.2 \times 10^{5} \times L_{w}^{-1} \ (\mathrm{cm}^{-1}) \qquad 3.3.2$$

where L_w is the well width in Å;

Exciton peak relative to continuum level

The ratio (f_{ex}) of the area under the exciton peak in photon-energy space divided by the continuum level, is a measure of exciton dimensionality. This deviates from pure 2-D in the case of MQW material where, as a consequence, f_{ex} takes a value lying between those corresponding to the 2-D and the 3-D cases [Klipstein and Apsley, 1986]. For a given barrier height, the confinement tends to the 3-D limit as the well width is increased. It is expected thus that f_{ex} will decrease with well width, being in fact a function sensitive to dimensionality. This decrease of f_{ex} manifests itself in the absorption spectra as a decreasing exciton peak in relation to the continuum level with

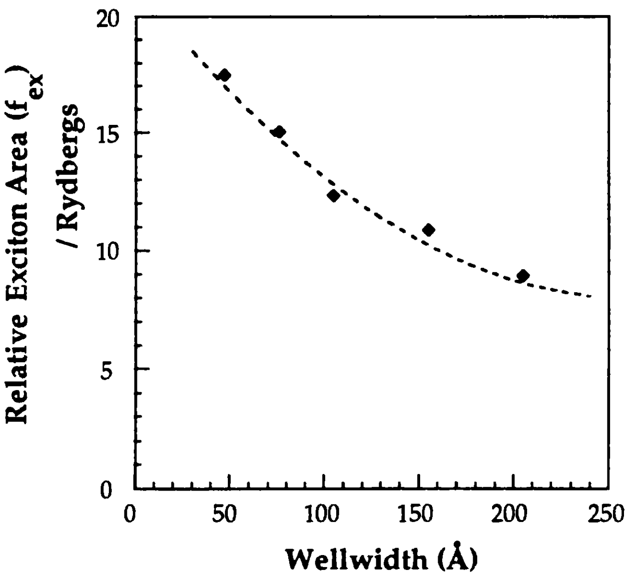

Fig.3.3.7 *The exciton area relative to the continuum level as obtained by a fit to experimental data by Jelley et al. The dashed line is a curve fit to the derived points, as discussed in text. Note that the Rydberg units differ for the two holes [Appendix].*

increasing well width. Values for f_{ex} expressed in Rydbergs [Appendix] are obtained from the experimental data of Jelley *et al.* and are shown in Fig.3.3.7. An empirical fit to these is

$$f_{ex} = 21.38 - 0.102 \cdot L_w + 1.94 \times 10^{-4} \times L_w^2 \qquad 3.3.3$$

where L_w is the well width in Å, and f_{ex} is in Rydberg units. The above equation is employed at all fields, i.e. f_{ex} is assumed field independent.

3.3.3 Evaluation of the field-dependent absorption spectra.

Having determined the relative strengths of the absorption features, we may proceed to the final calculation of the absorption spectra. Broadening mechanisms, both inhomogeneous and homogeneous, are included in the simulation and are applied to the heavy hole and light hole contributions independently. In the following we will describe the calculation method limiting mathematical expressions to those absolutely necessary; detailed equations are included in the Appendix. The masses used here refer to the motion of the particles -or rather the pair- within the layers and differ from the values used in the evaluation of the energy levels and wavefunctions [Chemla *et al.*, 1985; Appendix].

Continuum and excitonic transition associated with each hole--Homogeneous Broadening

Initially, the continuum may be represented by a step-function at the subband energy E_{cv} (Fig.3.3.8a) whereas the excitonic transition is represented by a delta function at E_{cv}-E_b (note that E_{cv} is field-dependent). A Sommerfeld factor is included in the continuum (Fig.3.3.8b) to account for an enhancement of transitions between free particles around the band-edge due to Coulomb attraction between the oppositely charged electrons and holes. The Sommerfeld factor varies 'slowly' with energy and could have been omitted, especially in the case where only wavelengths longer than the heavy hole peak are of any interest (see Appendix).

So far we have been referring to energy *levels*. A lifetime-related broadening, originating mainly from phonon interaction, must be accounted for. To do so, a convolution with a lineshape of a temperature dependent FWHM [Appendix] is included (Fig.3.3.8c), and also the exciton is now represented by the same lineshape instead of the unphysical delta-function. This broadening mechanism is assumed field-independent, i.e the lineshape employed is the same irrespective of the electric field applied to the wells. At this stage the values for α_∞ and f_{ex}, introduced in the previous section, are employed in the calculation (Fig.3.3.8c). The position of the spectrum depends on the subband energy E_{cv}, and is thus field dependent, and the spectra are scaled according to the field-dependent oscillator strength calculated for the associated transitions.

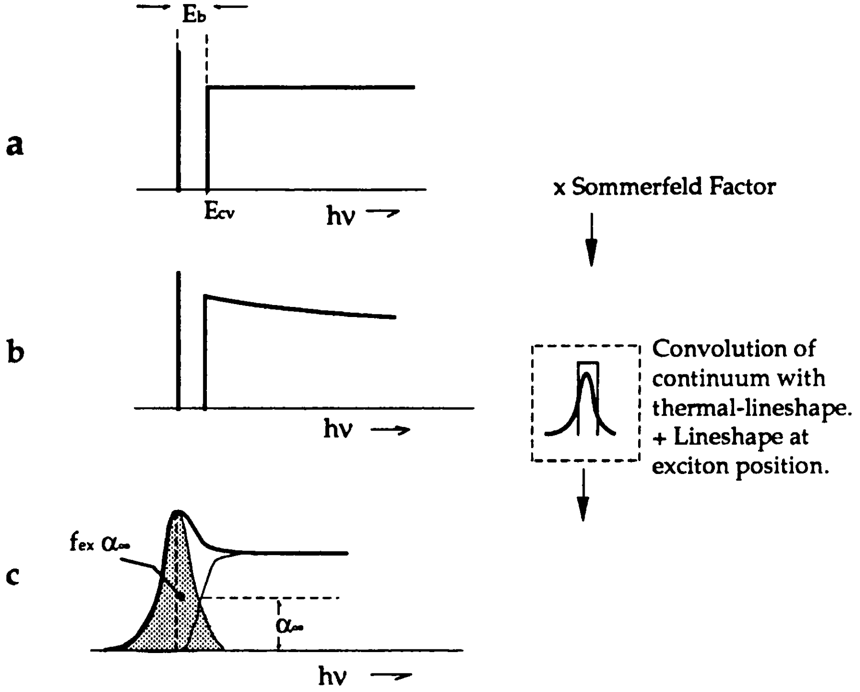

Fig.3.3.8. *Steps used in the calculation of the homogeneously broadened absorption spectrum associated with each hole. The whole spectrum is shifted accordingly upon the application of an electric field, while also it is multiplied by the corresponding square overlap integral.*

The lineshape used by P.J. Stevens to account for homogeneous ('thermal') broadening is a Lorentzian [Appendix] which is commonly used for dampening-oscillator like mechanisms. The FWHM of that function is temperature dependent modelled by a Bose-Einstein distribution since phonons are being dealt with. Other workers have used a Gaussian function lineshape [Chemla *et al.*, 1984]. Lorentzians overestimate the exciton absorption tails, while we found that Gaussians underestimate them. In the case of resonant devices, such inaccuracies are amplified and result in non-reliable performance evaluations. This was verified by an original modelling of CB145, the first demonstrated AFPM (Chapter 2), using the Lorentzian of

Stevens *et al.*, which resulted in a calculated insertion loss of 5.2dB as opposed to the experimental 3.5dB. In order to obtain realistic reflectivity spectra, the respective lineshape has been modified. For continuity purposes we present the details of this in a subsequent section (3.3.4).

Inhomogeneous broadening

i. Well-width fluctuations

The interfaces between the well and the barrier are in practice neither perfectly abrupt nor flat [Ourmazd, 1990; Kim, 1989]. The implication of the latter is that the well width fluctuates laterally across a certain well layer. Additionally, during the growth of MQW layers the well width is controlled to about a monolayer implying well width fluctuations between wells. The effect of both the above on the absorption spectra may be indistinguishable provided the fluctuations in both scales are comparable. In that case, excitons within a single well may 'see' different well widths in the very same way that excitons in different wells may experience unequal well widths as these vary across the MQW region thickness. Since the subband energies and consequently the wavefunctions are well width dependent, well width fluctuation imposes a broadening of the excitonic features in the absorption spectra.

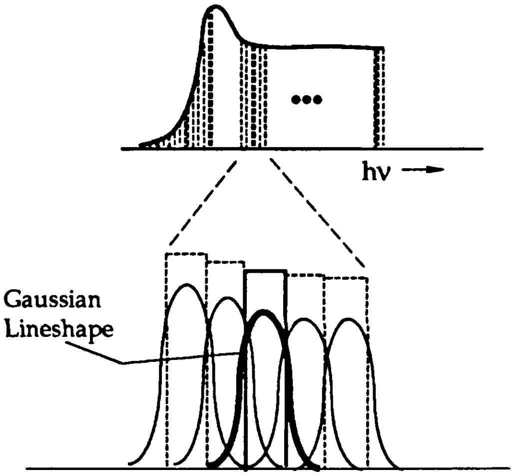

Fig.3.3.9 *Schematic of the convolution with a normalised Gaussian lineshape to account for inhomogeneous broadening due to well width fluctuations.*

This broadening mechanism is modelled by a convolution of the spectra with a Gaussian function that represents a normally distributed fluctuation of well width. The standard deviation σ of that distribution is taken equal to the change in subband energy ΔE_{cv} caused by the estimated mean well width fluctuation ΔL_w and is thus

$$\sigma = \frac{\partial E_{cv}}{\partial L_w} \cdot \Delta L_w \qquad 3.3.4$$

where ΔL_w is assumed equal to one monolayer (≈2.83Å) when modelling our devices. This is also typical of other experimentally obtained values [Nelson *et al.*, 1987b; Ourmazd, 1990].

This broadening mechanism is well width dependent, narrow wells being more sensitive than broader wells as a result of the strong dependence of E_{cv} to well width for narrow wells (note also that one monolayer is a larger relative change in well width for smaller wells). There is also a marked field-dependence which stems from the higher sensitivity of the subband levels to well width at higher fields [Stevens, 1989].

ii. *Field induced broadening*

The voltage V applied across the wells results in an average field F_{ave} seen by the wells

$$F_{ave} = (V + V_{bi})/L_{MQW} \qquad 3.3.5$$

where V_{bi} is the built-in field and L_{MQW} is the width of the MQW region. Were the MQW region highly intrinsic, F_{ave} would be the field experienced by all the wells across the region. In reality there is a background doping of about 5×10^{15} cm^{-3} in our samples which leads to the situation depicted in Fig.3.3.10. For instance in the case of a 1μm thick MQW region this gives rise to a field difference of ≈7kV/cm from the top

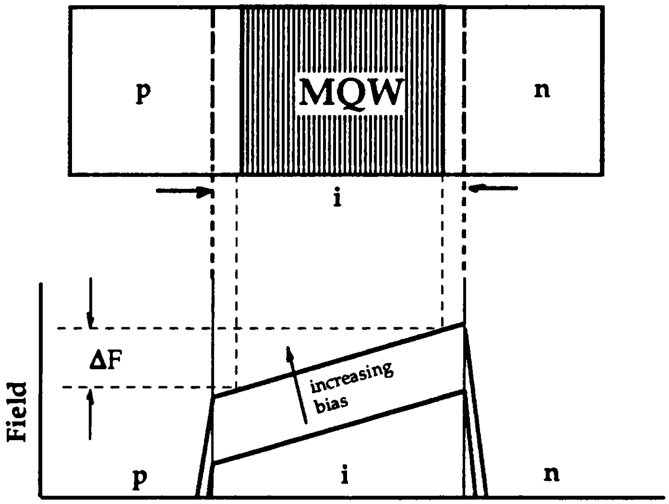

Fig.3.3.10 *Schematic of the electric field profile along an MQW p-i-n diode in the unbiased and the reverse biased case (π–type intrinsic).*

to the bottom well [Appendix]. This inhomogeneity causes different wells to experience different fields and consequently unequal QCSE-associated red-shifts since the subband energies are strongly field dependent. This gives rise to further broadened absorption spectra. It should be mentioned that very high purity (doping levels of the order of $1\text{x}10^{14}$) MQW samples have been reported grown by MBE [Amano *et al.*, 1991], thus field-induced broadening may in practice be eliminated.

In order to account for this broadening mechanism, the absorption coefficient at a certain photon energy E under an average electric field F_{ave} is calculated as the mean value along the MQW region

$$\alpha(E,F_{ave}) = \frac{\sum_{i=1}^{N_{MQW}} \int_{z_i}^{z_i+L_W} \alpha_z(E,F_z)\cdot dz}{N_{MQW}\cdot L_W} \qquad 3.3.6$$

where F_z is a z-dependent field, z being the direction perpendicular to the layers, and N_{MQW} is the number of wells in the intrinsic region. This broadening mechanism becomes increasingly significant in the wider well case, as a result of the relatively faster field-induced red-shifts. Note that we are still referring to the absorption coefficient of the well material only and not to that of the composite MQW layers.

3.3.4 Lifetime -related lineshapes (Homogeneous broadening).

In order to overcome the problem of overestimated insertion losses that arise from the use of a Lorentzian function as the lifetime-related lineshape, we need to determine an alternative function that gives a better fit to experimental absorption tails. It should be clarified that the incentive here is to devise a reliable design-tool and not to develop of a new theory. As described by Urbach's empirical rule, the absorption tails follow a temperature dependent exponential roll-off [Pankove]. This is associated with the formation of energy band tails in k-space arising from the presence of impurity centres. In the following, we aim at identifying the exponential function describing the absorption tails, based upon experimental data .

Firstly, we need to eliminate inhomogeneous broadening from our test sample. The sample chosen is thus a single 80Å well p-i-n diode (MV301) with 44Å $Al_{0.34}Ga_{0.66}As$ barriers and another 0.4027μm superlattice forming intrinsic buffers either side of the well. Field-induced broadening is not present in this case, however, well width fluctuation broadening still affects the spectra, as discussed in the previous section. The required absorption spectra are obtained from photocurrent data. Photocurrent (i_{pc}) values are converted to absorption coefficient values (α) using the following expression that relates the two:

$$i_{pc} = P\cdot(1-R_f)\cdot\eta\cdot\frac{e\lambda}{hc}\cdot e^{-\alpha_G\cdot d_G}\cdot\left[1-e^{-\alpha d}\right] \qquad 3.3.7$$

where η is the internal quantum efficiency, d the total thickness and α the absorption coefficient of the absorbing medium in the QW region, d_G and α_G the corresponding values for the GaAs capping layer, R_f is the reflectivity at the air-semiconductor front interface, and P is the incident optical power. All these are wavelength dependent. Values for α_G were obtained from a fit to data reported by Sturge [1962]. Equation 3.3.7 was used to obtain absorption spectra in arbitrary units, whereafter the final absorption coefficients were derived by a scaling of the heavy hole peak to the

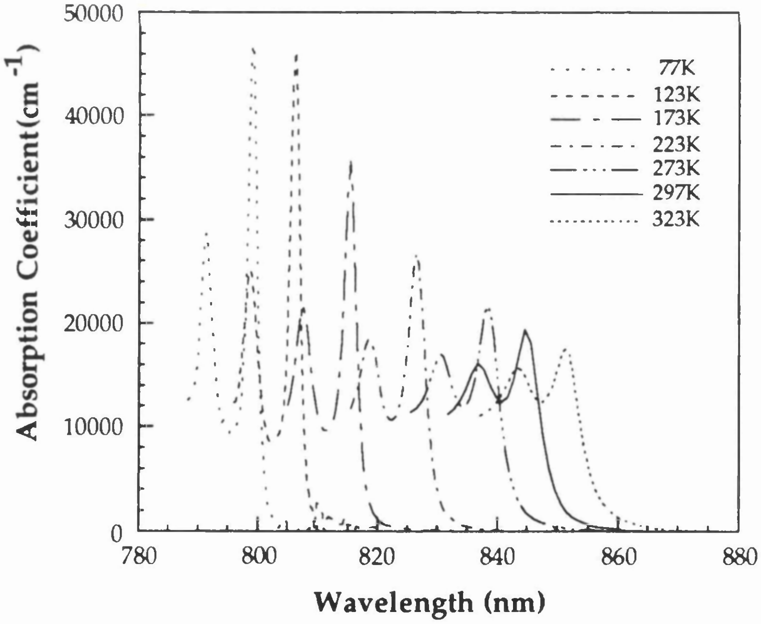

Fig.3.3.11 *Absorption spectra of an 80Å single quantum well at different temperatures. Spectra derived from photocurrent measurements obtained by means of a liquid Nitrogen Cryostat; photocurrent measurements by M. Ghisoni.*

appropriate value from Jelley *et al.* [1989]. Absorption spectra at different temperatures derived in this manner are shown in Fig.3.3.11, where the spectra at other than room-temperature are scaled assuming that the continuum level remains unaltered. This does not impose any errors in the evaluation of the temperature dependent absorption tail function, in that the latter expresses the roll-off of the absorption relative to the peak value.

We assume an absorption tail function starting from the half-point of the lineshape and having the form

$$f(E) = 0.5 \cdot \alpha_{max} \cdot e^{-b \cdot |E - E_{HM}|} \qquad 3.3.8$$

where E_{HM} is the photon-energy at the position of half-maximum, α_{max} is the absorption coefficient at the exciton peak and b is the sought-after constant. A

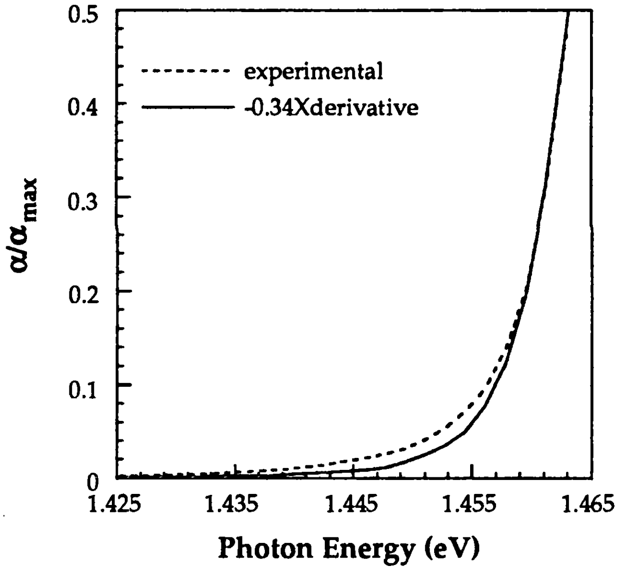

Fig.3.3.12 *Experimental quantum well absorption tail (dashed line) at room temperature and its derivative multiplied by a constant.*

convenient characteristic of an exponential function is that its derivative regenerates the function, i.e.

$$\frac{d(f(E))/d(E)}{f(E)} = -b \qquad 3.3.9$$

This relation leads to the derivation of b from experimental data by means of a calculation of the point to point derivative of the latter. After performing the required mathematical steps, it is evident in Fig.3.3.12 that the result indicates a slight deviation from the pure exponential dependence. This is at least partly due to broadening caused by well width fluctuations as is evident from the sufficiently good final fit to experimental data. That is presented in the next section. The values of b derived in the same manner by means of the absorption spectra in Fig.3.3.11 are shown in Fig.3.3.13. The exponential constant decreases with temperature as the exciton tails-off 'slower' in photon-energy- (and equivalently in wavelength-) space.

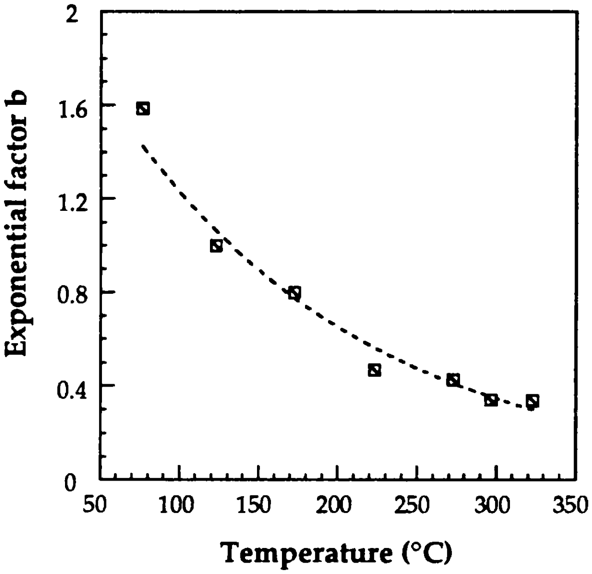

Fig.3.3.13 *The dependence of the exponential absorption tail on temperature as derived from the absorption data in Fig.3.3.11. The dashed line is a polynomial fit to the obtained points.*

Summarising the above, the homogeneous broadening lineshape employed in our simulation is a combination of a Lorentzian function located centrally within the FWHM (FWHM as by P.J. Stevens; see Appendix) rolling off exponentially from the half-point and 'outwards' with a dependence $e^{-0.34|E-E_{HM}|}$ (at room temperature), where E_{HM} is the position of the half maximum of the exciton peak in photon-energy. The obtained spectra provide a significantly improved fit to the experimental, as compared to those evaluated when using simply a Lorentzian function (Fig.3.3.14). It may now be noted that as a result of the altered 'area' under the finally used lineshape, our values for f_{ex} in section 3.2 differ from those employed by Stevens by a constant multiplication factor.

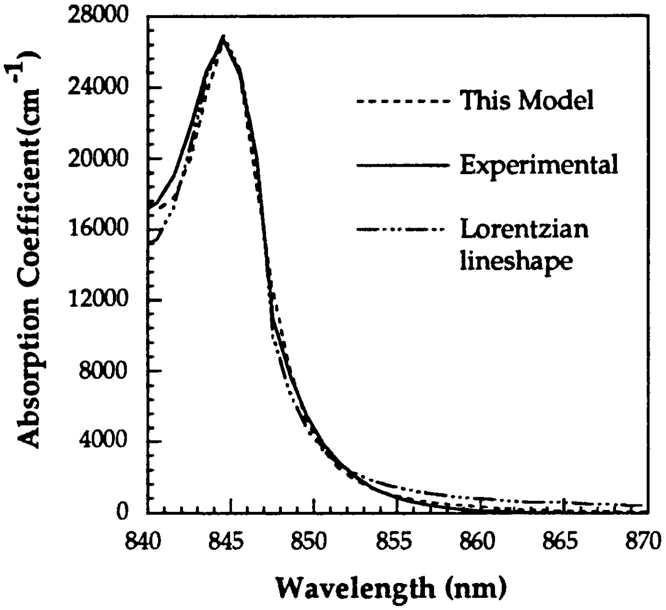

Fig.3.3.14 *Absorption coefficient spectra for a single 80Å well defined by* $Al_{0.34}Ga_{0.66}As$ *barriers. The experimental spectrum is compared with the calculated spectrum obtained by our model and with that obtained when a simple Lorentzian thermal lineshape is used, as by P.J. Stevens.*

3.4 COMPARISON WITH EXPERIMENT

The field-dependent energy levels obtained by the tunnelling resonance technique have been found [Stevens, 1989] to be in very good agreement with experiment. An example is illustrated in Fig.3.4.1, where we compare the calculated to the experimental position of the heavy-hole exciton peak as a function of the electric field applied perpendicular to the wells. The sample used (MV370) for this comparison has been grown by MOCVD and the MQW region consists of 50 nominally 85Å GaAs wells and 60Å $Al_{0.31}Ga_{0.69}As$ barriers. The built -in voltage is assumed equal to 1.4V. This value has been suggested by detailed measurements carried out by colleagues at Imperial College (Jenny Nelson, private communications) on samples that incorporate identical MQW material. These samples were, moreover, also grown by John Roberts at the University of Sheffield.

The corresponding calculated absorption coefficient spectra for the same sample as in Fig.3.4.1 (MV370) are an excellent simulation of the experiment, as depicted in Fig.3.4.2. A well width fluctuation of one monolayer (2.83Å), and a background doping of $5\times10^{15}\text{cm}^{-3}$ have been used in the calculations.

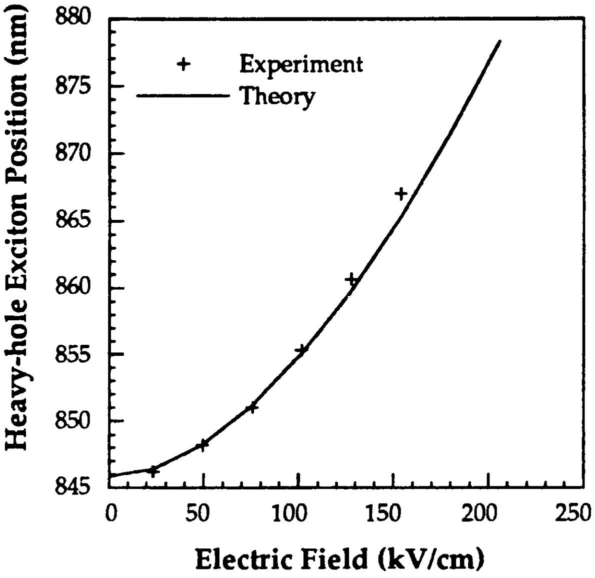

Fig.3.4.1 *Calculated and experimental dependence of the heavy-hole exciton position on the electric field applied perpendicular to the wells, referring to a 85Å MQW sample (MV370).*

The model routinely agrees with experimental measurements for other samples and various results found in the literature. For example, the large experimental FWHM of the excitonic peaks obtained for narrow wells [Jelley *et al.*, 1989], is remarkably well predicted by the theory. This has been thought by other workers to be solely the result of enhanced tunnelling through the barriers in the narrow well case [Lee *et al.*, 1989], where the wavefunction is 'squeezed' within the well and penetrates thus further into the barriers. According to this simulation, that large experimental FWHM is in fact a manifestation of the increased sensitivity to well width fluctuation characterising narrow wells. Similarly, the fast decrease of the excitonic peaks with field in the case of wide wells is predicted with excellent accuracy as a combination of both the fast drop in oscillator strength and the field-induced broadening that becomes increasingly significant in this case.

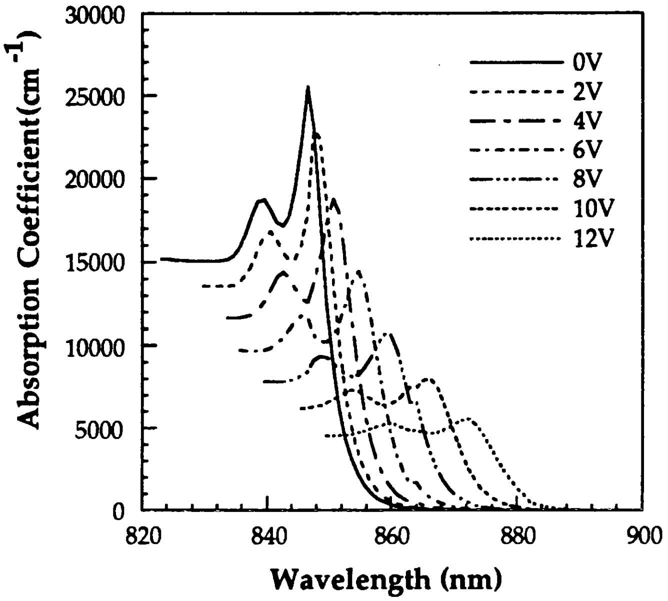

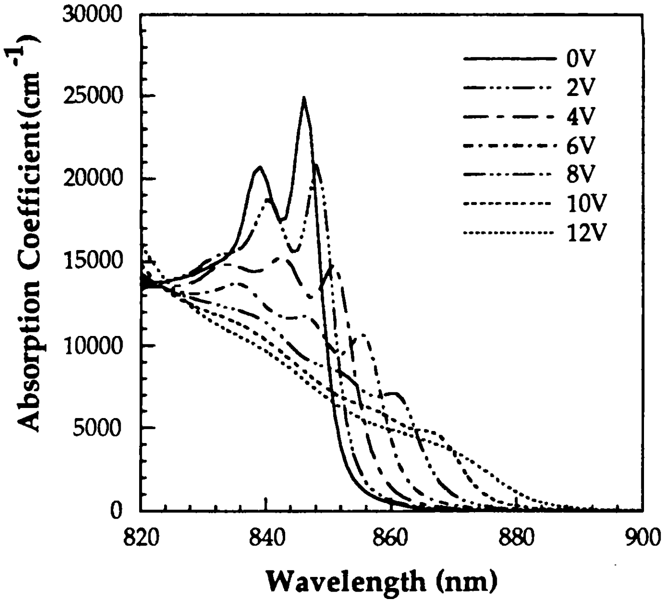

Fig.3.4.2 *Calculated (top graph) and experimental (bottom graph) spectra for an 85Å well sample (MV370). A background doping level of* $5x10^{15}cm^{-3}$ *and a well width fluctuation of one monolayer have been assumed for the calculations. The sample was grown by MOCVD at the University of Sheffield.*

Assessment of the modelled reflectivity spectra

In order to assess the final model, we compare calculated to experimental spectra for two AFPMs. In Fig.3.4.3 we show calculated spectra for CB145-the AFPM device presented in Chapter 2. The thickness of the $Al_{0.3}Ga_{0.7}As$ spacer layer has been adjusted so that the FP resonant position coincides with the experimental of the device

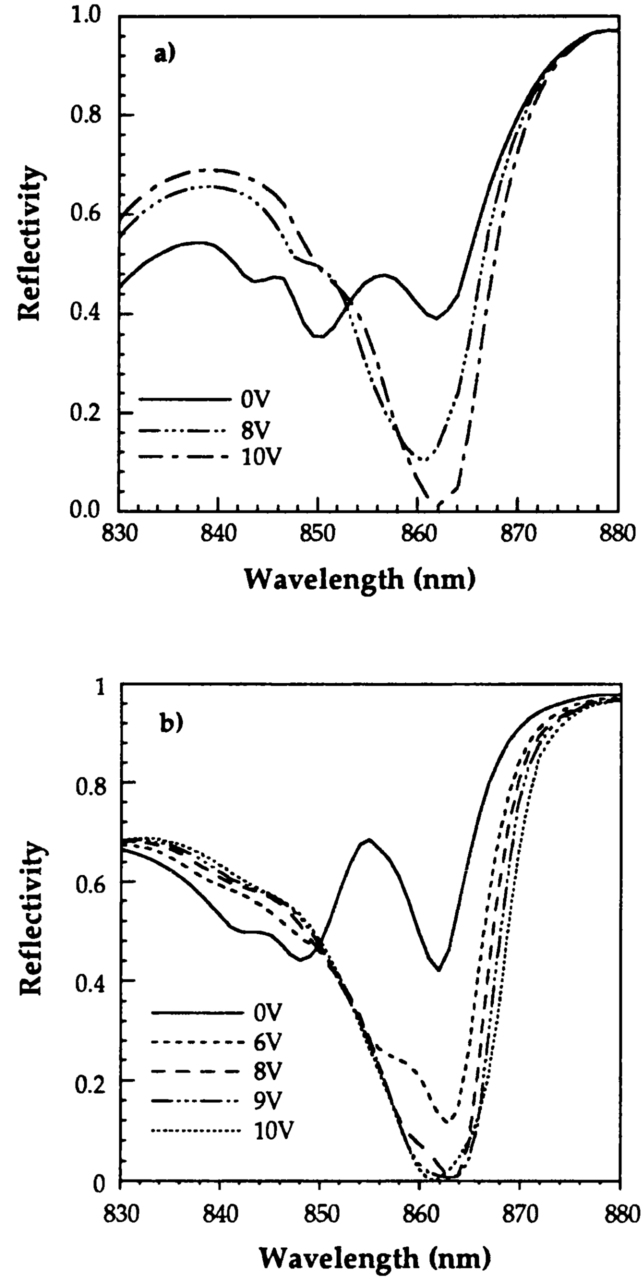

Fig.3.4.3 *Calculated spectra for CB145 AFPM experimental data from which have been presented in Chapter 2 (Fig.2.3.3). Theoretical absorption spectra are used in a), while in b) we use experimental absorption spectra and include the electrorefractive effects. See text for details.*

measured, while otherwise the layer-thicknesses are the nominal ones (Chapter 2). Theoretical absorption coefficient spectra are used for the simulation in Fig.3.4.3a, whre it is assumed that the background doping in the intrinsic region is equal to $5\times10^{15}cm^{-3}$, the rms well width fluctuation is one monolayer (≈2.83Å), and the built-in voltage is taken to be equal to 1.4V as previously. Note that the absorption of the top 1000Å GaAs has been taken into account, as we discuss later in this section. The calculated spectra presented in Fig.3.4.3a are in good agreement with the experimental while it is important to note again here that the use of a Lorentzian lineshape to account for thermal broadening (see Fig.3.3.14) resulted in an estimated insertion loss of 5.2dB for the same structure, as opposed to the experimental value of 3.5dB. The operating voltage is, however, slightly overestimated by our model. Since the absorption coefficients and QCSE-induced shifts are not underestimated by the model (Fig. 3.4.2), this slight discrepancy between theory and experiment may be attributed almost solely to the omission of the electrorefractive effects. Indeed, calculations using experimental absorption spectra where the electrorefractive effects and the correct QW index dispersion (section 2.3.3) are included, show an indeed *excellent* agreement with the experiment (Fig.3.4.3b). This demonstrates quite clearly that the optical transfer matrix technique is appropriate for the simulation of such devices and, additionally, further confirms the validity of our analysis of the effect of electrorefraction in Chapter

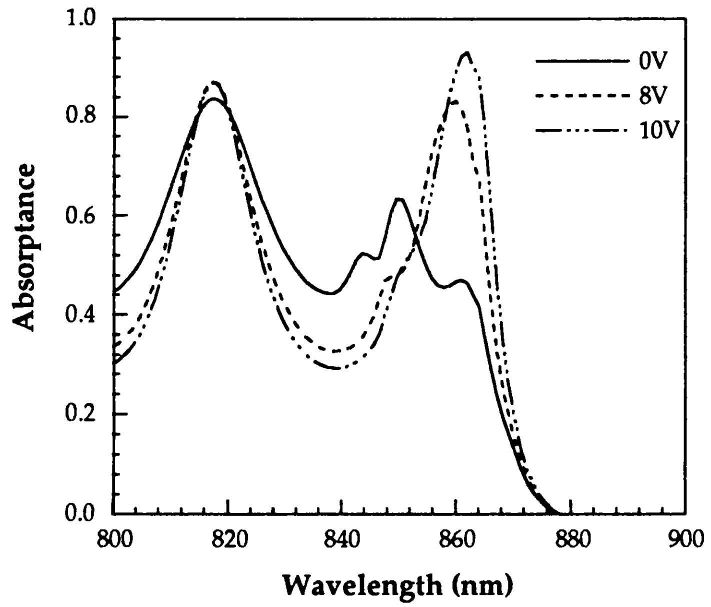

Fig.3.4.4 *Calculated spectra for CB145 AFPM experimental data from which have been presented in Chapter 2. Modelled reflectivity spectra are shown in Fig.3.4.3.*

2.

In Fig.3.4.4 we show calculated absorptance spectra for the same structure. These will largely resemble the photocurrent spectra obtained from the real device (see section 3.4.4 and Chapter 2). As a result of our not including the forbidden transition el-hh2, the spectra in both Figs.3.4.3 and 3.4.4 show a good agreement with experiment for wavelengths longer than the zero-bias heavy-hole but not so for shorter than that peak wavelengths. This, however, does not impose any errors in our evaluation of the modulator performance since we are interested in operation at the longer wavelengths (normally-on AFPMs).

Calculated spectra for a device with a front reflector stack, as well as a bottom one, are shown in Fig.3.4.5. We present results from this device in Chapter 6. This structure (QT223) was designed to have a front mirror reflectivity of ≈55%, a back mirror reflectivity of ≈99% and an intrinsic region incorporating 32 90Å GaAs wells with 55Å $Al_{0.3}Ga_{0.7}As$ barriers. The model suggests a well width of 98Å. We assume therefore this well width for our calculations and adjust the thickness of the spacer layer so that the resonance is obtained at the same position as for the experimental data presented in Chapter 6. The parameters used in the calculations are as for CB145 above. The obtained spectra are not a very precise reproduction of the experimental

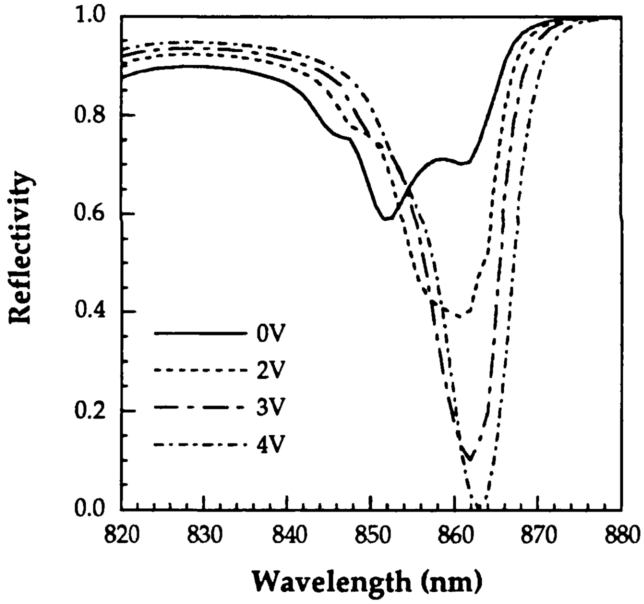

Fig.3.4.5 *Calculated spectra for QT223 experimental data from which are presented in Chapter 6.*

ones. In particular the insertion loss is underestimated by the model, where the experimental value was about 3dB (Chapter 6), and the experimental operating voltage (3.4V) for this device was lower than that predicted here. However, this pointed towards a possible reason that was further supported by the measured data (Chapter 6).

Limitations

The accuracy of the modelled spectra for the reflection modulator are firstly limited by the use of theoretical absorption spectra. We examined the imposed limitations above. One of the factors challenging the reliability of this simulation is the exclusion of the electrorefractive effects, i.e. of the QCSE induced refractive index changes and consequent shifts of the resonant wavelength. In general, it is not essential to include these effects when modelling normally-on AFPM devices since the electroabsorptive effects by far dominate the spectra. This has also been pointed out by Livescu *et al.* [1992] and Boyd and Livescu [1992], who did take these effects into account in their calculations that were based on experimental absorption spectra. The magnitude of the electrorefractive effects is highly wavelength dependent around the sub-band edge (Chapter 2). As a result, the effect on the reflectivity spectra may vary in significance depending upon the position of the resonant wavelength in relation to the heavy-hole exciton peak, and the accuracy of the calculated spectra will vary accordingly. Obviously, the spectra are increasingly modified when the proportion of well material incorporated in the cavity is higher, since the induced refractive index changes concern the well material only. In some cases in this thesis we prefer to use experimental absorption spectra and include the electrorefractive effects, as is the case for the devices in Chapter 8. In summary, the omission of electrorefraction affects the fidelity of the evaluated spectra to a small extent, but this is usually limited to a slight under- or over-estimation of the operating voltage.

The absorption of bulk GaAs is included in the calculation so that the effect of the top GaAs capping layer is, for example, accounted for. The values used for the relevant absorption coefficients are an empirical fit to experimental values reported by Sturge [1962]. On the other hand, refractive index dispersion is not included, bar that of the quantum well region when experimental absorption data are implemented. This should not impose any major limitations to the calculations, provided that the indices used refer to the wavelengths of interest, i.e. in the vicinity of the operating wavelength.

One of the assumptions of the optical transfer matrix technique that clashes with real experimental conditions, is that a plane wave is assumed incident upon the layers. In practice, the incident beam profile is not a plane wave, it is in fact best approximated by a Gaussian-like profile as it will as a rule originate from a laser and will have to go through focusing optics. The simulation accuracy is not severely limited by this when modelling spectra tested on the experimental set-ups used in this work (Chapter 2). Simulating the case where a highly convergent beam is incident upon the structure, which will be the situation when using small device sizes, will be necessary for future devices.

Finally, graded interfaces may not be directly modelled by means of this analysis, since abrupt 'perfect' interfaces are assumed. Here we are not concerned with regions of the order of a monolayer since these have no effect on the propagation of the optical wave at the wavelengths of interest where λ is two orders of magnitude larger than the total extent of a region of such dimensions. Larger graded interfaces have attracted a lot of interest recently. Specifically, work on surface emitting lasers has indicated that such interfaces between the high and low index layers comprising the reflector stack attain an improvement of the electrical characteristics of these layers, i.e. lower resistance [see for example Wang *et al.*, 1992; Sugimoto *et al.*, 1992]. The transfer matrix technique used here may simulate sufficiently large non-abrupt interfaces if these are approximated by a step-like profile. Nevertheless, this technique is not best suited for such calculations. A more elegant approach applicable to the case of an arbitrary-profile interface has been developed by Corzine *et al.* [1991].

In summary, we have used the (optical) transfer matrix technique to calculate the reflectivity, absorptance, or transmittance of a multilayer structure that incorporates quantum wells in the intrinsic region. The simulated device spectra are evaluated at different fields applied perpendicular to the wells. The field-dependent quantum well absorption spectra required for this, are derived using the theoretical method developed by Peter Stevens [1988], and this may be performed for well widths in the range between 50Å-200Å. Using an empirical technique, we have slightly modified the thermal lineshape used in that model in order to obtain a realistic simulation for the case of resonant devices. Modelled QW absorption coefficient spectra as well as modelled reflectivity spectra for resonant devices are in good agreement with those experimentally obtained. Nevertheless, better agreement with the experiment is attained when using experimental absorption spectra and taking the electrorefractive effects into account.

CHAPTER 4: THE TEMPERATURE TOLERANCE OF THE ASYMMETRIC FABRY-PEROT MODULATOR

4.1 INTRODUCTION

The tolerance of a modulator device to changes in the ambient temperature is one of the prime practical considerations. We may gain a feel for the required operational temperature range by considering the specifications for electronic circuitry with which the optoelectronic components will need to be integrated. Successful operation within the 0-70°C range is a typical specification for electronics which is not expected to be matched by optoelectronic devices as they rely generally on absorption -or absorption related- phenomena that are strongly affected by temperature.

The issue appears at first sight especially important for the AFPM the operation of which relies very much on the 'correct' relative alignment between the Fabry-Perot (FP) resonance (λ_{FP}) and the heavy-hole exciton peak. Its performance might thus be expected to be severely temperature dependent since both the exciton and the resonance shift to longer wavelengths with (rising) temperature and, moreover, at different rates. In this Chapter the effect of temperature on the performance of the AFPM is studied experimentally. The significance of various parameters is assessed and possible means of improving the temperature tolerances are discussed.

4.2 THE EFFECT OF TEMPERATURE ON THE FABRY-PEROT MODULATOR

The ambient temperature affects firstly the absorption spectra of the MQW material and secondly the refractive indices of all the layers that comprise the modulator. The latter effect is specifically significant for resonant devices, like the AFPM, since it results in a modification of the optical length of the FP cavity and thus alters its resonant function. We address these separately below.

Effect of temperature upon the MQW absorption spectra

The prime effect of temperature upon the quantum well absorption spectra is the red-shift of the excitonic features with temperature that stems directly from the temperature dependence of the bandgap energy E_g which for (bulk) GaAs is

$$E_g = 1.519\text{eV} - \frac{5.405\text{x}10^{-4}(\text{eV}/\text{K})\cdot T^2}{T + 204\text{K}} \qquad 4.2.1$$

[Casey and Panish]. According to this equation, the heavy-hole exciton is estimated to shift by about 0.27nm/°C around room temperature in this material system, which is in good agreement with experimental observations by several workers [Fujiwara *et al.*, 1988].

The absorption spectra are also affected by phonon broadening which is obviously temperature dependent (Chapter 3). Broadening of the excitonic peaks diminishes the achievable modulation of the absorption coefficient at a certain field, degrading thereby the performance of the device. Nevertheless, the effect is insignificant in comparison to the thermally induced reduction of the bandgap, which is by far the dominant mechanism responsible for the observed changes in the absorption spectra of multiple quantum well material.

Effects of temperature on the refractive index

The refractive index n of semiconductor materials generally increases with temperature (T) according to the expression

$$n = n_o \cdot (1 + c \cdot T) \qquad 4.2.2$$

where n_o is obviously the refractive index of the material at 0 K and c is a constant [Blakemore, 1982]. Here, the indices considered are measured far from the bandgap edge and the corresponding effect has been referred to as the thermo-optic effect. It is interesting to remind ourselves that the refractive index and the bandgap energy are intimately -albeit in a complex way- related parameters. The empirical trend observed is that the larger the bandgap the lower the index of the material. Around room temperature and at 860nm

$$dn/dT = 3.411 \times 10^{-4} / K$$

for GaAs with n_o=3.533 [Kisting *et al.*, 1990]. It is reasonably valid to assume the same temperature dependence for the index of $Al_xGa_{1-x}As$, for any Al concentration x. The index n_o (eqn.4.2.2) will of course depend on x.

Irrespective of the cause, a change of the mean refractive index n of the materials comprising the cavity gives rise to a shift of the FP resonance as follows from the consequent change of the optical length L_{opt}. This is given by

$$\Delta L_{opt} = \frac{L \cdot \Delta n}{\lambda} \qquad 4.2.3$$

where L is the physical length of the cavity medium. Note that no other cavity parameters, such as front and back mirror reflectivities corresponding cavity finesse etc., come into this relation. The consequent shift of the FP resonance is

$$\Delta\lambda = \frac{\lambda}{n} \cdot \Delta n \qquad 4.2.4$$

Considering the thermo-optic effect alone for a moment, an estimated value of the shift of the FP resonance at 860nm (assuming a mean value n=3.5) is

$$\Delta\lambda/\Delta T = 0.083 \text{nm}/^\circ C$$

The assumption here, however, has been that n is not wavelength dependent which of course is not accurate. In reality, n decreases with wavelength [Blakemore, 1982; Sell *et al.*, 1974]. This tends to impede the overall thermal shift of the resonance. Indeed, as illustrated by eqn.4.2.4, a positive Δn (higher T) leads to a red-shift of λ_{FP} which on the other hand induces a negative Δn. This latter stems from the fact that we are observing n at a longer wavelength and $dn/d\lambda$ is negative (typically $dn/d\lambda = -6.83 \times 10^{-4}$/nm [Sell *et al.*, 1974]). Hence, the net Δn is lower than $(dn/dT) \cdot \Delta T$ and this causes the thermal shift of the resonance to slightly decrease from the value quoted above.

Whereas the above suffice to describe the main effect in bulk material, the situation is somewhat more complex where the quantum well layers are concerned. As we have discussed in Chapter 2, the excitonic features in quantum wells give rise to a modification of their refractive index spectrum in relation to that of bulk via the Kramers-Krönig relations. The underlying cause of the thermally induced shift of both the bulk and the quantum well absorption spectra is identical: the reduction of the band-gap energy of GaAs. Hence the characteristic shape (Fig.2.3.6) of the quantum well index spectrum will by and large remain the same at all temperatures but shift to the wavelength dictated by the absorption edge. As far as the performance of the modulator is concerned, however, it is also important to consider the QCSE induced changes of the refractive index (Fig.2.3.7). Let us assume that the thermal broadening of the absorption peaks is negligible within the small temperature range considered here (Chapter 3). In the same manner as above, we may deduce that these field-induced changes $\Delta n(F)$ will also retain their general characteristic features and will occur at the same relative wavelength separation from the exciton at all temperatures.

From our discussion in this section, the exciton shifts with temperature faster than the FP resonance does and, as a result, the separation between the two decreases. Thus, according to the qualitative picture drawn above, we may summarise the effect of this enhanced spectral non-linearity of the index in quantum wells as follows:-

i. With no field applied, the position of the resonance will be led to shift slightly faster with temperature than the 0.083nm/°C quoted earlier. This is brought about by the fact that the index of the quantum well material increases as the relative wavelength separation from the exciton peak decreases (Fig.2.3.6) at the wavelength regions concerned.

ii. Upon the application of a field, there is a QCSE induced shift of the resonance the magnitude and the sign of which depend again upon the relative wavelength separation from the exciton peak (see Fig.2.3.7). As this separation is altered with temperature, the wavelength misalignment between the unbiased and the biased position of the resonance will also be modified. Hence an increase of this QCSE induced shift of the resonance is expected with temperature, resulting from the increasingly negative Δn when operating closer to the exciton. This is the case for CB145 where the FP resonance is ≈10nm away from the unbiased exciton peak.

Summarising, the exciton will approach the FP resonance as the temperature is increased (and move apart as T is decreased) since it red-shifts approximately 3-times as fast as the resonance does. As a result, the overall performance of the modulator may be notably modified. An effect that was not mentioned above, is the thermal expansion effect which will lead to a further modification of L_{opt} by affecting the physical cavity length L. The GaAs thermal expansion coefficient, that can be used as a guideline for the GaAs/AlGaAs system, is equal to $5.2\times10^{-6}/°C$ which is two orders of magnitude smaller than dn/dT and thus relatively negligible.

4.3 EXPERIMENTAL STUDY OF THE TEMPERATURE SENSITIVITY OF CB145

4.3.1 Experimental set-up.

Biased and unbiased spectra of a device fabricated from CB145 (Chapter 2) were obtained on the OMA system at different temperatures around ambient (≈24°C). The temperature of the device was varied using a Peltier heat pump of a capacity of 0.32W which implies a potential maximum temperature difference of 67°C. The temperature was monitored using a K-type fine thermocouple thermally connected about 2mm away from the device on the usual copper header and electrically isolated from it using an insulating thermal adhesive. The arrangement is illustrated in Fig.4.3.1.

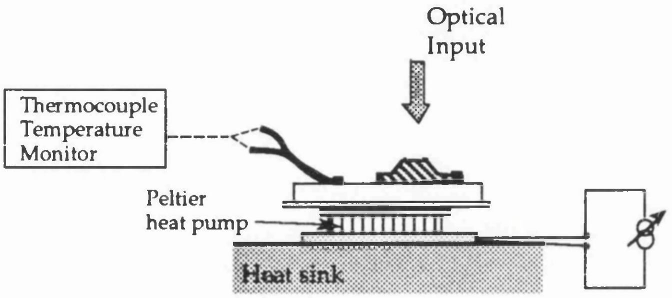

Fig.4.3.1 *A schematic of the experimental arrangement used to vary the temperature of the modulator.*

The current to the Peltier plate was adjusted initially for each temperature and then measurements were taken when, according to the monitor, thermal equilibrium was achieved (stabilised temperature reading). It was expected that there could be a small temperature gradient between the thermocouple and the device, which ought to be insignificant since both were directly on top of the Peltier plate. A *constant* gradient (i.e. non-dependent upon the amount of heat pumped) imposes no errors because it is the accuracy in temperature differences and not in the absolute values that we are concerned with. Judging from the experimental value of the shift of the exciton position with temperature, it appears that the achieved temperature differences were slightly under-estimated as we will see in the next section.

4.3.2 Experimental spectra with varying temperature.

We investigated the temperature range between 14° and 45°C. Some field-dependent spectra at different temperatures are shown in Fig.4.3.2. The device was designed to operate at ≈25°C where virtually zero reflectivity is obtained at the off-state (R_{off}) under 9V reverse bias (Chapter 2). The reflectivity at the resonant position depends upon the amount of absorbing medium (αd) that is present at that wavelength. As the temperature is increased from 24°C, the exciton (heavy-hole) approaches the resonance and thus in the unbiased spectra the amount of αd at the resonant wavelength λ_{FP} is increased. This leads to a reduction of the on-state reflectivity R_{on} or, equivalently, an increase of the insertion loss. For the same reason, the bias under which R_{off} is minimum is decreased with rising temperature. The opposite trends are observed in the other direction ($\Delta T<0$). At 14°C the optimum bias is over 10V and also contrast in excess of 20dB cannot be attained at any voltage. This is because the exciton-resonance separation is significantly increased at that temperature and thus the amount of absorber αd that is induced at the resonance upon the application of the appropriate field (larger than that required at 24°C) is not sufficient to balance the cavity (see Chapter 2).

The mean experimental thermal shift of the heavy-hole peak is ≈0.3nm/°C (Fig.4.3.3) which is close to, but slightly larger than the expected 0.27nm/°C. Nevertheless, this is not considered to challenge the validity of the conclusions drawn since, in any case, such an inaccuracy would cause the tolerances to appear poorer than they actually are. The position of the FP resonance at the on-state shifts by an average 0.14nm/°C. The deviation from the theoretically predicted value of 0.083nm/°C calculated for bulk material is attributed to two factors:-

i. The achieved temperature differences have been under-estimated leading to an over-estimation of the obtained shifts.

ii. As discussed in the previous section, at the concerned wavelength separations from the unbiased exciton there is a large spectral non-linearity of the quantum well index. This results in an increase of the index as the resonance approaches the exciton, i.e. as the temperature rises. As a consequence, the rate by which the optical length that corresponds to the quantum well layers changes with temperature is further increased.

The lower order resonance, that occurs at about 822nm, exhibits a slower shift of about 0.088nm/°C. This is a result of the wavelength dependence in equation 4.2.4., but it is also largely due to the fact that this resonance is away from the quantum well edge

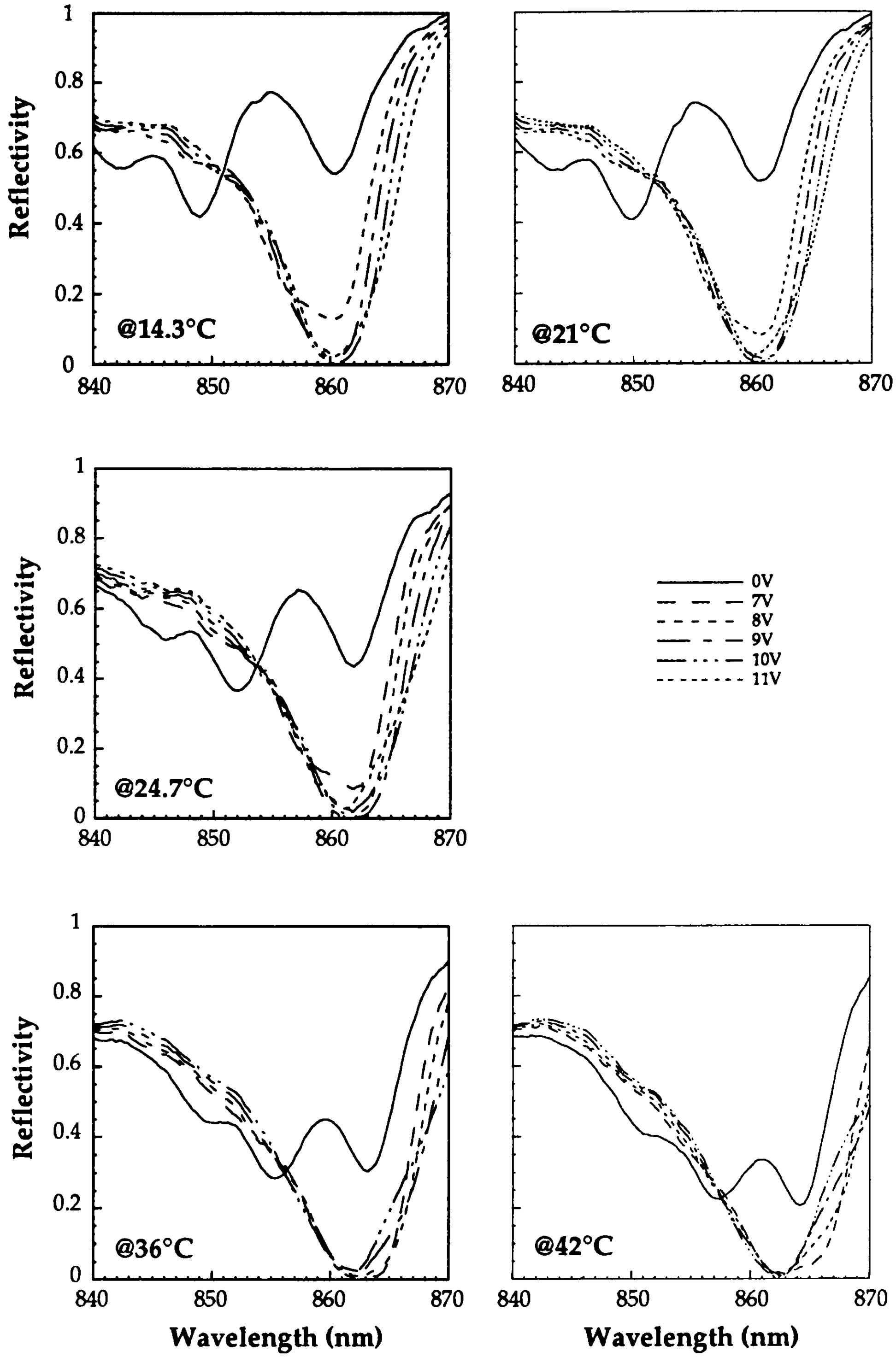

Fig.4.3.2 *Experimental reflectivity spectra for a device from CB145 at different temperatures. The device was designed to operate at ≈25°C.*

and thus its shift is governed by the thermo-optic effect.

Unbiased spectra at different temperatures as well as spectra at 9V reverse bias are shown in Fig.4.3.4. The position of minimum R_{off} at 9V can be seen to be temperature dependent experiencing a shift of 0.07nm/°C (Fig.4.3.3). The observed resonance is a consequence of both the thermo-optic and the QCSE related index changes. The on- and off-state resonances in Fig.4.3.4 occur at increasingly mutually differing wavelengths as the temperature rises. This results from the enhanced voltage induced index changes with temperature that stem from the reduced exciton-resonance separation, in agreement to our predictions in section 4.2. We will see that the misalignment between the on- and the off-state resonance have a positive effect upon the insertion loss.

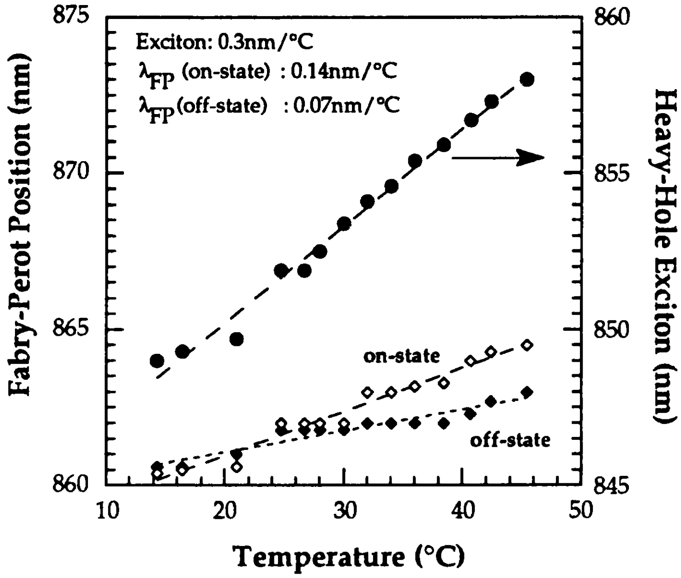

Fig.4.3.3 *The obtained temperature dependent positions of the heavy-hole exciton and the Fabry-Perot resonance at both the on-state (0V) and the off-state (at 9V reverse bias). Linear fits to the experimental points have been used, the slopes of which are shown in the inset.*

It was evident from Fig.4.3.2 that the effect of temperature upon the on-state reflectivity is by far more profound than the respective effect upon the off-state. This is due to the fact that the finesse of the cavity at the on-state (0V) is effectively that of a cavity with $R_f=0.3$ and $R_b^{eff}=0.77$ (where R_f is the front and R_b^{eff} is the effective back mirror reflectivity), while in the off-state (9V) $R_f=R_b^{eff}=0.3$. The effective finesse decreases thus from $\mathcal{F}=4.12$ in the on- to $\mathcal{F}=2.45$ in the off-state and, as a result, the off-state is far less sensitive. We discuss this further in Chapter 5.

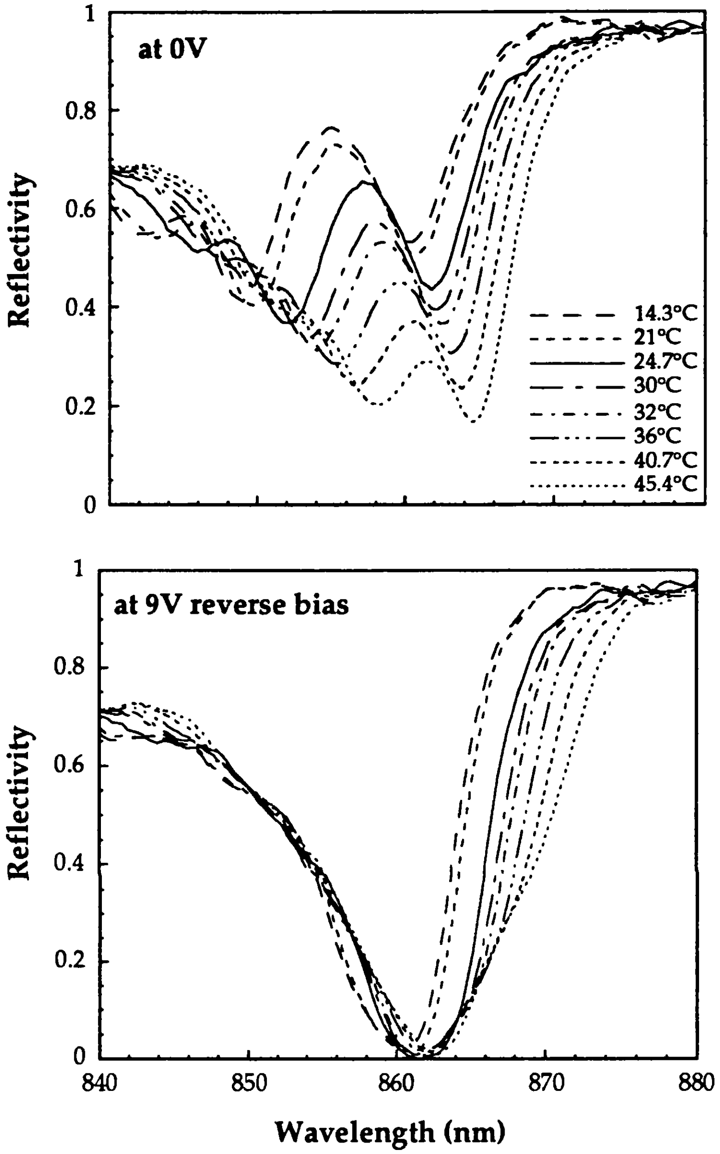

Fig.4.3.4 *Experimental reflectivity spectra for a device from CB145 at various temperatures. The spectra are shown at both 0V and 9V, which is the optimum operating voltage at 24°C.*

4.3.3 Fixed wavelength operation

In this section, we will assess the practical implications of the temperature dependence of the reflectivity spectra upon the operation of the device.

Contrast

The wavelength of maximum contrast at ≈25°C is 861.8nm. The contrast obtained at that wavelength and at a fixed 9V reverse bias (optimum) is reduced when the temperature deviates from 25°C as can be seen in Fig.4.3.5. It nevertheless remains over 10dB for the whole range investigated and over 15dB within the 25°-35°C temperature range. The insertion loss increases significantly with temperature (Fig.4.3.5.) as expected (section 4.3.2). At 8V reverse bias and at 25°C, the absorption induced at the resonance is not enough to reduce the reflectivity to zero. However, as T increases the exciton-resonance relative wavelength separation decreases, and the contrast obtained at 8V is increased as a result of the larger induced αd. This takes place until the exciton is shifted to wavelengths longer than the resonance when αd starts dropping again and consequently so does the contrast. Exactly the opposite happens as T decreases below 25°C (Fig.4.3.6). Similarly, at 10V the contrast ratio is reduced with T rising from 25°C as the exciton moves further away from the resonance and then experiences a small increase possibly because the light hole exciton approaches the resonant position. Also a slight improvement is obtained when T is reduced below 25°C. Obviously the above qualitative explanation of the experimental data is a simplification of a more complex situation since we are observing the effect at a fixed wavelength and not following the shifting resonance. One should bear in mind, however, that the total shift of the resonance is ≈2nm for the entire temperature range

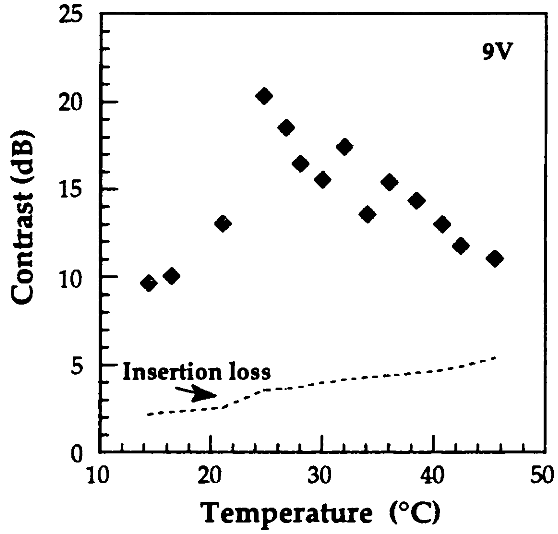

Fig.4.3.5 *The contrast obtained at 861.8nm and 9V, that are the optimum operating conditions at 25°C, is plotted as a function of temperature. The insertion loss at the same wavelength is also shown.*

investigated and therefore the resonance is effectively fixed by comparison to the shift of the exciton peak.

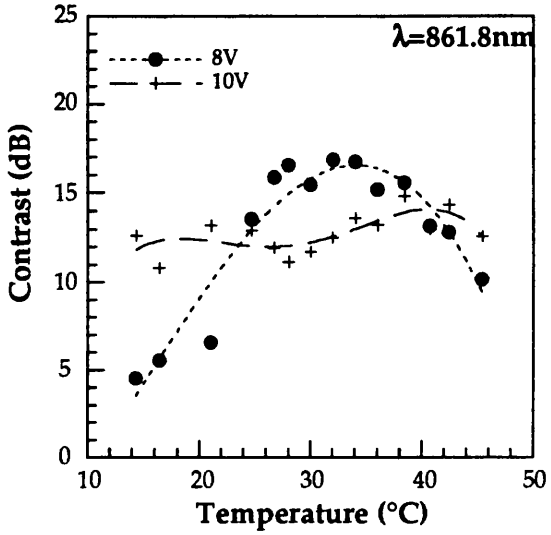

Fig.4.3.6 *Experimental results at the wavelength where optimum contrast is obtained at 24°C. The contrast at 8V and at 10V is shown, which is below and above the optimum of 9V respectively.*

Reflection Change

At 861.8nm, where the obtained contrast ratio is maximum at 25°C, the reflection-change ΔR is lower than its optimum value ΔR_{max} at the same temperature. At this wavelength ΔR shows a slow dependence on temperature (Fig.4.3.7). Interestingly, the rate of change is virtually voltage independent at the high T end of the range, while at low T the biasing voltage starts becoming more important. In fact this reflects the dominant role of R_{on} in this case where, with the exception of the lower temperatures, R_{off} is maintained at very low values, as a result of operation at-the-resonance. In other words ΔR is effectively directly determined by R_{on} when operating at the resonance.

Maximum reflection-change at 25°C is obtained at 864nm (2nm away from the wavelength of maximum contrast for the same temperature) and at this wavelength ΔR decreases markedly when the temperature deviates from the optimum one (Fig.4.3.8a). The temperature at which maximum ΔR is attained can be seen to be voltage dependent. The prime cause of the reduction of ΔR is the large effect on the insertion loss shown in Fig.4.3.8b (compare to Fig.4.3.5) which arises from the fast red-shift of the 0V resonant position. Contrary to the 'on-resonance' operation above, here the values of both R_{on} and R_{off} become significant in defining ΔR and this is

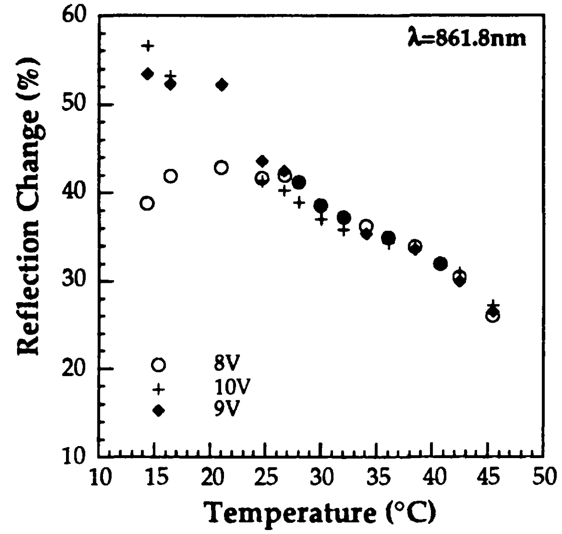

Fig.4.3.7 *Experimental reflection-change as a function of temperature at the wavelength where maximum contrast is obtained at 25℃.*

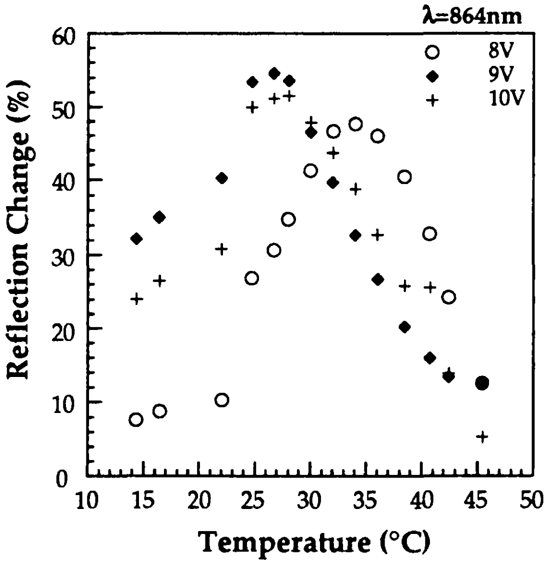

Fig.4.3.8a *Experimental reflection-change at the wavelength where the reflection-change shows its maximum at 25℃. The insertion loss at that wavelength is shown in Fig.4.3.8b.*

manifested in the marked voltage dependence in Fig.4.3.8a. The wavelength misalignment between the biased and unbiased resonances further enhances the reduction of ΔR.

Although the reflection-change is not maximised at the resonant position, it is evident that 'on-resonance' operation is preferable even when reflection change is the parameter of interest because the tolerances are notably improved at that wavelength.

The above results are encouraging indeed. Operation at fixed voltage and wavelength yields contrast in excess of 10dB over a 30°C temperature range. Furthermore, this appears possibly extendable to the higher temperature side.

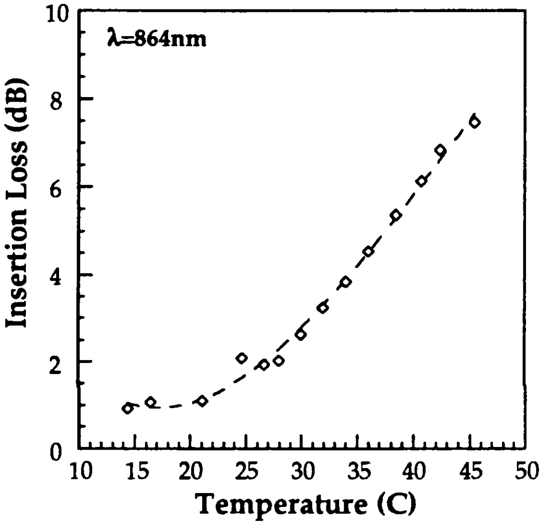

Fig.4.3.8b *Insertion loss at the wavelength where the reflection-change is maximum at 25°C.*

4.3.4 Tracking the optimum operating wavelength.

In the previous section the performance characteristics were considered at a fixed wavelength. It is more likely though that the wavelength of operation will also vary with temperature as it will originate from a laser source. As to whether the modulator and the laser will experience the same temperature is hard to tell at this stage particularly without a specific application in mind. It basically depends on whether we are concerned with ambient temperature or 'local' (on-chip) variations. As far as optical interconnection arrays are concerned, one may regard ambient temperature tolerances as the prime consideration and may expect that the laser and the modulator will not be physically in proximity. The benefits of wavelength tracking the resonance are assessed below.

Contrast

With the biasing voltage fixed at 9V, maximum contrast (Fig.4.3.9a) is achieved at different wavelengths (Fig.4.3.9b) when the temperature is changed. These values are derived directly from the experimental spectra used in this study. The optimum wavelength (as far as contrast is concerned) is determined by the point where R_{off} is minimum, thus it can be seen to shift by an average 0.07nm/°C coinciding in other words with the off-state resonance. The implication, therefore, is that the operational temperature range would be extended, or an improvement in contrast within a certain range could be accomplished, if the wavelength of operation were to track the resonance. Comparison with the fixed wavelength operation in Fig.4.3.5 points out that the improvement is mainly attained from the low temperatures side.

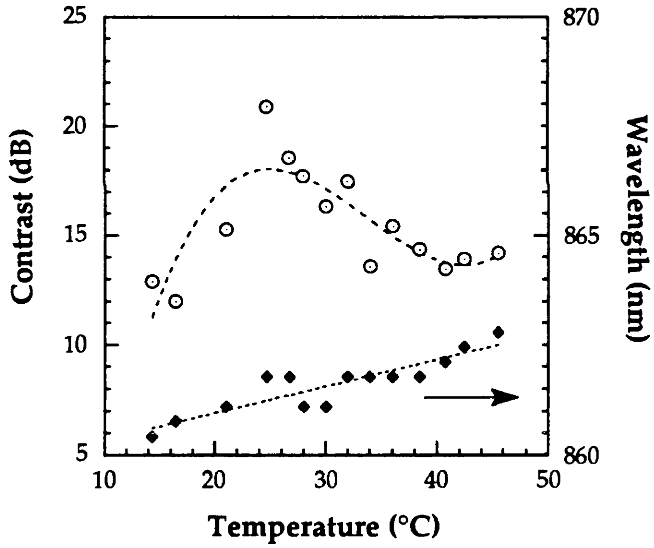

Fig.4.3.9 *Operation at the wavelengths where maximum contrast is obtained at each temperature. The required wavelength shift is 0.07nm/°C.*

The emission of a DFB laser diode shifts with T as determined by the resonant position of the structure. This shift is governed by the thermo-optic effect, and is independent of other cavity parameters. Consequently, the effect of temperature on the emission wavelength of such a laser diode will be very much like that on the modulator. The situation is a bit more complex as the optical confinement may be affected by the differing effects on the grating and the cavity medium (Cai Bo, private communications). For small temperature changes, however, a DFB laser may track the modulator if both devices experience the same temperature.

A conventional FP laser diode, on the other hand, emits at the cavity mode that experiences the highest gain. The cavity length determines the optical resonances, and the gain function is determined by the active medium. When the temperature changes the FP resonances shift in the same manner as these of our FP modulator whereas the gain curve follows the temperature induced reduction of the band-gap energy. The total effect on the lasing wavelength is that for a small change in temperature the emission follows the position of the resonance until the relative shift of the modal spectrum and the gain curve result in another mode being favoured. Lasing then hopps to that wavelength. In conventional edge-emitting lasers the modal spacing is very small so that this mode hopping takes place very easily and is manifested as an effectively uniform shift of the operation determined by the position of maximum gain. In surface emitting lasers however, the modal spacing is large due to the very short cavity lengths. As a result, temperature changes lead to shifts of the wavelength of emission as this is dictated by the position of the resonance. Thus a surface emitting laser would to some extent track the wavelength of optimum contrast of an AFPM. It should be made clear, nevertheless, that the range where an improvement can be accomplished is limited and particularly so at the low temperatures side, since high contrasts are not obtainable at any wavelength for T lower than a critical value. The exciton is then, as discussed earlier, too far away from the resonance for the required amount of absorber αd (Chapter 2) to be induced in the cavity. Additionally, the optimum voltage is altered (increased) so that voltage tracking is also required for any significant improvement to be attained. Finally, it should be noted that the operation of lasers is also governed by changes of the refractive index induced by changes in carrier concentration. Notwithstanding, we have identified two types of lasers for which the temperature shift of the wavelength of emission will be in the right direction to yield an improvement of the overall temperature tolerance.

Reflection change

As based upon our experimental spectra, maximum ΔR at 9V is obtained with the wavelength shifting by an average 0.3nm/°C with temperature (Fig.4.3.10). Reflection changes in excess of 40% are then obtained within the temperature range investigated. The position of ΔR_{max} appears to roughly follow the exciton in its thermal shift which appears surprising if we consider the resonant nature of this device. However, this may be attributed to the combined effect of the previously discussed dominant role of the on-state spectra upon ΔR and the faster shift of the exciton as compared to that of the resonance. The implication is that this cannot be stretched over a much wider temperature range, but it nevertheless appears that an improvement of the sensitivity of the reflection-change upon temperature may be accomplished if the operation is set at a some fixed relative wavelength separation from the exciton peak at each temperature.

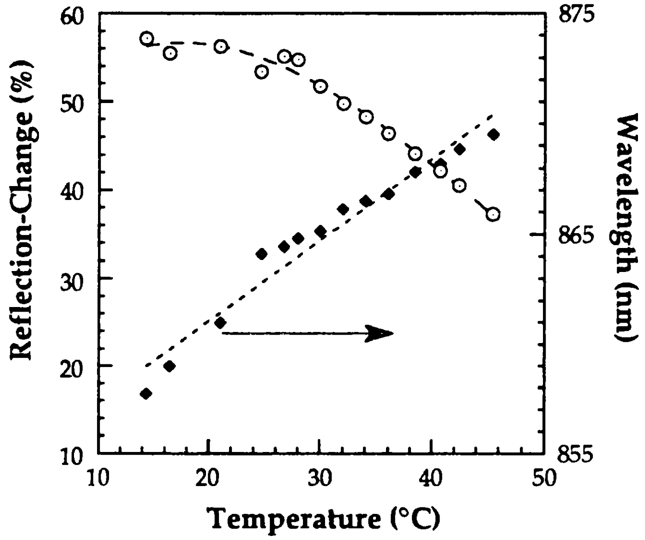

Fig.4.3.10 *The maximum reflection-change is shown as a function of temperature when the voltage is fixed at 9V and the wavelength is varied.*

We can identify a FP laser diode as the suitable source in this case since the emission wavelength of that type of laser is governed by the bandgap energy of the active medium, as we discussed previously. What is rather unfortunate is that the general tolerances are poor at these wavelengths that lie off the resonant position.

Summarising this section, wavelength tracking the resonant position, while keeping the biasing voltage fixed, would partly compensate for the deteriorated performance that results from a deviation of the temperature from its optimum. This is to some extent automatically achieved if the correct type of laser is chosen for applications where the laser and the modulator experience the same temperature.

4.3.5 Self-linearised operation.

In the previous sections fixed voltage operation has been considered when in fact it is indicated by Fig.4.3.2 that varying the biasing voltage may improve the achieved performance. Although clearly that would add an extra complication to the electronic circuitry, it is nevertheless a feasible option. We will consider this below.

Experimentally obtained values for the optimum wavelength and voltage of operation are shown in Fig.4.3.11. These were independent measurements obtained parallel to the reflection spectra in section 4.3.2 so that any errors in temperature monitoring do not inhibit conclusions being drawn from combined observations. The optimum wavelength shifts by an average 0.1nm/°C. This value is larger than the (also experimental) 0.07nm/°C required at a fixed 9V operation due to the QCSE related refractive index changes, i.e. the fact that the position of the resonance is slightly modified at different voltages. Under the operational conditions shown in Fig. 4.3.11, the contrast exhibited is well in excess of 15dB at all temperatures. Yet one ought to keep in mind that sole wavelength tracking attains contrasts >13dB for the same range.

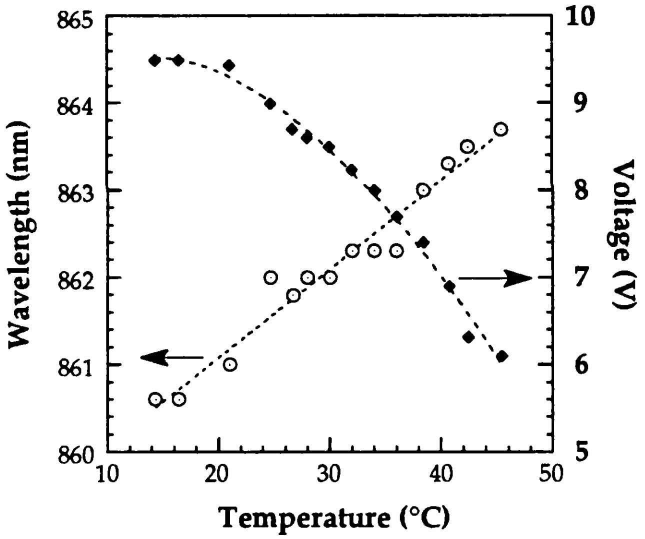

Fig.4.3.11 *Experimentally obtained operating conditions under which maximum contrast is achieved. Both wavelength and voltage are optimised.*

Self-linearised operation has been proposed by Miller, D A B, *et al.* [1985b] for a non-resonant device but it can be applied to any absorption-based device. Indeed, self-linearised AFPM operation has been demonstrated by Grindle and Midwinter [1991]. In any case it involves biasing the modulator by a current rather than a voltage source so that effectively the voltage applied is such that a certain optical power is absorbed regardless of operational variations such as temperature etc. This corresponds to absorption-controlled negative feedback, consequent optimum biasing, and thus to self-linearised operation. The implication on the systems side is that a simple gate is no longer sufficient; circuitry involving transistors in a simple form or in an op-amp arrangement is required in order to realise the constant current source.

Depending on the application, this may or may not be justifiable. Should the laser wavelength be fixed, e.g. because the laser is temperature stabilised or external, and not subjected therefore to the same temperature changes, self-linearising the modulator would be more justified an option. Note also that if the operational temperature range needs to be extended markedly beyond the range investigated here, some means of temperature compensation may be demanded.

The most significant drawback of self-linearised operation is that it is optical power sensitive, i.e. the required biasing current is determined by the absorbed optical power which is directly proportional to the power incident upon the device. Variations in the latter would cause the performance to degrade and could result in lower tolerances after all. One way to attain self-linearised operation is to provide the biasing current from a voltage source connected in series with a photodiode (PD) [Miller DAB *et al.*, 1985b]. The current output of that arrangement is controlled by the optical power on the PD. Therefore, if a fraction of the light input were incident on the PD, and provided the components were carefully chosen, the current biasing the modulator would always be the appropriate for self-linearised operation irrespective of the input powers. A more detailed evaluation shows that this is a complex solution.

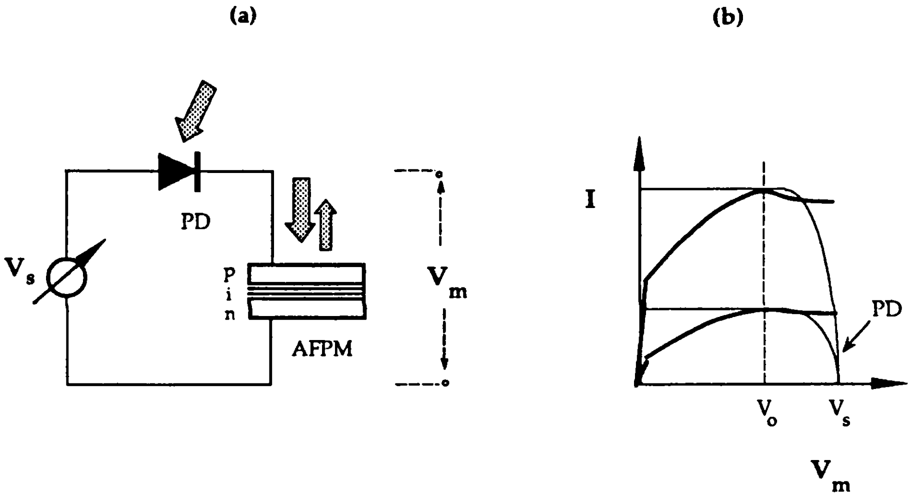

Fig.4.3.12 *Self-linearised operation may be attained a photo-diode (PD) arrangement (a). Optimum biasing (V_0) of the modulator is then achieved, (b), irrespective of the input power.*

The current-voltage characteristics in Fig.4.3.12 serve to clarify the situation. The current through the two devices obviously has to be identical implying that the responsivity (i.e. absorption times quantum efficiency) has to be identical for both. As a result, the PD will be required to be 99% efficient as a detector so that it will not consume more than 50% of the input optical power. Note that the AFPM is ≈99% efficient at its off-state (Chapter 2) under optimum biasing conditions. The consequence of the above argument is that the PD would either have to be a resonant device itself, or it would have to consist of a thick absorbing medium and also be anti-reflection coated. The former option would require care to ensure that the combined temperature and wavelength tolerances of the PD do not impose any constraints on the biasing current. The second option implies that the PD could not be made from the same wafer as the modulator and would thus preferably be part of the electronics (see Chapter 9). Needless to say, either of these arrangements is optical power inefficient, it would complicate the addressing optics and also the device processing. As an additional unwanted consequence, the voltage required for that circuit would be increased as caused by the voltage-drop across the photodiode. Nevertheless, self-linearised operation is an option to be taken under consideration which, as we said earlier, may or may not be implemented depending on the specific system.

4.4 DISCUSSION AND SUMMARY

Prior to summarising and drawing conclusions, it is necessary to compare the temperature sensitivity of the AFPM to that of non-resonant as well as electrorefraction-based resonant devices.

Temperature sensitivity of other types of MQW modulators

Let us start from the **resonant** devices. Although no conclusive study of the temperature sensitivity of the symmetric Fabry-Perot modulator (SFPM) exists in the literature, it is expected that it has inferior tolerances to those of the AFPM. The SFPM operation relies on the refractive index induced shifts of the FP resonance with voltage [Simes *et al.*, 1988] at a wavelength where the absorption has a negligible effect (away from the sub-band edge). For these structures the reflection-change is the parameter of interest since the general contrast tolerances are very low. A change in temperature alters the FP wavelength similarly to the corresponding shift for the AFPM. The voltage-induced modulation at the new resonant position is modified as stemming from the strong dependence of the electrorefractive effects upon the relative wavelength separation from the exciton. As a result, severe reductions of the obtained reflection-change occur when the temperature changes, both with fixed and with varying operating wavelength. These are partly consequences of the extremely narrow FP resonance of SFPM that result from the high cavity finesse. Additionally, an increase of temperature will result in more absorption at the resonance since the exciton shifts in that direction. This would not only increase R_{off}, but it would also cause the device to cease to operate in transmission mode for temperatures higher than a critical value.

Non-resonant absorption-based devices, in transmission reflection or waveguide form, are obviously governed solely by the effects on absorption. The effect of temperature is straightforward in this case where the spectra shift following the decrease of the energy bandgap, thus by 0.27nm/°C. This, in conjuction with a narrow optical bandwidth determined by the exciton linewidth (≈5.5nm), leads to considerably lower fixed wavelength operation tolerances as compared to those of the AFPM. However, tracking the optimum wavelength yields stable reflection (transmission) operation over a temperature range significantly broader than that allowed by the AFPM. This stability of performance is only ultimately challenged by thermal broadening where very large temperature ranges are involved.

Conclusions

In this Chapter we have studied experimentally the effect of small temperature changes upon the operation of the AFPM. The temperature range over which contrast in excess of 10dB is obtained at fixed voltage fixed wavelength operation is over 30°C albeit with a severe effect on the insertion loss of the device. Wavelength tracking the resonance at a fixed bias increases the obtained contrast to over 13dB within the 30°C range attaining thus an extension of the operational range. This can be realised to some extent if a DFB or a surface emitting laser diode is used as the light source. Finally, within the same temperature range, contrast in excess of 15dB can be accomplished if both wavelength tracking of the resonance and self-linearised operation are implemented.

The negative effect of temperature on contrast is notably more pronounced to the low temperature side where the increased exciton-resonance separation gives rise to poor contrasts under any operational conditions (bias, wavelength). Therefore, an efficient design ought to account for that and extend the operational range to that direction by incorporating excess amount of absorber. This was the case for the device studied (albeit in order to ensure high contrasts in this first attempt of an integrated AFPM). This 'extra' amount of absorbing material gives rise to an unwanted enhancement of the effect on the insertion loss that increases with rising temperature. As a consequence, the reflection-changes have been shown to be significantly affected by temperature and more so when operating off the initial (at 25°C) resonance. Thus if reflection-change is the parameter of interest it is preferable to incorporate less absorbing material in the cavity in order to minimise this effect. As we will discuss in Chapter 7, the reflection-change is actually optimised (at a certain operating voltage) when a fraction of the critical amount of absorber is incorporated.

An obvious way to tackle the temperature sensitivity of the device is to implement a stabilisation of the temperature. This may be achieved in an integrated form using Peltier coolers comprised by the substrate [Berger *et al.*, 1991a]. Whereas, however, such temperature controllers are needed when using laser diodes, they would best be avoided in the case of modulators where their use partly defeats the object of using a modulator (see Chapter 1).

The conclusions of this investigation are not only relevant to the temperature dependence of the performance but also help to point out the factors that affect the overall tolerances. The FP resonance has been shown in fact to assist in maintaining the contrast at high values; 'on-resonance' operation, i.e. at the position of the resonant wavelength, has been seen to result in markedly better tolerances to temperature variations, while also small changes of the voltage or the wavelength around that position have less of an effect upon the performance. Therefore, high contrast AFPM designs are not only preferable for the achievable contrast, but also because the tolerances are maximised in that mode of operation. A measure of the tolerances of the device is the width of the resonance. It has thus been indicated that a broader, in wavelength terms, resonance would improve the tolerances in addition to increasing the optical bandwidth *per se*. Finally, it has been made clear that the AFPM is far more tolerant as a high contrast rather than as a large reflection change device. The gained insights are extended and employed in the study of the overall tolerances in the following Chapter.

CHAPTER 5: TOLERANCES OF THE ASYMMETRIC FABRY-PEROT MODULATOR

5.1 INTRODUCTION

One of the decisive merits demanded from a practical device is that its operation is not critically sensitive to growth inaccuracies, operational conditions and environmental factors (i.e. ambient temperature). In the case of the Fabry-Perot modulator the optical thickness of the resonator is one of the critical parameters to control during device fabrication. This involves achieving accurate layer thicknesses and compositions. Similarly, one of the effects of temperature on the fabricated device is a change in the optical thickness of the resonator. There are many other factors to be included when evaluating device tolerances: voltage sensitivity, wavelength sensitivity, angle of incidence. Many effects are interrelated and need to be considered in conjunction with one other.

In this Chapter a detailed calculation of the combined tolerances is performed. Yan *et al.* [1991] have also attempted an evaluation of the tolerances but their study is not comprehensive. We start by considering the required growth calibration and the effect of lateral non-uniformities across the wafer and compare the relative merits of various growth techniques in that respect. We identify a parameter of merit and that facilitates an optimisation of the design with respect to tolerances. The validity of the analysis and optimisation process are demonstrated experimentally. The whole analysis refers to structures with various front mirrors since this is required for an optimisation of the modulator performance, as we will see in the next two Chapters.

Another issue addressed is the optical angle of incidence employed. Work on AFPMs has so far been restricted to normal incidence although clearly oblique incidence offers certain advantages in practical implementations. We examine theoretically the effect this may have on the performance of the modulator as well as the respective tolerance. A brief account of the alignment requirements and the optical addressing of arrays of modulators is also presented.

5.2 TOLERANCES TO GROWTH INACCURACIES

5.2.1 Growth calibration.

The successful operation of Fabry-Perot (FP) multiple quantum well devices relies upon the correct alignment of the heavy-hole exciton peak and the FP resonance. This imposes stringent requirements upon both the growth calibration, i.e. the control of the thickness and the Al concentration of the grown layers,and on the uniformity of these across the epitaxial wafer. We will refer to the calibration of the growth process in this section.

To obtain the exciton peak at the designed wavelength implies accurate control of the quantum well thickness and the Al concentration in the barriers, since these are the factors that determine the subband energies (Chapter 3). Extensive work on non-resonant quantum well structures in recent years, has lead to a well established control of the growth of quantum well layers yielding accurate well thicknesses, sharp interfaces between the well and barrier materials, and excellent depth uniformity. Hence clearly resolved excitonic features are routinely obtained at the prerequired wavelength. The optical quality of the quantum well layers is commonly assessed by Photoluminescence (PL) studies, Photoluminescence Excitation (PLE), x-ray diffraction microscopy, and Transmission Electron Microscopy (TEM). Such studies have shown that the thickness of quantum wells grown by the most common MOCVD and MBE is typically controlled to within a monolayer throughout the MQW region, while the Al concentration in the barriers is controlled to about 1%. As a result, the exciton position is controlled to within 1nm for a typical 100Å well. This remarkable precision is achieved by the employment of low growth rates (1 monolayer/sec) during the growth of that region. Alternative growth techniques, that have evolved in recent years, may have certain advantages but on the whole they seem to attain similar accuracies. We will discuss the relative merits of different epitaxial growth processes in a separate section in this chapter (section 5.2.3).

Whereas non-resonant devices can therefore be grown with an excellent precision, in the case of resonant structures the requirements on growth are not restricted to the MQW region but are extended to the entire vertical thickness of the device. Specifically, the optical length of the FP cavity has to be 'correct' (Chapter 2) for destructive interference to occur at the designed wavelength, and also the centre wavelength of the Bragg reflector stacks (top and bottom) needs to be placed at the same wavelength. Note that although the high reflectivity band of such stacks is sufficiently broad (Chapter 2), the phase of the reflected wave varies greatly within that range (Fig.5.2.1). This means that the resonant wavelength is not determined solely by the optical length of the cavity. The cavity length implies a resonant wavelength given by

$$\lambda_o = \frac{2 \cdot \sum_i L_i n_i}{m} \qquad 5.2.1$$

where L_i and n_i are the physical length and the refractive index (respectively) of layer i within the cavity length, the factor 2 refers to the mirror design in Fig.5.2.2, and m is the order of the FP cavity (Chapter 2). However, since the multiply reflected beams have to be in antiphase with the directly reflected one, the following have to be fulfilled

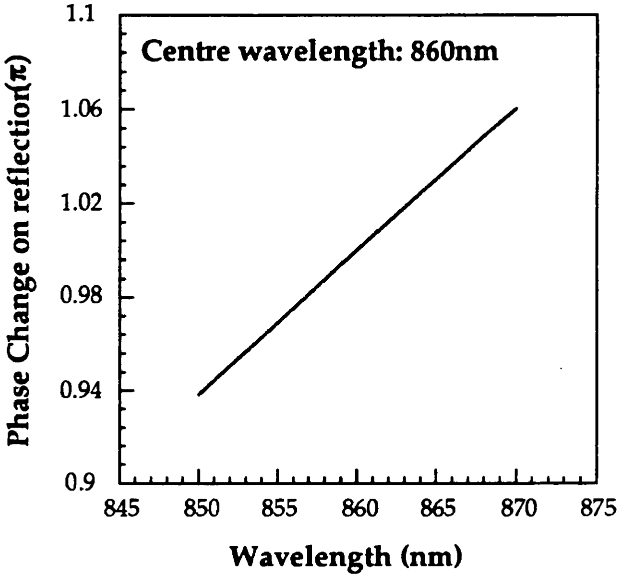

Fig.5.2.1 *The phase-change upon reflection from a Bragg stack is wavelength dependent. Here we plot the phase-change imposed by a stack starting with a high-index layer (Chapter 2) [Macleod].*

$$\begin{aligned} 2\phi_l + 2\phi_c + \phi_{R1} &= j\pi \\ 2\phi_l + 4\phi_c + \phi_{R1} + \phi_{R2} &= k\pi \end{aligned} \qquad 5.2.2$$

where j and k are even integers and the respective phases are marked in Fig.5.2.2. These expressions are obtained when the above mentioned antiphase condition is applied upon the beams that experience one and two reflections within the cavity before reappearing at the front to contribute to the interference. If the wavelength λ_o from eqn.5.2.1 coincides with the centre of the stack, eqns.5.2.2 are fullfilled at λ_o and that is the resonant position.

When growing the structures by MOCVD, small errors in growth are self-compensated as follows. The physical thickness L of a grown AlGaAs layer is controlled by the Al flow assuming a certain Al content within the epitaxial material. A slight error in the estimated percentage of Al between the group-III elements will eg. overestimate (underestimate) the grown thickness. However, the refractive index n of the layer will simultaneously be underestimated (overestimated), since the refractive index of $Al_xGa_{1-x}As$ decreases with x. Consequently, as it is the product Ln that determines the optical length L_{opt}, the total effect on L_{opt} will be, if not compensated, at least diminished.

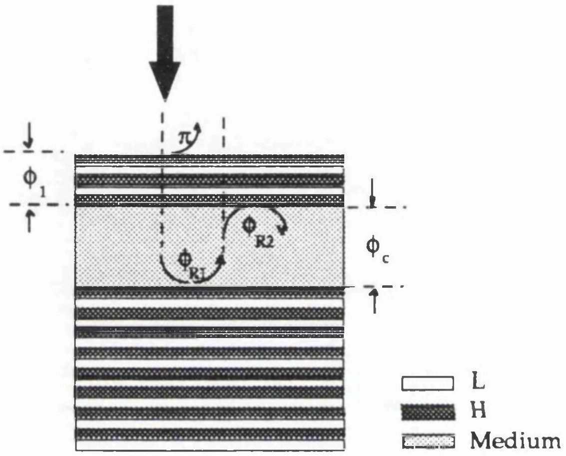

Fig.5.2.2 *The phases introduced by different parts of an integrated cavity.*

When using MBE growth, the thicknesses are much more accurately controlled (section 5.2.3). The fluxes of the group-III elements are set independently and the relation between these determines the Al content of the grown layer, while the thickness is directly determined by the respective growth duration. Although a small error in the Al flux is self-compensated as above, the manifestation of an error in the Ga flux is by contrast enhanced for the same reason. Consequently, the self-compensating action does not take place in this case.

Nevertheless, the reliable way to minimise growth inaccuracies is in-situ monitoring. Some sort of in-situ diagnostics are used in MBE growth but they are not specifically suited to resonant optical devices. A sensitive method to measure optical lengths is by means of monitoring the interference experienced by monochromatic light of the appropriate wavelength (i.e. the resonant wavelength when dealing with FP structures). This technique has been employed in the deposition of dielectric optical filters and results in a very fine control. The difficulty introduced in the case of semiconductor epitaxial growth is that this takes place in considerably high temperatures (600°C) and as a result the refractive indices of the materials differ greatly from their room temperature values (Chapter 4). Therefore, the wavelength of the light used for monitoring has to be adapted accordingly, which prerequires a sufficient knowledge of the dependence of the refractive indices on temperature. However, experimental calibration of the monitoring procedure ought to eliminate any ambiguities.

Summarising this section, a precise control of the growth process is mandatory for reproducible fabrication of successful FP devices. Although the current laboratory-grown samples have not achieved the required level of accuracy, there is no major practical limitation prohibiting such an accomplishment. In fact, the main consideration as far as growth is concerned is the lateral uniformity of the structures across the epitaxial wafer. This is discussed in the next section.

5.2.2. Lateral uniformity.

The thicknesses L of epitaxially grown layers are not uniform across a wafer. Instead, these vary laterally by an amount ΔL proportional to L; hence, the appropriate way to characterise lateral non-uniformity is to quote the ratio $\Delta L/L$. The absolute value of $\Delta L/L$ as well as the distribution of these thickness variations upon the wafer are determined by factors associated primarily with the very nature of the epitaxial method, the geometry of the growth process and, in the case of gas flow based techniques, on the growth rates.

The growth rates employed during the epitaxy of quantum wells by both MBE and MOCVD, are typically 1 monolayer per second (roughly $\approx 1\mu m/hr$), while the barriers are grown at an average 1.4 monolayers/sec. In the case of the commonly used 2" wafers, the lateral non-uniformity of the well layers is about 3%, which corresponds to a thickness variation of about one monolayer in the case of 100Å wells. Similar to our discussion in the previous section, the consequent shifts of the exciton energy levels, yield a mere 1nm change of the exciton position across the entire 2" wafer (excluding the edges). As a result, an excellent lateral uniformity is obtained in the case of non-resonant devices.

When using MBE growth, the employed growth rates do not affect the lateral uniformity which is predominately determined by the geometry of the growth machine. The rates are roughly stable throughout the epitaxial process. In the case of MOCVD on the other hand, the growth rates do affect the uniformity pattern. The rates employed during the bulk of the epitaxial process are typically three to four times higher than these employed during the quantum well growth. These cannot currently be reduced in a major way not only due to the corresponding prohibiting growth length, but also because long-run drifts of the process would give rise to a diminished control. Consequently, the lateral uniformity of the total grown thickness is inferior to that of the quantum well layers.

Typical values of non-uniformity referring to the total structure have been 3-5%, as quoted for both MBE and MOCVD. Thus similar to our discussion in the previous section, whereas non-uniformity of the well thickness does not give rise to a considerable variation of the electroabsorptive effects, the Fabry-Perot effect is critically dependent upon the optical length of the cavity. When resonant devices are dealt with, the implied changes of the layer-thicknesses within the cavity as well as of those comprising the reflector stacks, is manifested in a shift of the FP resonance when observing the spectra at different lateral positions (eqn.5.2.1). Hence, whereas non-resonant devices are virtually uniform, the performance of resonant devices may vary considerably in the lateral direction. Since the exciton position is effectively fixed, the relative separation between the exciton and the resonance is not constant across an epitaxial wafer, and as a result only a part of the wafer may, potentially, yield successfully operating devices. The consequence of this is not only a limited yield, that would imply mainly cost inefficiency; more importantly, it imposes restrictions upon the maximum size of integrated two dimensional arrays of devices. It is primarily this latter consideration that makes lateral non-uniformity a very crucial issue. However, it is important to note that most of the work that has been carried out in low-dimensional structures has been concerned with non-resonant devices, where the total device thickness is of no significance. Clearly thus, lateral uniformity extended to the total device thickness -typically ≈3μm for a resonant device- is a new challenge for epitaxial growth processes. The introduction of resonant devices has fuelled considerable effort towards an improvement in this direction. In the following, we will present the current state-of-the-art for MOCVD grown structures that have been used in this work, and discuss the target uniformity levels.

Current state-of-the-art

In our analysis below we will make the assumption that the growth process is perfectly calibrated and hence the specified structure is obtained at the centre of the wafer. Also the exhibited non-uniformity ($\Delta L/L$) of individual layers is assumed independent of the Al content of the material these consist of, as is indicated in practice. These assumptions do not limit our evaluating the problem in the general case, but are rather employed in order to simplify the analysis. A change of the layer thicknesses comprising the resonant structure (i.e. in both the cavity and the reflector stacks) implies an error in the position of the resonance λ_0 according to eqn.5.2.1. Hence, the resonant position is altered by an amount $\Delta\lambda$ according to the expression

$$\frac{\Delta\lambda}{\lambda}=\frac{\Delta L}{L} \qquad 5.2.3$$

Note that the shift of the centre wavelength of the Bragg reflector is also given by eqn.5.2.3. Hence, non-uniformity of 3-5% gives rise to a lateral variation of the FP resonance by 26 to 43nm (at 860nm). It is clear that these values need to be improved considering that the wavelength range over which 10dB contrast is achieved is ≈5nm for a low finesse AFPM. Typical attained uniformities are presented in the following.

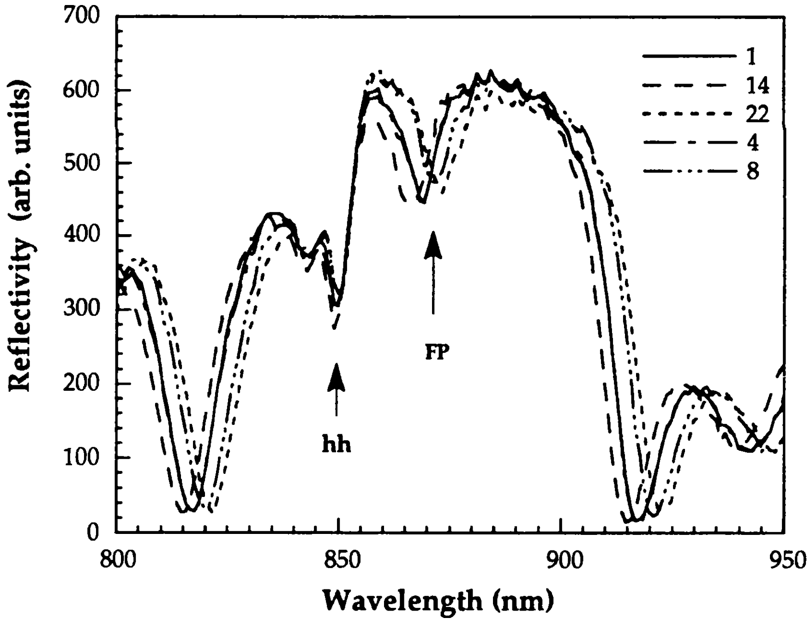

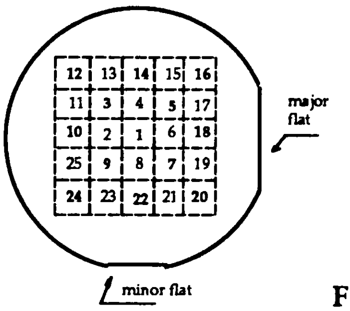

Fig.5.2.3a *Uniformity across the wafer (QT238B).*

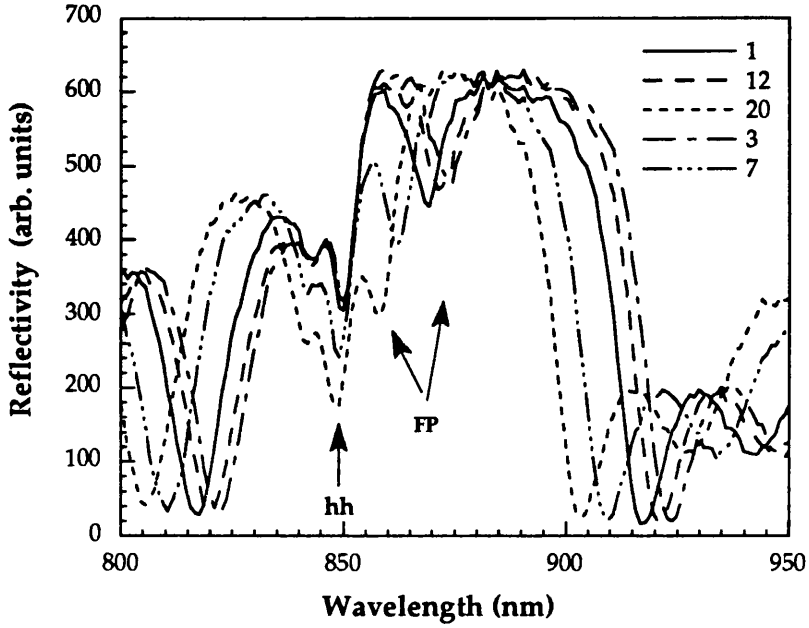

Fig.5.2.3b *Uniformity across the wafer QT238B, grown by MOCVD at the University of Sheffield. The respective positions are shown in Fig.5.2.3a.*

Scans from different parts of an AFPM wafer (QT238B) of typical uniformity are shown in Fig.5.2.3, the respective positions being depicted in the inset. Within the region shown, the resonance varies by 7.5nm in the direction parallel to the gas flow, i.e the uniformity is ≈0.87%, and by 16nm in the perpendicular direction (uniformity ≈1.9%). The position of the exciton is, within experimental error, unchanged in the same area. A full mapping of the resonant position extended over the total area (excluding the edges) of the same epitaxial wafer is shown in Fig.5.2.4. The uniform regions form a stripe-like geometry parallel to the direction of gas-flow, which is characteristic of MOCVD. The uniformity across the illustrated 55% of the wafer may be calculated by means of the information in Fig.5.2.4 using eqn.5.2.3 as

$$\frac{\Delta L}{L} = 1.9\%$$

The layer thicknesses drop rapidly towards the edges so that the total uniformity is about 3%. The exciton position was found to vary by a total of 2nm.

Since neither the Fabry-Perot nor the electroabsorption effects are linear with wavelength, it is rather tedious to attempt to quantify accurately, let alone in the general case, the implications of lateral non-uniformity on the performance of the resultant modulators. Instead, let us assume the modulator performance of CB145-

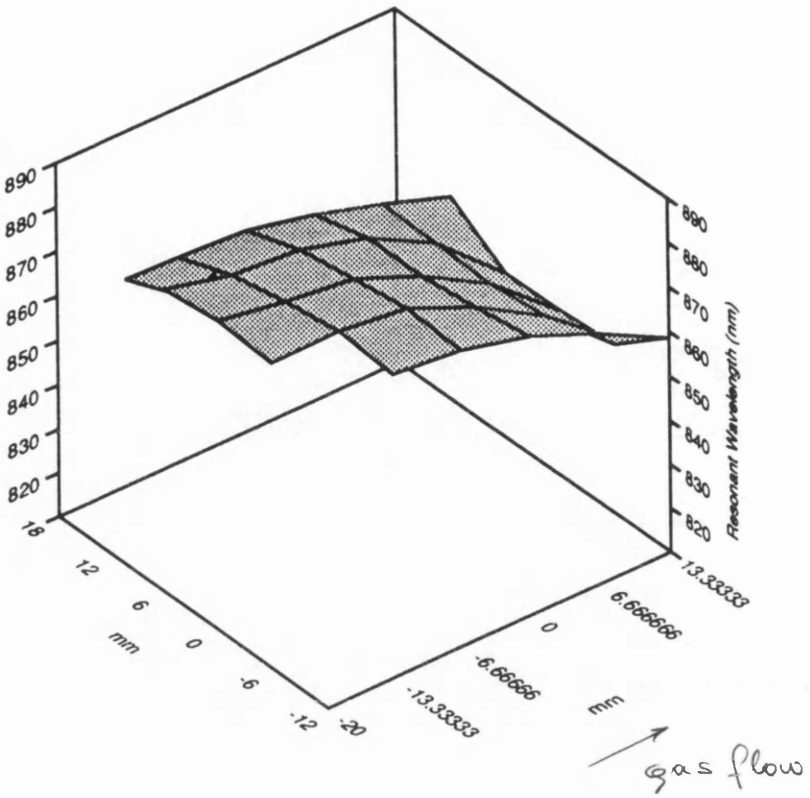

Fig.5.2.4 *The FP resonant wavelength as a function of lateral position across the wafer QT238B. This was grown by MOCVD at the University of Sheffield.*

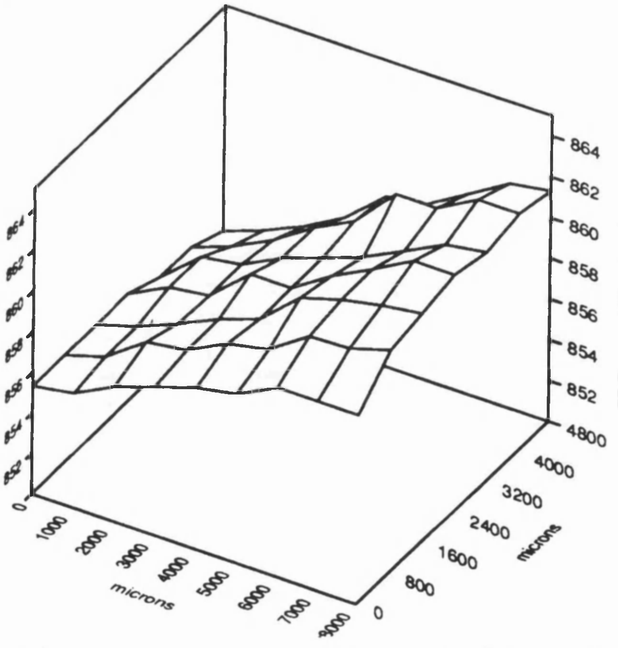

Fig.5.2.5 *The FP resonant position across a 0.4cm^2 sample from wafer QT238B. The sample was obtained from about 1" off the centre of the wafer (along the diagonal between areas labelled 5 and 16 in Fig.5.2.3).*

AFPM (Chapter 2) and extend this discussion when studying the overall tolerances in section 5.3. Let us also define 10dB as the minimum required contrast. That condition is fulfilled over a range of 5.5nm for that device. Considering uniformity alone, i.e. independently from any tolerances to temperature, operating wavelength and voltage, etc., we may roughly estimate the implied minimum uniformity to be

$$\frac{\Delta L}{L} = \frac{\Delta\lambda}{\lambda} = \frac{5.5}{860} = 0.64\%$$

This appears rather beyond the present growth capabilities.

It is worth assessing the implications of the current state-of-the-art on the maximum size of an array of devices. Fig.5.2.6 shows a mapping of the FP resonance at a decreased scale, scans taken every 800-1000μm on a ≈0.4cm^2 sample. As has been indicated in Fig.5.2.4, the uniformity is diminished at wafer positions further away from the centre. The mapped sample is taken from the vicinity of areas labelled 5,15,16,17 (Fig.5.2.3) which implies a rather moderate uniformity. Even so, the total variation of the resonance is 0.68% so that a sample of such dimensions may be assumed as acquiring the required uniformity level.

We may now evaluate the maximum number of devices that may be fabricated on a sample of such dimensions according to the current state-of-the-art. Presently, the smallest optically and electrically addressible modulator (S-SEED) devices have been reported by workers at AT&T labs [Chirovsky *et al.*, 1991]. Based upon the dimensions of these, we may assume 5μmX5μm optical window devices with 10μmX10μm mesas. Requirements on optical alignment and focusing make it difficult to predict a major reduction of these (section 5.4). Further, taking into account an interdevice spacing of 100μm, the average area per device is calculated to be ≈14,400μm^2 which yields a total number of just below 86X86 devices on a 'uniform' sample. This array size is well sufficient for optical interconnect applications but may be of restricted capacity with regard to data processing applications (see Chapters 1,2).

The lateral non-uniformity of Fabry-Perot based multiple quantum well devices has caused a lot of scepticism regarding the actual applicability of such devices. In this section we have presented the issue and the current state-of-the-art. We revisit the subject in conjunction with the sensitivity to other parameters in section 5.3 where we study the overall tolerances of the modulators. In the next section we discuss the relative merits of the available growth techniques and we attempt to predict the degree of improvement in this direction.

5.2.3. Relative Merits of Growth Processes regarding Lateral Uniformity.

The epitaxial techniques that acquire the finesse needed for quantum well structures are molecular beam epitaxy (MBE) and metal-organic chemical vapour deposition (MOCVD). A brief account of these is given in the following.

Molecular Beam Epitaxy

This technique takes place in ultra high vacuum (10^{-10}- 10^{-11} Torr) conditions. Beams of atoms are produced from (solid) elemental sources that are contained in independent cells. That way the fluxes can be controlled separately for each element as determined by the respective cell temperature. The atoms are incident radially on a heated (typically 600°C) substrate where the growth takes place at a rate determined by the group III elements (i.e. Ga, Al in our case). Commonly the substrate is rotated typically at one revolution per second in order to improve the attained uniformity. This yields a reproducible wafer cross-section of a certain uniformity pattern which is primarily determined by the specific geometry of the growth kit. Such a pattern is shown in Fig.5.2.7. This may be further modified depending upon the temperature uniformity of the substrate in the lateral direction. The centre 50% area of a 2" wafer

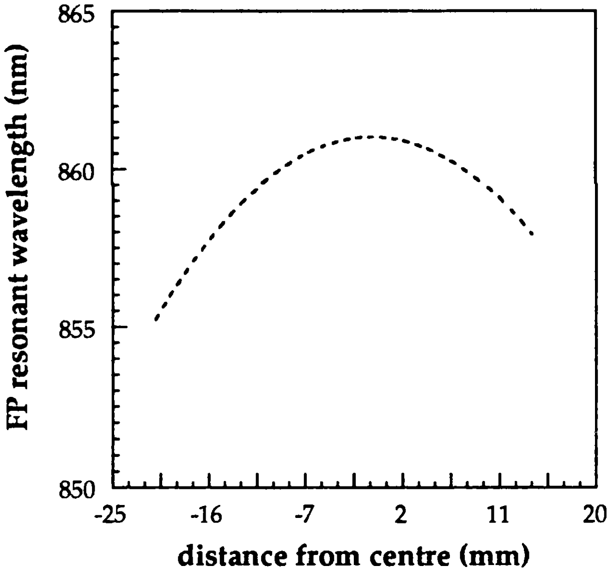

Fig.5.2.7 *Typical latteral uniformity attained by MBE. The data is taken from a GaAs on Si wafer (data obtained by P.Barnes, wafer grown by K.Woodbridge).*

may be uniform to 2%, while the thickness drops off rapidly towards the edges.

MBE is a high resolution technique allowing a remarkably fine control of the grown layers such as barrier Al compositions as low as 2% controlled to less than 1%, or well-controlled 40% Al in the well material yielding thus operation in the visible [Goossen *et al.*, 1990; 1991]. Additionally, the ultra high vacuum conditions allow for in-situ monitoring such as Reflection High Energy Electron Diffraction (RHEED), that may be used to determine the growth rates, and mass spectrometry. However, MBE is inherently not best suited to large throughput of broad areas of uniform material. Indeed, the throughput is limited firstly by the required reloading each time the solid sources are exhausted, while also large areas or multiple substrates may only be grown at the expense of uniformity. Although the latter trade-off exists for any growth technique, MBE is inherently especially susceptible to it.

The uniformities so far attained have, nevertheless, by no means exhausted the potential for improvement in that direction. Better uniformities may be attained by using larger cell areas and by an increase of the distance between the cells and the substrate. The latter option would, however, require higher cell temperatures in order to maintain the growth rates within reasonable levels and would therefore result in larger contamination levels. However, it appears that there is a limit to the degree of improvement in lateral uniformity that may be achieved by MBE. On the whole, it is difficult to forsee MBE growth attaining uniformities below 1% on an area of the order of 2" (K. Woodbridge, private communications).

Metal-Organic Chemical Vapour Deposition

Here the material sources are in the gas phase. These are mixed prior to entering the chamber where the growth takes place with the gas mixture flowing in a direction parallel to the plane of the substrate. The growth is of a chemical nature since the group III metal-organic compounds dissociate thermally on the heated substrate in the presence of the group V hydride. This is not carried out under vacuum, in fact the structures reported in this work have been grown in atmospheric pressure.

MOCVD is a lower resolution, faster growth technique when compared to MBE. For example, low Al concentrations cannot be finely controlled to any level comparable to those achieved by MBE. The attained accuracies, however, are sufficient to meet the requirements of quantum well structures such as these reported here. Another disadvantage of MOCVD is the strict safety measures required.

However, MOCVD has fast source replacement and large wafer throughput as big advantages to offer, making it a popular technique for commercial use. It is inherently a scalable process allowing for growth on several substrates simultaneously, which may be further expanded by the use of a vertical reactor with the substrates arranged in a cylindrical manner. The lateral uniformity obtained by MOCVD is a function of the temperature uniformity of the substrate and the distribution of the gas flow over the substrate surface. This makes the uniformity pattern less predictable compared to MBE but it also manifests a certain flexibility inherent to MOCVD growth. There is arguably the potential for an improvement of the attained uniformities. The use of larger reactors (while keeping the substrate diameter fixed) can smooth the flow profile and consequently result in better uniformity. This would also cause a considerable waste of material but it might be a justifiable penalty to pay. Still, as far as may be judged by present information, MOCVD growth requires in-situ monitoring in order to attain the growth precision needed for resonant structures. On the other hand, as far as lateral uniformity is concerned, it appears that there may be the potential to achieve the levels discussed in the previous section.

Alternative epitaxial growth processes that are essentially variations of MBE and MOCVD have emerged in recent years. The three techniques mentioned in the following use an MBE chamber, hence the growth takes place under high vacuum. *Atomic Layer Epitaxy* (ALE) is essentially MBE growth with the group III elements (Ga, Al) grown subsequently rather than simultaneously by means of fast shutters that interrupt the flux of one of these elements when the other is taking part in the growth [Pessa *et al.*, 1984]. This has certain advantages concerning the attained interface sharpness, virtually layer to layer control of the epitaxial process, and the possibility for reduced temperature growth. It has also been claimed to help prevent the formation of antiphase domains in the case of growth on a substrate material with large thermal and atomic spacing mismatches to these of the superstrate material (eg. GaAs on Si). However, the lateral uniformity is expected to be identical to that of MBE grown structures. *Metal-Organic Molecular Beam Epitaxy* (MOMBE) uses gas sources for the group-III elements [Panish *et al.*, 1984], while in *Chemical Beam Epitaxy* (CBE) all sources are gas sources [Tsang *et al.*, 1984]. The latter method is regarded best suited to selective area epitaxy with the consequent advantages concerning the monolithic integration of complex structures [Goodfellow, 1991]. These techniques have not as yet reached a mature stage and have had difficulties in achieving the material quality reported by MBE and MOCVD. The use of high vacuum makes them potentially superior to MOCVD while the use of gas sources increases the throughput attained especially by CBE as compared to that of MBE since reloading is not required. As to whether these techniques will prove to combine the precision and reproducibility of MBE with the versatility and potential for large area uniform growth of MOCVD, is hard to tell at this stage.

5.2.4 Post-growth compensation for lateral non-uniformity.

A post-growth correction of the cavity length can be performed by etching off a sufficient amount of the superstrate in order to adjust the position of the resonance to the desired wavelength. The wafer under correction would have to be patterned and different etch depths used at each area; the unit area dimensions would be defined by the local uniformity in conjunction with the required uniformity and the accuracy of the etch process. For instance, the central 55% of the wafer in Fig.5.2.3 would need to be divided in an estimated number of twenty individual areas in order to attain an overall non-uniformity $\leq 0.7\%$. Both wet-etching and reactive ion etching (RIE) seem to be equally suited to the etching process as far as the surface smoothness is concerned; ultimately however, the reduction of the device features to the order of microns will require a high resolution technique and therefore RIE will be favoured. In order to attain a high degree of accuracy during such a process, one may employ optical monitoring of Fabry-Perot interference fringes in a manner identical to that proposed in section 5.2.1 for an in-situ control of the epitaxial growth. The commercially available RIE machines could accommodate such monitoring and subsequent automatic control of the etching process.

The situation becomes less easy when we consider the requirement for a decrease of the operating voltage to less than 5V (Chapter 2). This is accomplished, as we will see in the next chapter, by an increase of the front mirror reflectivity which in turn implies the incorporation of a front reflector stack. In that case, there is obviously no access to the cavity length, and as a result a correction of the optical length by post-growth etching is not applicable. If post-growth tailoring of the FP resonances is indeed necessary, then it would be obligatory to use a dielectric front reflector stack (eg. SiO_2/TiO_2, Chapter 2) so that the etching step could take place prior to the deposition of the stack. From another point of view , it may be that the use of a front reflector stack would be in fact required were post-growth correction to be employed. The front reflectivity is expected to be slightly affected after such a step [Ünlü *et al.*, 1990], and a front reflector could compensate for this reduction

The incorporation of dielectric front mirrors could cause the modulator designs to deviate from their optimum. As discussed in Chapter 2, the indices of the materials involved are small while also the corresponding index differences between two materials may be quite large. Whereas this has the desirable result that a small number of periods yields large reflectivities, by the same token the choice of reflectivities obtained by a certain pair of materials is rather limited. This inflexibility is however offset to a great extent by the large range of compatible materials available for both the high and the low index layer. Furthermore, the deposition of these commonly takes place in an e-beam evaporator and therefore, unlike epitaxial growth, many different compounds may be obtained using the same machine. Effectively thus, this should add only a minor complexity. In fact, the use of dielectric mirrors offers certain attractive advantages regarding the potential for single-chip integration of devices performing diverse functions, as is discussed in Chapter 9. Therefore, dielectric front mirrors may ultimately be commonly used in practical implementations.

Bearing in mind that only recently has there been any motivation to address the total device uniformity, it is clear that the corresponding performance of growth processes has not been stretched to anything close to the absolute limits. Nevertheless, we have discussed the possibility of post-growth correction of the cavity length, although clearly it may in the future prove unnecessary.

5.3 COMBINED TOLERANCES

Thus far we have been studying the tolerance of the modulator to deviations of one single parameter from its 'ideal' value. In a practical situation, however, devices in a non-uniform two-dimensional array will be simultaneously subjected to variations in the ambient temperature and possibly of the operating wavelength and voltage. It is the combined tolerances that we will concentrate upon in this section.

5.3.1 High Contrast Modulation.

Let us first consider the case when the parameter of interest is the exhibited contrast ratio (Chapter 2). This is defined by the ratio of the reflectivity of the on-state divided by that of the off-state. As a result, in the cases when high contrasts are involved, this is critically dependent upon the reflectivity of the off-state R_{off}, since for low values of R_{off} large contrast is achieved irrespective of the value of R_{on}. The total reflectivity is given by

$$R = \frac{R_o + F\sin^2\phi}{1 + F\sin^2\phi} \qquad 5.3.1$$

where R_0 is the reflectivity at the resonant position, F is the coefficient of finesse, and ϕ is the phase introduced by the cavity (Chapter 2). We may thus identify two contributions to R: one from the value of R_0, which is determined by the amount of absorber at the resonant position, and one from the value of $F\sin^2\phi$, which dictates the position of the operating wavelength in relation to that of the resonance.

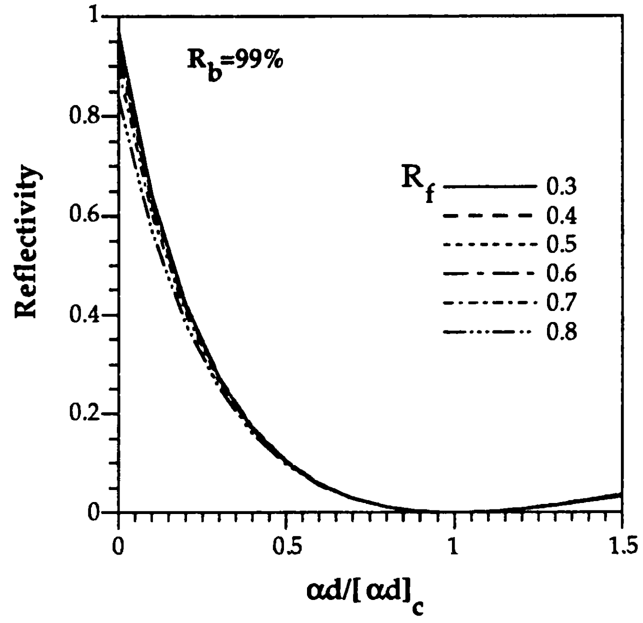

Fig.5.3.1 *The total reflectivity R plotted as a function of the relative amount of absorber for the case of a 99% reflecting back mirror and various front reflectivities R_f.*

The dependence of R_0 on the amount of the absorber αd present at the resonance is shown in Fig.5.3.1 for a cavity with R_b=0.99 and various front reflectivities. Note that we have chosen to use the relative amount of absorber $\alpha d/[\alpha d]_c$ as the horizontal axis (where $[\alpha d]_c$ is the critical amount of absorber, i.e. that required to zero the reflectivity) to allow for a comparison among different front reflectivity structures. The insensitivity of the off-state reflectivity to αd at large contrasts, i.e. for values of $\alpha d \approx [\alpha d]_c$, is evident in this figure. Indeed, for example, $R_0 \leq 0.01$ when $|\Delta(\alpha d)| \leq \pm 25\%[\alpha d]_c$. It is also interesting that this holds irrespective of the front reflectivity R_f in this case where the back mirror reflectivity R_b is quite high. By contrast, one may compare with Fig.5.3.2 where the respective curves are reproduced for R_b=0.95. Here, there is a marked difference among the various curves showing a decreasing sensitivity with increasing R_f. However, this is restricted to the low-αd end of the curve and does not have any effect around the 'off 'state. We discuss the choice of back mirror reflectivity in the next chapter.

Due to this insensitivity to changes in the amount of absorber present in the cavity for values close to the critical $[\alpha d]_c$, the contrast tolerances are maximised in the cases of high contrast modulator designs, i.e. when the off-state $R_0 \approx 0$. We will thus restrict our analysis to such modulators henceforth. Furthermore, due to the complexity involved, the following study of the tolerances will not be kept strictly along the lines of orthodox error propagation analysis. Instead, we will evaluate the combined tolerances via a numerical route that certainly involves approximations but will lead us to the right conclusions, both qualitatively and quantitatively.

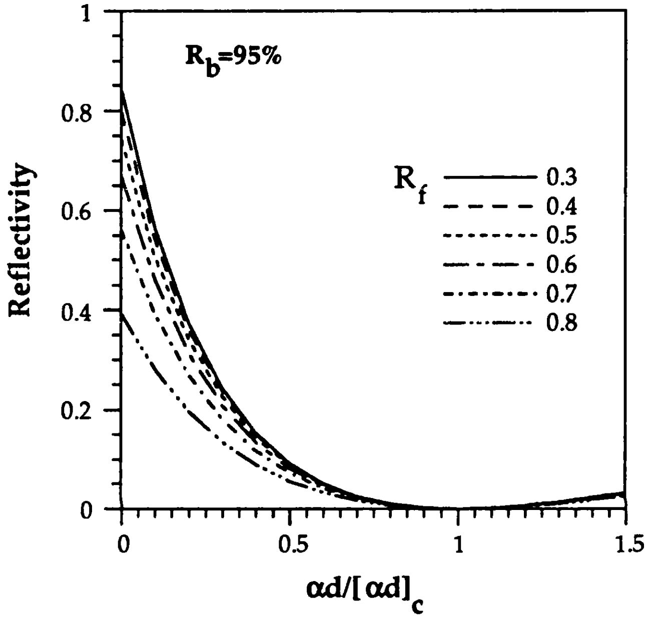

Fig.5.3.2. *The total reflectivity R plotted as a function of the relative amount of absorber for the case of a 95% reflecting back mirror and different front reflectivities R_f.*

Let us define 10dB as the minimum required contrast. That will be achieved if $R_{off} \leq 0.1 R_{on}$, i.e. our requirements dictate

$$\frac{R_0 + F\sin^2\phi}{1 + F\sin^2\phi} \leq 0.1 \cdot R_{on} \qquad 5.3.2$$

If an allowable maximum R_0^{max} is established for the on-resonance reflectivity at the off-state R_0, it follows from eqn.5.3.2 that

$$\sin^2\phi \le \frac{0.1\cdot R_{on} - R_o^{max}}{(1-0.1\cdot R_{on})\cdot F} = B \qquad 5.3.3$$

where B is a constant and F is taken as a constant equal to its value at the resonant position where $R_b^{eff}=R_f$ (Chapter 2). In effect this assumes that the absorption (αd) does not vary dramatically around the resonant position and is close to its critical value. The constraints imposed upon R_o make this a realistic approximation.

Making use of the periodicity of the sin function, eqn.5.3.3 enables us to find an expression for the tolerable phase variation $\Delta\phi$

$$\Delta\phi = 2\cdot\sin^{-1}(\sqrt{B}) \qquad 5.3.4$$

Before proceeding from this point it is important to clarify the significance of variations in the operating parameters with reference to eqn.5.3.3 :-

Operating Voltage: This determines the amount of αd at the resonance and therefore affects R_o. As has been indicated in Figs. 5.3.1 and 5.3.2, the contrast will be relatively insensitive to the operating voltage, bearing in mind that the absorption coefficient at the biased exciton peak drops slowly with field. The above in conjunction with the voltage output stability of electronic gates (within 1%) suffices to justify our regarding voltage variations as non-critical in our analysis.

Operating Wavelength: This alters the phase ϕ solely, since the value of R_o is effectively constant around the resonant position.

Lateral Non-uniformity: The position of the FP resonance is altered directly due to lateral non-uniformity both in real terms (i.e. relative to a fixed wavelength) and in relation to the zero-bias heavy-hole (hh) exciton peak, the position of which is in practice virtually laterally uniform, as has already been discussed. Consequently, both R_o and ϕ in eqn.5.3.3 are affected by lateral non-uniformity. The effect on ϕ is straightforward, as has been presented in section 5.2. The reflectivity R_o at the resonance is changed as a result of the significant change in αd caused by the relative shift of the resonance with respect to the exciton position. This effect is minimised when self-linearised operation is implemented, but becomes quite limiting in the case of fixed voltage operation.

Ambient Temperature Instabilities: As we have discussed in Chapter 4, temperature changes induce a shift of the resonance by ≈0.08nm/°C and of the exciton peaks by ≈0.27nm/°C. The consequent change in the relative exciton-resonance position is ≈0.2nm/°C. This altered resonance-exciton separation clearly affects R_o, similar to above. Additionally, the phase ϕ at a given operating wavelength is also altered stemming from the absolute shift of the resonance.

Cavity-imposed restrictions

Returning to eqn.5.3.4 we may now evaluate the restrictions imposed upon the operating conditions by the cavity design exclusively. The phase ϕ is a function of the resonant position and the operating wavelength. According to our discussion above, the position of the resonance is modified as dictated by both the lateral non-uniformity and the temperature variations. The result of this is an altered ϕ at the operating wavelength. The parameters involved are independent so that the tolerances are given by

$$\left(\frac{\Delta\phi}{\phi}\right)^2 \geq \left(\frac{\Delta\lambda_{NU}}{\lambda}\right)^2 + \left(\frac{\Delta\lambda_n}{\lambda}\right)^2 + \left(\frac{\Delta\lambda_{op}}{\lambda}\right)^2 \qquad 5.3.5$$

where $\Delta\lambda_{NU}$ is the absolute variation of the resonance (eg., across an array) due to non-uniformity, $\Delta\lambda_n$ is the absolute variation of the resonance due to temperature induced changes of the refractive index (Chapter 4), and $\Delta\lambda_{op}$ is the allowable drift of

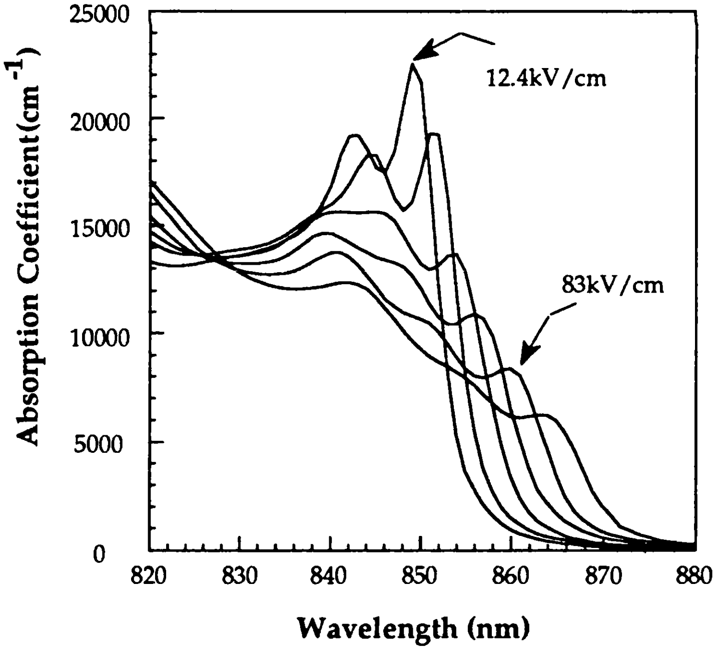

Fig.5.3.3 *Electric field dependent absorption spectra for 95Å wells at about 18kV/cm steps. The 83kV/cm spectrum corresponds roughly to the 9V operation of CB145 (data from CB308).*

the operating wavelength. The phase can be converted to wavelength terms as follows

$$\Delta\phi = \frac{2\pi L n}{\lambda^2}\Delta\lambda_\phi \qquad 5.3.6$$

so that

$$\frac{\Delta\phi}{\phi} = \frac{\Delta\lambda_\phi}{\lambda} \qquad 5.3.7$$

where $\Delta\lambda_\phi$ is the corresponding wavelength range as this will be manifested in the reflectivity curve for a certain fixed R_0, i.e. the wavelength range over which the phase ϕ differs from its value at the resonance by less than $\Delta\phi/2$. Equation 5.3.5 may thus be rewritten as

$$\begin{aligned}\left(\Delta\lambda_\phi\right)^2 \geq \left(\Delta\lambda_{NU}\right)^2 + \left(\Delta\lambda_n\right)^2 + \left(\Delta\lambda_{op}\right)^2 = \\ \left(\Delta\lambda_{NU}\right)^2 + \left(0.08\cdot\Delta T\right)^2 + \left(\Delta\lambda_{op}\right)^2\end{aligned} \qquad 5.3.8$$

Restrictions imposed by the wavelength-dependence of the MQW electroabsorption effects

Simultaneously, the requirements on R_0 impose another set of restrictions upon the

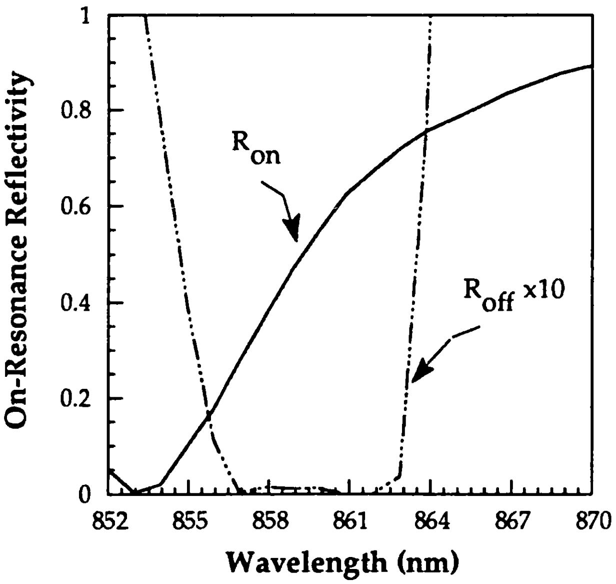

Fig.5.3.4 *The on-resonance reflectivity as a function of the resonant wavelength for both the on- and the off-state. Note that these are not reflectivity spectra. The data have been calculated from the 13kV/cm (on) and 84kV/cm (off) absorption spectra in Fig.5.3.3, for an AFPM cavity design similar to CB145.*

operating parameters. A deviation of the exciton-resonance relative separation from its optimum, causes the on-resonance reflectivity R_0 to increase from zero. This is a consequence of the dependence of R_0 on the absorber αd (Fig.5.3.1) and therefore stems from the wavelength dependence of the MQW electroabsorptive effects.

In order to examine the restrictions imposed by the electroabsorptive effects, let us consider a modulator structure incorporating 95Å wells as is the case for CB145 (Chapter 2). The field dependence of the absorption coefficient of such wells is shown in Fig.5.3.3 as derived from photocurrent data of sample CB308 in the manner

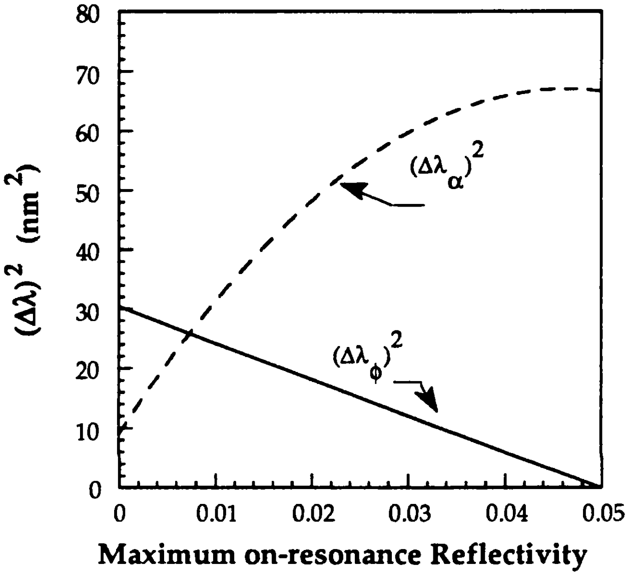

Fig.5.3.5 *The squares of the wavelength ranges determined by the cavity design and the electroabsorptive effects plotted versus as a function of the admissible upper limit for the on-resonance reflectivity. See text for further explanation.*

described in Chapter 3. In order to keep the analogy with our reference modulator CB145, let us assume fixed voltage operation at ≈861nm of a high contrast AFPM (i.e. one incorporating such a number of wells that $R_{off} \approx 0$). From the data in Fig.5.3.3 we calculate the respective on- and off-state reflectivities at the resonant position, as functions of the relative exciton-resonance separation using the ≈13kV/cm and 83kV/cm curves that corresponds roughly to 0V and 9V operation of CB145. Note that a top 1000Å GaAs layer, which contributes to αd irrespective of the applied voltage, has been included in the calculations as for CB145. The results, plotted in Fig.5.3.4, allow the evaluation of the maximum variation $\Delta\lambda_\alpha$ of this relative separation that will comply with the requirements that a) R_0 does not exceed a certain maximum value and b) the contrast at the resonance is maintained over 10dB. The obtained range $\Delta\lambda_\alpha$ is consequently a function of R_0^{max} and is plotted in Fig.5.3.5.

As discussed previously, variations of the relative position of the resonance with respect to the exciton are induced by lateral non-uniformity and by temperature changes. In the former case the exciton is effectively fixed, while in the latter the relative shift is ≈0.2nm/°C. The independence of the parameters allows for an expression relating $\Delta\lambda_\alpha$ with the maximum allowable variations of the resonance $\Delta\lambda_T$ and $\Delta\lambda_{NU}$ as caused by temperature-changes and non-uniformity respectively. Hence,

$$\begin{aligned}(\Delta\lambda_\alpha)^2 &\geq (\Delta\lambda_{NU})^2 + (\Delta\lambda_T)^2 = \\ &(\Delta\lambda_{NU})^2 + (0.2\cdot\Delta T)^2 \end{aligned} \qquad 5.3.9$$

The above contains information on the tolerances imposed solely due to the exciton 'linewidth', i.e. they are inherent in the MQW electroabsorptive effects. These will clearly be modified depending upon the well width and the designed relative separation between the exciton and the resonance.

Derivation of the combined tolerances

If we incorporate the temperature dependence of $\Delta\lambda_n$ and $\Delta\lambda_T$ in inequalities 5.3.8 and 5.3.9 and rearrange we obtain the set

$$\begin{aligned}(\Delta\lambda_{NU})^2 &\leq (\Delta\lambda_\alpha)^2 - (0.2\cdot\Delta T)^2 && \text{(a)}\\ (\Delta\lambda_{NU})^2 &\leq \left(\Delta\lambda_\phi\right)^2 - (0.08\cdot\Delta T)^2 - \left(\Delta\lambda_{op}\right)^2 && \text{(b)}\end{aligned} \qquad 5.3.10$$

These inequalities refer to the same parameters and therefore have to be fulfilled simultaneously. Fig.5.3.5 depicts the dependence of $\Delta\lambda_\alpha$ and $\Delta\lambda_\phi$ on the chosen R_0^{max} for the case of the reference structure CB145, where R_f=0.3, R_b=0.95, F=2.449 (at the off-state), and L≈1.77μm. Note that whereas $\Delta\lambda_\alpha$ does not depend critically upon the above specific modulator parameters, the value of $\Delta\lambda_\phi$ is determined by these as is shown by equations 5.3.6 and 5.3.7.

In order to evaluate the maximum tolerances it is required to take the optimum combination of $\Delta\,\lambda_\alpha$ and $\Delta\,\lambda_\phi$ each time. For example, when systems requirements impose a certain operating temperature range ΔT, the maximum $\Delta\lambda_{NU}$ is obtained when

$$(\Delta\lambda_\alpha)^2 - \left(\Delta\lambda_\phi\right)^2 = \left((0.2)^2 - (0.08)^2\right)\cdot(\Delta T)^2 \qquad 5.3.11$$

Let us consider the case where the operating wavelength is practically fixed (eg. using highly stabilised or external laser sources) and the temperature is expected to vary by a total $\Delta T=30°C$. Equation 5.3.12 yields $(\Delta\lambda_\alpha)^2-(\Delta\lambda_\phi)^2=30.2nm^2$ which from Fig.5.3.5 implies $\Delta\lambda_\phi \approx 4.2nm$ and $\Delta\lambda_\alpha \approx 7nm$. Consequently, the maximum variation of the resonant position due to lateral non-uniformity is calculated from eqn.5.3.10 to be

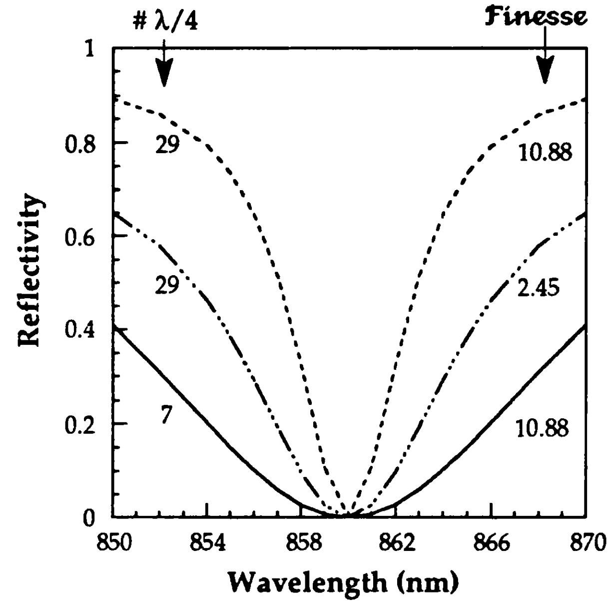

Fig.5.3.6 *Calculated FP resonances for three cases. The finesse is noted at the right-hand side and the number of quarter wavelengths within the cavity at the left-hand side of the graph.*

$\Delta\lambda_{NU}=3.6nm$. This means that the tolerable lateral non-uniformity, eg., of an array of devices operating at ≈860nm would in this case be 0.41%. Similarly, with the operating wavelength allowed to drift within a 1nm range, and the operating temperature range required to be $\Delta T \approx 30°C$ as before, the maximum admissible lateral non-uniformity is deduced to be ≈0.37% ($\Delta\lambda_{NU} \approx 3.2nm$). With the operating wavelength set to track the temperature shifting resonance (Chapter 4), the ΔT term in eqn.5.3.10b is eliminated (but not so in eqn.5.3.10a). This yields $\Delta\lambda_{NU}=4nm$ so that the acceptable lateral non-uniformity is then increased to 0.47%. Finally, if the temperature of the modulators is well stabilised, using for example integrated Peltier coolers [Berger *et al.*, 1991a], then an acceptable non-uniformity of ≈0.7% can be calculated, which agrees with the calculations in section 5.2.

It follows from our above analysis that the contrast tolerances of a modulator will be improved if $\Delta\lambda_\alpha$ and $\Delta\lambda_\phi$ are increased. $\Delta\lambda_\alpha$ is optimised for lower insertion loss and, more critically, the further the (designed) operating point is from the exciton peak. Clearly, for a certain well width incorporated in the MQW region and a given operating wavelength (i.e. when $\Delta\lambda_\alpha$ is a fixed function of R_0^{max}), *the width of the Fabry-Perot resonance is a measure of the tolerances.* This width is narrowed for higher finesse modulators since the phase range $\Delta\phi$ that complies with the 10dB-contrast requirement is, as a consequence, decreased (eqn.5.3.3). However, the respective wavelength range is also dependent upon the cavity length, as shown by eqn.5.3.6 and 5.3.7, and this offers ground for optimisation. This is illustrated in Fig.5.3.6, where the higher finesse structure may have a broader FP resonance if its cavity length is sufficiently short.

The accurate expression ought to account for the wavelength dependence of the phase-change on reflection from the Bragg stack (section 5.2.1). Finally then the wavelength range $\Delta\lambda_\phi$ is given by

$$\Delta\lambda_\phi = \frac{\Delta\phi \cdot \lambda^2}{2\pi L n} \cdot \frac{n_H - n_L}{n_H - n_L + n_L/m} \qquad 5.3.12$$

This is still a decreasing function of L despite the fact that the second term, which is introduced by the Bragg stack, increases with L. Hence, the tolerances are maximised when the cavity length is minimum. Experimental confirmation of this is presented in section 5.3.3. Note that L is the *total* length of the cavity and does not refer to the MQW region alone. The latter is determined by the requirement that the amount of absorber αd is equal to the critical value $[\alpha d]_c$. The consequence of the above conclusion is that an increased front mirror reflectivity does not necessarily lead to diminished tolerances as compared to those of CB145, since a) CB145 is not an optimised structure in that respect, i.e. the optical length of the cavity is not minimised, and b) the increased finesse results in a narrower required MQW thickness (Chapter 6) and consequently allows for a further reduction of the cavity length. We will examine the trade-offs closely in Chapter 7 where we proceed to a thorough optimisation.

5.3.2 Large reflection-change modulators.

Various applications require large reflection change rather than high contrast modulation (Chapter 2). The exhibited reflection change (ΔR) is the difference between the on- and off-state reflectivities (R_{on}, R_{off}) and, as a result, both R_{on} and R_{off} are equally significant in the determination of ΔR. This has been pointed out already by our study of the temperature sensitivity in Chapter 3.

The reflection change is given by

$$\Delta R = \frac{R_o^{on} - F^{on}\sin^2\phi}{1 + F^{on}\sin^2\phi} - \frac{R_o^{off} - F^{off}\sin^2\phi}{1 + F^{off}\sin^2\phi} \qquad 5.3.13$$

where $R_o^{on\ (off)}$ is the on-resonance reflectivity at the on-(off-)state, $F^{on\ (off)}$ is the coefficient of finesse at the on-(off-) state, and ϕ is the phase introduced by the cavity (Chapter 2). Since the effective back mirror is dependent upon the amount of absorber present in the cavity, the coefficient of finesse F reaches its minimum at the off-state (Chapter 2). Therefore, we may rewrite from equation 5.3.13 we

$$\Delta R \le \frac{R_o^{on} - R_o^{off}}{1 + F^{off}\sin^2\phi} = \frac{\Delta R_o}{1 + F\sin^2\phi} \qquad 5.3.14$$

where ΔR_o is the on-resonance reflection change, and F_{off} is replaced by F for simplicity. We may thus identify two contributions to ΔR: one from the value of ΔR_o, and one induced by the operating wavelength deviating from that of the resonance. Lateral non-uniformity causes a variation of the FP resonant position while the exciton position remains effectively unaltered. Temperature instabilities, on the other hand, have a far more pronounced effect on the exciton (0.27nm/°C shift) than on the FP resonance (0.08nm/°C), so that the relative separation of the two is varied by ≈0.2nm/°C. We have already discussed the above in greater detail in the previous section. Similar to that analysis, the exciton-resonance relative separation affects ΔR_o while the actual position of the resonant wavelength determines the phase ϕ at the operating wavelength.

Eqn.5.3.14 allows the evaluation of the reflection change tolerances. For example, let us assume that the obtained reflection change is required not to deviate from its maximum value ΔR_{max} by any more than 20%. Equation 5.3.15 yields

$$\frac{(\Delta(\Delta R\ ))^2}{\left(\Delta R_o^{max}\right)^2} = \frac{(\Delta(\Delta R_o))^2}{\left(\Delta R_o^{max}\right)^2} + \frac{\left(\Delta\left(F\sin^2\phi\right)\right)^2}{1} \qquad 5.3.15$$

where F is assumed constant.

In the following, we will adopt a treatment similar to that in section 5.3.1. We implement thus the experimental absorption data shown in Fig.5.3.3 to derive in this case the reflection change ΔR_0 at the resonant position when the latter shifts in relation to the exciton. A modulator identical to CB145 is again assumed and, therefore, we use the absorption spectrum at 83KV/cm which corresponds roughly to the 9V operation of CB145. Before we proceed further, it is useful to point out that contrary to the study of high contrast modulation, in the case of large reflection change modulators it is not obvious that the *critical* amount of absorber ought to be incorporated in order to maximise the obtained ΔR and/or maximise the reflection change tolerances. Indeed, by incorporating a fraction of the critical amount $[\alpha d]_c$, one would increase both R_{on} and R_{off}. In the cases where the (as-designed) operating wavelength is close to the exciton peak, and therefore the absorption at the on-state is relatively high, Fig.5.3.1 shows that a decrease of the incorporated absorber (αd) down to $0.5[\alpha d]_c$ will indeed result in an increase of the obtained ΔR. This is a consequence of the fact that the slope of R with αd is approximately linear up to $\alpha d = 0.5[\alpha d]_c$ while it is decreased for higher values of αd from then onwards. We plot ΔR as a function of the exciton-resonance relative separation in Fig.5.3.7 for the cases where 100%, 80%, and 50% of $[\alpha d]_c$ is

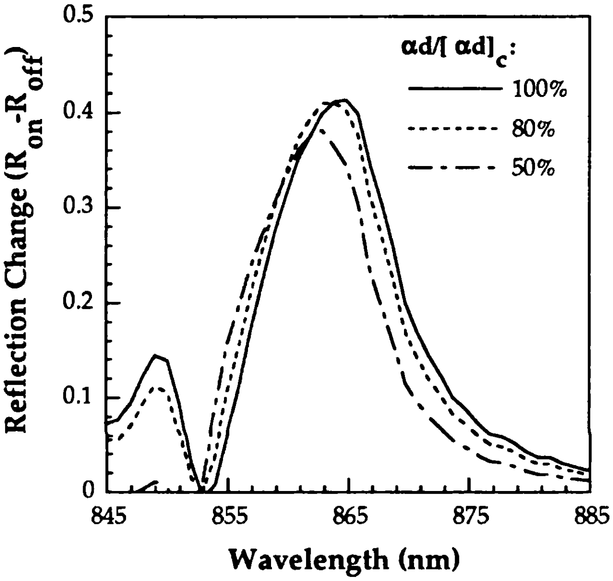

Fig.5.3.7 *The obtained reflection-change at the resonant position plotted as a function of the resonant wavelength. Calculations are based upon the absorption spectra in Fig.5.3.3, and are performed for an AFPM similar to CB145, for different relative amount of absorber incorporated.*

incorporated in the modulator. The results do not indicate any significant improvement, neither of the obtained reflection-change nor of the tolerances, for this fixed voltage operation at the particular designed operating wavelength (≈861nm). Furthermore, it will be seen that the respective tolerances are maximised when setting the operation far from the zero bias exciton peak where the obtained reflection-change is also optimised. Especially in these cases, the choice of incorporated $\alpha d/[\alpha d]_c$ does not have any effect upon the obtained tolerances.

Thus, based on the above, we restrict the analysis to the case where the critical amount of absorber is incorporated. Using the respective curve from Fig.5.3.8, we may evaluate the allowable variation $\Delta\lambda_\alpha$ of the relative exciton-resonance separation as a function of the maximum relative variation of ΔR_0. The obtained values are plotted in Fig.5.3.7. Calculations at different operating fields did not indicate any improvement of the wavelength range $\Delta\lambda_\alpha$ with a decrease of the amount of incorporated absorber.

Using eqn.5.3.15 we may next evaluate the maximum $\Delta\phi$ as a function of the

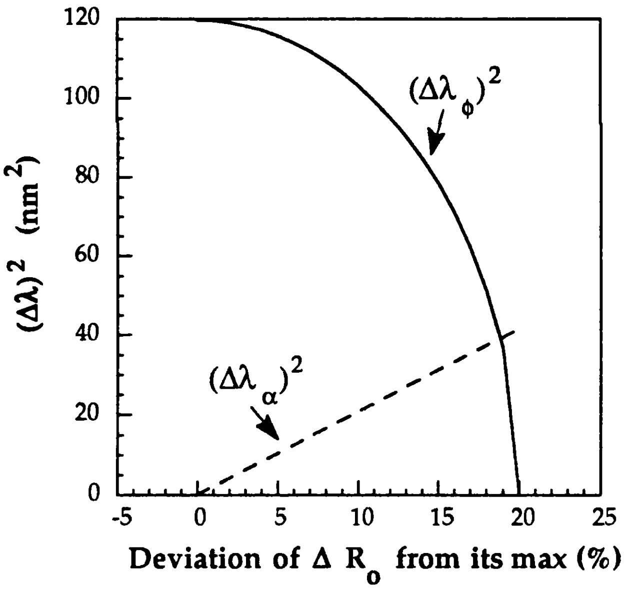

Fig.5.3.8 *The characteristic wavelength ranges determined by the electroabsorptive effects and the cavity design, plotted versus the percentage deviation of the on-resonance reflection-change from its maximum value. The calculations are based on the information in Fig.5.3.7, and are carried out for an AFPM similar to CB145.*

permitted variation of the on-resonance reflection change ΔR_o

$$\Delta\phi = 2\cdot\sin^{-1}\left[\sqrt[4]{\frac{(0.2)^2-\left(\Delta(\Delta R_o)\right)^2\Big/\left(\Delta R_o^{max}\right)^2}{F^2}}\right] \qquad 5.3.16$$

This phase range $\Delta\phi$ may be expressed in wavelength terms ($\Delta\lambda_\phi$) by means of eqns.5.3.6 and 5.3.8 in the previous section. The derived $\Delta\lambda_\phi$ is also plotted in Fig.5.3.7. The ranges $\Delta\lambda_\phi$ and $\Delta\lambda_\alpha$ are related to the variation $\Delta\lambda_{NU}$ of the resonant wavelength as this is caused by non-uniformity and to the temperature changes ΔT, by inequalities 5.3.10 in the previous section. Again, these have to be fulfilled simultaneously. In the previous section both the cavity- and electroabsorption-imposed restrictions were equally limiting the maximum tolerances at least when the temperature range ΔT does not exceed ≈40°C. Here, however, the restrictions imposed by the electroabsorptive effects are the limiting ones, i.e. the maximum tolerances are in fact determined mainly by inequality 5.3.10a. This is primarily a result of our arbitrary requirement that the reflection-change remains within at least 80% of its peak value. Clearly, relaxed requirements upon the attained ΔR will affect the relative significance of inequalities 5.310 (a,b). Nonetheless, the electroabsorptive 'linewidth' does play a more important role in the cases where large reflection changes are concerned as compared to high contrast designs. We ought to emphasise, on the other hand, that systems requirements will in fact determine the allowable drift of the obtained reflection-change.

Subsequently, in a manner identical to that adopted in section 5.3.1, we perform example calculations. The requirement that the operating temperature range is ΔT=30°C yields Δ_{NU}=2nm, i.e. a maximum tolerable lateral non-uniformity of 0.23%. This is determined by the limiting inequality 5.3.10a, while according to inequality 5.3.10b the operating wavelength may vary within a total 5.5nm range. The maximum non-uniformity that may be tolerated is obtained when $\Delta T=\Delta\lambda_{op}=0$, and is according to our analysis estimated to be about 0.74%.

Hence, the reflection change tolerances are improved when the operation is set far from the zero bias exciton peak to maximise $\Delta\lambda_\alpha$, and the FP resonance is broad so as to maximise $\Delta\lambda_\phi$. The range $\Delta\lambda_\phi$ was found in the previous section to broaden for shorter cavity lengths. Similarly to our discussion in that section, we may conclude that a decrease of the cavity length leads to improved reflection-change tolerances. These will be implemented in our designs in Chapter 7.

Based on this latter conclusion, the reflection-change tolerances may be improved by the implementation of a double-cavity arrangement. where the top cavity is of very short optical length. This is done as follows. A second cavity is formed atop the modulator by the growth of a spacer layer and a reflector stack. Alternatively, this second cavity may be formed by dielectric layers deposited after the growth has been concluded and, possibly, after the devices have been fabricated. The reflectivity of the very front mirror must be almost equal (preferably slightly larger) to the reflectivity of the on-state of the bottom modulator. With careful design it is possible to realise a structure where the two cavities are decoupled, i.e. where the cavity formed between the very top and the very bottom mirror is not at a resonance. An example of such an arrangement is given in Chapter 8. In total the situation is effectively a top passive cavity the back mirror of which is electrically controlled. Thus when the bottom active cavity is at its reflecting state, the overall composite structure is off whereas when the bottom cavity is off the composite structure shows a reflectivity of a value close to that of the very front mirror. An inverted operation is thus attained where the resonance may be broader as a result of the shorter cavity. Assuming that the growth is well calibrated to realise such a structure, the tolerances are otherwise increased with respect to reflection-change.

This may not, unfortunately, attain an increase of the contrast associated tolerances. Indeed, the AFPM shows good contrast-associated tolerances exactly because the off-state, that effectively determines the attained contrast, is a least sensitive state. When using a double cavity arrangement the final off-state corresponds to the on-state of the initial modulator and therefore its sensitivity is high. As a result the contrast associated tolerances will actually deteriorate.

5.3.3 Experimental confirmation. QT238B.

In order to confirm the above mentioned concerning the significance of the width of the FP resonance as a measure of the tolerances, we designed an AFPM structure where the cavity length is kept minimal. The structure is otherwise identical to our reference modulator CB145 in Chapter 2. The nominal epitaxial thicknesses and compositions of this structure are shown in Fig.5.3.9. Thus the MQW region and the back reflector stack are as for CB145 but the top $Al_{0.3}Ga_{0.7}As$ spacer-layer has the minimal thickness required to make the cavity length an odd number of quarter wavelengths at 861nm (Chapter 2). The insertion loss, contrast, operating voltage and wavelength are, therefore, expected to be identical to those of CB145. A marked difference, however, is predicted regarding the width of the FP resonance which, according to our analysis in the previous sections, ought to be broader in this case. As a result, the tolerances of this modulator are expected to be superior.

Reflectivity spectra of two different devices fabricated from QT238B are shown in Figs. 5.3.10 and 5.3.11. These are chosen so that the positions of the FP resonances are not coincident. As can be seen from both spectra, the exciton position is at ≈845.5nm whereas the corresponding position for CB145 was 851nm. According to theoretical calculations (Chapter 3) assuming 30% Al concentration in the barriers the well width is estimated to be ≈83Å, i.e. the final structure is far from the designed 95Å-well. This was caused by a temporary erroneous calibration of the MOCVD growth kit at the University of Sheffield. As a result the amount of absorber is well in excess of the critical amount $[\alpha d]_C \approx 0.57$ for this particular device, which is manifested in the spectra as an increase of the off-state reflectivity within the resonant width at the biased exciton peak position for device A (Fig.5.3.10). Photocurrent data obtained for device A are shown in Fig.5.3.12. The interesting feature is the virtually 'flat' absorption response at the optimum 9V reverse bias.

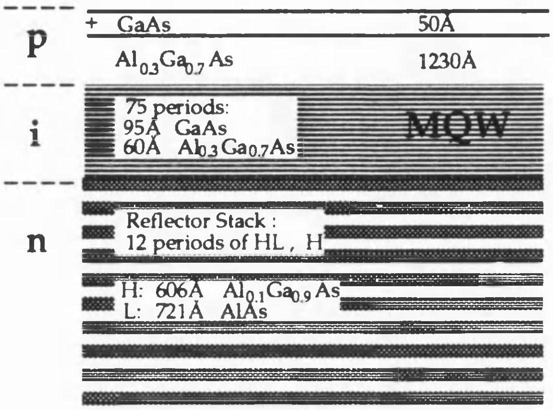

Fig.5.3.9 *The epitaxial structure of QT238B. This was grown by MOCVD at the University of Sheffield. The MQW region and the mirror design are identical to these of CB145.*

Contrast ratio curves are illustrated in Fig.5.3.13 for both devices. An increase of the 10dB-contrast optical bandwidth, as compared to CB145, to ≈7nm has been achieved, despite the fact that neither device presented here is ideal. The same figure (5.3.13) points out the benefits offered by self-linearised operation discussed in Chapter 4. The optimum voltage is 9V for device A in Fig.5.3.10, and 11V for device B in Fig.5.3.11. This is strongly dependent upon the relative wavelength separation of

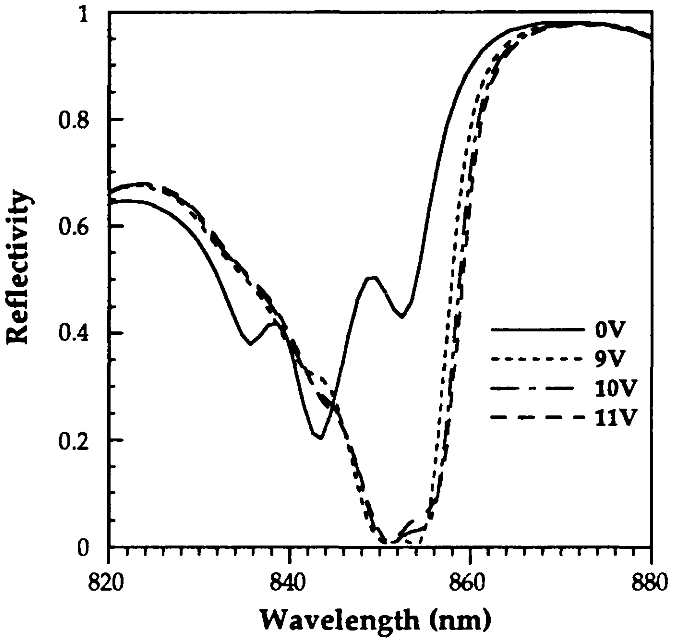

Fig.5.3.10 *Reflectivity spectra for device A from QT238B.*

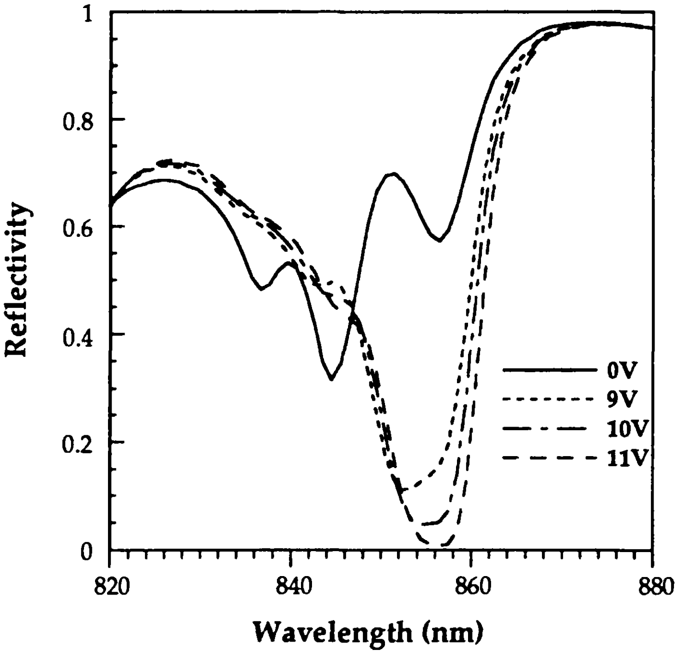

Fig.5.3.11 *Reflectivity spectra for device B from QT238B.*

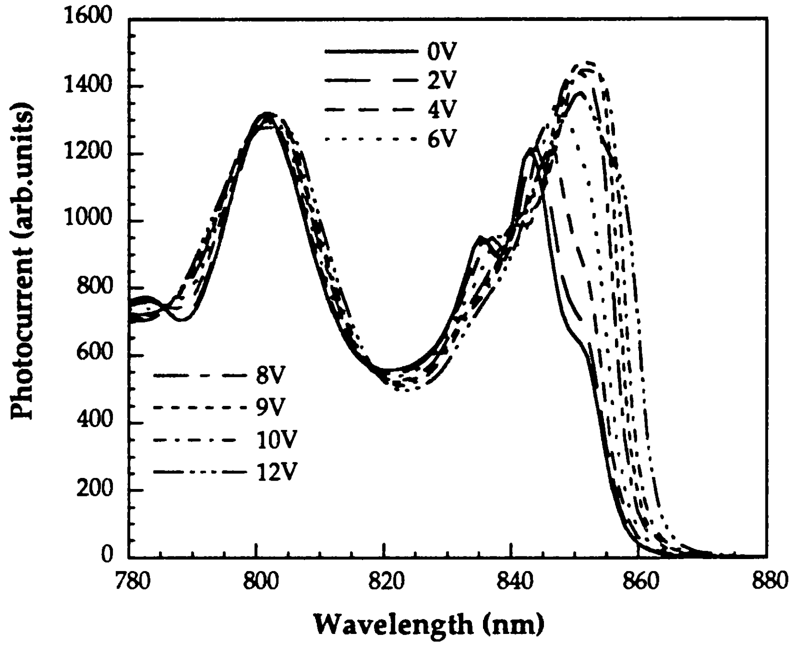

Fig.5.3.12 *Photocurrent data obtained for device A, the reflectivity of which is presented in Fig.5.3.10.*

the resonant position and the exciton for this modulator stemming mainly from the excessive amount of absorber incorporated. Indeed as a result of this, the operation is away from the $\alpha d=[\alpha d]_c$ point (Fig.5.3.2) giving rise to larger sensitivity to changes in αd. The 'perfect' modulator would be one operating at about 854nm and 10V reverse bias. Fixed voltage (at ≈10V), fixed wavelength (at ≈854nm) operation would result in device A yielding just over 12dB and device B around 11dB. However, self-linearised operation at the same wavelength would allow both devices to achieve a contrast of ≈15dB. Thus the maximum tolerable non-uniformity would that way be increased or, alternatively, the operating temperature range would be extended.

Let us next compare this to the corresponding result for CB145. A fair comparison requires two devices from CB145 with their resonances roughly 4nm apart. However, we may use the reflectivity data presented in Chapter 4, i.e. obtained from a single device at different temperatures, since the exhibited contrast is determined by the relative separation between the exciton and the resonance. Thus the curves in Fig.5.3.14 are obtained from reflectivity data at 14° and 38°C with the higher temperature spectra shifted accordingly so that the exciton peaks align with those of the lower temperature spectra. The advantage of the broader resonance structure is

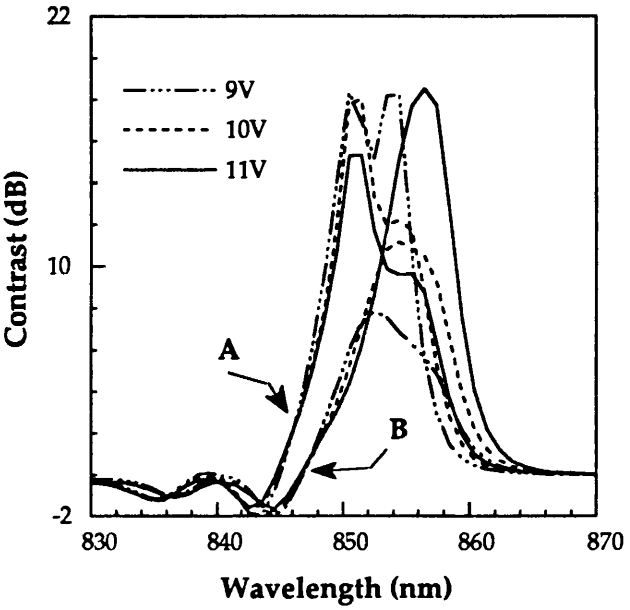

Fig.5.3.13 *Contrast ratio curves (R_{on}/R_{off}) shown for both devices A and B from QT238B.*

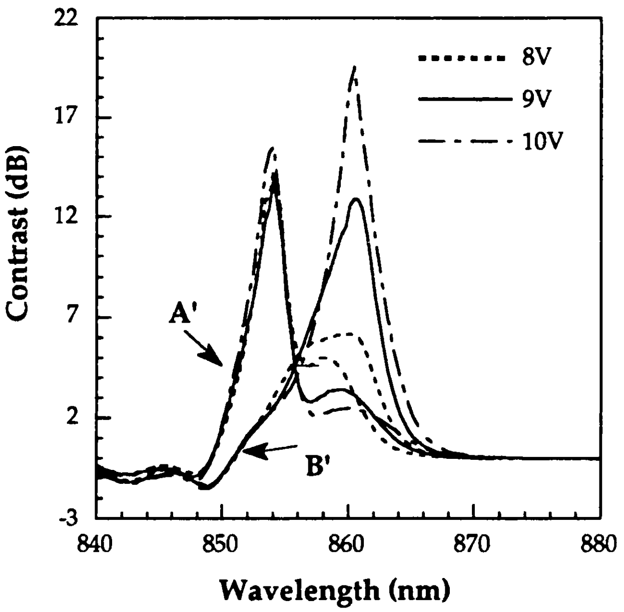

Fig.5.3.14 *Contrast curves illustrating the effect of non-uniformity in the case of CB145. The data have been obtained by a manipulation of reflectivity data for one single device at different temperatures. The two resonant positions differ by less than 4nm.*

obvious from a comparison between Fig.5.3.13 and 5.3.14 where we can see that good performance may be obtained for both devices within a broader range of wavelengths. This denotes the better tolerances of QT238B as compared to those of CB145.

QT238B is, unfortunately, not an ideal structure for a direct comparison with CB145 regarding the tolerances. The differing well widths in the two structures give rise to dissimilar restrictions imposed by the electroabsorptive effects. Furthermore, as a result of the fact that this well width difference was unintentional, a non-optimum amount of absorber is incorporated in QT238B causing its performance to deviate markedly from ideal. Nevertheless, we have demonstrated that the length of the optical cavity does have a significant effect upon the width of the FP resonance, as predicted in the previous sections. Subsequently, the broader resonance has been shown to affect directly the tolerances of the resultant modulator.

5.4. OPTICAL ALIGNMENT

5.4.1. Optical addressing of two dimensional arrays of modulators.

As discussed in Chapter 2, high-speed operation implies small device sizes since the capacitance is proportional to the mesa area. This, in conjunction with the need for dense integration in large two-dimensional arrays stretches the requirements on optical addressing.

Precise alignment is mandatory to ensure that the light spots are 'tightly' focused upon the centre of the optical window of each device. This demands 6-fold alignment (Fig.5.4.1) in the case of 2-D arrays since then all the devices have to be well focused and correctly illuminated simultaneously [Tooley *et al.*, 1991]. The above are important for any vertical modulator. The extra difficulty introduced by reflection modulators is that the reflectivity is far more sensitive to incorrect focusing than, for example, transmission is for the corresponding devices. Also, any fraction of light incident on the metal contacts is directly reflected *unmodulated* leading to a decrease of the final contrast at the detector plane. The latter could be diminished by a covering of the contacts with non-reflecting (eg. rough-surfaced) layers. These difficulties are not restricted to resonant structures. The operation of double-pass reflection modulators (Chapter 1) is, for example, equally limited.

As the dimensions of the devices are pushed down to the order of a few microns, the use of high quality microlenses is obligatory. An array of microlenses may be aligned with a great accuracy on top of an array of modulators using eg. the solder-bump technique [Moseley *et al.*, 1991]. Alignment associated requirements are as a consequence relaxed, and greatly improved alignment is achieved [McCornick *et al.*, 1991]. Several techniques have been used for the fabrication of lenslets and lenslet arrays; among them are photolytic techniques in photosensitive glass [Borrelli *et al.*, 1985], and ion-milling of glass or other transparent material [Tsai *et al.*, 1990]. Alternatively, micro-Fresnel lenses can be produced on glass or semiconductor substrates. These are essentially binary or multilevel phase gratings that cause light to interfere at a common focus. High resolution photolithographic techniques such as e-beam lithography and laser lithography are used for the production of these patterns [Jahns *et al.*,1989; Haruna *et al.*, 1990].

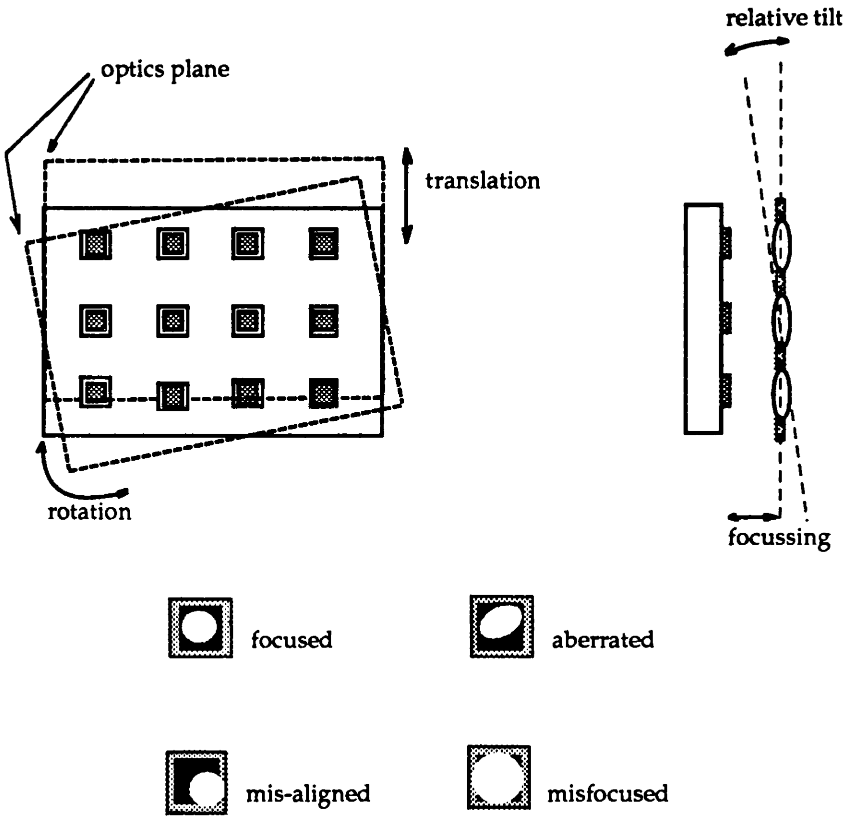

Fig.5.4.1 *Schematic of the optical alignment of an array of modulators with an array of lenses. A tightly focused spot at the centre of the optical window is obtained when correct alignment and focusing are achieved.*

It was mentioned earlier (section 5.2) that the smallest reported optically and electrically addressible devices are 5μmX5μm optical window devices [Chirovski *et al.*, 1991]. Although smaller devices may be fabricated, it is difficult to forsee the implementation of any reduced scale devices since the alignment requirements and the focusing on such dimensions becomes rather prohibiting. The effect of the highly convergent beams, implied by the latter, upon the modulator performance needs further investigation.

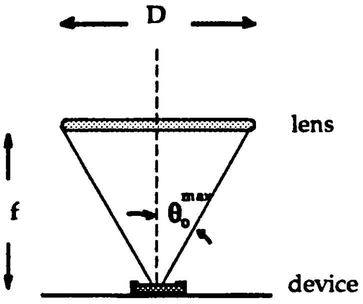

Fig.5.4.2 *The convergence of the incident beam is a function of the lens focal length f and the lens aperture D.*

5.4.2 Effect of the optical angle of incidence.

Normal incidence has been assumed in our analysis so far. However, operation at oblique incidence may be favourable in many cases as it offers the possibility for direct interconnection among islands on the same chip and overall system compactness [Guha *et al.*, 1990]. Another advantage is the elimination of a double pass through a beam splitter that is needed in the case of normal incidence and which causes a 6dB total power loss.

The issue of the angle of incidence is two-fold. Firstly, it regards the possibility of oblique incidence and the effect that might have on the modulator performance, and also the sensitivity to changes of the angle of incidence. Further, as we discussed in the previous section, small device features require accordingly scaled down spot-sizes. The diffraction-determined (i.e. the minimum possible) spot radius w_S is a function of the lens diameter D and focal length f as described by the Rayleigh formula

$$w_s = \frac{1.22 \cdot f \cdot \lambda}{D} \qquad 5.4.1$$

where λ is the wavelength of the light used. This will ultimately result in a significant angular convergence of the incident beam (Fig.5.4.2). Indeed, the total convergence of the incident beam may be calculated as $\tan\theta = D/2f$. For example, the spot-size required in the case of 5μm windows is estimated to be about 3μm; the beam convergence is then calculated to be ≈20°. It is of great importance to quantify the effect on the modulation since this will reflect the actual performance under real conditions.

It follows from Rayleigh's formula that the larger the lens diameter and the shorter the focal length the tighter are the resulting light spots. However, the diameter of the microlens obviously has to be smaller than the device interspacing. Consequently, short focal length lenses will be required to ensure that, both, the spot-size is sufficiently small and the array density is not restricted. Lenses of the appropriate sizes for addressing 5μm-window, 100μm apart devices have been fabricated producing diffraction limited spot-sizes [Dhoedt *et al.*,1991] but further work is required in that direction.

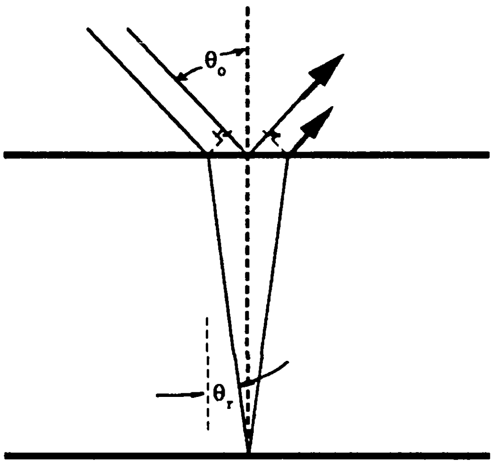

Fig.5.4.3. *A schematic of the interference between two beams one of which is directly reflected and the other experiences propagation through a layer r.*

The angle of incidence affects both the FP resonant action and the MQW electroabsorptive effects. Firstly, let us concentrate briefly upon the logistics of these separately. In the following a plane wave is assumed incident at an angle upon the device.

Effect on the FP action

The main effect caused by an angle of incidence $\theta_0 \neq 0°$ is the fact that the optical lengths of the layers comprising the structure appear altered (Fig.5.4.3). This gives rise to a shift of the resonant wavelength. The phase difference between two interference beams, one of which propagates through a layer of thickness d and index n, is given by

$$\delta = \frac{2\pi \cdot n \cdot d \cdot \cos\theta_r}{\lambda} \qquad 5.4.2$$

where θ_r is the internal angle. This has already been presented in Chapter 3. It follows from eqn.5.4.2 that the layers appear in fact thinner at oblique incidence which causes the FP resonance to shift to shorter wavelengths. For small angles of incidence θ_0, the internal angles are $\theta_r \approx \theta_0/3.5$ as it follows from Snell's law. However, the relative change $\Delta\lambda/\lambda$ of the resonant wavelength is exactly equal to the relative change $\Delta L_{opt}/L_{opt}$ of the optical thickness. As a result, the consequent shift is not insignificant. The corresponding shift of the FP wavelength for a modulator operating at ≈860nm is plotted in Fig.5.4.4 as a function of the angle of incidence. The mean refractive index is assumed ≈3.55 in these calculations, as is typically the case for our modulators. The implications of this wavelength shift are discussed in the next sections.

Another effect of oblique incidence is an altered reflection coefficient associated with each interface. The magnitude and sign of this change is polarisation dependent. The reflection coefficient r of the interface between two materials is given by

$$r = \frac{y_0 - y_i}{y_0 + y_i} \qquad 5.4.3$$

where $y_i = N/\cos\theta_i$ for p- and $y_i = N\cos\theta_i$ for s-polarisation, where N is the complex refractive index of the medium.

At small angles of incidence, this has a negligible impact upon the overall reflectivity as the internal angles are small. The effect upon the interface reflectivity is larger for smaller index mismatches between the materials defining that interface. However, small index steps have hardly any significance towards the FP action. On the other hand, reflecting interfaces, that have a considerable contribution to the FP action, are minimally affected. For example, the large index mismatch air-GaAs interface is 30% reflecting for s- and 32% for p-polarised waves at 45° of incidence, as opposed to 31% at normal incidence; this is clearly a small variation.

Large angles of incidence, on the other hand, modify the interface reflectivities considerably. For example, the reflection coefficients of the interfaces between two subsequent quarter wave layers comprising the reflector stacks may be altered by as much as 20-30% for linearly polarised light of either polarisation. This change is always negative (i.e. the reflectivity is reduced) for s-polarised, and positive for p-polarised beams. Consequently, in the case of s-polarised waves a larger number of periods is required in the mirrors to attain the same reflectivity as at normal incidence. Generally, this effect is diminished for non-polarised light when

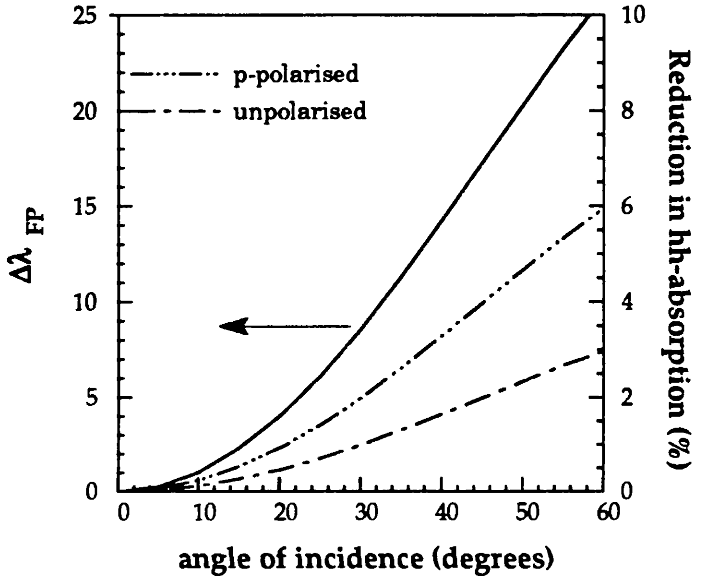

Fig.5.4.4. *The shift $\Delta\lambda_{FP}$ of the resonant wavelength is plotted as a function of the angle of incidence for a device with the resonance at 860nm when addressed at normal incidence. On the other axis, we plot the relative reduction in the heavy-hole absorption coefficient for the cases of unpolarised and p-polarised light incident on the modulator.*

$$y_i^{ave} = \frac{1}{2}N(\cos\theta_i + 1/\cos\theta_i) \qquad 5.4.4$$

where y_i^{ave} is the corresponding average value of the characteristic admittance of layer i.

Effect on the MQW electroabsorption

As mentioned in Chapter 3, the MQW absorption coefficient is also dependent upon the polarisation of the light. In this case, however, it is not the polarisation of the incident light in relation to the plane of incidence that is of interest, but rather the direction of the electric (E) vector in relation to the plane of the quantum wells. When the E-field is parallel to the wells (TE-polarisation), the ratio between the heavy-hole and light-hole continuum contributions is 3:1 [Schmitt-Rink *et al.*, 1989; Weisbuch, 1986], and this is the case at normal incidence with light of any polarisation (only TEM waves are supported by free space). At oblique angles, however, there may be a component of the E-field perpendicular to the well layers (TM-polarisation) (Fig.5.4.5). For this component, the heavy-hole associated transitions cannot take place [Weisbuch, 1986] and thus the absorption coefficient due to the heavy-hole is zero, while the light-hole associated level is twice as large as for TE polarisation [Weiner *et al.*, 1985]. Since the operation of our modulators relies upon the heavy-hole absorption modulation, the fraction (in power terms) of light in TM polarisation causes a direct reduction of the amount of absorber αd in the cavity. Light in the s-polarisation incident upon the device always results in TE-polarised light within the wells, and therefore the absorption coefficient is not modified. However, p-polarised light results in a TM-component of relative power

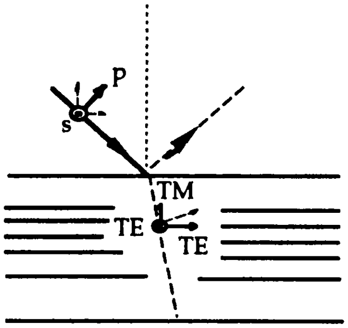

Fig.5.4.5 *Within the device the optical wave may be analysed in a TM and a TE component the relative power of which is determined by the polarisation of the incident light and the angle of incidence.*

$$P_{TM} = P \cdot \sin^2 \theta_r \tag{5.4.5}$$

where P is the total internal optical power, P_{TM} is the power in TM-polarisation, and θ_r is the internal angle. Unpolarised light may be considered as consisting of equal amounts of p-and s-polarisation so that on average

$$P_{TM} = \frac{1}{2} P \cdot \sin^2 \theta_r \tag{5.4.6}$$

The percentage reduction in absorber αd as a function of the angle of incidence θ_0 is plotted in Fig.5.4.4 for both p-polarised and unpolarised light (in the case of s-polarisation the corresponding reduction is equal to zero, as explained earlier). Thus when operating at an angle other than the normal, the number of wells incorporated in the intrinsic region will have to be increased accordingly (Fig.5.4.4) to compensate for this effective absorption reduction. However, since the absorption at the on-state is equally reduced, operation at a smaller wavelength separation from the zero-bias exciton may yield effectively identical insertion-loss and contrast as at right angles.

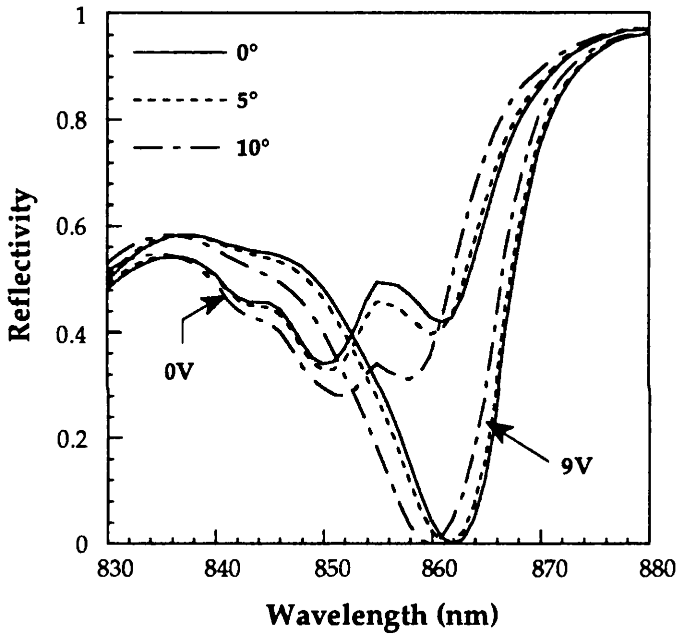

Fig.5.4.6a *Modelled reflectivity spectra for CB145 using the experimental electroabsorptive effects in Fig.5.3.3. Spectra are plotted at different angles of incidence assuming a plane wave of non-polarised light.*

5.4.3 Tolerance to the angle of incidence.

Having gained a qualitative understanding of the ways oblique incidence affects the operation, let us now proceed to accurate evaluations. These are performed using the model presented in Chapter 3, but using experimental absorption coefficient data in order to achieve increased liability. Fig.5.4.6 shows the obtained modelled reflectivity spectra with the incidence angle θ_0 varying from normal (0°) to 15°, for CB145 assuming upolarised light incident on the device. For such small angles, the reduction in the heavy-hole absorption is negligible (Fig.5.4.4), and the main effect is similar to that caused by lateral non-uniformity, i.e. the FP resonance is shifted due to an altered effective optical thickness. As a result, the polarisation of the light does not limit the performance critically in the case of small angles.

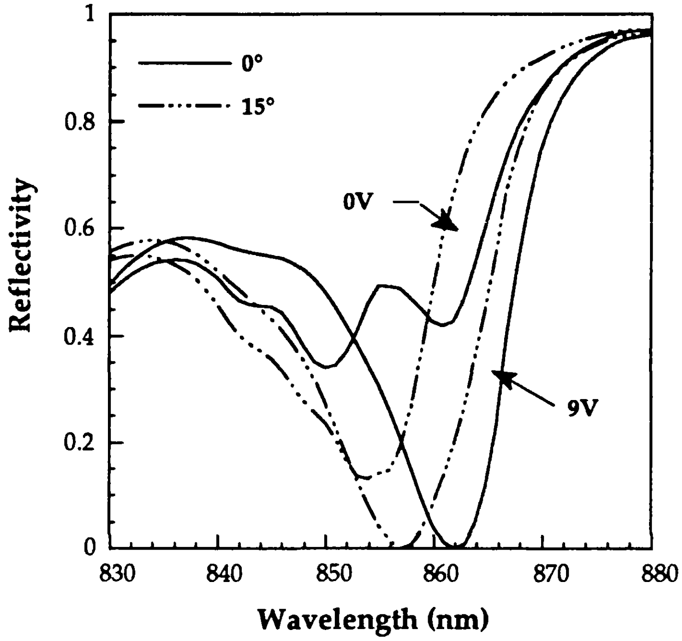

Fig.5.4.6b *Modelled reflectivity spectra for CB145 using the experimental electroabsorptive effects in Fig.5.3.3. Spectra are plotted at different angles of incidence assuming a plane wave of non-polarised light.*

Whereas a modulator may be designed to operate at any angle, albeit at a slightly different wavelength, the tolerance to the angle of incidence is markedly increased at normal incidence and diminishes rapidly the larger the angle. This is evident in Fig.5.4.4 where the slope $\Delta\lambda/\Delta\theta_0$ can be seen to increase significantly when larger angles are involved. For example, it may be deduced from Fig.5.4.4 that the FP wavelength shift by a maximum of 1nm for a variation of the angle θ_0 by ±10° at normal incidence. By contrast, a similar variation around an angle of 40° would cause a shift $\Delta\lambda_{FP}$ of up to 12nm, since in this case a change of the angle by a mere couple of degrees suffices to cause a shift of about 1nm.

It may thus be concluded that the minimum angle of incidence ought to be chosen when oblique incidence is employed. This would benefit possibly the operating voltage and insensitivity to polarisation but, more critically, the angle tolerances of the system. It is useful to point out that the respective tolerances in the case of double-pass reflection modulators (Chapter 1) are determined by the requirement that the top antireflection coating is indeed anti-reflecting. Bearing in mind that the refractive index of such a layer is considerably lower than these of the semiconductor layers (ideally this ought to be equal to the square root of the index of the coated material), the angle sensitivity is quite large.

5.4 CONCLUSIONS

Separate conclusions have been drawn at the end of each section in this Chapter. In summary, we have evaluated in detail the effect simultaneous variations of the operating conditions have on the modulator performance, be it contrast or reflection-change. Subsequently, we are in the position to trade-off performance characteristics for tolerances that comply with the operational realities each time.

The tolerances have been found to improve the further the operating wavelength is set from the zero-bias exciton peak. This becomes increasingly important in the case of applications that demand large reflection-changes. Also, the temperature tolerances are critically determined by the limitations imposed by the wavelength dependence of the electroabsorptive effects. The width of the FP resonance has been identified as a measure of the tolerances. The 10dB-contrast wavelength range of a high contrast device is a fraction (≈ 0.07 for a 3dB insertion loss device) of the FWHM of the off-state virtually regardless of the finesse of the cavity. This is the primary factor determining the maximum tolerable lateral non-uniformity. The resonant width has been predicted and experimentally demonstrated to increase with decreasing cavity length. Thus a modulator that operates at a lower voltage, yet with tolerances similar to CB145, is realisable.

Although successful individual devices and small arrays of devices may be fabricated (see also Chapter 9), the present growth capabilities do not appear sufficient to meet the requirements of an implementation of the resonant structure in large 2D arrays. This is further limited by the fact that the tolerances to temperature and to lateral non-uniformity are inter-related. Since temperature control of the modulators using integrated Peltier coolers [Berger *et al.*, 1991a] would relax the temperature tolerances, it would allow for an increase of the growth-associated tolerances. Also we have proposed that the lateral non-uniformity is compensated for by a post-growth correction of the cavity length. This calls for dielectric front reflector stacks when high finesse cavities are used. The above options encounter an arguably high degree of complexity which, however, may be justifiable when one considers that we are concerned with an expensive high-performance technology in the first place.

The angle of incidence has been found to affect the modulator considerably, yet not as much the performance characteristics as the operating wavelength. It has been concluded that small angles of incidence ought to be employed should oblique incidence be preferable. Finally, this dependence on the angle of incidence points out that there may be a trade-off between the operational speed and the exhibited contrast of resonant modulators in practice. Indeed, high speed requires small device sizes which will need tight spot sizes. Thus, as the beam will then be highly convergent, it is expected that the obtained contrast may be diminished. Further investigation in this direction is of great importance.

CHAPTER 6: TRADE-OFFS INVOLVED IN THE AFPM PERFORMANCE IMPOSED BY THE FABRY PEROT MIRROR DESIGN

6.1 INTRODUCTION

The modulation characteristics of an AFPM device, namely the operating voltage, insertion loss, contrast, and reflection-change, are determined by the combination of two factors. One is the MQW electroabsorption, and the other is the mirror design of the Fabry-Perot cavity. In this chapter we study the trade-offs imposed upon the operation solely by the FP cavity design. Firstly, we study the way different performance characteristics are affected, and how various operation parameters may be optimised. Subsequently, we present experimental results from two AFPM structures and compare their operation to that of CB145 (Chapter 2).

6.2 THE FABRY-PEROT CAVITY DESIGN

The reflection from a Fabry-Perot (FP) cavity becomes zero at the FP resonant wavelength when the front (R_f) and the effective-back mirror (R_b^{eff}) reflectivities are equal. The absorber αd controls the effective back mirror reflectivity $R_b^{eff} = R_b\, e^{-2\alpha d}$. As a result, with $R_f < R_b$ as is the case for an AFPM, the cavity is 'balanced', i.e. the total reflectivity is zero, when a critical amount of absorber $[\alpha d]_c$ is induced at the resonance. This is given by

$$[\alpha d]_c = \ln\sqrt{\frac{R_b}{R_f}} \qquad 6.2.1$$

The operating voltage is

$$V = F \cdot \ell \qquad 6.2.2$$

where F is the electric field applied perpendicular to the wells and l is the thickness of the intrinsic region. With a slight modification brought about by the inevitable doping-guarding buffer layers (Chapter 2), l is proportional to the number of wells comprising the quantum well layer. If we assume a given field-induced absorption modulation (from α_o without bias to α_{max}) at the operating wavelength, obtained under a certain field F, it is evident from eqn.6.2.1 that a reduction of $[\alpha d]_c$ gives rise to a reduced number of wells required for high-contrast modulation, thereby achieving a lower operating voltage (eqn.6.2.2).

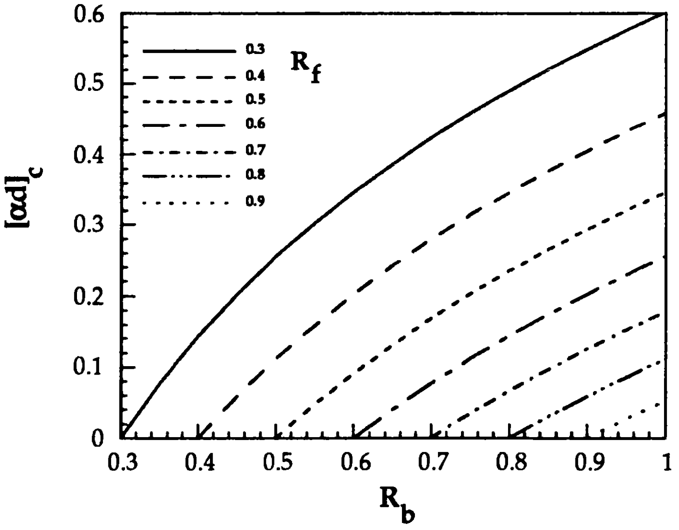

Fig.6.2.1 *The dependence of the critical amount of absorber required to balance an asymmetric cavity, upon the front and back reflectivities.*

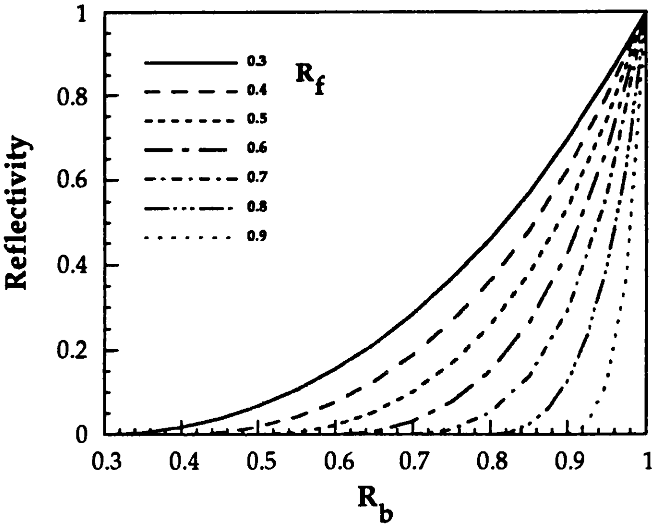

Fig.6.2.2. *The reflectivity of an asymmetric cavity that incorporates no absorber, plotted against the back mirror reflectivity for various front mirror reflectivities.*

According to eqn.6.2.1 the critical amount of absorber is decreased for lower values of the ratio R_b/R_f. We plot $[\alpha d]_c$ as a function of R_b for different values of R_f in Fig.6.2.1. The vertical axis may be directly converted to operating voltage with a small offset to account for the intrinsic-region buffer layers. Clearly V falls with decreasing R_b and increasing R_f. A reduction of the back mirror reflectivity seems at first favourable since the consequent low-finesse cavity would yield an improvement of the tolerances (Chapter 5). Yet, the reflectivity at the on-state stems effectively from the back mirror, and therefore when this is reduced so is R_{on}, i.e. the insertion loss is dramatically increased. The total reflectivity of an asymmetric cavity with zero absorber incorporated is plotted in Fig.6.2.2. The low-R_b case leads indeed to an enormous insertion loss and is consequently rejected as an option. A few important points may be drawn from Figs. 6.2.1 and 6.2.2.

i. The higher the back mirror reflectivity the lower the insertion loss.

ii. The higher the back mirror reflectivity the less marked is the effect of the front reflectivity upon the insertion loss.

iii. For a given front mirror reflectivity the operating voltage is not significantly affected when R_b varies between 0.95 and 1, while the insertion loss may be severely modified.

The insertion loss is brought about by two effects. One is the FP-related reduction of the reflectivity stemming from the fact that the operation is at a reflection minimum. This is obviously inherent to asymmetric FP modulators, and is more pronounced the closer the value of the ratio R_f/R_b to 1, as depicted in Fig.6.2.2. Insertion loss is also induced by the on-state absorptance

$$A = \frac{\left(1 - e^{-\alpha d}\right) \cdot \left(1 - R_f\right) \cdot \left(1 + R_b e^{-\alpha d}\right)}{\left(1 - R_\alpha\right)^2} \qquad 6.2.3$$

A fraction of this causes a reduction of the reflectivity. We plot the dependence of the on-state absorption A_{on} upon R_f for R_b=0.99 in Fig.6.2.3. In these calculations it is

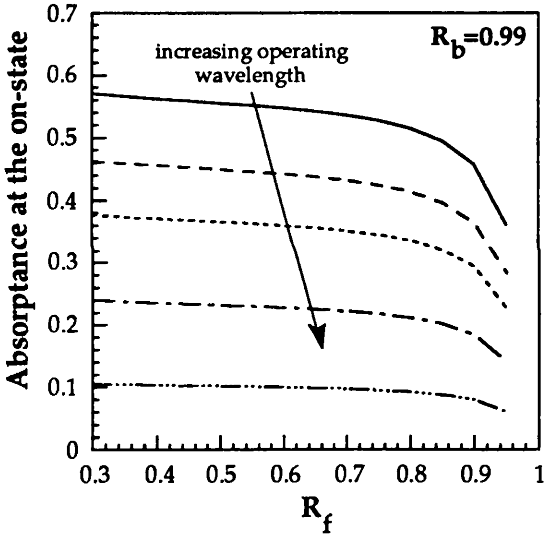

Fig.6.2.3. *The absorptance at the on-state as a function of the front reflectivity for a normally-on AFPM. The various curves correspond to different operating wavelengths and are based upon experimental absorption coefficient values off a 95Å well sample (Fig.5.3.3.). The number of wells is calculated so that 'infinite' contrast is attained.*

assumed that the critical amount of absorber is incorporated, i.e. upon application of the suitable field, the absorber αd at the resonance will be equal to $[\alpha d]_c$ (and infinite contrast will be obtained). The implemented absorption coefficients are derived from the experimental values from a 95Å sample (section 5.3.1) at various operating wavelengths (longer than the zero-bias exciton). Despite the fact that these are specific cases, it is obvious that the absorptance decreases in fact with R_f. Note that fewer wells are incorporated with increasing R_f (eqn.6.2.1). Thus, while the higher finesse cavity is more efficient in absorbing the light, simultaneously the amount of absorber is accordingly scaled down. The insertion loss is rapidly reduced at longer operating wavelengths. This results from the fact that while the absorption tail follows an exponential roll-off with wavelength, the peak-absorption coefficient at increasing fields drops much slower exhibiting roughly a linear dependence (Fig.5.3.3 for

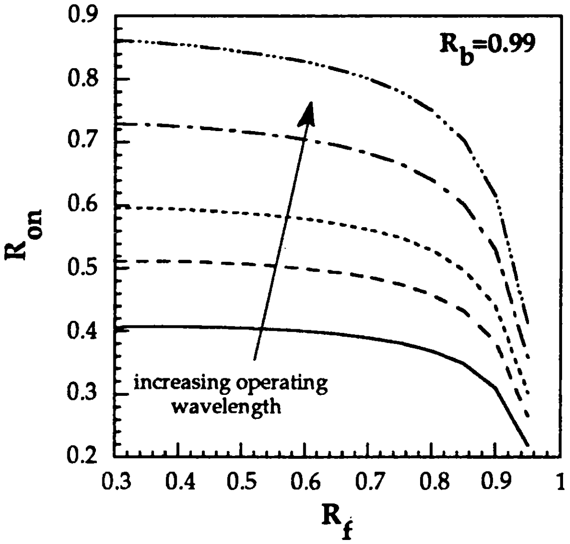

Fig.6.2.4. *The on-state reflectivity plotted as a function of the front mirror reflectivity for 'infinite' contrast operation. The calculations are based on experimental absorption coefficient data as for Fig.6.2.3.*

example). Therefore, the number of wells is increased only marginally while the absorption coefficient α_0 at the on-state is notably decreased, so that the on-state absorber αd is markedly reduced thereby lowering A_{on}. Finally, a plot of the on-state reflectivity R_{on} for the cases when R_b=0.99, yields a decrease of R_{on} with increasing R_f (Fig.6.2.4). The two mechanisms that are responsible for the insertion loss are competing, one causing R_{on} to decrease (Fig.6.2.2) and the other to increase (Fig.6.2.3) with R_f. Pezeshki *et al.* [1991b] have claimed the insertion loss dropping with R_f. In fact, this is the case only when R_b=1. Any analysis based on this preassumption is rather misleading, however, since R_b may tend to, but never reaches, 1 (Chapter 2). In practice, and for the typical QCSE obtainable from the GaAs/$Al_{0.3}Ga_{0.7}As$ system, the insertion loss increases with R_f. Nevertheless, when $R_b \geq 0.99$, this increase is rather insignificant for R_f up to 0.7-0.8, and more so for increasing R_b. Experimental confirmation of our analysis in this section is presented in the following sections.

6.3 EXPERIMENTAL CONFIRMATION OF THE EFFECT OF THE FP CAVITY DESIGN UPON THE MODULATOR PERFORMANCE

6.3.1 QT131 AFPM.

Epitaxial structure

This structure was designed to incorporate the same well and barrier width as CB145 and also an identical back reflector stack. The cavity design differs from CB145 in that the front reflectivity is increased to ≈45% by the use of a front (1.5 period) stack.

The operating wavelength was also intended to be as for CB145. Although the back reflector is not increased compared to that structure, the insertion loss is not expected to exceed that of CB145. This is mainly the result of a ten-fold reduction of the top GaAs capping layer, from 1000Å to 100Å, in the present design. Clearly, the fact that the absorption coefficient of that layer is not field-controlled causes the overall modulation to diminish. The nominal thicknesses and Al concentrations of the layers comprising this structure are shown in Fig.6.3.1. It is important to point out that the cavity length has been kept minimal in this design in order to achieve maximum tolerances (Chapter 5).

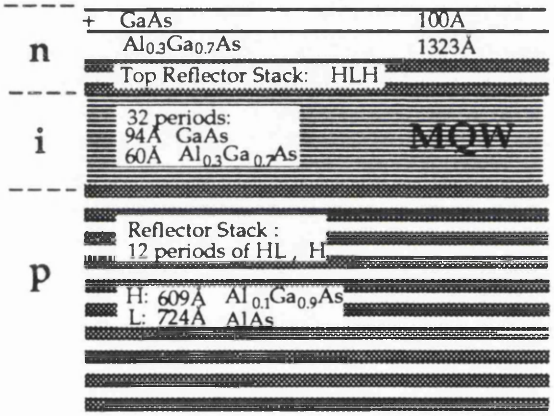

Fig.6.3.1 *The epitaxial structure of QT131, grown by MOCVD at the University of Sheffield. Below the bottom reflector stack there is a 1μm-thick GaAs buffer layer grown on a SI substrate.*

Experimental Results

Reflectivity spectra from QT131 are shown in Fig.6.3.2. The operating voltage is reduced to 4.2V which is less than half that of CB145 (9V). The on-state reflectivity R_{on}

at the maximum contrast wavelength of ≈857nm is about 50%. Contrast ratio curves are plotted in Fig.6.3.3 yielding a maximum contrast of ≈15dB and a 10dB-contrast bandwidth of ≈4.5nm at 4.2V. This compares unfavourably with that of CB145. In reality, the off-state FWHM of the FP resonance is increased slightly for this device in agreement with calculated values (eqn5.3.12, Table.6.3.1). The 10dB bandwidth is however drastically narrowed by the fact that the off-reflectivity never falls to zero.

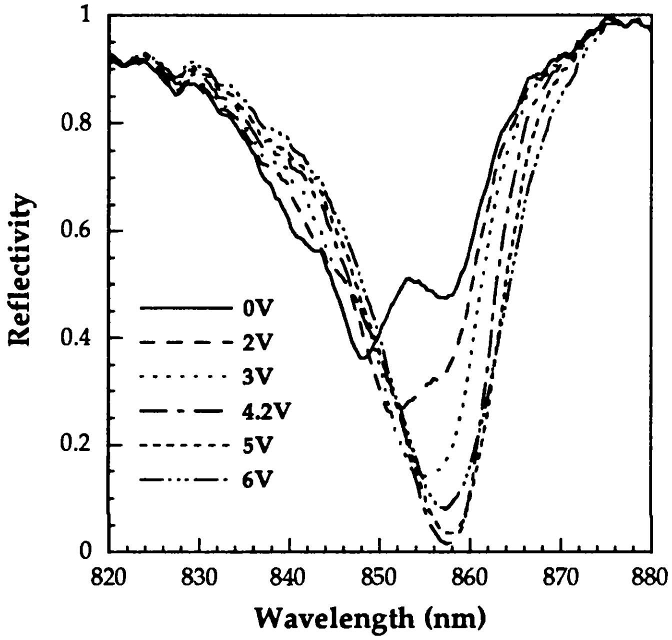

Fig.6.3.2 *Reflectivity spectra from QT131 AFPM*

At 15dB this is arguably a high contrast device. However, the implied operation away from the $\alpha d=[\alpha d]_c$ point (Chapter 5) does not allow this device to exhaust its full potential with regard to tolerances. Specifically, although the reflection-change associated tolerances are comparable to those of CB145, as we discuss below, the contrast-associated tolerances are lower (see Table 6.3.A).

Reflection-change curves derived from Fig.6.3.2 are presented in Fig.6.3.4. A maximum ΔR of ≈48% has been attained while also $\Delta R \geq 45\%$ is obtained over a 6.5nm range at 4.2V. This indicates good reflection-change tolerances that stem from the broad off-state resonance. Note that the fact that R_{off} is always non-zero does not diminish the reflection-change tolerances (Chapter 5). Finally, photocurrent data, scaled at 750nm to account for the voltage-dependent quantum efficiency (section 2.3.2), are presented in Fig.6.3.5.

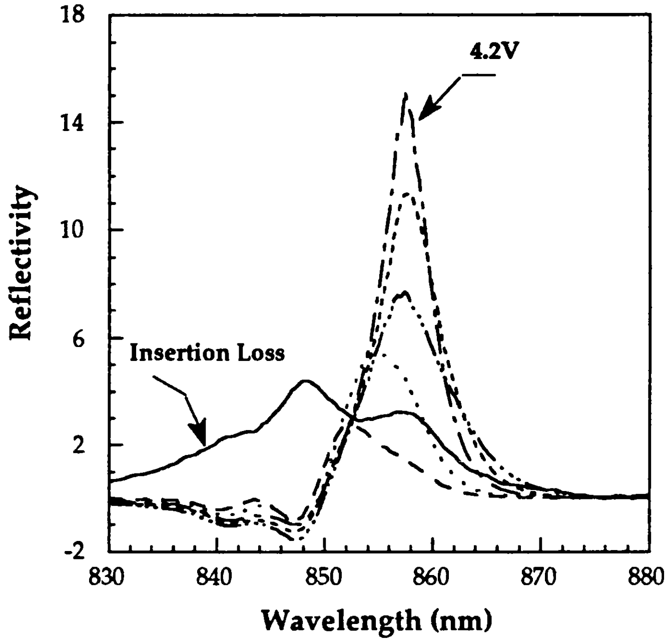

Fig.6.3.3 *Contrast ratio curves obtained from the spectra in the previous figure. Linetypes as in Fig.6.3.4 below.*

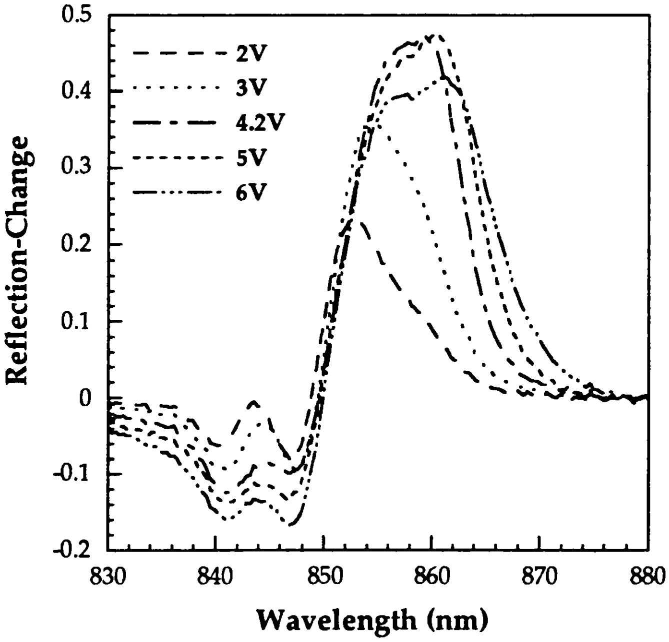

Fig.6.3.4 *Reflection change curves for the spectra in Fig.6.3.2.*

Further discussion

A comparison between QT131 and CB145 is done in Table.6.3.A. The finesse $\mathcal{F}$ is calculated at the off-state assuming that then $R_f=R_b^{eff}$, which in the case of QT131 is a good estimate though not strictly true . The capacitance is compared to that of a device with a 1μm-thick intrinsic region, assuming identical mesa areas for all structures. This is two-fold increased in comparison to CB145. Assuming 30% Al concentration in the barriers, the well width may be estimated theoretically (Chapter 3) to about 90Å, i.e. slightly thinner than the intended 95Å. The results agree well with theoretical predictions. Any deviations from the designed performance are mainly caused by the erroneous well width.

Table.6.3.A *Comparison among the three AFPM structures.The finesse $\mathcal{F}$is calculated at the off-state assuming that the front and effective-back mirrors are equal. The FWHM refers to the experimental width of the off-state, while the reference capacitance C_0 is that of a structure with 1μm-thick intrinsic region.*

	CB145	QT131	QT223
R_f	0.31	0.45	0.55
R_b	0.95	0.95	0.997
$[\alpha d]_c$	0.5599	0.3736	0.2974
#wells	75	32	32
$\mathcal{F}$ (off-state)	2.535	3.8317	5.1775
Capacitance	$0.82C_o$	$1.97C_o$	$2.09C_o$
FWHM (off)	14nm	15nm	9nm
10dB-BW	5.5nm	4nm	2nm
80% ΔR_{max}range	8.5nm	7.5nm	6.5nm
Insertion Loss	3.5dB	3dB	2.8dB
Voltage	9V	4.2V	3.4V

One interesting feature of the experimental spectra is that there is no obvious voltage-induced shift of the FP resonance. This is quite pronounced in the respective spectra of CB145 in Chapter 2. The length of the cavity consists mainly of well (plus barrier) material for QT131 while in the case of CB145 only a 65% is MQW. This ought to enhance the effect of electrorefraction for the former (Chapter 2), modifying thereby the spectra far more markedly. However, it should be noted that the well widths differ for the two structures and so does the relative exciton-resonance separation. The electrorefractive effects are critically dependent upon both these (Chapter 2). It appears thus, that in this case the operating wavelength is in the vicinity of the node where the electrorefraction is minimal.

In summary, we have achieved a reduction of the operating voltage to 4.2V for a high-contrast (15dB), low insertion loss (3dB) device, by an increase of the front reflectivity to ≈45%. Most importantly, the contrast-associated and the reflection-change associated tolerances of this structure are comparable to those of CB145 (Chapter 5).

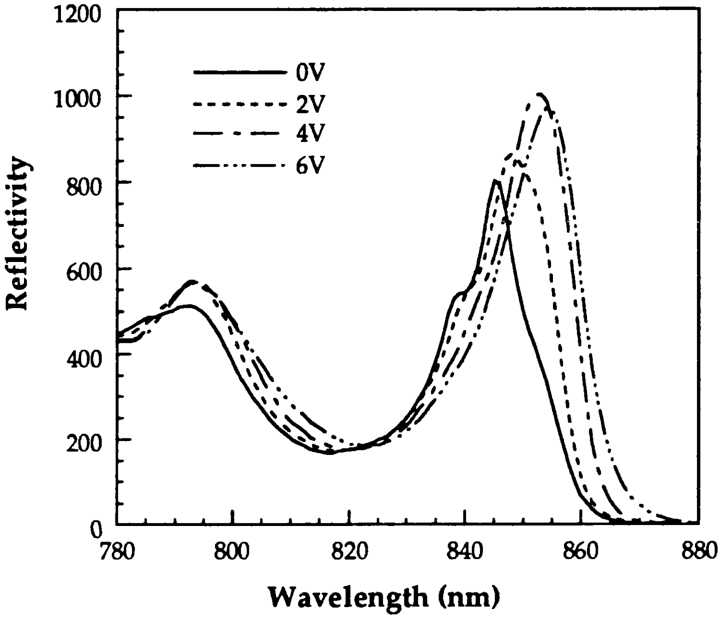

Fig.6.3.5 *Photcurrent data obtained for a device from wafer QT131. The data have been scaled at 750nm (see section 2.3.2).*

6.3.2. QT223 AFPM.

Epitaxial structure

It was shown in section 6.2 that an increase of R_b leads to a reduction of the insertion loss or, alternatively, should one aim at a certain insertion loss, it allows for operation closer to the zero-bias exciton peak, thereby attaining lower operating voltage. The results from QT131 have been a confirmation of the analysis in section 6.2. This next structure comprises a further improvement. The epitaxial layers are shown in Fig.6.3.6.

The back mirror is increased here to a theoretically estimated R_b=99.7%, and the front to R_f=55%. The top reflector stack consists of 2.5 periods of high- and low-index quarter-wave layers, part of the top $Al_{0.1}Ga_{0.9}As$ layer having been replaced by a 50Å GaAs capping layer. The cavity length is kept minimum to achieve maximum tolerances (Chapter 5). A reduction of the barrier width has also been implemented here based upon calculations on inter-well coupling using the theoretical model developed by D. Atkinson [1990]. The 55Å barrier used here is rather to the safe side, the theory suggesting that this could be reduced to ≈40Å for 90Å wells; detailed analysis is presented in Chapter 7.

This structure has been designed for epitaxial-lift-off (ELO) and subsequent mounting on a Si substrate at IMEC, Belgium. This requires the inclusion of stress compensating layers below the reflector stack that, nevertheless, do not affect the modulator design and operation otherwise. However, after the entire processing and mounting on Si has taken place the reflectivity spectra are modified at long wavelengths. This technique is discussed in detail in Chapter 9. At the time when QT223 was designed a full understanding of the trade-offs involved in AFPM design had been achieved. It was therefore known that far better performance could be attained by such devices, albeit at the expense of the tolerances. A full optimisation of the modulation characteristics has not been implemented in this design, however. The ultimate goal was a successful modulator integrated with Si electronics and as a result the design is rather to the conservative side.

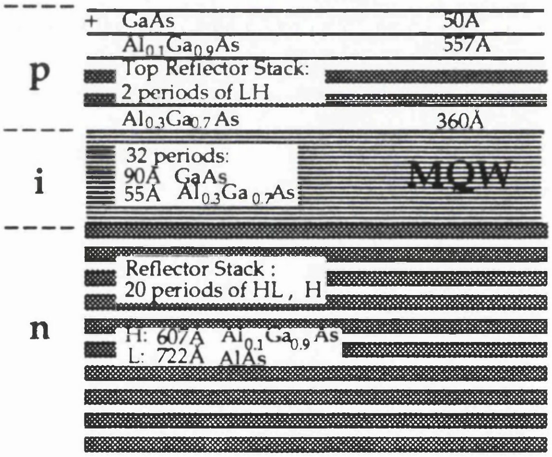

Fig.6.3.6 *The superstrate of QT223 grown by MOCVD at the University of Sheffield. A 100Å-thick AlAs etch-stop layer is grown on the SI substrate, followed by 3.5μm of* $Al_{0.3}Ga_{0.7}As$ *and 0.75μm GaAs stress-compensating layers (not shown).*

Experimental results

Reflectivity spectra from QT223 are shown in Fig.6.3.7. The on-state reflectivity is ≈52% and the off-state reflectivity reaches as low as 1.5% at the optimum 3.4V reverse bias.

Contrast ratio curves derived from Fig.6.3.7 are shown in Fig.6.3.8. Contrast of ≈12dB has been achieved at ≈863nm under 3.4V reverse bias with an insertion loss of ≈2.8dB. The 10dB-contrast bandwidth is 2nm, notably reduced from that of CB145. This is a consequence of the increased finesse but in fact the prime limitation is imposed by the relatively low maximum contrast. A reflection-change of 52% is attained at 865nm, and ΔR≥45% is obtained over a 6nm range at 3.4V (Fig.6.3.9). This is a further confirmation that the bandwidth is limited primarily by the low contrast and not by the cavity design. Photocurrent spectra are presented in Fig.6.3.10.

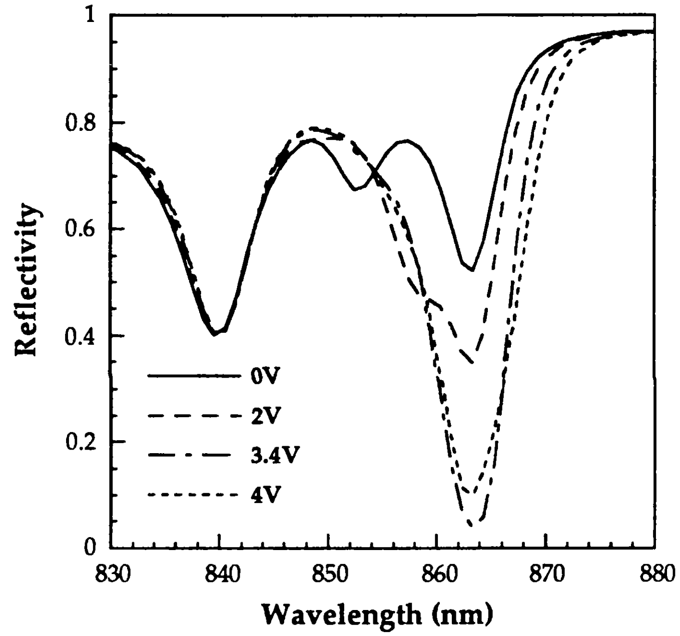

Fig.6.3.7 *Bias-dependent reflectivity spectra from QT223 AFPM.*

Further discussion

The well width is estimated to be 98Å if we assume 30% Al concentration in the barriers (Chapter 3). The theoretical calculations for the designed 90Å structure predict 3dB insertion loss, >20dB contrast at 3.75V. The larger well width is partly responsible for this deviation from the originally intended performance. Comparison with the modelled data for this structure when 98Å wells are assumed are presented in Chapter 3. The insertion loss is underestimated by the model while the operating voltage is

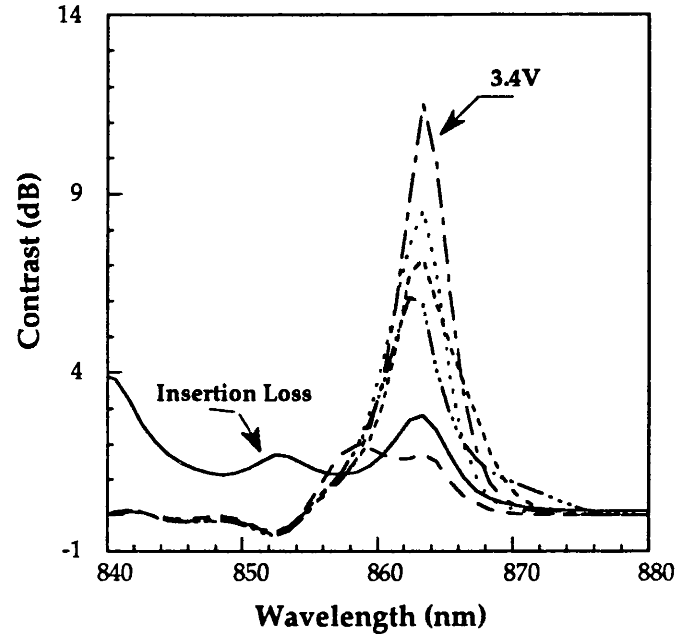

Fig.6.3.8 *Contrast ratio curves obtained from the data in Fig.6.3.7. Linetypes as in Fig.6.3.9 below.*

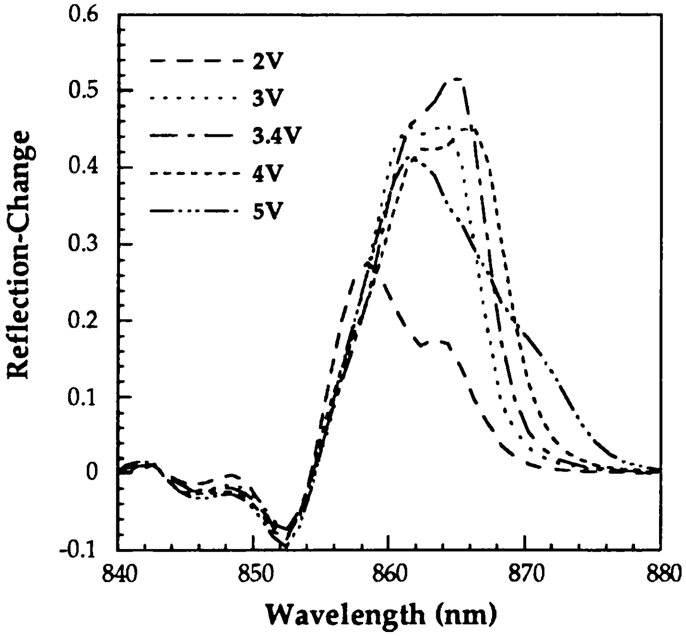

Fig.6.3.9 *Reflection Change corresponding to the data in Fig.6.3.7.*

overestimated. One interesting feature to note when comparing the experimental to the modelled spectra, is the apparent resonance at ≈840nm which is present in the experimental but not in the modelled spectra. This suggests that the corresponding feature is in fact not a resonance but is rather caused by the misposition of the centre wavelengths of at least one of the stacks. Indeed, a back reflector centred at a wavelength longer than the intended ≈860nm would account for both the higher than predicted insertion loss and the lower operating voltage.

A shift of the FP resonance to slightly shorter wavelengths at voltages in excess of 3.4V is apparent from the reflectivity spectra in Fig.6.3.8. This is caused by the MQW electrorefraction. The effect is, nevertheless, not pronounced.

In summary, the operating voltage is further reduced to 3.4V for this 12dB contrast, 2.8dB insertion loss AFPM, by an increase of both the front mirror reflectivity to 55% and the back mirror reflectivity to 99.7%. The contrast tolerances of this structure are, however, severely diminished in comparison to those of QT131 (previous section) and CB145 (Chapter 2). The reflection-change tolerances are comparable to those of these structures indicating that the performance of this structure is mainly limited by the decreased contrast rather than the increased finesse.

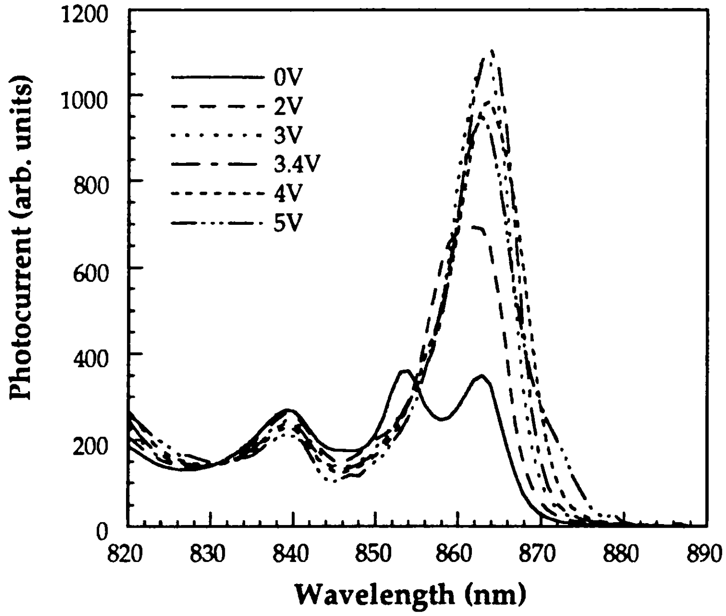

Fig.6.3.10 *Photocurrent spectra obtained for the same device as above from QT223. The data have been scaled at 750nm (see section 2.3.2).*

6.4 CONCLUSIONS

In this chapter we have studied the effect of the FP mirror design upon the modulation characteristics of asymmetric Fabry-Perot modulators. It became clear that the back mirror reflectivity of such devices needs to be as close to unity as possible in order to minimise the insertion loss. For a given MQW absorption-modulation, lower operating voltage is obtained when the front mirror reflectivity is raised by the incorporation of a front Bragg stack. Although the absorption-induced insertion loss falls as a result, the overall insertion loss is increased. This is, however, marginal for front reflectivities up to 0.7-0.8 provided $R_b \geq 0.99$. The absorption-induced insertion loss has been shown to decrease when operating further from the zero-bias exciton peak since the absorption coefficient is markedly lower. This yields subsequently an improvement of the obtained reflection-change. As a consequence of the reduced peak absorption coefficient when operating at longer wavelengths a larger number of wells is required. This combined with the associated higher electric fields gives rise to increased operating voltages.

Experimental results from two AFPM structures confirm the calculated predictions. The operating voltage is reduced from 9V (CB145) to 4.2V (QT131) and 3.4V (QT223) as a result of an increased front reflectivity from 0.31 to 0.45 and 0.55 respectively. The consequent higher finesse cavities cause a narrowing of the FP resonance and thus a reduction of the tolerances (Chapter 5). However, minimal cavity lengths implemented in these structures counteract this effect. This is further assisted by the smaller MQW region thickness implied by the increased front mirror reflectivity. Hence the reflection-change tolerances of both QT131 and QT223 are improved despite the larger cavity finesse in comparison to CB145. The contrast tolerances are comparable to those of CB145 and are diminished mainly due to the lower exhibited contrasts.

In parallel to this work, Pezeshki *et al.* [1990] demonstrated an AFPM with 66% reflection-change at 5V and an insertion loss of 1.2dB, using a device with 50Å GaAs wells and $Al_{0.33}Ga_{0.67}As$ barriers. The exhibited contrast is relatively low at 7.2dB and the resonator is formed by an $R_f \approx 50\%$ and $R_b \approx 99\%$ for that device. Although the authors attributed the improved performance characteristics to the narrow incorporated well width, this is in fact due to the more efficient cavity design (see Chapter 7). Additionally, successful AFPMs in material systems other than the GaAs/AlGaAs have been demonstrated during the course of this work, as we discuss in Chapter 9. The relatively good performance obtained by these devices is solely due to the use of high finesse structures.

Although the structures presented here are not ideal, significant improvements in performance have been obtained. Their value, however, lies mainly with the conclusions that may be drawn regarding the trade-offs involved in the cavity design. These, in conjunction with the choice of incorporated well and barrier width as well as the relative exciton-resonance separation, are implemented in a comprehensive optimisation of the AFPM in the next Chapter.

CHAPTER 7: ASYMMETRIC FABRY-PEROT MODULATOR DESIGN

7.1 INTRODUCTION

In the previous Chapters we have studied theoretically and shown experimentally the trade-offs involved in the design of the Fabry-Perot (FP) cavity of an asymmetric Fabry-Perot modulator (AFPM). We have examined the tolerances (Chapters 4 and 5), and identified ways to maximise these, as well as the parameters that minimise the insertion loss and the operating voltage of such devices (Chapter 6).

In this chapter we will proceed to a detailed calculation of the achievable AFPM performance and a quantitative study of the trade-offs involved in the device characteristics, with wells of different widths incorporated in the quantum well region. The evaluation is based upon theoretical absorption spectra (Chapter 3) and is therefore restricted to $GaAs/Al_{0.3}Ga_{0.7}As$ quantum wells, since a comprehensive set of experimental absorption coefficient data exists for this material (Chapter 3). In order to compare well widths, it is important to first determine the required width of the barrier that ensures insignificant coupling between wells. We calculate these using the theory and method of D. Atkinson [1990]. Finally, based upon the information derived from the performance evaluations, specific modulator designs are presented and their reflectivity spectra are calculated using the model discussed in Chapter 3.

7.2 DETERMINATION OF THE MINIMUM BARRIER WIDTH

The operating voltage of an AFPM, or indeed any multiple quantum well device, depends on the thickness of the intrinsic region, assuming a certain modulation of the absorption coefficient from α_0 to α_{max} at a given electric field applied perpendicular to the layers. The required performance characteristics determine the number of quantum wells that need to be incorporated in the intrinsic region (Chapters 2 and 6). Clearly, however, the width of the barrier ought to be minimised for low voltage operation. So far the barrier widths used have been based upon empirical grounds. The role of the barrier in multiple quantum well material is to ensure that the carriers are sufficiently confined within each well and there is, as a result, insignificant coupling between adjacent wells. We may thus determine the minimum barrier width using exactly this criterion. David Atkinson [1990] has first taken this into account to evaluate the barrier width needed for the common 95Å wells. In this section we use his model and method to calculate the minimum barrier, required for sufficient separation between wells, as a function of well width. Subsequently, this facilitates our evaluation of the relative merits of different well widths with respect to the AFPM performance presented in the following section.

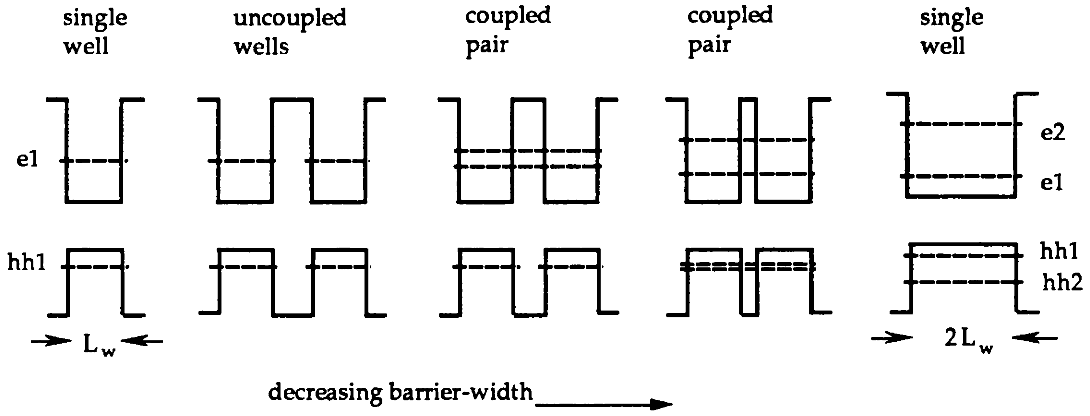

Fig.7.2.1 *Schematic diagram illustrating the effect of the width of the separating barrier upon the energy levels of pairs of (symmetric) wells at zero field. Refer to text for further explanation.*

Coupling effects in quantum wells

As discussed in Chapters 1 and 3, the confinement in single quantum wells and (uncoupled) multiple quantum wells results in the discretisation of the allowable energy levels within the well. When the wells are not sufficiently separated, coupling of the wavefunctions between adjacent wells causes a splitting of the energy levels of the single well. This is clarified in Fig.7.2.1 which refers to the case of pairs of wells. In that case (two wells) the energy levels of the single well (SQW) split in two when there is coupling, whereas for three wells there would be three energy levels, for four wells four, and so on. In the limit of a superlattice a miniband is formed. The splitting occurs for the electron energy levels in the conduction band before (i.e. at larger barrier widths) that of the hole energy levels in the valence band, due to the lower mass of the electron. The energy levels of the SQW of thickness L_w split into two levels, in this case, centred around the initial level. The separation ΔE between these is widened as the coupling is increased, i.e. as the barrier separating the wells becomes thinner. The maximum possible separation may be considered to be that between the energy levels of the n=1 and the n=2 electron of a well of thickness $2xL_w$, which is the limit with L_b=0 (Fig.7.2.1). The effects of coupling upon the absorption spectra may be seen in Fig.7.2.2 for a pair of 90Å GaAs wells separated by $Al_{0.3}Ga_{0.7}As$ barriers. The spectra are calculated [D.Atkinson, 1990] at zero field. The heavy-hole exciton of the SQW is split into two resolvable peaks in the spectrum that corresponds to a pair of 90Å wells separated by 20Å barriers.

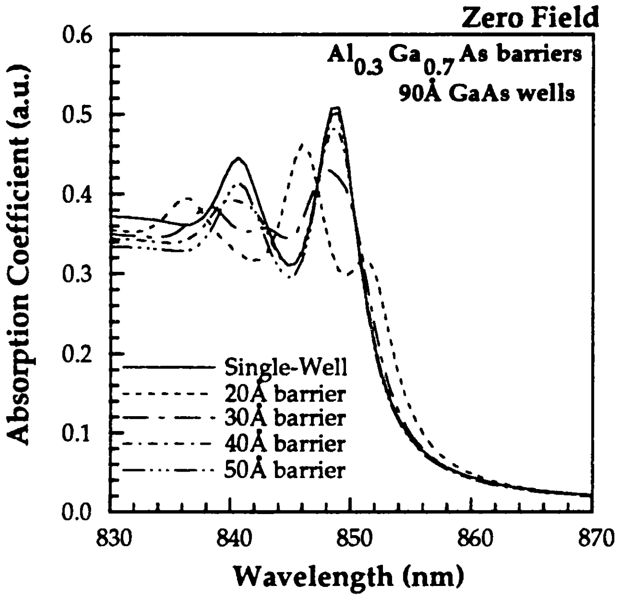

Fig.7.2.2. *Calculated absorption spectra for a single well and for pairs of wells separated by a barrier of varying width. The due to coupling splitting of the electron energy causes a dichotomy of the exciton peak. This is less prominent as the barrier is increased.*

Evaluation of the minimum barrier width

There is more than one way to calculate the required barrier width $L_b(L_w)$ as a function of the well width L_w. One may calculate the wavefunctions of the single well and conclude there is insignificant coupling when those of adjacent wells do not overlap for both carriers considered. Alternatively, the energy levels may be calculated for a multiple quantum well system for various barrier widths and the condition of no coupling is deduced when the evaluated energy levels for both the electron and the heavy-hole correspond to these of the single well. The method adapted by D. Atkinson was to calculate the absorption spectra of pairs of wells for varying barrier widths. The minimum required L_b is defined as that which results in spectra that do not deviate significantly from these of a single well. This may be viewed as a criterion of practical value rather than one of strict theoretical validity. We next need to decide upon the number of wells that will be used for the calculations as well as the electric field at which the calculations will be performed. In Table 7.2.A we present the calculated maximum energy separation between the energy levels that have resulted from the splitting as a function of the number of wells in the structure, for 50Å, 90Å, and 150Å wells. The total separation of the created levels does increase with increasing number of wells but it levels off quickly. Thus, since the effect is not dramatic, it is valid to perform the calculation for a pair of wells. Additionally, work on coupled wells [Atkinson *et al.*, 1990; Lee *et al.*, 1989] has shown that coupling effects are more prominent at zero field in symmetric structures (i.e. structures with the same well being repeated over and over) which is intuitively understood since coupling requires a certain degree of alignment of the individual energy levels. Thus we perform calculations of the absorption spectra of a pair of wells at zero electric field, for various separating barrier widths.

TABLE 7.2.A *The calculated maximum separation ΔE among the n=1 electron energy levels that are created due to coupling for different numbers of wells. ΔE increases as the number of wells is increased. The separation levels off for about 5 wells. The maximum separation for 10 150Å wells was computation limited.*

	2	3	4	5	10
50Å wells 65Å barriers	1.450meV	2.051meV	2.347meV	2.513meV	2.785meV
90Å wells 45Å barriers	1.458meV	2.062meV	2.359meV	2.525meV	2.789meV
150Å wells 25Å barriers	1.877meV	2.647meV	3.024meV	3.235meV	

Such spectra for 90Å wells are shown in Fig.7.2.2. The spectra correlate well with that of a single well when the barrier is larger than ≈40Å. Note that at a wavelength longer than the zero-field exciton peak, where a normally-on AFPM would operate, the biased spectra of a single well and of wells that are separated by barriers of $L_b \geq 40$Å are expected to correlate perfectly. Based on the calculations in Fig.7.2.2, a 45Å thick $Al_{0.3}Ga_{0.7}As$ barrier may be considered broad enough to prevent coupling from affecting the performance of an AFPM. Calculations performed in an identical manner for various well widths, yielded the values of L_b that are presented in Fig.7.2.3. Clearly, normally-off modulators, that operate at the vicinity of the unbiased heavy-hole exciton and rely upon the unbiased absorption peak, are more prone to coupling effects and thus require slightly larger L_b than these in Fig.7.2.3. The barrier widths in Fig.7.2.3 are notably lower than those commonly used and will therefore considerably reduce the operating voltages. Furthermore, based on the above, a fair comparison among wells of different widths may be performed.

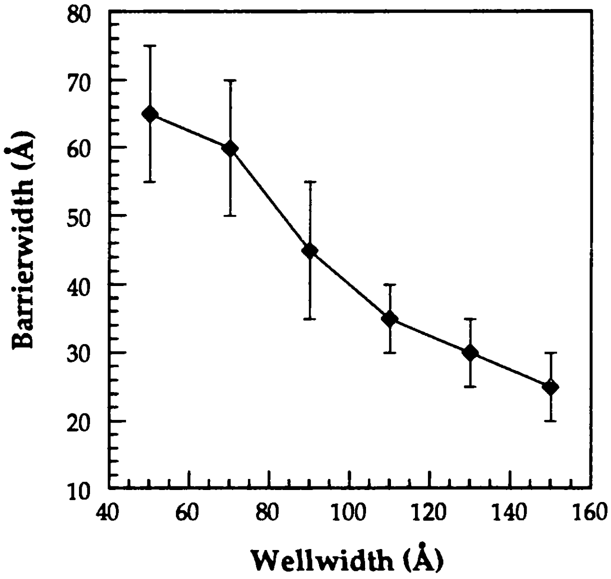

Fig.7.2.3 *Evaluated minimum barrier widths that are required to prevent coupling between adjacent wells.* $Al_{0.3}Ga_{0.7}As$ *barriers have been used.*

7.3 DETAILED STUDY OF TRADE-OFFS

From our study in the previous Chapters we may draw a few conclusions that mainly concern the effect of the Fabry-Perot cavity design upon the AFPM performance. Briefly we summarise these as follows:-

It has been shown that the FWHM of the Fabry-Perot (FP) resonance at the off-state is a measure of the overall tolerances of the device. The contrast associated tolerances may, in the case of a high contrast (>20dB) modulator, be best expressed by the 10dB-contrast bandwidth. This is directly related to the FWHM of the FP resonance and to the insertion loss. The finesse of the cavity is one of the factors that determine the FP-FWHM but has little other effect on the tolerances. For a given cavity finesse the FP-FWHM is maximised when the cavity length (meaning the separation between the two mirrors) is minimum. Increasing the front mirror (R_f) results in lower operating voltage (at a certain wavelength) while increasing the back mirror (R_b) has the opposite effect to an extent but it also dramatically lowers the insertion loss. The insertion loss is also decreased when operating (i.e. setting the FP resonant position) further from the zero-bias exciton in the case of a normally-on device, as the absorption coefficient α_0 of the on-state falls faster (exponentially) with wavelength than the maximum (biased) α_{max} does. Finally, one aims at high contrast devices and on-resonance operation in order to optimise the operating stability.

The above are implemented in the following. The design parameters are

TABLE 7.3.A. *Parameters used in the calculations of the biased-dependent absorption spectra, for all wells. The same parameters are subsequently used for the evaluation of the performance characteristics of AFPMs.*

MQW	
Well Material	GaAs
Barrier Material	$Al_{0.3}Ga_{0.7}As$
Barrier Width	Fig.7.2.3
Background Doping level	$1 \times 10^{15} cm^{-3}$
Built-in Voltage	1.4V
CAVITY	
Back-Mirror Reflectivity	99.8%
Intrinsic Buffer	200Å
Cavity Length (kept minimum)	odd # $\lambda/4$

shown in Table 7.3.A. Various front mirror reflectivities are used in the calculations, as shown in the graphs, and correspond to 0, 1, 2, 3 , and 4 periods of $Al_{0.1}Ga_{0.9}As/AlAs$ reflector stacks. Note that for small well widths, below 70Å, larger than 10% Al concentrations are required in the mirrors to ensure that the layer is not absorbing at the operating wavelength. Theoretical field-dependent absorption spectra have been used for the calculations as obtained from the model in Chapter 3. The spectra have been calculated specifically for different numbers of wells in the intrinsic region to

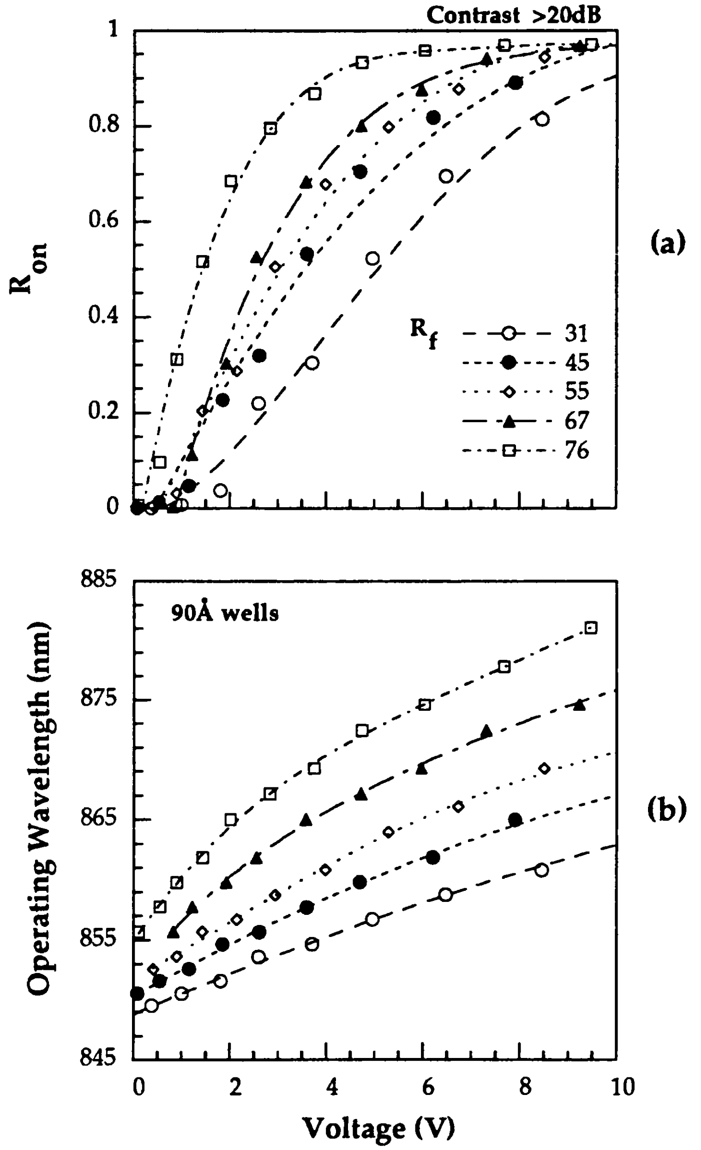

Fig.7.3.1 **(a)***The calculated on-state reflectivity R_{on} plotted versus the operating voltage of AFPMs with R_b=0.998 and various front mirror reflectivities. 90Å wells have been incorporated in the intrinsic region. See Table 7.3.1 for a list of design parameters.* **(b)** *The operating wavelengths that correspond to (a).*

deduce realistically broadened absorption features. In the case of large wells (>100Å) especially, the broadening caused by the field non-uniformity across the quantum well region becomes significant, while also the built-in field has a dramatic effect upon the unbiased spectra. A 200Å intrinsic region buffer has been used in all the designs which is in practice implemented to ensure low doping across the quantum wells. The cavity length has been kept minimum for all the designs, i.e. the shortest possible spacer-layer ($Al_{0.3}Ga_{0.7}As$) has been added to the multiple quantum well thickness in order to make the optical length equal to an odd number of quarter wavelengths at the operating wavelength each time.

In Fig.7.3.1a we plot the reflectivity of the on-state for high-contrast (>20dB, i.e. $[\alpha d]_c$ incorporated in the cavity) operation of modulators that incorporate 90Å wells. The reflectivity R_{on} is plotted as a function of the operating voltage for different front mirror reflectivities. The performance points have been obtained by setting the operation, and hence the FP resonance, at the wavelengths shown in Fig.7.3.1b. It is evident from Fig.7.3.1, that the insertion loss decreases while the operating voltage increases when the operation is set to longer wavelengths. The latter is a result of the combined effect of a) the higher electric fields that are required to attain the larger red-shifts, and b) the larger number of wells that are needed since the maximum

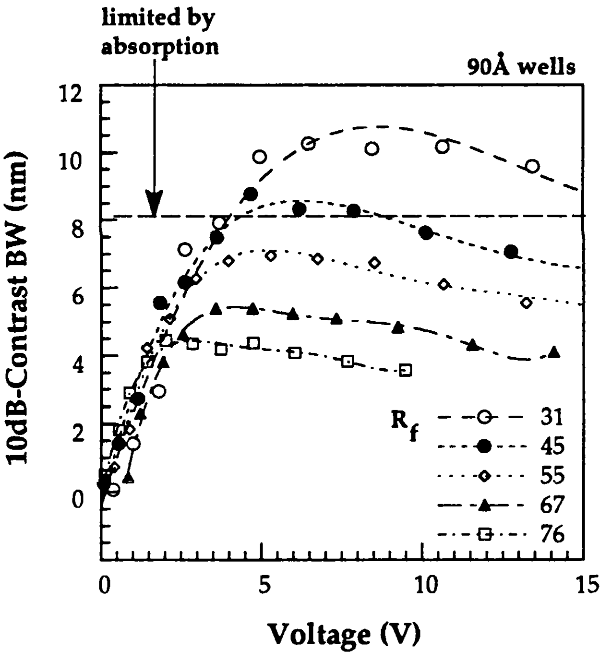

Fig.7.3.2 *Calculated 10dB contrast bandwidth corresponding to the operating points in Fig.7.3.1. See design parameters there and in Table7.3.A.*

absorption coefficient drops with field. Whereas low insertion loss, low voltage operation may be obtained by an increase of the front mirror reflectivity, the tolerances of the structure decrease with increasing finesse (Fig.7.3.2.). The 10dB contrast range has been calculated as the range where $R_{off} \leq 0.1R_{on}$ and upon the assumptions that i) the front and the effective-back mirrors are equal at the off-state, and ii) the on-state reflectivity is not wavelength dependent within the region on interest. This may be slightly underestimating the bandwidth in the general case. There is a limit to the 10dB bandwidth, however, inflicted by the quantum well absorption at the on-state (0V). This modifies the respective spectra as we discuss in section 7.4.

As a guide-line for comparison purposes, the 10dB-contrast of the first AFPM device in Chapter 2 is ≈5.5nm. A device with similar tolerances may be realised with 90Å wells by using 76% reflecting front mirror. This will operate at just below 5V with an insertion loss of just over 2dB. An unavoidable consequence of large finesse low

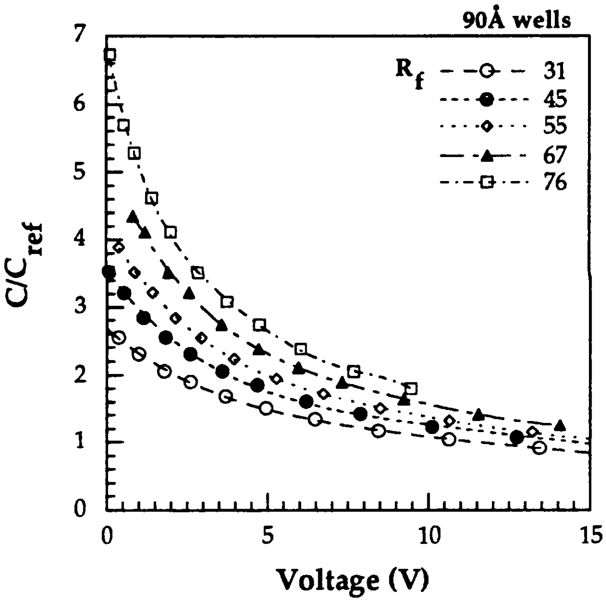

Fig.7.3.3 *The capacitance of the structures in Fig.7.3.1 and 7.3.2 expressed in multiples of a reference capacitance that corresponds to that of a device with 1μm of intrinsic region.*

voltage structures is the increased device capacitance. Indeed, the reduction of the operating voltage relies upon the incorporation of fewer wells in the intrinsic region to attain the required critical amount of absorber $[\alpha d]_c$ in the cavity. Consequently, the thickness of the intrinsic region is reduced. For a given device area, the capacitance is that of the corresponding parallel plate capacitor (Chapter 2), and thus it is inversely proportional to the thickness of the intrinsic region. The capacitance of the structures that correspond to the operating points in figures 7.3.1 -2 are plotted in Fig.7.3.3. The reference capacitance C_{ref} is that of a device of identical mesa area the intrinsic region of which is 1µm thick. This has been arbitrarily chosen as a reference value but it does correspond to the commonly used thicknesses while it is also roughly that of CB145 (Chapter 2). The capacitance drops when operating at longer wavelengths and thus larger voltages, since this implies a larger number of wells, as explained earlier when commenting on Fig.7.3.1.

Device performance for different well widths

The performance characteristics may be evaluated for different well widths in a manner identical to that used for the structures that incorporate 90Å wells above. The barrier widths in section 7.2 (Fig.7.2.3) are used in the multiple quantum well region.

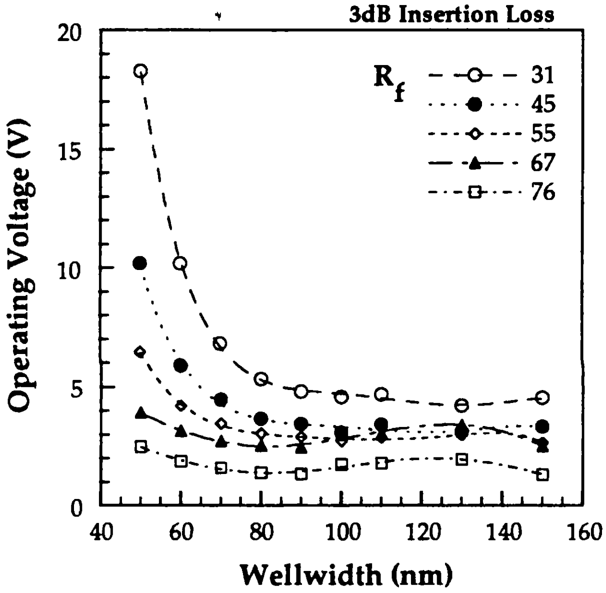

Fig.7.3.4 *Calculated operating voltage versus well width for >20dB contrast, 3dB insertion loss operation. The back mirror reflectivity is 99.8% and various front mirror reflectivity cases are shown. Design parameters are listed in Table.7.3.A.*

Extrapolation from the resulting data allows for a comparison among the different well widths. Thus in figure 7.3.4 we plot the operating voltage of >20dB contrast 3dB insertion loss modulators, as a function of the well width incorporated in the intrinsic region, at various front mirror reflectivities (see section 7.2.1). The optimum performance is obtained in the range of 80Å-150Å wells at all R_f. It was initially expected that large wells would yield the lowest operating voltages (and hence would be preferable) at high front mirror reflectivities. This intuitive prediction was based on the fact that the absorption spectra of large wells are significantly affected by broadening due to electric field variations across the quantum well region. Whereas, however, this effect is minimised when the intrinsic region is thinner, and hence at larger front mirror reflectivities, any improvement is offset by the increased built-in field resulting in these cases. The net result, therefore, is that the performance of wide wells (>100Å) becomes increasingly unfavourable at larger front mirror reflectivities

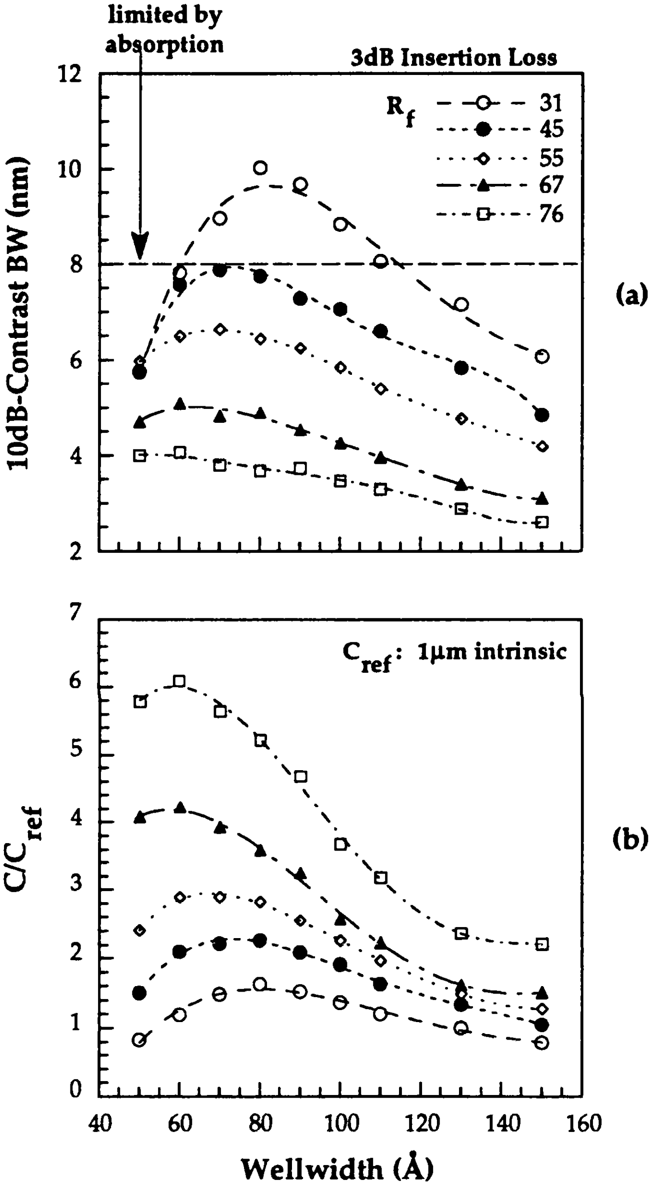

Fig.7.3.5 *Calculated 10-dB contrast band-width,*(a)*, and capacitance,* (b)*, corresponding to the operating points in Fig.7.3.4.*

by comparison to 80Å-100Å wells. Narrow wells (<70Å) on the other hand, show larger absorption coefficients that also retain their strength with field. However, the field-induced QCSE shifts are very limited while also the unbiased exciton peaks are

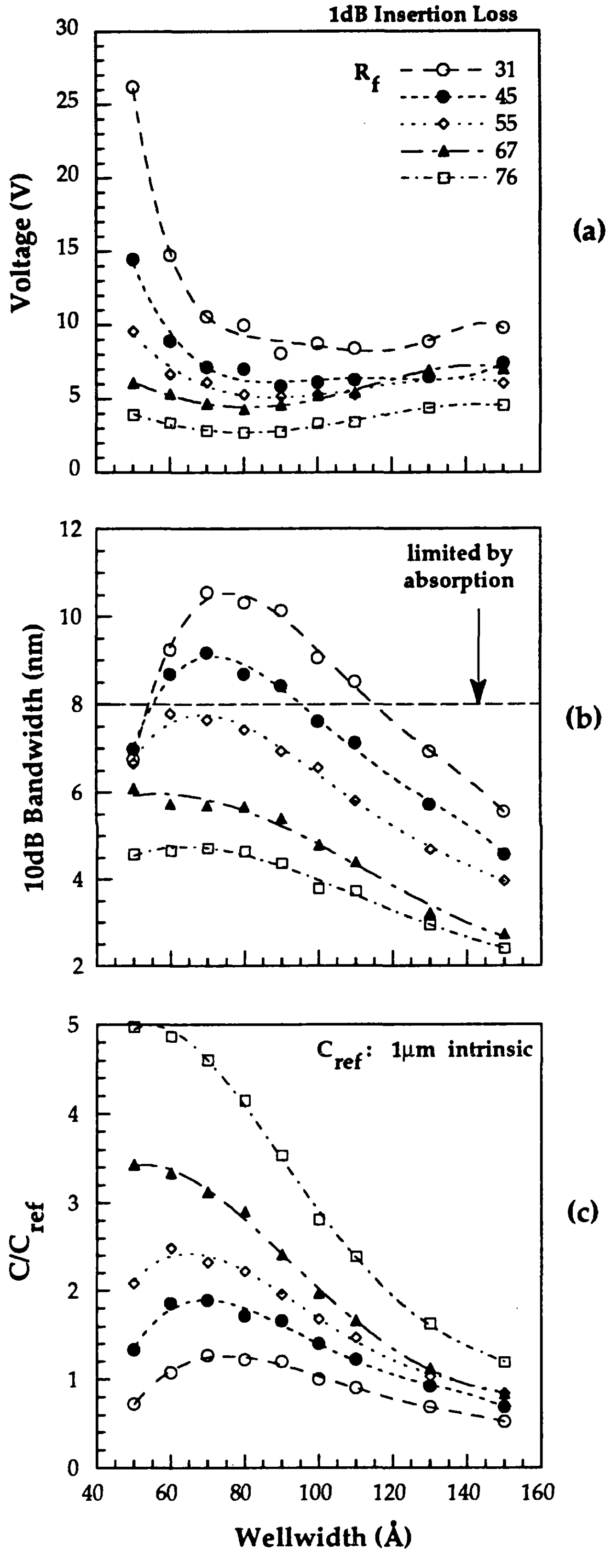

Fig.7.3.6 *Operation parameters at 1dB insertion Loss.*

broader. The latter necessitates a large exciton-FP resonance separation and thus operation at high fields. This, in conjunction with the required wide barriers, put narrow wells at disadvantage. Pezeshki *et al.* [1990] have claimed to have obtained an improved modulator performance as a result of the increased ratio α_{max}/α_0 of the maximum to minimum absorption coefficient for small wells (50Å in that case). In reality, the improvement was by and large due to the higher R_f and R_b used in that structure as compared to the first AFPMs by Whitehead *et al.* [1989b] and Yan *et al.* [1989]. Additionally, the relatively low barrier width (75Å), the operating wavelength having been shifted away from the zero-bias exciton peak, and the relatively low contrast of that structure, further contribute to the overall performance characteristics. It was also thought initially that well widths of around 130Å could possibly achieve an optimisation of the performance as a result of the maximum value of the change in absorption coefficient per unit field for these wells [Jelley *et al.*, 1989]. After the barrier width is taken into account, however, and detailed calculations are performed, the well widths around 90Å and above appear to yield lower voltage operation.

The 10dB contrast range of the same structures as these in Fig.7.3.4, are plotted in Fig.7.3.5a. This favours the well widths in the 70Å-90Å range depending on the finesse. Finally, the capacitance is minimised for large wells as their low absorption coefficients imply a wider intrinsic region (Fig.7.3.5b). Summing up the performance

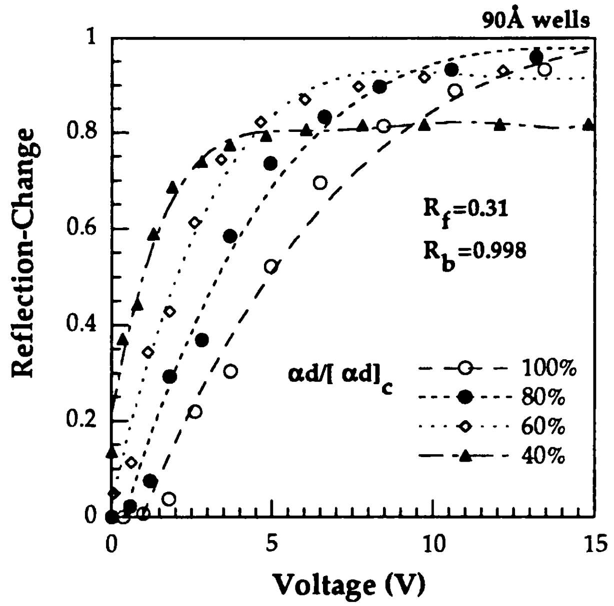

Fig.7.3.7 *Calculated reflection-change plotted as a function of the operating voltages for structures where different fractions of the critical absorber have been incorporated. 90Å wells have been used.*

characteristics, best results are obtained for well widths of around 90Å, that are the most commonly used.

commonly used.requirement that the insertion loss is 1dB for high contrast (>20dB) the plots in Fig.7.3.6 are obtained. As expected, the operating voltages are higher in comparison to those yielded from the corresponding designs for 3dB insertion loss. The 10dB-contrast bandwidths are marginally larger here due to the increased reflectivity of the on-state, and the capacitance is reduced since now the operation is at longer wavelengths (see Fig.7.3.1, 2).

In summary, very high contrast, low insertion loss operation may be obtained at considerably lower voltages than originally suggested by the performance of CB145 (Chapter 2). The trade-offs involved in the design of high contrast modulators have been clearly shown. Finally, according to our calculations, optimum overall characteristics are obtained around the commonly used 90Å wells.

Large reflection-change modulators

Although large reflection changes require both a low value of the off-state reflectivity R_{off} and a high value of the on-state reflectivity R_{on}, it is not obvious that the maximum reflection-change, at a fixed voltage, is attained when the critical amount of absorber $[\alpha d]_c$ is incorporated in the structure. Indeed, the reflectivity of an asymmetric FP cavity depends strongly on αd at small values of the latter but as the

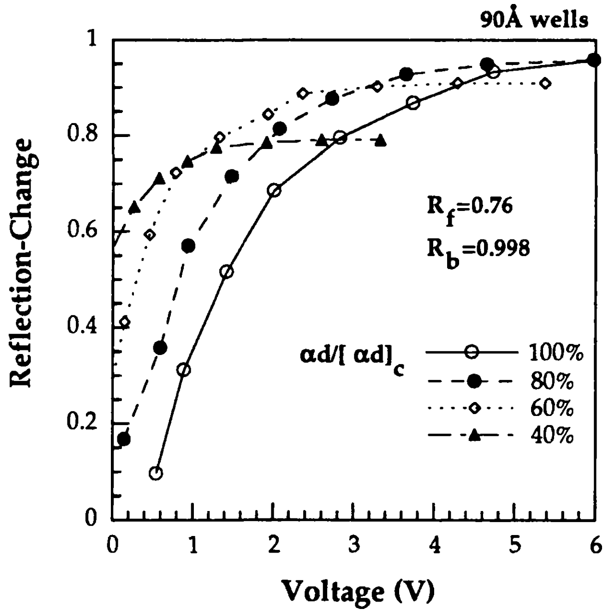

Fig.7.3.8 *Calculated reflection-change plotted against operating voltage for structures where fractions of the critical amount of absorber have been incorporated. 90Å wells have been used.*

effective finesse decreases with the incorporation of more absorber the derivative $\partial R / \partial(\alpha d)$ drops with αd until it becomes zero around $\alpha d=[\alpha d]_c$. This has already been discussed when evaluating the tolerances in Chapter 5. As a result, the incorporation of a fraction of $[\alpha d]_c$ in the cavity may have an insignificant effect on R_{off} while dramatically increasing R_{on} and hence may in fact increase ΔR.

In Fig.7.3.7 we plot the evaluated reflection-change as a function of the operating voltage for 90Å wells and a cavity with $R_f=0.31$ for different amounts of absorber in the cavity. At relatively low voltages, ΔR increases with decreasing $\alpha d/[\alpha d]_c$ until the incorporated αd is not sufficient for a substantial reduction of the off-state reflectivity and thus the reflection-change drops. Higher voltage operation corresponds to operating wavelengths where the absorption coefficient α_0 at the on-state is very low and therefore there is no improvement when the absorber αd is reduced. Clearly, the cause of the increasing ΔR with decreasing $\alpha d/[\alpha d]_c$ is the

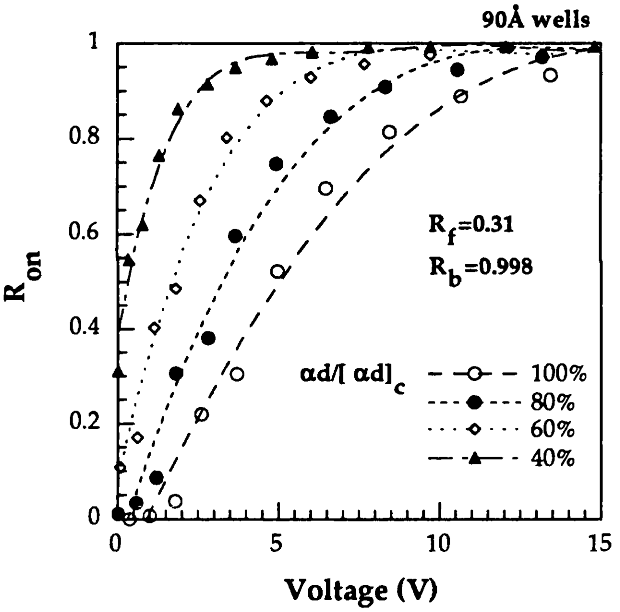

Fig.7.3.9 *The reflectivity at the on-state that corresponds to the operating points in Fig.7.3.7.*

reduced insertion loss, shown in Fig.7.3.9. Similar characteristics are observed for the case where the front reflectivity is R_f=0.76 (Fig.7.3.8), albeit at operating voltages scaled down in comparison to previously. In general, the effect should be (marginally) less profound for larger values of R_f. Finally, the reflection-change associated tolerances increase, slightly, when the incorporated relative absorber is reduced, for two reasons:- a) assuming a certain maximum reflection-change, the bandwidth is larger for the case with the higher R_{on} and thus for the case when $\alpha d/[\alpha d]_c<1$, b) the cavity length is reduced with decreasing $\alpha d/[\alpha d]_c$. The capacitance is, however, larger by a factor corresponding to the relative decrease of the intrinsic region thickness.

Thus, at a certain voltage, better reflection-changes are obtained when the incorporated absorber is a fraction of the critical absorber that is required to make the off-state reflectivity zero. It should be noted that the maximum possible reflection-change obtained by a given mirror design, is attained when operating far from the unbiased exciton peak, to increase the on-state reflectivity R_{on}, and incorporating the critical $[\alpha d]_c$, to minimise R_{off} (=0). The operating voltage is, however, very high in that case.

Summary

In this section we have evaluated the achievable performance of normally-on AFPM devices that use GaAs/$Al_{0.3}Ga_{0.7}As$ quantum wells. This establishes a thorough understanding of the limitations in the modulator characteristics of such devices and facilitates the design of useful structures.

Pezeshki *et al.* have also attempted an optimisation that addressed the mirror design solely [1991b] but have assumed a back mirror reflectivity equal to 1. The direct effect of the front mirror upon the insertion loss becomes immaterial in that case (Chapter 6) and thus erroneous conclusions are drawn. We have assumed a realistically high, realisable, back mirror reflectivity (0.998) in our calculations. The work of a colleague, Roya Mottahedeh (private communications), on power saturation effects on AFPMs has highlighted that the reflectivity of the mirrors may be diminished at high optical powers as the generated photocarriers enhance the free-carrier absorption in the layers that comprise the stack. This ought to be further investigated for the cases where high powers are intended to be used.

The background doping has been assumed $1 \times 10^{15} cm^{-3}$ here, which is a currently realisable value. Far lower (10^{14}) background dopings have been reported [Amano *et al.*, 1991]. These would lead to sharper excitonic absorption peaks and would thus allow for even lower voltage operation.

7.4 SPECIFIC NORMALLY-ON AFPM DESIGNS

It is clear from our study in the previous section that there is no unique recipe for the perfect modulator. Indeed, some modulator characteristics have to be traded-off to obtain the optimum performance for a specific application (see also Chapter 2). In this section we proceed to examples of modulator designs where certain performance characteristics have been optimised. Some design parameters, that are common to all structures, are listed in Table 7.4.A. We have chosen to omit a top GaAs capping layer that would cause a slight deterioration of the performance. In practice such a layer could be grown initially and etched-off the optical window of the device after metallisation.

TABLE 7.4.A. *Design parameters that are common to all the structures presented in this section.*

Well	90Å GaAs
Barrier	45Å $Al_{0.3}Ga_{0.7}As$
Intrinsic Buffer	200Å
Spacer Layer	$Al_{0.3}Ga_{0.7}As$
Reflector Stack	HLHL...H
H	$\lambda/4$ $Al_{0.1}Ga_{0.9}As$
L	$\lambda/4$ AlAs

Low voltage, low insertion loss, high contrast modulator

For this structure, operation away from the zero-bias exciton and use of a large back mirror reflectivity allow for low insertion loss operation, while also the use of a large front mirror (≈76%) results in low operating voltage. The epitaxial structure is shown in Fig.7.4.1 with details of layers listed in Table 7.4.A. The reflectivity spectra are calculated using the model in Chapter 3, and shown in Fig.7.4.1. Contrast in excess of 20dB is achieved at 2.75V reverse bias and with an insertion loss of 0.6dB. The 10dB contrast bandwidth is ≈4nm (inset, Fig.7.4.1) which is lower than the 5.5nm of CB145 in Chapter 2, but arguably comparable. This characteristic, which denotes the good contrast associated tolerances, is a result of the short cavity length and, equally importantly, of the larger on-state reflectivity of this device. The parameter that is significantly deteriorated, however, is the capacitance which is $\approx 3.5C_{ref}$ for this design compared to $\approx 0.87C_{ref}$ for CB145. The overall performance is by far superior to that of CB145. Although lower voltage operation may be obtained (Fig.7.31,4,6), this design is probably a good compromise in terms of the estimated tolerances and the capacitance of the resulting device.

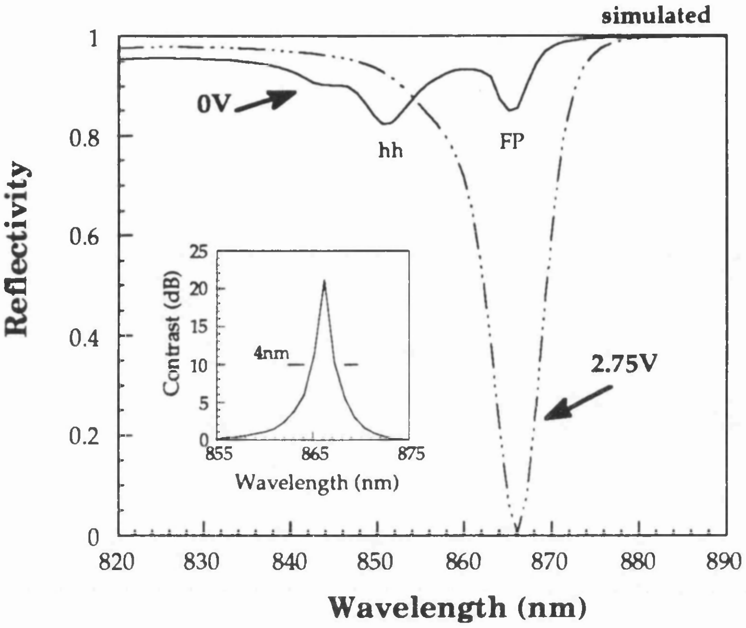

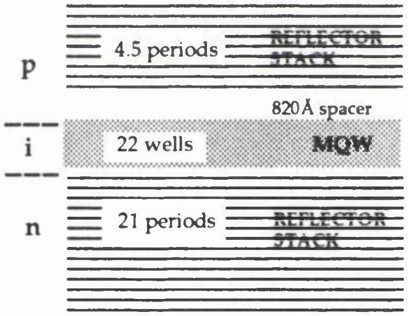

Fig.7.4.1 *Calculated reflectivity and contrast ratio (inset) spectra for the epitaxial structure shown schematically on the left. For design details see Table.7.4.A.*

Low insertion loss, high contrast modulator with good tolerances

Despite the fact that the cavity length may be further shortened when using high reflectivity front mirrors (Chapter 6), the tolerances are maximised for low front mirror structures (Fig.7.3.2). We present here an example of a high contrast low insertion loss modulator with good contrast associated tolerances. The epitaxial structure is schematically shown in Fig.7.4.2 and so are the calculated reflectivity spectra. Contrast in excess of 20dB and insertion loss of ≈0.45dB are obtained while the 10dB contrast bandwidth is ≈7nm. However, the operating voltage is now 12V, which is well in excess of that of CB145 and indeed far too high for compatibility with common electronic circuitry (Chapter 2). The capacitance of this structure is $\approx C_{ref}$. It is interesting to note how the 10dB contrast BW is limited by the excitonic absorption at the on-state. Although the off-state resonance is very broad, the obtained BW is

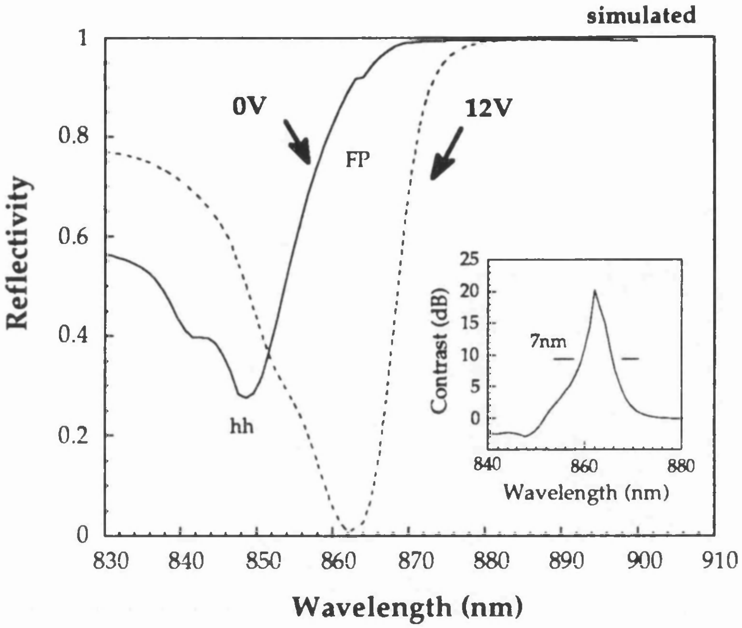

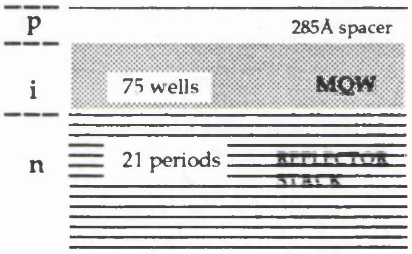

Fig.7.4.2 *Calculated reflectivity and contrast ratio (inset) spectra for the epitaxial structure shown schematically on the left. For design details see Table.7.4.A.*

relatively low as a result of the accordingly broadened on-state resonance. This extends, as a result, to the excitonic absorption peak and thus leads to a reduction of the zero-bias reflectivity at wavelengths to the left of the resonance. Larger well widths are affected to a lesser extent as stemming from their sharper (unbiased) excitons and the fact that the operation may be set to larger exciton-FP separations without a dramatic increase of the required number of wells.

A modulator with identical contrast tolerances to these of CB145

This design is similar to the very first we presented in this section. The aim here is to obtain identical tolerances to these of CB145 with a marked improvement in other parameter characteristics. The structure, shown in Fig.7.4.3, incorporates a 67% reflecting front stack. High contrast (>20dB) operation is exhibited at 5V with an insertion loss of just below 1dB. The 10dB contrast bandwidth is ≈5nm, i.e. close to that

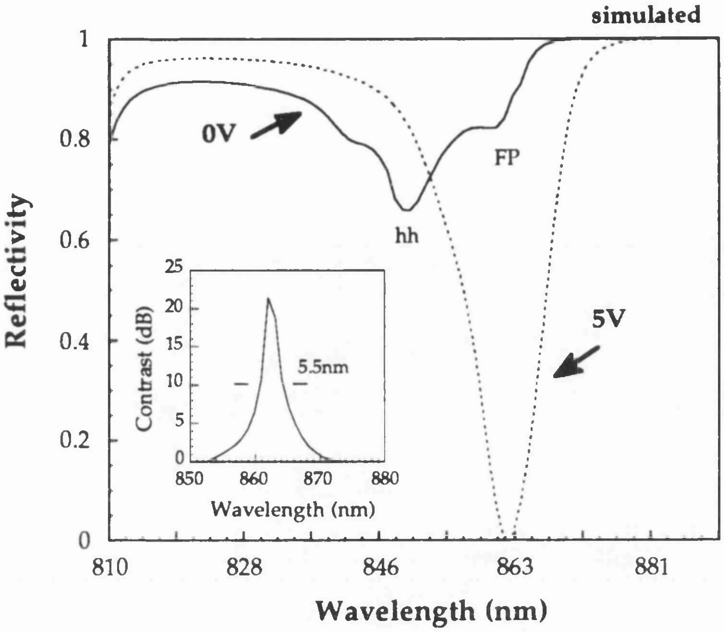

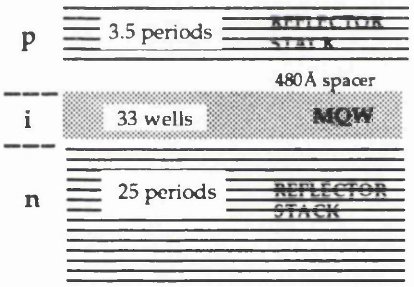

Fig.7.4.3 *Calculated reflectivity and contrast ratio (inset) spectra for the epitaxial structure shown schematically on the left. For design details see Table.7.4.A.*

of CB145. The capacitance of this structure, however, is increased to ≈2.3C_{ref}.

Large reflection-change modulator

As discussed in the previous section, optimum large reflection-change designs are not necessarily the high contrast designs. Here we present a large reflection-change device (Fig.7.4.4). The mirror design is identical to the first structure in this section but fewer wells are incorporated. The net reflection-change is ≈90%, which is larger than that of the modulator in Fig.7.4.1 at the marginally lower voltage of 2.5V. The insertion loss is decreased to 0.36dB and, very importantly, the wavelength range over which the reflection-change is above 50% is 6.5nm. One should note that the *maximum* reflection-change of CB145 is ≈45%. Also, for comparison, the respective range for the structure in Fig.7.4.1. is 6nm. There is no dramatic improvement attained by the present design as compared to the one in Fig.7.4.1. This is because very large front mirror reflectivities are involved in these designs and also the operation is relatively far from the zero-bias exciton where the on-state reflectivity is not really limited by the absorption. Nonetheless, the current design is specifically optimised with large reflection-change applications in mind.

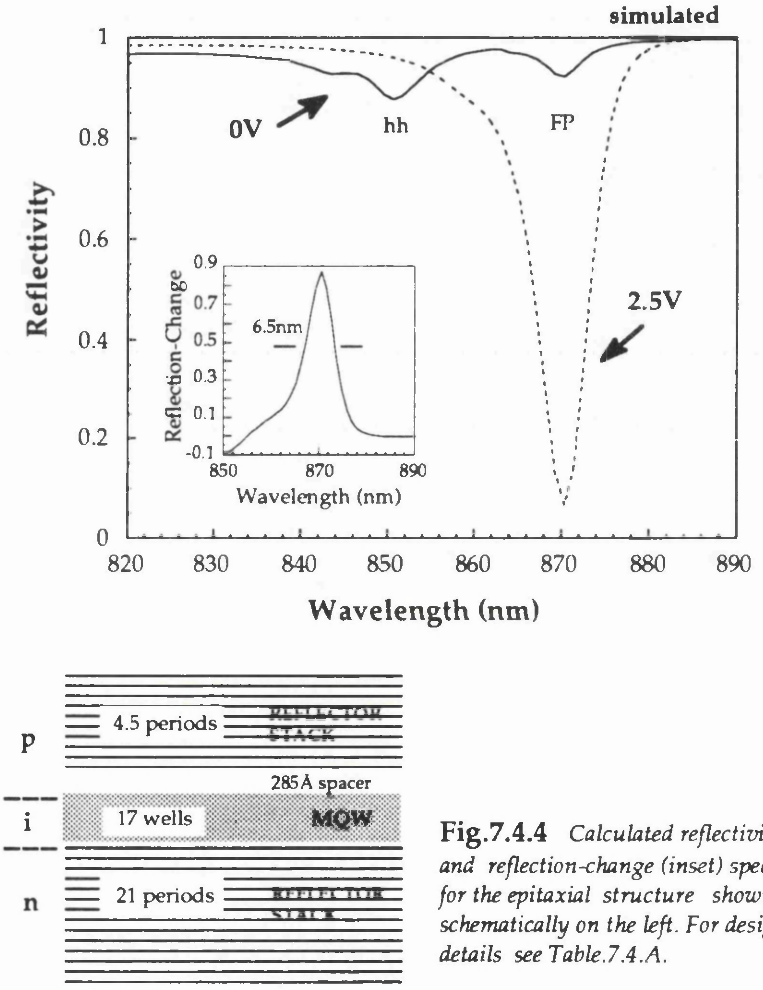

Fig.7.4.4 *Calculated reflectivity and reflection-change (inset) spectra for the epitaxial structure shown schematically on the left. For design details see Table.7.4.A.*

Comments

High speed operation requires low RC time constants (Chapter 2). Whereas we have taken the capacitance into account in this study, it is also important to minimise the contact resistances. The reflector stacks give rise to an unwanted increase of these. Graded interfaces offer a way round this problem, as has been shown by work on surface emitting lasers [see for example Sugimoto *et al.*, 1992]. Additionally, the bottom contact should preferably be deposited on top of the bottom stack to virtually eliminate this difficulty [Barron *et al.*, 1992]. The designs we present here would not allow for the appropriate processing step to take place, since the quantum wells are assumed directly on top of the respective stack. The implication on modified designs that would accommodate this, is the inclusion of additional layers between the quantum wells and the bottom Bragg stack. The resulting longer cavity lengths would lead to a deterioration of the tolerances and would further favour low front mirror structures in that respect. Indeed, the additional cavity length, required for contacting on top of the back mirror, has clearly a more profound effect on the smaller cavity structures. Finally, the increase of the top contact resistance caused by the front semiconductor reflector stacks, may be overcome by the implementation of dielectric front mirrors (Chapter 2).

Finally, we ought to point out at this point that the evaluated design performances are subject to the limitations of the model discussed in Chapter 3.

7.5 CONCLUSIONS

In this chapter we have concluded the design of normally-on AFPM devices that use GaAs/$Al_{0.3}Ga_{0.7}As$ quantum wells. The trade-offs among the various performance characteristics have been studied quantitatively based upon modelled absorption spectra for this quantum well material. It is evident that devices far superior to the original CB145 (Chapter 2) and to those presented in Chapter 6 may be realised. The operation of the modulators may be tailored to suit the requirements of specific implementations and examples of such designs have been presented.

Different workers (section7.3) have suggested that narrow wells are preferable due to their larger α_o/α_{max} values. It also appeared possible that wells of around 130Å might be preferable as a result of their maximum change in the absorption coefficient per unit field (section 7.3). After a full optimisation for different well widths we have concluded that optimum performance is in fact obtained, for normally-on AFPM structures, by the commonly used 90Å wells. It should be noted, however, that alternative well widths may be favoured for operation at a target wavelength.

There is scope for further investigation in the use of alternative aluminium concentrations in the barrier. Larger Al concentrations yield higher absorption coefficients [Pezeshki *et al.*, 1992a] and require smaller barriers, thereby attaining lower operating voltages. On the other hand, the carrier escape out of the wells is faster when the Al concentration is reduced [Fox *et al.*, 1990]. This is very important for SEED devices (Chapter 8) but is not critical for modulators. It may, however, become significant when high power, high speed operation is aimed for since a direct result of the faster carrier sweep-out is an increase of the saturation intensities. Our work may be extended in that direction. Additionally, the conclusions of this study should offer valuable guidance for the optimisation of AFPM devices in other III-V material systems, such as InGaAs/GaAs or InGaAsP/GaAs, as well as for such devices in II-VIs or Si/Ge. Finally, some of the insights gained are also applicable to normally-off AFPM devices (Chapter 8).

CHAPTER 8: THE SYMMETRIC CAVITY ELECTROABSORPTION MODULATOR

8.1 INTRODUCTION

In this Chapter we present another class of MQW electroabsorption modulators where, in contrast to the asymmetric Fabry-Perot modulator, the Fabry-Perot cavity is symmetrical. We call this the 'symmetric-cavity-electroabsorption-modulator' (SCEM) in order to distinguish it from the symmetrical structures where the electrorefractive effects are used to shift the position of the FP resonance [Simes *et al.*, 1988].

Firstly, we discuss the principle of operation of SCEMs and introduce the trade-offs involved in the performance characteristics. Experimental results from two different devices are presented and compared to modelled spectra. Subsequently, we refer to the tolerances of such structures and show how the tolerances may be improved using a double-cavity configuration. SCEMs offer certain advantages in the normally-off mode, as compared to other types of modulators. This makes them potentially useful for SEED operation. We consider this possibility starting from a study of the limitations of normally-off AFPMs. Subsequently, we give a brief account of the parameters that affect SEED operation and proceed to demonstrate a symmetric-SEED using SCEMs. The relative merits and disadvantages of SCEMs are given a short note at the end of this Chapter.

8.2 OPERATION OF THE SYMMETRIC CAVITY ELECTROABSORPTION MODULATOR

The absorber αd incorporated in a Fabry-Perot (FP) cavity controls the effective back mirror reflectivity, as described by the expression $R_b^{eff}=R_b e^{-2\alpha d}$, where R_b is the back mirror reflectivity, α the absorption coefficient and d the thickness of the absorbing material respectively. This holds irrespective of the specific mirror design. A cavity where the front and the back mirror reflectivities are equal, i.e. a symmetric mirror structure, is balanced with no absorber incorporated. Note that when the two mirrors are equal the total reflectivity of a FP cavity is zero. Contrary to the asymmetric case, the absorber incorporated in such a cavity serves to unbalance the cavity by means of an effective reduction of the back reflectivity, thereby causing an increase of the total reflectivity.

The on-resonance reflectivity of an FP cavity with $R_f=R_b$ is plotted in Fig.8.2.1 as a function of the incorporated absorber for different mirror values. As R_b^{eff} is reduced with increasing αd, the total reflectivity R tends to that of the front mirror R_f. The equations governing the FP operation are identical to those presented in Chapter 2. In Fig.8.2.2 we plot the reflectivity R as a function of R_b^{eff} for various front reflectivities R_f. Here both the AFPM ($R_f<R_b$) and the SCEM operation are included.

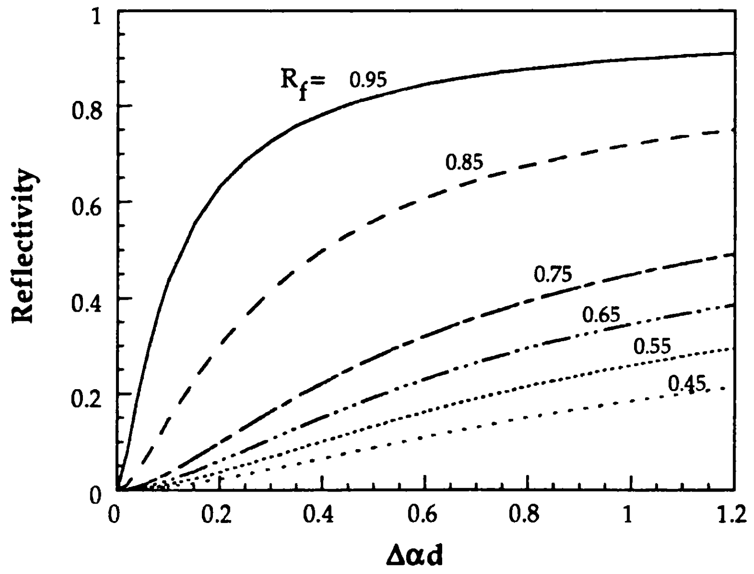

Fig.8.2.1 *The reflectivity of a Fabry-Perot cavity with equal front and back mirrors plotted against the amount of absorber incorporated in the cavity.*

Clearly, the incorporation of MQWs in a symmetric structure will yield a voltage induced modulation of the reflected intensity. SCEM devices exhibit the reverse function of that obtained by AFPMs at a certain wavelength, since in the case of SCEMs an increase of the absorber yields an increase of the reflectivity (Fig.8.2.1 and 8.2.2). As a result, operation at a wavelength longer than the zero-bias exciton peak gives rise to normally-off operation, i.e. a bias-reflecting device, whereas similarly operation at the vicinity of the exciton peak results in normally-on operation, i.e. a reduction of the reflectivity with bias. As was the case with AFPM devices, an integrated MQW SCEM may be realised using Bragg reflector stacks as integrated mirrors (Chapter 2). Our discussion concerning the imposed difficulties, design considerations, and the possibility for dielectric front mirrors apply here as well. In practice, the fact that the minimum absorption coefficients of MQWs may be non-zero at the chosen operating wavelength alters the mirror design. The front mirror reflectivity has to be slightly lower than the back mirror ($R_f<R_b$) in order to attain a balanced cavity at zero volts, i.e. low off-state reflectivity.

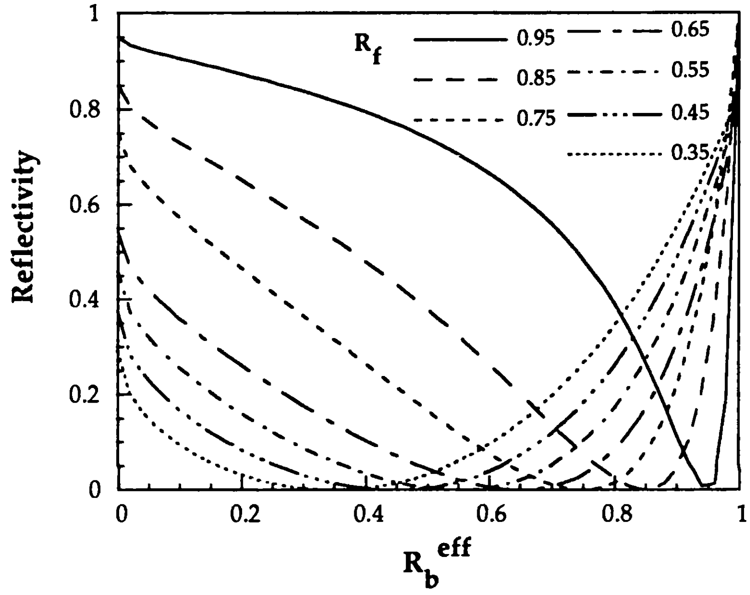

Fig.8.2.2 *The reflectivity of a Fabry-Perot cavity plotted against the effective back mirror reflectivity for various front reflectivities. Both the AFPM and the SCEM cases are included.*

Let us first examine the effect of the mirror design upon the modulation characteristics of an SCEM. For this we use the experimental absorption modulation values from a 95Å well sample (see Fig.5.3.3) Aiming at large reflection changes we choose $0.7<\alpha d<1$, as is implied necessary by Fig.8.2.1. In Fig.8.2.3 we plot the evaluated

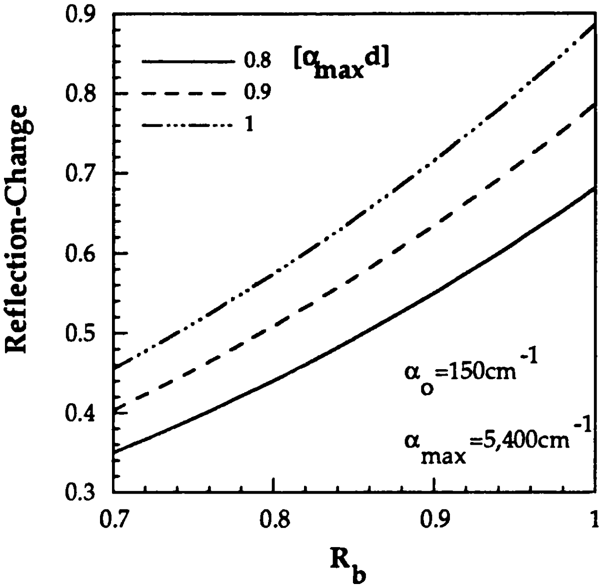

Fig.8.2.3 *The reflection-change attained by a SCEM plotted against the back mirror reflectivity for various values of the amount of absorber that is induced into the cavity upon the application of a field. A field of 96kV/cm and 95Å GaAs wells with* $Al_{0.3}Ga_{0.7}As$ *barriers are assumed (Fig.5.3.3).*

reflection-change ΔR as a function of R_b. Fixed values have been used for the minimum and maximum absorption coefficients taken from experimental results. The values, noted in the inset of the figure, correspond to operation at 96kV/cm (at 866nm) of 95Å wide GaAs wells with $Al_{0.3}Ga_{0.7}As$ barriers (CB308, Fig.5.3.3). The front reflectivity is calculated such that $R_f=R_b^{eff}$ at zero volts. The attained reflection-change is increased when moving farther from the zero-bias exciton peak; indeed operation 4nm to shorter wavelengths shows a maximum ΔR of 70% when the rest of the parameters are left the same as in Fig.8.2.3. It is evident from Fig.8.2.3 that ΔR is increased with increasing mirror reflectivities. It may be seen that large reflection changes (90%) may be attained, albeit at high voltages.

Before proceeding any further, it is useful to note the following. Normally-on SCEM operation is exhibited, as mentioned above, at the vicinity of the zero-bias exciton where the absorption modulation is limited. As a result, poor characteristics are obtained by such devices. Considering the excellent modulation characteristics that may be obtained by a normally-on AFPM, as those have been studied in the previous Chapters and especially Chapter 7, the performance of a normally-on SCEM compares unfavourably. On the other hand, normally-off AFPMs, that have to operate at the vicinity of the heavy hole exciton, exhibit very large insertion loss and moderate reflection changes (section 8.5) so that SCEMs may offer a possibility for improvement in this case. Thus the primary interest in SCEMs is in normally-off structures. Another point to be made regards the tolerances of SCEMs which are discussed in section 8.5. However, it is important to note at this stage that the off-state of such devices is one of high finesse both in absolute terms, since low mirror reflectivities result in limited ΔR (Fig.8.2.3), and in comparison to the on-state where one of the mirrors is effectively reduced by the absorber. Note that the tolerances of the off-state determine the contrast-associated tolerances (Chapter 5). Consequently, the tolerances of the off-state are indeed limited and therefore it is impractical to aim at high contrasts using SCEMs. Large reflection changes are, however, attainable. In accordance to the above, we will concentrate upon normally-off SCEMs aiming mainly at low insertion-loss, large reflection change operation.

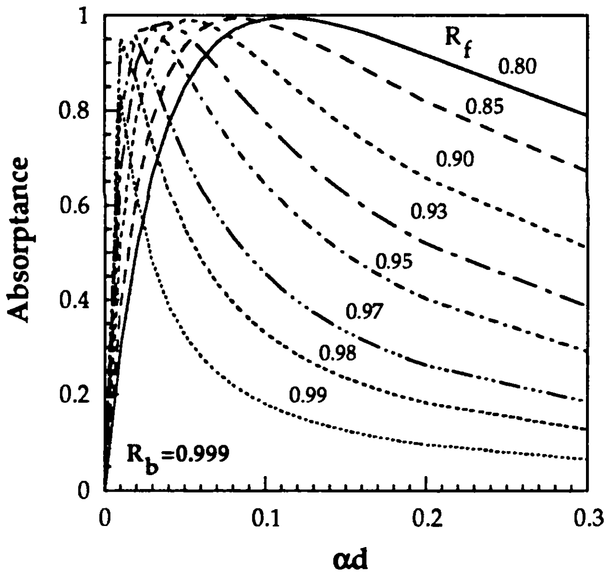

Fig.8.2.4 *The absorption of a SCEM plotted against the absorber incorporated in the cavity for various front reflectivities. A fixed large value has been used for the back mirror as was implied from Fig.8.2.3.*

A possible incentive for such devices is their application in SEED configurations. Thus another important performance parameter is the negative differential resistance (NDR) that is a precondition for SEED operation. This is directly related to the current and thus to the absorptance A. The dependence of the modulation of the absorptance A upon the mirror design of SCEMs is shown in Fig.8.2.4. At low values of αd both R_f and R_b^{eff} are high. The resulting large cavity-efficiency leads to high absorptance at low values of αd. As αd increases R_b^{eff} is reduced and so is the cavity efficiency (Chapter 2) so that the absorptance actually drops. The corresponding curves for the reflectivity R are shown in Fig.8.2.5. A few interesting points may be drawn from figures 8.2.4 and 8.2.5. Firstly, it is evident that small modulation of the absorber αd yields a considerable ΔR and ΔA in the case of large front reflectivities R_f. The drawback is that the amount of absorber that results in a well-defined off-state is indeed restricted to a very narrow range of values. This reflects the difficulties imposed upon the design and also the low tolerances associated with such structures. These are relaxed for lower front reflectivities. At the same time though, the amount of absorber required to raise the reflectivity by a significant degree is considerably increased, often to an impractical amount. Another point is that the amounts of absorber that result in maximum ΔA and maximum ΔR for a given mirror design do not absolutely coincide. This, in the case of large mirror reflectivities, may mean that large ΔA and ΔR may not be obtained simultaneously.

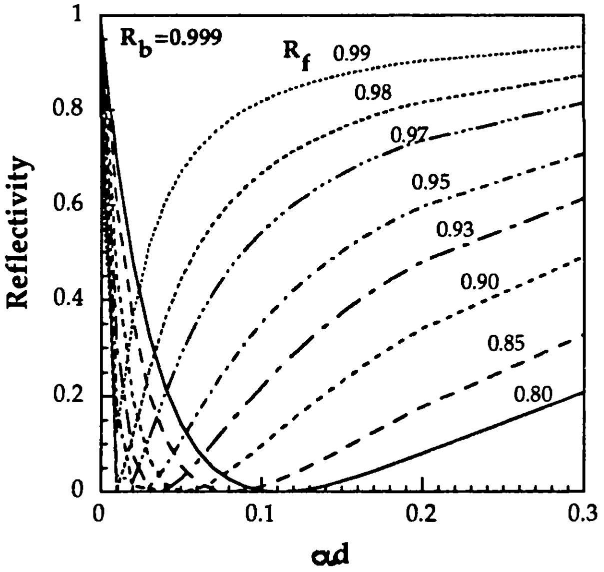

Fig.8.2.5 *The reflectivity of a SCEM plotted against the amount of absorber incorporated in the cavity for the same mirror values as in the previous figure.*

8.3 EXPERIMENTAL RESULTS

8.3.1 QT153 SCEM.

Epitaxial structure

As a first attempt at a SCEM we designed a structure to yield large-ΔR operation at moderate voltages. The epitaxial structure is shown in Fig.8.3.1. The back mirror consists of 17.5 periods of HL with an estimated reflectivity of ≈99% and the front of 8.5 periods yielding an estimated 92% reflectivity. The 55Å barrier width is well above the minimum value required for no inter-well coupling (Chapter 7).

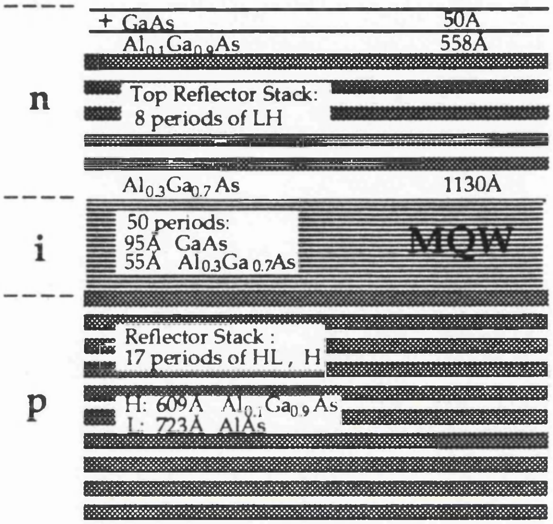

Fig.8.3.1 *A schematic of the epitaxial structure of QT153 grown by MOCVD at the University of Sheffield.*

Experimental results

Reflectivity spectra from QT153 are shown in Fig.8.3.2. A reflection change of 35% is obtained under 5V reverse bias at ≈852nm. The insertion loss is ≈0.86dB. These results do show the principle of operation but otherwise they are unimpressive. Modelled results and discussion on the possible cause of the diminished performance are presented later on in this section. The heavy hole exciton is obtained at ≈846nm suggesting a well width of ≈84Å. As bias is applied the heavy hole appears at first as a local minimum (up to 2 Volts). With the exciton approaching the resonance the reflectivity increases, its peak at the vicinity of the resonance being now at the position of maximum αd. Thus the heavy hole is in fact a local maximum in the spectra at 3V and beyond. One important feature is the evident voltage-induced shift of the FP resonance. We have already discussed (Chapter 2) the effect of electrorefraction upon the position of the FP wavelength. The cavity finesse has been seen to leave this shift unaffected (Chapter 5). The shift is dependent upon a) the proportion of absorbing material within the total cavity length which determines the relative change of the optical length, b) the well width since this governs the MQW electrorefraction (Chapter 2), and c) the wavelengths involved since the magnitude and sign of these effects are wavelength dependent. However, although the mirror design does not affect the magnitude of the shift, the impact on the modulation characteristics is far greater in the case of high finesse cavities resulting from the fact that the wavelength range over which large modulation may be obtained is severely restricted. It appears therefore that the electrorefractive effects ought to be taken into account in the modelling of such devices in order to get a full picture of the modulation spectra.

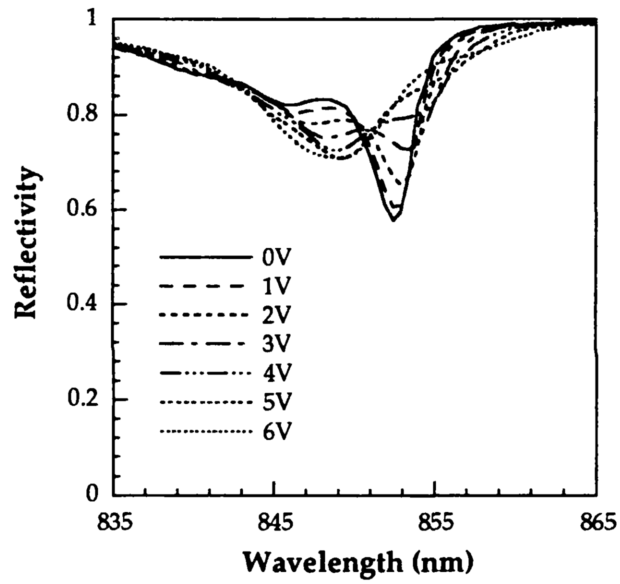

Fig.8.3.2 *Reflectivity spectra at different reverse bias voltages obtained from a device off QT153.*

Scaled photocurrent data are presented in Fig.8.3.3. The scaling (section 2.3.2) was performed at ≈750nm where absorption and photocurrent measurements on similar MQW material show no change with bias. The features clearly correspond to those in the reflectivity spectra explained previously. The internal quantum efficiency of this particular structure was rather poor as deduced from the fact that the photocurrent increases with bias at ≈750nm. From that the internal quantum efficiency at 0V may be estimated to be about 70% of its maximum value at higher voltages. This is quite important for SEED operation as it limits the responsivity of the device at low

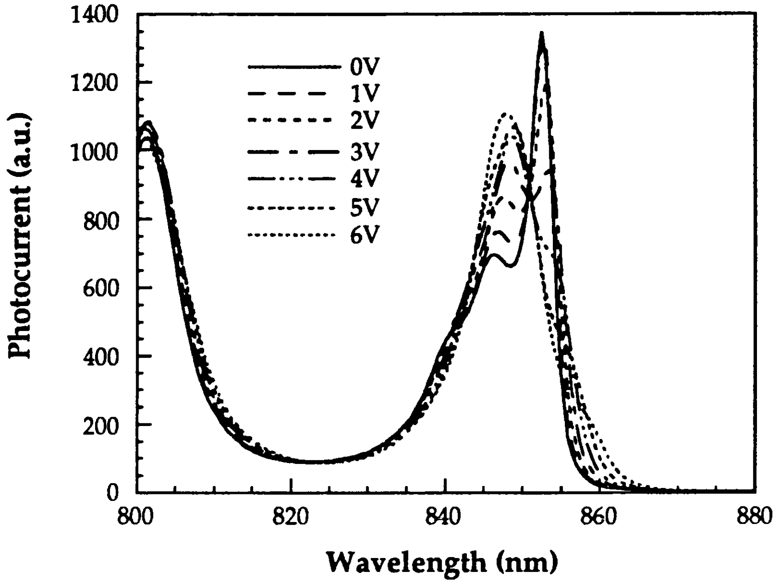

Fig.8.3.3 *Photocurrent spectra at different reverse biases obtained from the same device off QT153 as in the previous Fig.8.3.2. The data have been scaled with respect to one other at 750nm.*

voltages, reducing thereby the negative differential resistance. Note, however, that the internal quantum efficiency is associated with the quality of the grown material and also with the well and barrier widths and Al compositions [Fox *et al.*, 1990]. It is thus independent of the existence of a FP cavity. A more detailed discussion on the application of SCEMs in SEEDs is presented in section 8.5.

Modelled spectra

The electrorefractive effects of MQW material are included when modelling SCEM spectra so as to obtain realistic evaluations. The refractive index of MQW material under bias (inclusive of the zero-bias case) may be deduced from that of bulk GaAs by use of the Kramers-Krönig relations. For this, it is required to know the absorption spectra of both bulk GaAs and MQW material (Chapter 2). In the following calculations we use bulk GaAs refractive index data from Sell *et al.* [1974] and absorption spectra of lightly doped GaAs from Sturge [1962]. Experimental absorption data are required for these spectra calculations since the modelled spectra do not include high-order excitonic transitions and would as a result induce a considerable error in the calculated refractive index change. Absorption data from a 95Å well sample were obtained from photocurrent spectra using the method described in

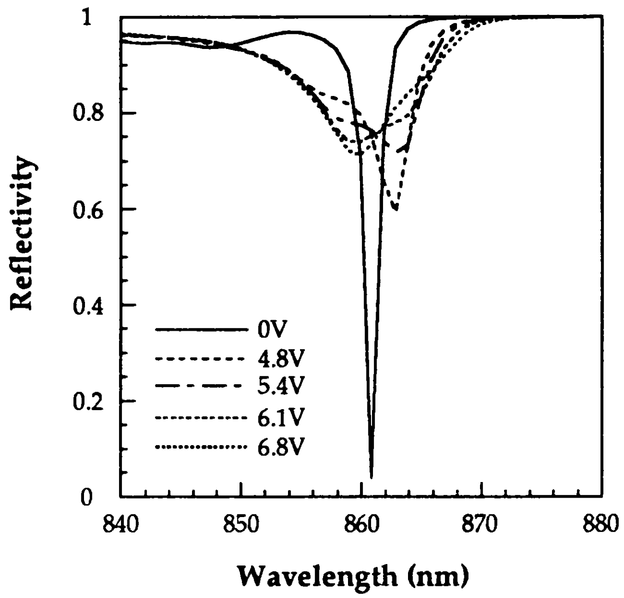

Fig.8.3.4 *Modelled reflectivity spectra for the nominal structure of QT153 (Fig.8.3.1). Experimental absorption spectra from 95Å wells have been used for the calculation. The electrorefractive effects are included.*

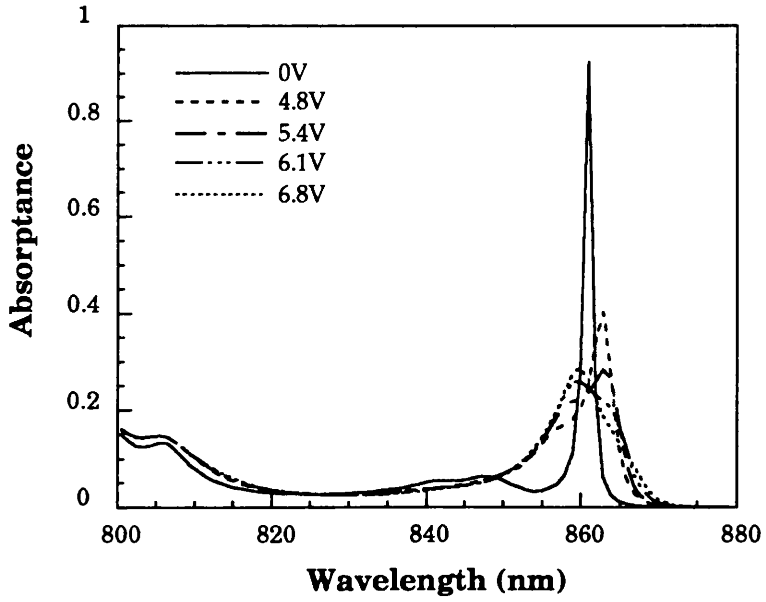

Fig.8.3.5 *Modelled absorption spectra for the nominal structure of QT153. Comments as in the previous Fig.8.3.4..*

section 3.3.4. The resulting data are shown in Fig.5.3.3.

The calculated reflectivity spectra for the structure shown in Fig.8.3.1 are presented in Fig.8.3.4. The expected reflection change is ≈75% obtained under 6V reverse bias at ≈860nm. Modelled absorption spectra are shown in Fig.8.3.5. A large absorption modulation from 95 to 25% is predicted by the theory. This is important for SEED operation as we discuss in section 8.5.

The well width of the actual structure differs from the 95Å used in the calculation. This, however, does not suffice to explain the dramatically diminished performance. The main reason appears to lie with the Bragg reflector stacks.

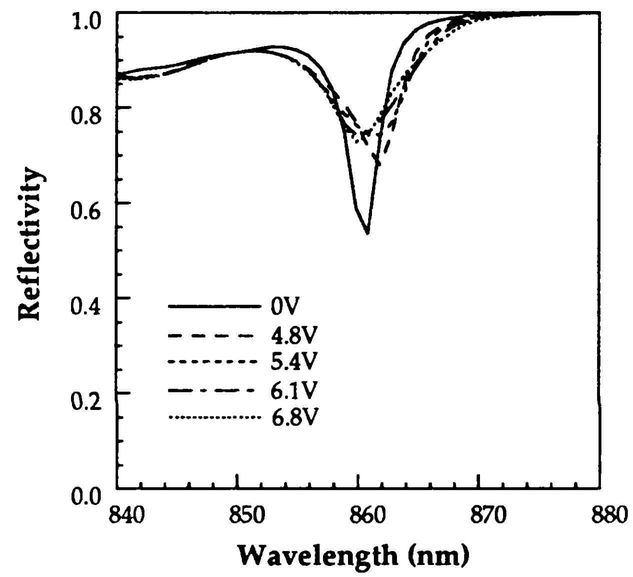

Fig.8.3.6 *Modelled reflectivity spectra that attempt to explain the large discrepancy between the predicted (Fig.8.3.4) and the experimentally obtained (Fig.8.3.2) spectra for QT153. The nominal epitaxial structure has been used in this calculation but for the back reflector where the AlAs and* $Al_{0.1}Ga_{0.9}As$ *thicknesses have been increased by about 6%.*

Specifically, it is mandatory that the reflectivities are as-intended at the wavelength of operation. In the case where one of the mirrors is e.g. below the intended value, the matching between the two mirrors is destroyed and the reflectivity of the off-state may be inadmissibly high. The experimental data do show a broader resonance than would be expected for the particular cavity design (compare to calculated data in Figs. 8.3.4, -5) which points towards a lower finesse, i.e. lower mirror reflectivities. X-ray measurements suggested that the thicknesses of the layers comprising the stacks differ for the front and the back mirrors in the case of QT153. This would cause the centres of the high reflectivity bands of these to be non-coincident and would indeed account for the diminished performance. In Fig.8.3.6 we present modelled spectra for the case where the thicknesses of the layers comprising the back mirror are increased to 769Å and 648Å for AlAs and $Al_{0.1}Ga_{0.9}As$ respectively., which would cause the centre of the respective high reflectivity band to be shifted to ≈910nm. The excellent agreement with the experimental data maintains that this may indeed reflect the actual case. The cause of the disparity between the two stacks may be a long-run drift of the growth process, and although this has been a problem for our structures it is not in principle unavoidable. Furthermore, the implementation of in-situ monitoring of the grown optical thickness (Chapter 5) would eliminate this difficulty.

Conclusions.

The data obtained from QT153 were rather poor. Double-pass (AR-coated) reflection modulators (Chapter 1) have in fact the potential for a better performance and without the complications and stringent growth requirements imposed by a high finesse Fabry-Perot structure. Nevertheless, the principle of operation was demonstrated at the time although this type of structure was independently first demonstrated by Walther and Ebeling [Sept. 1990] and later by Pezeshki *et al.* [March 1991].

Our results have identified the limitations of SCEMs. Indeed, it has been pointed out how the SCEM is by far less tolerant than the AFPM. On the other hand, this configuration does present the opportunity for low insertion-loss large reflection-change modulation in the normally-off mode and it is therefore worth further assessing as we do the next structure.

8.3.2 QT280B SCEM.

Epitaxial structure

This structure is similar to the previous in many respects, the epitaxial layers being shown in Fig.8.3.7. The front mirror consists of 8.5 periods of HL, as in the previous structure, with an estimated reflectivity of 92%. The top 50Å of the high-index layer in the front mirror have been replaced by a p+ GaAs capping layer for contacting purposes. The number of periods in the back mirror have been increased to 20.5 in order to ensure a very high reflectivity estimated to be 99.7%. The number of wells has also been increased to 60 to allow operation farther from the zero-bias exciton peak where the resulting modulation is improved. In order to minimise the penalty on the operating voltage, the barrier thickness is reduced to 50Å, still well above the no-coupling limit (40Å). Another modification with respect to the previous design comprises of the inclusion of a 500Å (bulk) GaAs layer. This ought to increase the saturation intensities by a factor of three, with the device being still an efficient absorber at the off-state. We discuss this advantage offered by SCEMs separately in this section.

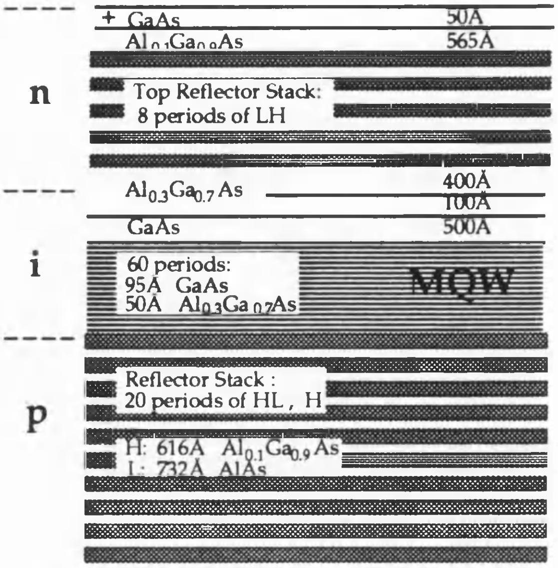

Fig.8.3.7 *A schematic of the epitaxial structure of QT280B, grown by MOCVD at the University of Sheffield.*

Results

Reflectivity spectra from QT280B are shown in Fig.8.3.8. A reflection-change of ≈45% is obtained at 853.3nm under 7.5V reverse bias, with an insertion-loss of 1.3dB. The features on the graph have been explained when discussing QT153. The contrast is low at ≈4.2dB. Photocurrent data for the same device are presented in Fig.8.3.9. The estimated maximum absorption is 68%. The peak in photocurrent at ≈854nm is underestimated due to the restricted resolution of the monochromator system.

Modelled spectra

Reflectivity spectra calculated in the manner presented in section 8.3.1 are shown in Fig.8.3.10. These refer to the epitaxial structure shown in Fig.8.3.7. The predicted reflection-change and absorption modulation are 70% and 65% respectively. The experimental results are, however, notably inferior. A relative misposition of the front

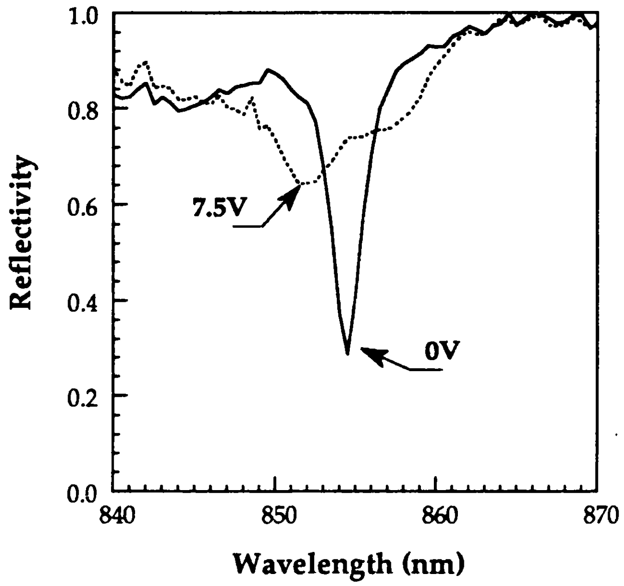

Fig.8.3.8 *Experimental Reflectivity spectra for a device from QT280B.*

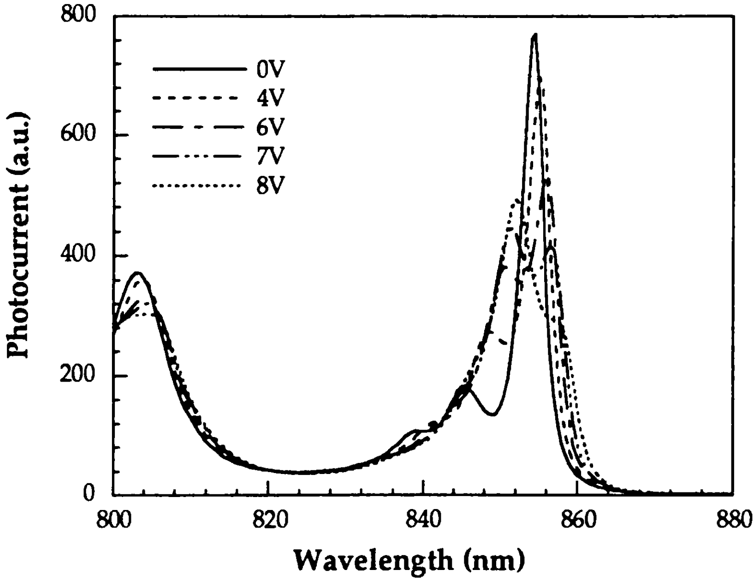

Fig.8.3.9 *Experimental photocurrent spectra for the same device as in the figure above. The data have been scaled with respect to one-other at 750nm. The peak at 0V appears cut-off due to limited resolution.*

and back reflector stacks appears responsible for the diminished modulation obtained for this structure in the same way that this inhibited the proper function of QT153. Indeed, a misposition, for example, of both stacks by 2-3% either way from the intended centre wavelength causes the off reflectivity to increase substantially enough to explain our experimental results. Absorption spectra for the relative FP-resonance heavy-hole exciton wavelength separation corresponding to the device presented here, as well as reflectivity and photocurrent spectra from other devices from QT280B point towards the reality of this view. Another possible cause could be an under-estimation of the absorption coefficient of bulk GaAs (in the intrinsic region), but this is unlikely.

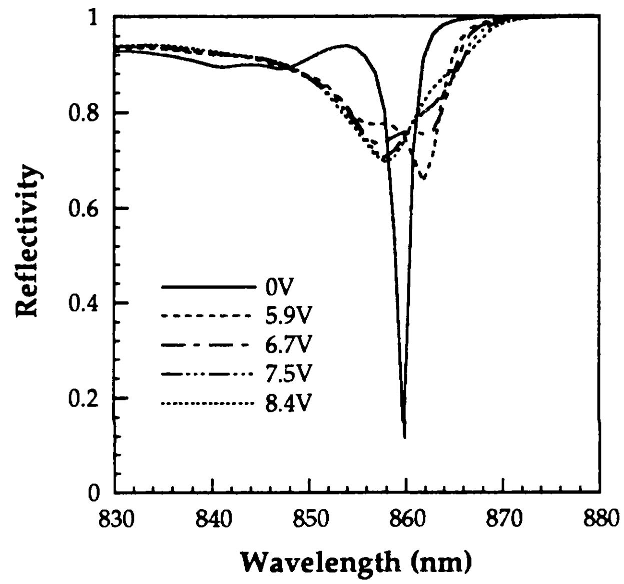

Fig.8.3.10 *Modelled spectra for the nominal QT280B structure. Experimental absorption spectra from 95Å wells (Fig.5.3.3) and electrorefractive effects (Chapter 2) are used in the calculation.*

Increase of the saturation intensity

When the intensity of the light that is absorbed within a semiconductor material exceeds a certain value, the absorption saturates [Chemla *et al.*, 1984]. The carriers that are created following the absorption may occupy certain allowable states. If these available states get filled-up faster than they are being freed by carrier sweep-out processes, saturation starts taking place. In quantum wells the lifetime of the states associated with excitons is larger in comparison to that in bulk material. As a result, the excitonic features start to saturate at far lower intensities than those that invoke an effect on the bulk material absorption. Since the saturation intensities are determined by carrier lifetime, they differ from one well/barrier system to another depending upon the well thickness, barrier Al concentration, barrier thickness, electric field etc [Fox *et al.*, 1991]. In the case of the typical 100Å GaAs/$Al_{0.3}Ga_{0.7}As$ wells, the saturation intensity of bulk is about three times as large at wavelengths around the quantum well band-edge. Note that this is wavelength dependent.

We have seen in Fig.8.3.5 that the absorption A falls with field for normally-off SCEMs whereas we are actually operating at a wavelength where the absorption coefficient α increases with field. This may be used to increase the saturation intensity of the final diode as follows. Let as assume the case where the diode absorbs 100% in its off state and 30% in its on state. Obviously, there is no point in increasing the maximum power that may be incident on a diode by merely reducing the percentage that is absorbed. As was done for QT280B, we include so much bulk GaAs in the intrinsic region that at 0V (maximum absorption) one third of the power is absorbed by the quantum wells and two thirds by the bulk GaAs. This only requires a small amount of GaAs as the absorption coefficient of the wells is very small at 0V. Indeed in the case of QT280B with no bias the quantum well absorption coefficient is about 1/20 that of GaAs at the wavelength of interest. With reverse bias applied to the device the absorption coefficient of the well material increases dramatically so that all the absorption is virtually due to the wells. Yet only one third of the incident intensity is actually absorbed now that the device is on. Therefore, the wells absorb one third of the power at all instances. Since the saturation intensity of GaAs is at least twice as large as that of the wells, and more so at smaller energies below the bandedge, it follows that the saturation intensity is in fact increased by a factor of three. This is an additional benefit on top of any improvements brought about by an optimisation of the quantum well material. However, there are two points to be made here. One is that as the saturation intensity of the wells is improved, it tends to that of the bulk. That way the improvement by this method will ultimately be restricted to a mere factor of just above two. Secondly, the inclusion of GaAs may affect the design of the modulator or else cause the performance to deviate from its optimum.

Conclusions

In summary we have achieved a reflection change of 45% with an insertion loss of 1.3dB at 7.5V in the normally-off mode. Although this is significantly below the potential of this SCEM design, this is a record performance for a normally-off device, and also the deviation from the intended performance is well understood. This structure is designed to achieve an increase of the saturation intensities by a factor of three in comparison with a device consisting of the same quantum well material and being 100% efficient in absorption at its off state. This is significant for SEEDs.

In Chapter 5 we discussed in detail the tolerances of asymmetric Fabry-Perot modulators. The equations leading to the evaluation of the tolerances of SCEMs are in principle identical. Both these classes of structures are electroabsorption based Fabry-Perot devices the function of which relies upon exactly the same principles. Thus the very sharp off-state resonance of the SCEM signifies its poor tolerances, in particular the contrast associated tolerances being especially slim. This stems from the fact that, contrary to the AFPM, the off-state is one of high finesse (typically ≈30 for 90% reflecting mirrors) and therefore very sensitive. This is depicted in Fig.8.2.1 where the reflectivity changes dramatically at low values of αd, whilst it is virtually insensitive to αd at larger values. Since it is the off-state that effectively determines the exhibited contrast, it follows that in fact it is impractical to aim at high contrasts using SCEMs. The reflection-change associated tolerances are also relatively poor, but certainly to a significantly lesser extent. This is a major disadvantage that may prohibit the practical implementation of SCEMs.

Double cavity structures

We have already discussed in Chapter 5 that in the case of an AFPM the tolerances with respect to lateral non-uniformity may be improved by the incorporation of a double-cavity. For SCEMs the situation is somewhat reversed in that the off-state is the

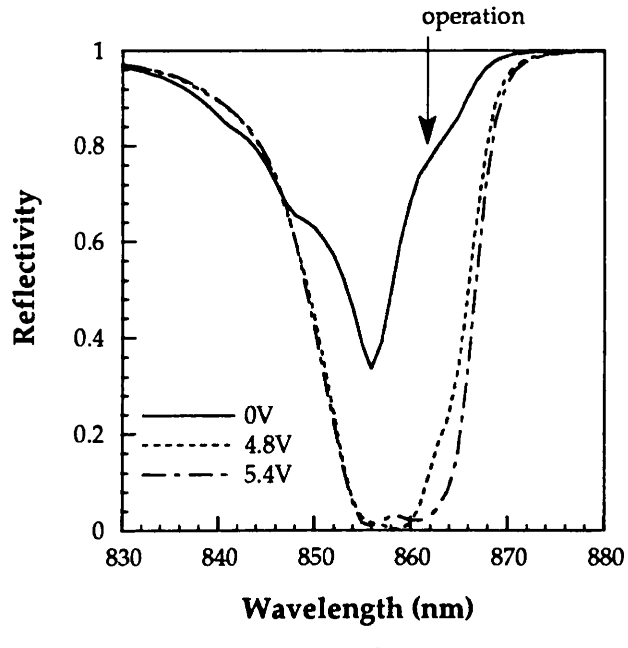

Fig.8.4.1 *Modelled reflectivity spectra for a double-cavity arrangement shown in Fig.8.4.2.*

high-finesse state, which leads to the possibility of an increase of the contrast associated tolerances. The use of a double-cavity generally does offer a practical solution provided that the growth process is controlled to a very fine degree. The top cavity would preferably be a dielectric cavity deposited after the end of the epitaxial step. This deposition is required to be very accurate in terms of both the thicknesses and the refractive indices of the deposited materials. An improvement in this direction is of great importance for SCEMs the performance of which is indeed drastically limited by their low tolerance.

In Fig.8.4.1 we present calculated reflectivity spectra of a double-cavity SCEM using experimental absorption data from 95Å wells (CB308, Fig.5.3.3) where the electrorefractive effects are also included (Chapters 2,3). The structure used for these calculations (Fig.8.4.2) consists of a SCEM similar to QT153 that comprises the bottom cavity, while the top cavity is formed by a deposition of a Y_xO_y spacer followed by 3 periods of Y_xOy/SiO_2 dielecticstack. A maximum reflection-change $\Delta R \approx 80\%$ is exhibited, while $\Delta R \geq 60\%$ is achieved over a 8nm range. This is substantially

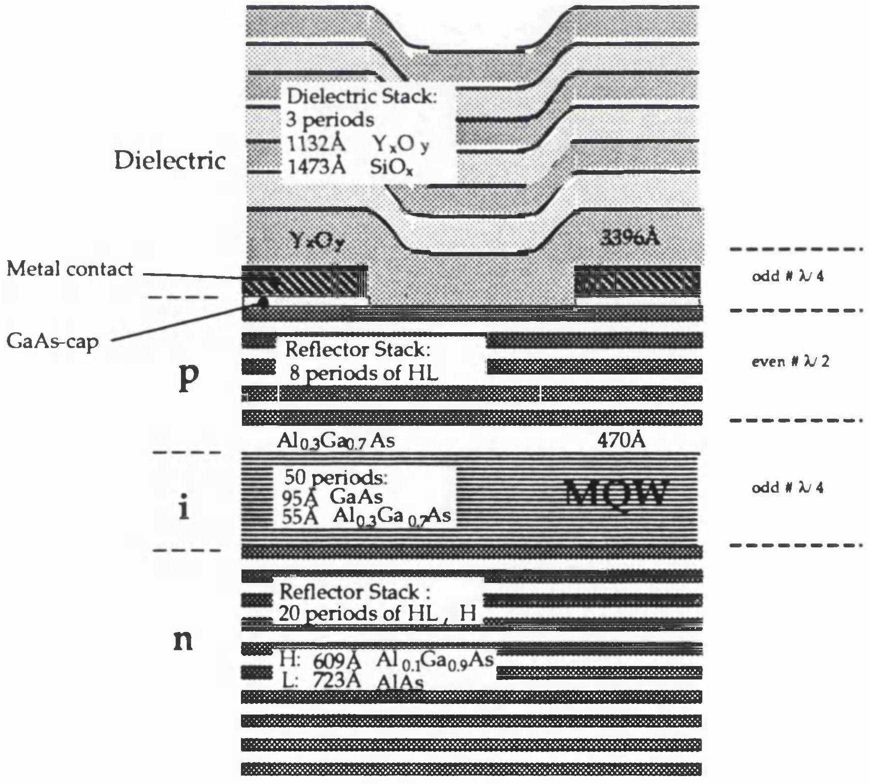

Fig.8.4.2 *A double-cavity structure may be formed by a deposition of a dielectric spacer and a dielectric reflector stack after the metallisation step has taken place. The epitaxial structure is similar to QT153.*

broadened in comparison to that of the initial single cavity structure (Fig.8.3.4) indicating an improvement of the tolerance to lateral non-uniformity. The contrast tolerances are markedly increased as now the off state is in fact one of large stability. Note that this is not the case when a double-cavity is implemented with AFPMs, where the reflection-change tolerances are improved and not the contrast associated ones.

The above and the operation of the double cavity may be clarified in the following. The design is such that the top cavity that is formed between the top dielectric mirror and the front epitaxial mirror is at resonance at ≈860nm. The cavity formed between the two epitaxial mirrors (similar to QT153) is also at resonance at 860nm. However the larger cavity defined by the very top dielectric mirror and the bottom epitaxial mirror is not at resonance. This is what we referred to as "decoupled cavities". Thus the structure may be viewed as a passive cavity (top cavity) the back mirror of which is electrically controlled. The off state of the composite structure corresponds to the on state of the single bottom (active) cavity and vice versa. In Fig.8.4.3 we illustrate the operating points for both cases, i.e. for the single and the double cavity. It follows that after this reversal the on-state of the double cavity is now the one most sensitive to variations in manufacture or operational parameters.

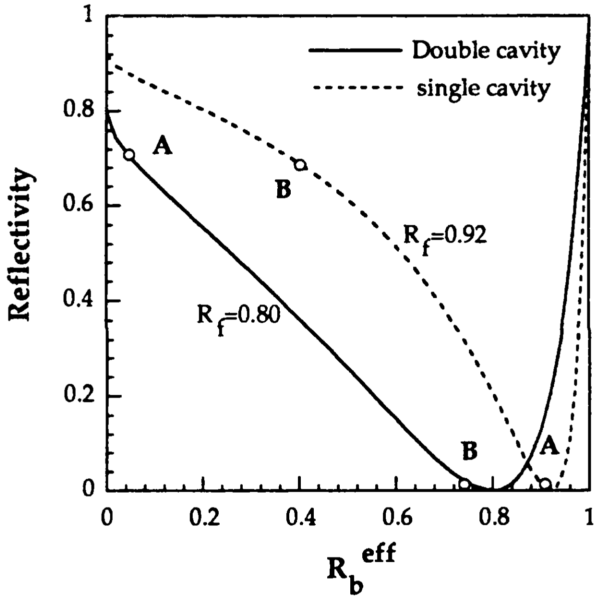

Fig.8.4.3 *The operation of the single cavity SCEM with a 92% front reflector is at point A without bias and at B with bias. The corresponding points are shown for a double-cavity arrangement with a front mirror of 80%, i.e. matching the on-state of the single-cavity. Near-ideal case.*

Depending mainly on the front mirror of the top cavity, the net reflection change may be lower and the contrast higher for the double-cavity case. The real gain lies with the increase of the contrast tolerance that stems from the fact that the off-state is defined by a non-sensitive state. As far as the reflection-change is concerned, in effect one gains in terms of tolerances at the expense of the peak performance characteristics, although it is also possible to attain an enhancement of the peak performance. Most importantly, the above may only be accomplished provided the manufacture is finely controlled, i.e. tolerances in fabrication precision are exchanged for better lateral non-uniformity and operational conditions associated tolerances. It should be noted that the affordable variations in ambient temperature should not be considered dramatically improved. The temperature-induced variations of the amount of absorber in the cavity (Chapter 4) has a profound effect on the off-state reflectivity of the initial single-cavity. This is well illustrated in Fig.8.2.1 where the sensitivity of that state (low values of αd) upon the amount of αd is evident. The resulting greatly modified off state reflectivity of the bottom cavity will disrupt the operation of the double cavity quite substantially. This will be manifested mainly as a drastically decreased R_{on}. In summary, the double cavity arrangement should be regarded as a means to improve mainly the lateral non-uniformity tolerances of SCEMs, while the problems that are caused by variations of the ambient temperature ought to be tackled by a dynamic stabilisation of this, possibly using integrated Peltier coolers (see Chapter 4).

8.5 APPLICATION OF SCEMs IN SEEDs

In this section we will examine theoretically and experimentally the potential of SCEMs in SEED configurations. Prior to this we evaluate the limitations of the performance of normally-off AFPMs that are also candidates for such composite devices.

8.5.1 Normally-off AFPMs: Performance limitations.

Asymmetric Fabry-Perot modulators may be used in SEED arrangements as they offer high contrast or generally enhanced-modulation switching at low voltages.

Normally-off AFPMs are implemented in this case where the absorption (and hence the photocurrent) drops with voltage thereby attaining negative differential resistance that is required for SEED operation. In this section we will evaluate the performance characteristics that may be obtained by normally-off AFPMs. This will then comprise a reference platform for the assessment of SCEMs.

Normally-off AFPM operation is obtained at the vicinity of the zero-bias exciton position where the absorption coefficient of the quantum well drops with field. Optimised performance is attained by larger wells [Whitehead *et al.*, 1990b] for two reasons. Firstly, the absorption modulation at the vicinity of the exciton peak is maximum for larger wells [Whitehead *et al.*, 1988]. Secondly, the electric field applied across the quantum wells is of prime importance for SEEDs since the switching energy of the devices is directly proportional to the field (next section). Large well widths operate at lower fields and they are therefore preferred for such devices.

In our calculations in the following we will assume a modulation of the absorption coefficient from α_{max}=13,200cm^{-1} to α_0=4,000cm^{-1} at 88kV/cm, as this is derived by experimental transmission data from 145Å wide GaAs/Al$_{0.3}$Ga$_{0.7}$As wells [Whitehead et al., 1988]. A large back mirror reflectivity has been proven to improve the operational characteristics, in particular to minimise the insertion loss (Chapter 6). In Fig.8.5.1 we plot the reflection-change and absorption-change that can be achieved by very high contrast (>20dB) normally-off AFPMs of various front reflectivities. Assuming barriers of 25Å, that is the minimum safe value to ensure no interwell coupling, we find that very low operating voltages are required ≈2-3V. It is evident from Fig.8.5.1 that the maximum reflection-change for a high contrast device is just 28%, implying a minimum insertion loss of 5.5dB (R_{off}=0). The large insertion loss limits the cascadability of such devices especially when high speeds are aimed for (see next section). At the same time the small absorption-change denotes a diminished negative differential resistance as well as a narrow bistability loop. The latter is very important as it is a direct measure of the tolerances of such devices to input power fluctuations. The obtained reflection-change is on the whole a very critical parameter and not only because the on and off levels are then well defined, which is always desirable in structures incorporating modulators or indeed any multi-state device. Most importantly, large reflection change means a large absorption change as well generally for AFPMs and this determines the feedback mechanism that establishes bistability. For a fixed R_b=0.997, as used in Fig.8.5.1, the reflection-change (ΔR) does not change dramatically with R_f. Additionally, ΔR increases when the number of wells is reduced slightly so that only a fraction of the critical absorption $[\alpha d]_c$ required to zero the off-reflectivity is incorporated in the cavity. In Fig.8.5.2 we calculate the

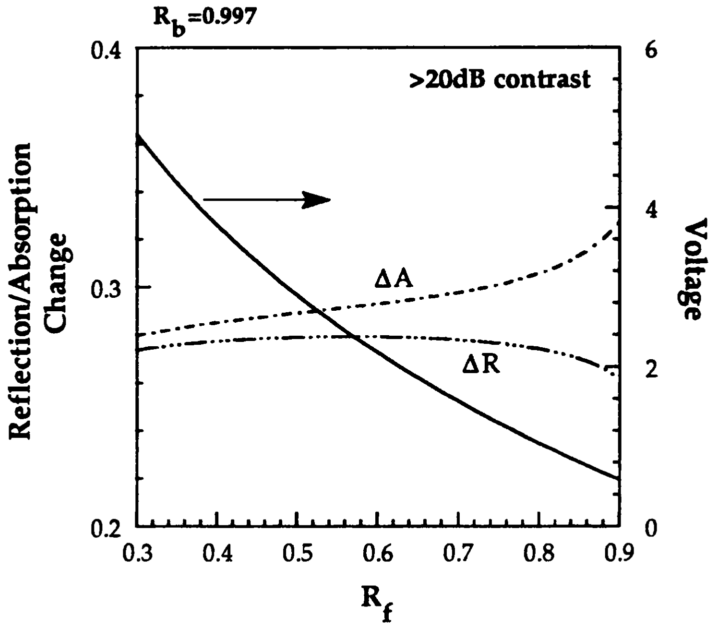

Fig.8.5.1 *Operating characteristics for a normally-off AFPM based on experimental absorption data obtained from 145Å wells. The minimum barrier ($Al_{0.3}Ga_{0.7}As$) width of 25Å has been assumed in the calculation of the operating voltage..*

reflection change as a function of the fraction of the critical absorber in a cavity with R_f=0.6 and R_b=0.997. The choice of R_b has been justified earlier, while that of R_f is arbitrary. However, bearing in mind that it is desirable to maximise both ΔR and ΔA and at the same time not impose an enormous toll upon the tolerances (i.e. not use very high values of R_f), R_f=0.6 is a good compromise (Fig.8.5.1). It is deduced from Fig.8.5.2 that the maximum reflection-change of 40% is obtained when just 0.4 of the critical absorber is incorporated. The same holds for the absorption-change. ΔA is not plotted in Fig.8.5.2 but it follows the reflection-change curve very closely. The reason for this maximum at $\alpha d=0.4[\alpha d]_c$ stems from the fact that whereas R_{off} increases 'slowly' with decreasing αd, R_{on} increases much 'faster'. The net result is that their difference ΔR increases in fact with decreasing αd until the latter is far too small to cause any substantial modulation. At the maximum ΔA point R_{on} is 70% (Fig.8.5.2). The absorption at the off state, i.e. the highly absorbing state, drops from 1 with decreasing αd, as expected. This is clearly not desirable as it means that only a fraction of the incident optical power will be actually used for the switching. It is evident from Fig.8.5.2 that A_{off} at the maximum-ΔR point is 80%, which is quite acceptable. Very high contrast S-SEED operation using AFPMs has been demonstrated [Grindle *et al.*, 1991].

It has been proposed [Livescu *et al.*, 1992] that by the incorporation of a larger amount of absorber than required ($\alpha d>[\alpha d]_c$) one may accomplish high contrast at a position closer to the light-hole exciton peak. The strong electrorefractive effects at that wavelength range shift the resonance to shorter wavelengths with bias allowing thereby larger reflection-changes (lower insertion-loss). Additionally, different well structures such as coupled wells [Atkinson, 1990], superlattices [Law *et al.*, 1991], or asymmetric coupled quantum wells [Miller DAB, 1988] may attain a better performance. In this section we have restricted our evaluations to a certain well system. Notwithstanding, our calculations are a good estimate of the limitations in the performance of normally-off AFPMs.

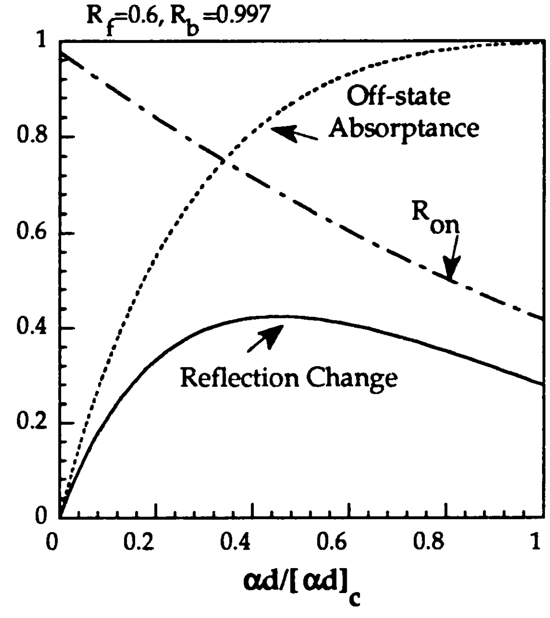

Fig.8.5.2 *Optimisation of the reflection- and the absorption-change with regard to the amount of absorber that is incorporated in the cavity. Very high contrast is only obtained when* $\alpha d=[\alpha d]_c$.

The optimisation of the modulator characteristics with respect to SEED operation is not a straightforward process. Additionally it depends greatly on the application and thus it may not be done for the general case. In this section we have merely hinted at some of the issues involved in the optimisation, while in the process of evaluating the limitations in the performance characteristics of normally-off AFPMs.

8.5.2 SCEMs in SEEDs.

General Considerations

Self-Electro-optic-Effect-Devices (SEEDs) have been presented in the Introduction (Chapter 1) of this thesis. A fair amount of work has been done on such devices and there are excellent introductory papers [Miller D A B *et al.*, 1985b; Lentine *et al.*, 1990] as well as recent reviews [Miller D A B, 1990] and optimisation orientated papers [Lentine *et al.*, 1991]. The case where two identical diodes are connected in series to create a symmetric SEED (S-SEED) is of particular interest. The S-SEED has the advantage of simplicity over the transistor incorporating SEED (T-SEED), while time-sequential differential logic and full integrability compare favourably with the resistor SEED (R-SEED). For a short introduction see Chapter 1.

The main parameters taking part in the function of SEEDs are:

i. Switching Energy. This is the absorbed optical energy that is required to switch the device from one state to the other and is given by

$$E_\alpha = \frac{\hbar\omega}{e}\cdot CV = \frac{\varepsilon\hbar\omega}{e}\cdot AF \qquad 8.5.1$$

where C is the capacitance of each device, V is the maximum voltage applied across a device, A is the mesa area, and F is the maximum electric field across the intrinsic region. It is evident that clearly it is the operating field and not the operating voltage that determine E_α.

ii. Switching Speed. This is determined by the time taken to switch the SEED from one state to the other. There are more than one mechanisms that play a role in this. Firstly, for switching to occur, the capacitance of the electroabsorptive diode must be charged by the generated photocurrent. The time τ_α required for this action to take place depends on the optical power. Indeed, the device switches to its new state when the total absorbed optical energy is E_α (eqn.8.5.1). The total absorbed energy, however, is the integral of the power ΔP absorbed over an interval Δt, times that time interval. Therefore larger optical powers allow for faster switching. Simultaneously there is an RC time τ_{RC} associated with the overall circuit. The resistance R is the series combination of the contact resistances and the source resistance. The total capacitance involved is the capacitance of the two diodes connected in series, i.e. half that of the individual device. Finally, a third process, the time needed for the carriers to escape from the wells and contribute to the photocurrent may also limit the switching speed. This vertical transport associated time τ_V is an average of the sweep out times over a varying electric field. In total, the switching speed is determined by the slowest of these processes.

A result of the above is that in the case of multi-stage devices, the bit rate may be ultimately affected by the insertion losses of the electroabsorptive diodes. This determines the power incident upon the second stage of devices and thus determines the time required for E_α to be absorbed at that stage of devices. Another point to be made with regard to switching speed is concerned with exciton saturation. There is a limit to the power that may be incident on MQW devices as dictated by the absorption saturation effects caused by excess optical power. This may impose restrictions upon the switching speed according to our earlier arguments. Typically optical switching energies of $\approx 10 \text{fJ}/\mu\text{m}^2$ are required for SEED operation. Assuming that the switching time should not exceed 100ps (corresponding to below 10GHz), the power incident upon the device ought to be of the order of $100\mu\text{W}/\mu\text{m}^2$. This is well above the saturation intensities of $\text{GaAs}/\text{Al}_{0.3}\text{Ga}_{0.7}\text{As}$ quantum wells [Fox *et al.*, 1990]. It is therefore valuable to increase the saturation intensities of the devices implemented in SEED configurations. Fast carrier escape out of the wells is one way of increasing the saturation intensities [Fox *et al.*, 1991], since as we mentioned in section 3 the saturation intensity is determined by carrier lifetime. As a consequence 'shallow' wells [Goossen *et al.*, 1990] are very advantageous in terms of switching speed. These have fast carrier sweep out which practically eliminates vertical transport (τ_V) as a factor that limits speed. Simultaneously, the saturation intensities are increased allowing thereby the use of larger optical powers and therefore a reduction of τ_α.

iii. Signal Beam Tolerances. In practical implementations it is vital that the operation is not critically sensitive to spurious fluctuations of the input powers. A measure of this insensitivity is the width of the bistability loop of the input- versus output-power diagram. The width of that loop depends on the biasing voltage, but is in any case directly proportional to the absorption change ΔA achieved by the electroabsorptive diode between the two states. Note that this is not necessarily the maximum ΔA that the diode may achieve under ideal biasing conditions. It follows thus that it is desirable to maximise ΔA in order to optimise the signal beam tolerances.

A couple of additional points may be made regarding the operation of SEEDs. The insertion loss of the diodes is an important parameter firstly with respect to device cascadability. Note that most functions require two stages of devices [Lentine *et al.*, 1990]. As far as exchange/bipass switches are concerned, however, a fresh clock may be applied at each stage so that the insertion loss becomes to some extent irrelevant. At the same time the reflection change and the absorption change are required to be maximised. These three parameters are, however, directly related so that optimising the performance with respect to one of them has a positive effect on the other two. Another point to be considered is that of the operating voltage and electric field. It was discussed above that it is important to minimise the electric field at which the devices operate since this causes a direct reduction of the switching energy (eqn.8.5.1). The operating voltage is of less significance. However, low operating voltages are an advantage mainly due to power consumption considerations and also for better integrability with electronic circuitry. Finally, the discussion with respect to AFPMs (Chapters 2 and 5) regarding the tolerances of the devices to manufacture, temperature and operating parameters (such as wavelength, voltage, angle of incidence, and alignment) clearly holds here as well. It is thus of great importance that the tolerances are optimised to comply with real conditions.

Experimental demonstration of S-SEED operation using SCEMs

Two devices from QT280B were connected in series (Fig.8.5.3) to create a symmetric SEED (S-SEED). The responsivity-voltage characteristic of diode 1 (D1) at the wavelength of maximum reflection-change is shown in Fig.8.5.4. A large change in responsivity with bias is evident from this plot and is a consequence of the relatively large absorption- (reflection-) change of this device. The two diodes used for the S-SEED operation were not identical in this experiment, the optimum wavelength of D2 being about 1nm longer than that of D1. Thus at 853.3nm, that the operation was set, the maximum absorption (low voltage) of D2 is lower than that of D1 while the minimum absorption is comparable for both diodes. The responsivity of D2 exhibited therefore a shallower decrease with voltage. A diagram of the experimental set-up is shown in Fig.8.5.5. Light at 853.3nm was obtained from a tunable argon-pumped Ti-Sapphire laser. A fixed power beam was incident on D2 while the power incident on D1 was ramped using a variable attenuator. The output was detected from D1. Before

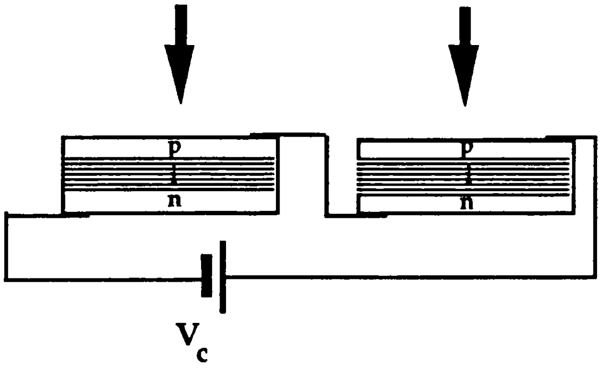

Fig.8.5.3 *Schematic of two diodes connected in series in the S-SEED configuration. The device is bistable in the ratio of the two input optical beams.*

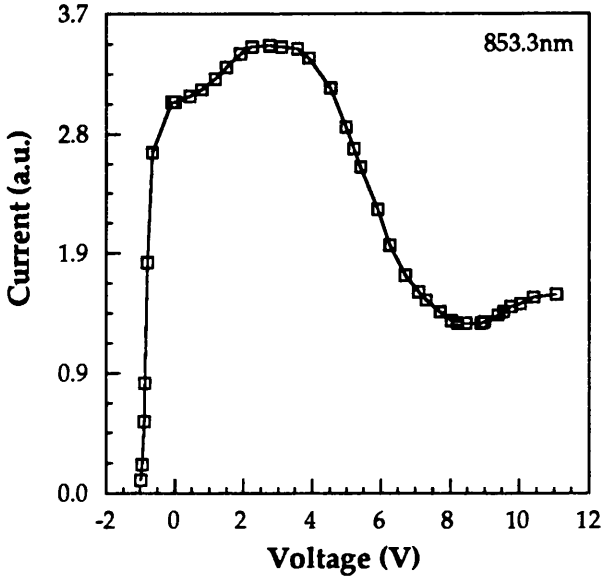

Fig.8.5.4 *Experimental responsivity versus voltage for the device used for the S-SEED (QT280B).*

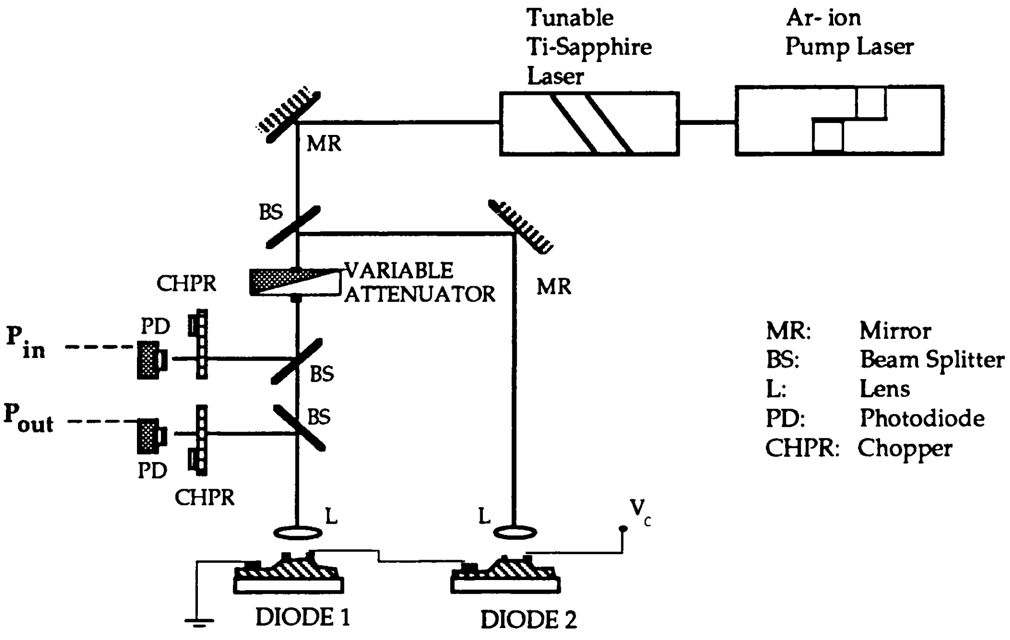

Fig.8.5.5 *A schematic of the experimental set-up used to demonstrate the S-SEED.*

connecting the two devices in the S-SEED arrangement, the power on D2 was adjusted such that the photocurrents on the two diodes were equal at the middle range of the attenuator. That way the bistability loop is ensured to be within the input power range. Because of the difference between the characteristics of the two diodes, this matching of the photocurrents could only be done over a limited range of voltages. It was decided to equalise the currents at about 5.5V since this resulted in similar I-V behaviour for both diodes at low voltages up to about 5.5V with an evident divergence at larger biases.

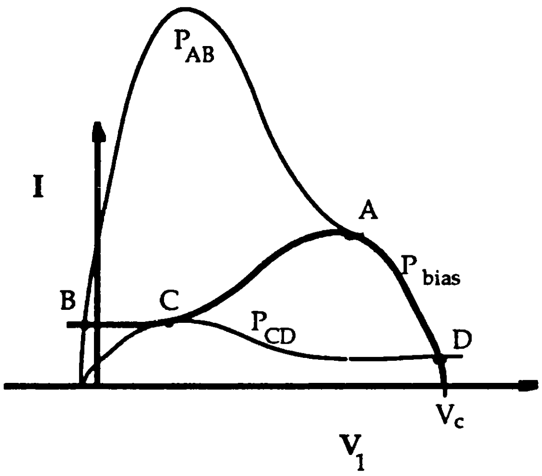

Fig.8.5.6 *A diagram of the loadlines and the operating points of two diodes with NDR connected in series in the S-SEED configuration. The horizontal axis is the voltage across diode 1 in the previous figure.*

By keeping the power (P_{bias}) on one diode (D2) fixed while ramping the power (P_{in}) on the other (D1) switching is achieved at two different input power values, creating thereby the bistability loop in the input-output power diagram. This is clarified in Fig.8.5.6 that depicts the load-lines of the two diodes for the ideal case where the diodes are identical. With very little power on D1, all the voltage is virtually dropped across that diode, setting it at the on-state. As the power increases, the operating point moves to slightly smaller voltages until it reaches point A where it switches down to point B. Now D1 is at its off state with little voltage dropped across it. The switching takes place at a power P_{AB}. As the power is decreased again switching occurs from point C to point D at a power $P_{CD}<P_{AB}$ where D1 switches back from the off to the on state.

The experimental input-output power characteristic at 6.5V and 853.3 nm is shown in Fig.8.5.7. The accuracy of the measured powers is not excellent in absolute terms. However, the whole diagram just scales with power so that this does not limit the validity of the results. Optimum operation in terms of the contrast $P_{out}^{max} / P_{out}^{min}$ was obtained under V_c=6.5V. In this case, switching from A to B (Fig.8.4.9) corresponded to a change of the bias V_1 across D1 from -7.3V to +0.9V, and from C to D corresponded to a change from around 0V to -7.5V. A contrast of ≈2.5 for AB and ≈2.4 for CD were exhibited. The very broad bistability loop signifies good tolerances to fluctuations of the input power. Indeed, the input power may fluctuate by ±45% around the median value without prohibiting bistability to occur (assuming here that P_{bias} is constant). Similarly, bistabiltity was observed over a wide range of voltages V_c from about 4V to 8V. Another feature worth pointing out is that the output at the on state is a large fraction of the input power as a result of the low insertion loss of the diodes.

The (normally-off) SCEM shows best modulation characteristics when using well widths ≈100Å. This stems from the operation at wavelengths longer than the zero bias exciton, as was discussed extensively in Chapter 7 with regard to the normally-on AFPM. As a consequence, the operating field is larger for SCEMs than for normally-off AFPMs or double-pass (AR-coated) reflection modulators. The resulting larger switching energy E_α is a clear disadvantage. Larger well widths may be used for SCEMs but the operating voltage will be significantly increased. Another disadvantage is that the large Bragg stacks that are used at the p and n regions cause an increase of

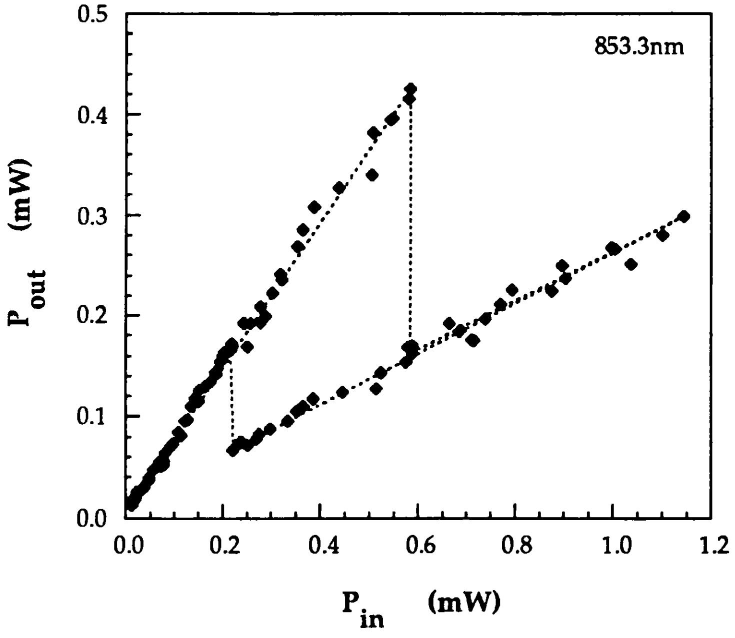

Fig.8.5.7 *Experimental input- versus output-power characteristic. Data fitted to straight-line but for the vertical switching points.*

the contact resistances and thus raise τ_{RC}. Graded interfaces [see for example Sugimoto *et al.*, 1992] almost eliminate this problem but they clearly add another complication to fabrication. The SCEM does offer the advantage of large absorption changes. However, the exhibited negative differential resistance (NDR) is in fact comparable to that of AFPMs. Firstly, one should note that the NDR is a function of the optical power. Assuming thus equal powers on both the AFPM and the SCEM, the typical attained change in responsivity is roughly twice as large for the SCEM as that of the AFPM. On the other hand, the required voltage is also twice as large so that finally the NDR, and thus the feedback mechanism, are of comparable magnitude.

Summarising this section, the AFPM offers high contrast operation [Grindle *et al.*, 1991] at low voltages but with a low absorption-change and a very high insertion loss. The SCEM offers low insertion loss large absorption-change operation resulting in better cascadability, possibly faster switching, and better tolerances to input power fluctuations. The obvious disadvantage of this configuration is, however, its low tolerance. Double cavity configurations attain an increase of the tolerances as well as higher contrast operation. Although NDR is still exhibited, the reflection is at the on-state with no bias, which might prove advantageous in terms of alternative logic functionality.

8.6 SUMMARY

The incorporation of quantum wells in a symmetric Fabry-Perot cavity allows for normally-off operation at wavelengths longer than the zero-bias exciton peak. The resultant device can exhibit very large reflection-changes in the normally-off mode thereby showing a large negative differential resistance. This latter is a precondition for SEED operation. This type of electroabsorption modulator was first demonstrated by Walther and Ebeling [Sept. 1990] and later by Pezeshki *et al.* [March 1991] while my independent first attempts had been unsuccessful due to erroneous growth (QT153). In fact Guy *et al.* had earlier [1987] proposed the SCEM configuration in a mainly theoretical paper, while even before Ryvkin [1981] had used an identical arrangement but in bulk GaAs material where he used the Franz-Keldysh effect. All this work was not to my knowledge when initially working on QT153 nor when designing QT280B.

In this Chapter we have presented a study of the symmetric Fabry-Perot electroabsorption modulator (SCEM). We have presented experimental results from two structures one of which exhibited 45% reflection change and 1.3dB insertion loss at 7.5V which is a record performance for a normally-off device. By way of comparison, a very high insertion loss is inherent to normally-off AFPM operation. In the case of GaAs/$Al_{0.3}Ga_{0.7}As$, a maximum reflection change of 28% can be predicted for a high contrast normally-off AFPM device, that can be only improved to 40% maximum for a low contrast one. The SCEM offers the advantages of very large absorption change and low insertion loss that are beneficial for SEEDs. Indeed, we demonstrated symmetric-SEED operation for the first time using SCEMs. Despite the non-ideal performance of the SCEMs incorporated in the demonstrated S-SEED, the large reflection-change (ΔR=45%) led to a relatively broad bistability loop, denoting an insensitivity to spurious input power fluctuations.

The big drawback of an implementation of the SCEM is its poor tolerance which puts it at disadvantage in comparison to the normally-off AFPM. A double cavity arrangement has been proposed to improve the tolerances with respect to lateral non-uniformity but at the expense of simplicity in manufacture and often of the maximum reflection-change. However, the exhibited contrast may be considerably enhanced in this way. Integrated Peltier coolers would be required to alleviate the effects of temperature sensitivity upon the performance (see Chapter 4). In addition, the incorporation of the double cavity configuration yields an inversion of logic which may prove useful in terms of alternative logic functionality. One possible advantage of the SCEM is that its saturation intensity may be increased by a factor between two and three in comparison with other highly absorbing structures. Nonetheless, it appears that the disadvantages of SCEMs with regard to SEED applications outweigh the advantages. On the other hand, the very wavelength selectivity of SCEMs that denotes their poor tolerances also signifies their potential for other applications where it is in fact an asset. A tunable- filter, detector, demultiplexer that utilises SCEMS is discussed in the next Chapter.

CHAPTER 9: APPLICATIONS OF THE FABRY-PEROT MODULATOR AT THE CHIP LEVEL

9.1 INTRODUCTION

So far in this thesis we have been dealing with the study of the Fabry-Perot (FP) MQW modulators and the optimisation of their performance. In this Chapter we return to their application not at the systems level (Chapter 1) but rather at the chip level. After a brief introduction to the importance of integration and the various available integration techniques, we concentrate on the methods of integration of optoelectronic devices with electronic circuitry.

Subsequently, we focus on the integrability of the FP modulator with other optoelectronic devices. We examine the versatility of the FP structure and its potential to realise multiple functions in the form of devices that are mutually integrable on the same chip. This allows the formation of both transmitter and receiver modules as well as composite devices of complex and new functionality. In the same section we also refer to the fabrication of two-dimensional arrays of devices and give a brief account on AFPMs realised in material systems other than the GaAs/AlGaAs considered in this thesis. Finally, in the last section of the Chapter, we present some novel configurations where the FP modulator is employed in composite devices of increased functionality.

9.2 INTEGRATION

9.2.1. General.

The key to the deployment of optoelectronic technology lies with the monolithic integration of high performance devices on the same chip. This has been the major factor promoting the great success of electronics. Integration eliminates parasitic reactances arising when interfacing discrete devices and thus yields an improvement of performance for the overall system [Wada, 1990]. Specifically, higher speed of operation and better receiver sensitivity, that stems from noise reduction, are achieved. Secondly, the combination of different components in close proximity leads to better and often new functionality and thus allows for higher complexity arrangements. Additionally, compact packaging results in overall better manufacturability and reproducibility thereby yielding increased reliability and a reduction of cost.

The issues involved in integrated circuit design are quite distinct from discrete device design. Indeed, in order to take proper advantage of the economics of integrated circuits it is necessary to select structures for both the electronic and the optoelectronic devices that provide processing compatibility and overall good component matching. Optoelectronic technology demands the integration of devices that are not inherently compatible and therefore necessitates a certain degree of compromise so as to obtain the best overall performance possible [Dagenais *et al.*, 1990]. The advancements in III-V (especially GaAs) technology, and in particular in electronic circuitry with GaAs MESFET ICs being at the mature stage, provides a solid foundation to build upon [Wada, 1990]. Clearly, components that are easily integrable and provide versatile functionality are much sought after. In this section we will examine the Fabry-Perot (FP) modulator in this respect.

The basic technologies for integrating a laser diode or a photodetector with electronic circuits were established by 1985 [Shibata *et al.*, 1984; Ohnaka *et al.*, 1985]. Subsequently, the trend may be seen to have separated in three directions [Matsuda and Shibata, 1992] that are distinguishable depending on the amount of optics incorporated and the applications they are predominantly aimed for. Each area poses quite distinct requirements. One area is directed at communications, large capacity optical fibre transmission systems using time-domain multiplexing techniques. Here only a single, mainly, optical device (such as a laser diode or a photodiode), is incorporated in a large electronic circuit [Fujita *et al.*, 1990]. Secondly, there is a class of optoelectronic circuits that have been named photonic integrated circuits (PICs) as stemming from the fact that the proportion of optical components is relatively high

[Koch and Koren, 1990]. Thus different optical and electronic planar devices are connected using waveguides involving a certain degree of complexity for the components used. A basic PIC may comprise, for example, a frequency stabilised DFB laser, a 3dB coupler, a balanced receiver and surrounding electronic circuitry. This would be required in wavelength division multiplexed (WDM) transmission and coherent optical receivers. Prototype PICs have been realised in both GaAs and InP [see for example Grande *et al.*, 1990; Hayashi *et al.*, 1991]. A third class of OEICs involves a large degree of complexity in both the electronic domain and possibly the optical domain, involving two dimensional arrays of optical nodes. This is directed at achieving parallel transmission eg. in parallel processing architectures (possibly 3D), optical interconnects, and optical computing.

The FP modulator falls into the last category of OEICs where at the early stages the node complexity is expected to be relatively low. Most of the effort has concentrated on PICs in recent years, however, the know-how gained may benefit other areas of integration.

Integration configurations may be classified into two types depending on the relative positioning of the layers used for various types of devices, namely vertical and horizontal integration [Dagenais *et al.*, 1990]. In the former case, as the name implies, the layers for the various structures are sequentially grown on top of one other and layers are etched to reveal individual devices. Often selective area epitaxy and regrowth may be employed, as is discussed later on. Horizontal integration, on the other hand, refers to the configuration where the various devices are formed horizontally on a semi-insulating substrate yielding a desired minimisation of capacitance coupling. In this case, and when integrating optics with electronics, the layers required for the optoelectronic devices are normally grown in a groove so that the top surface is at the same height as that of the rest of the substrate [Hayashi *et al.*, 1991]. The resulting planar surfaces are of great importance mainly because they allow for processing of very fine features. The FP structures discussed in this thesis are inherently vertical structures. However, several devices may be produced from the same basic epitaxial structure and may thus be integrated in an horizontal manner. The mesa structure prevents large scale integration and also causes difficulties encountered with the electrode wiring, it is nevertheless obviously the only approach to densely packed devices suitable for free-space links. Also, for many applications, such as interconnections in VLSI, where the devices act as optical 'pads' that replace electronic connections, both the feature sizes and the array density may be determined on different grounds, i.e. not limited by the nature of vertical integration.

The integration on the same wafer of various components that individually need distinct structures poses certain requirements (see section 9.2.3) that may be met using selective etching or masking combined with regrowth [Berger *et al.*, 1991b] or selective area growth [Gaihanou *et al.*, 1991]. Such techniques are also employed when integrating optics with electronics. This brings about considerable problems mainly due to the complexity of the growth process and the effect on the quality of the regrown or selectively grown layers. In the case of quantum well structures selective area control of the growth speed, such as the in-plane bandgap-energy control technique [Aoki *et al.*, 1992] may be employed to yield differing QW thicknesses selectively on a wafer. Alternatively, post growth techniques may be employed to either destructively disorder the quantum well region and produce a passive area (applicable mainly to waveguide devices), or controllably tailor the absorptive and electroabsorptive (and consequently also the electrorefractive) effects of the QWs. Impurity induced layer disordering (IILD) [Deppe *et al.*, 1988] is commonly used for the former. On the other hand, impurity free vacancy diffusion (IFVD) [Ghisoni *et al.*, 1991] yields a controllable degree of interdiffusion between the well and barrier materials and results in a blue shift of the excitonic features while retaining at the same time the QCSE. Thus individual devices may be operating at different wavelengths and the technique lends itself to large scale integration. This may be employed with the FP modulator, as we discuss later, moreover acquiring suitable lateral resolution to be applied to very small features and to not degrade the performance of individual devices [Ghisoni, 1992]. The intermixing process is encouraged by the deposition of SiO_x on the front surface and therefore deposition of different oxide thicknesses yields differing degrees of interdiffusion for a single annealing cycle enabling thus fully integrated configurations [Ghisoni, 1992]. Finally, several techniques that are very popular in other types of structures and in particular in horizontal integration, such as for example ion implantation or selective area diffusion of dopants, do not really apply to the vertical modulator [Wada *et al.*, 1989], although they may apply to the rest of the circuitry the modulator is attached to.

9.2.2 Integration with electronics.

As discussed in Chapter 1, the role of optics is in intimate relation with electronics [Midwinter, 1987] and thus the integration of optoelectronic with electronic circuitry is of paramount importance. Electronic circuitry is almost entirely Si-based.

This is not only because Si is a cheap material readily available in large quantities and Si technology is a mature well-established technology. Si electronics acquire certain unbeatable advantages in terms of the obtainable overall characteristics of the final integrated chips. These have to do, firstly, with the robustness of Si and its other physical properties that make it suitable for fabrication of active electronic devices with good characteristics. Secondly, its native oxide allows the construction of capacitor structures and field-controlled devices and additionally acts as an excellent insulating and impurity protecting layer thereby facilitating the formation of densely packed integrated circuits [Sedra and Smith].

GaAs-based electronics, on the other hand, have received a lot of attention since the 70's when it was envisaged that GaAs ICs would find a widespread use in high speed system applications. Higher carrier mobilities in GaAs compared to these in Si allow operation at higher speeds. But the main advantage of GaAs is the availability of low-defect semi-insulating substrates. This has a major impact on circuit design since the device to device and device to substrate parasitic capacitances are then considerably minimised [Haigh and Everard] enabling operation at higher speeds. Si-on-Saphire and Si-on-Insulator CMOS technologies have also evolved to overcome the limitations imposed by the doped Si substrates. In general, despite the progressively maturing GaAs technology, in particular MESFET technology being a bright example, there are major disadvantages that have made it apparent that GaAs is not going to displace Si in the majority of applications [Haigh and Everard]. The disadvantages of GaAs are its relatively high power dissipation, relatively small voltage swing, and correspondingly low noise margins, low packing density (mainly a result of the high power dissipation), and low manufacturing yield [Sedra and Smith].

Thus whereas GaAs appears useful for specialised applications requiring high speed and relatively low complexity, Si is expected to be used in the majority of applications as it is ideally suited for lower speed high complexity circuitry. For example, entirely GaAs-based technology may be considered for LANs, but Si electronics are almost certainly going to be used in VLSI. It is evident thus that integration with Si electronics is of great importance.

Integration of III-V optoelectronics with Si electronics

There are three ways III-V optoelectronics may be integrated with Si electronics:-

i. Flip-Chip solder bonding. This technique is more of a hybrid mounting than integration as such [Wada *et al.*, 1990]. The optoelectronic chip is mounted top side down to the electronic chip using solder bump contacts. These act as connections between metallisations on the optoelectronic chip and corresponding ones on the electronic chip simultaneously yielding a self-aligned assembly of the two [Moseley *et* *al.*, 1991]. The optical addressing is done from the substrate thus requiring good AR coatings. This flip-chip bonding may only be employed when the substrate material is transparent at the wavelengths of operation such as for the InGaAs/InP, InGaAs/GaAs and other QW material systems. In the case of the Fabry-Perot modulator, addressing from the substrate requires modified designs since the front mirror of the FP cavity is at the interface with the substrate [Moseley *et al.*, 1990]. Mounting of III-V *electronic* circuitry on a Si supporting block is actually often employed for the reason that the resulting assembly has better mechanical and thermal behaviour as a result of the superior properties of Si in these respects compared with GaAs and InP. This results in overall improved packaging.

ii. Epitaxial lift-off (ELO). Here the main part of the optoelelectronic structure is stripped off the substrate and subsequently mounted on the host substrate either by aligned metallisations [Yoffe *et al.*, 1991] or using Van der Waals bonds on a dielectric finish [Pollentier *et al.*, 1990]. Processing of the optoelectronic part may be done before or after the ELO step in the latter case. This approach, in common with flip-chip bonding, has advantages associated with the much easier processing since the epitaxial regrowth steps are eliminated. Additionally, and very importantly, integration of lattice mismatched semiconductors (such as GaAs and Si) or even non-crystalline materials may be realised without compromising the quality of the materials involved. Spatial alignment of the ELO films to host substrate features may be achieved with good accuracy using rotationally-asymmetric geometries for the sample footprint (Luc Buydens, private communications). Problems that are encountered with the use of Van der Waals bonds are linked with the mechanical robustness of the final assembly and flip-chip is superior to ELO in this respect. ELO is, on the other hand, superior to flip-chip bonding with regard to the avoidance of metal interconnections over large steps that result in increased reactances.

One of the AFPMs in this thesis, QT223 (Chapter 6), has been designed specifically for ELO mounting on a Si substrate at IMEC, Belgium. For this purpose, an AlAs etch-stop layer and several stress-compensating layers have been incorporated in the epitaxial structure below the bottom reflector stack. The front surface of the sample to be mounted on Si is covered in wax and the substrate is etched off to the incorporated etch-stop AlAs layer underneath the reflector stack. The thin sample is now supported by the wax until it is bonded on the new substrate. This latter bonding is in this case achieved using Van der Waals bonding onto a SiO_2 layer on Si. After the substrate is etched off, the difference in lattice constants among the layers that comprise the device will result in a warpage of the sample which, when Van der Waals bonding is used, may prevent successful mounting. Thus stress-compensating layers need to be included which in the case of FP structures is quite difficult due to the high

Al content in the stacks (see Chapter 6). Finally, the devices are electrically connected to the Si electronic circuitry using either fine wires or, ultimately, metal tracks on polyimide (see section 9.2.3).

An AFPM structure mounted on Si has been demonstrated by Yoffe *et al.* [1991], where the back reflector is formed by a thick Au film. This film also comprises one of the contacts as well as the bonding means to an Au metallisation on the Si substrate.

iii. Monolithic heteroepitaxy on Si. This approach is more sophisticated and by far the most demanding. Monolithic integration is no doubt desired, however, it encounteres a number of difficulties. The 4.1% lattice mismatch between GaAs and Si as well as their difference in thermal properties result in a degradation of the quality of the heteroepitaxial material. High densities of dislocations are generated at the interface between the two materials. Consequently, good quality lasers or other minority carrier devices are difficult to be realised [Chong *et al.*, 1987]. Several techniques have been used in attempts to improve the quality of the grown material using for example superlattices at the heterointerface [Yamaguchi et al., 1989; Nozawa and Horikoshi, 1991]. An effective way to diminish the problems associated with this heteroepitaxy seems to be, however, growth on patterned substrates [Dagata *et al.*, 1990; Woodbridge *et al.*, 1992] or in restricted areas using for example some masking process [Coudenys *et al.*, 1992] or other selective growth techniques.

Reflection modulators do not rely on radiative recombination and thus their performance is by far less sensitive to the presence of dislocations. Moreover, because the power dissipated is generally lower than that of lasers there do not seem to be any apparent problems associated with the strain due to the mismatch of the thermal properties between the two materials [Barnes P. *et al.*, 1992]. Indeed, very good AFPM performance has been demonstrated from GaAs on Si [Barnes P. *et al.*, 1991] which is in fact comparable to a similar modulator design in GaAs (51% reflection-change at 8V for a device with no front Bragg stack).

9.2.3 The integrability of the Fabry-Perot modulator.

The class of modulators presented in this thesis falls mainly in the category of vertically integrated structures (section 9.2.1). The same structure can be both a modulator and an efficient detector (Chapter 2) while also the same basic structure may comprise a vertical optical amplifier [Tombling *et al.*, 1991]. This ability to realise different functions is a big advantage of this type of modulator. Thus different types of devices may be realised from the same epitaxial layers and may be integrated in an horizontal form. There are of course disadvantages connected with the compromises brought about by the inevitable non-optimum design. These are, however, to a significant extent relaxed by the possibility of using a dielectric front mirror (Chapter 2) which allows a large degree of flexibility in optimisation of the design of individual devices. Note that the back mirror is, in any case, always preferably highly reflecting. The three types of devices mentioned above may form, when integrated together, a receiver or transmitter module in which case all devices must operate at the same wavelength. This imposes some difficulties since an optical amplifier operates at the vicinity of the exciton peak whereas, as we have seen in this thesis, modulators give their optimum performance at wavelengths longer than the zero-bias exciton peak. Also a QW detector will have a better quantum efficiency when operating under a bias, which implies operation at a wavelength longer than the zero bias exciton. It is evident thus that the integration of these components on the same chip necessitates the use of some bandgap engineering technique to selectively yield different quantum well structures laterally on a wafer (see section 9.2.1). Selective growth poses packing density restrictions which is a very important issue when many complex optical nodes are required to be integrated to achieve parallel architectures (Chapter 1). Impurity free vacancy diffusion appears the technique most suited to this case of vertical devices (section 9.2.1).

The use of the same post-growth technique can be employed to produce a normally-on and a normally-off AFPM from the same wafer [Ghisoni *et al.*, 1991]. Goosen *et al.* [1992] have also demonstrated such operation by selective tailoring of the cavity effects by means of antireflection coatings. However, their technique is not very effective as it does not enable operation of both devices at the same wavelength, which would be a great drawback for most systems, neither does it allow for any form of optimisation of the performance of the individual devices. When using IFVD, and although the absorption coefficient drops with increasing intermixing, the normally-off device (i.e. the most intermixed) will have excess absorber (αd) compared to the normally-on (Chapter 6). The use of dielectric mirrors again enables the minimisation of the effect of the imposed compromises. In this case, the use of a higher front mirror for the normally-on than for the normally-off structure will enable both devices to attain very high contrast. This will also attain a better matching of their operating voltages thereby optimising the performance of composite structures in SEED-like configurations (Chapter 8).

Alternatively, the use of a dielectric cavity on top of an epitaxially grown normally-off AFPM, may produce a device with inverted logic (i.e. reflecting at no bias, in this case) while still showing negative differential resistance (Chapter 8). This would eliminate the need for painful selective growth or post-growth steps. Finally, another element, that is in principle compatible with the FP structure with regard to integration, is the HBT phototransistor the basic structure of which requires an extra n-doped layer on top of, for example, a p-i-n diode.

Thus, normally-on and normally-off devices as well as phototransistors are integrable in close proximity on the same chip. This allows a large flexibility in the realisation of various types of logic, and in general increases the scope for new functionality. For example, Chen *et al.* [1991] have demonstrated a bistable switch using an AFPM, a detector, and a resonant tunnelling diode (this is in the InGaAs/GaAs system). The combination of such a broad variety of functions is a very powerful characteristic of the structures discussed in this thesis, that consequently enhances the potential for the realisation of high complexity smart pixels.

The FP structures may be integrated in dense two-dimensional arrays of devices. The processing of such arrays involves covering of the finished mesa devices (Chapter 2) in an insulating material, such as polyimide, which is subsequently selectively etched off to reveal the top and bottom contact metallisations as wells as to leave the optical windows exposed. Metal tracks connecting to the remote pads are then deposited following the photolithographic step required for lift-off. A completed 4x4 array of devices is shown in Fig.9.2.1. Much larger arrays of individually addressable 10μmX10μm mesa devices are possible to fabricate as has been done for the more complex S-SEEDs [Chirovski *et al.*, 1991].

Finally, it is useful to discuss at this point the successful realisation of AFPM structures in material systems other than GaAs/AlGaAs. An inverted (i.e. addressed from the substrate) AFPM in the InGaAs/InP system has been demonstrated by Moseley *et al.* [1990]. A short period InP/GaAlInAs Bragg stack comprises the front mirror in that structure while the back mirror is formed by a Ti/Au film deposited at the top surface (note that the device is inverted). InP/AlGaAsP mirrors may also be used in this system [Choa *et al.*, 1991].

Hu *et al.* [1991a] have demonstrated AFPM operation in InGaAs/GaAs using GaAs/AlAs mirrors both in addressing from the top and in addressing from the substrate configurations [1991b]. Sale *et al.* [1991] have actually shown S-SEED operation in the InGaAs/GaAs system. Also Buydens *et al.* [1991] have demonstrated an AFPM with InGaAs/AlGaAs quantum wells using again GaAs/AlAs mirrors. Fritz *et al.* [1991] have realised an AFPM using InGaAs/AlGaAs strained layer superlattices as the active medium, while the mirrors are formed by unstrained InGaAs/InAlAs quarter-wave layers grown on a strain-relaxed InGaAs buffer on GaAs. In the GaAs/AlGaAs system, excellent results (high contrast, 1.65dB insertion loss at 4V swing) have been obtained by short period superlattices [Law *et al.*, 1991]. However, this latter result as well as the relatively good results in other material systems the electroabsorptive effects of which are weaker compared with those of GaAs, are solely due to the good cavity designs, i.e. to the increased front and back mirror reflectivities (see Chapter 6). Finally, Pezeshki *et al.* [1992] have realised an AFPM operating in the visible using $Al_{0.45}Ga_{0.55}As$ wells with AlAs barriers (see also Goossen *et al.*, 1992) where the reflector stack is formed by $AlAs/Al_{0.6}Ga_{0.4}As$ quarter wave layers.

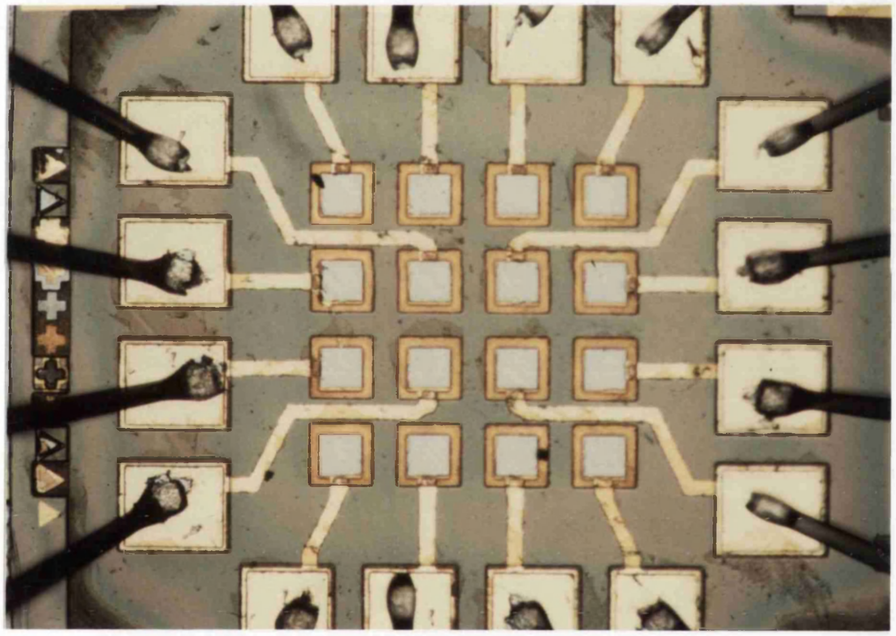

Fig.9.2.1 *A complete bonded 4x4 array of 85μmx85μm mesa devices with 60μmx60μm optical windows. Processing and photograph by Tony Rivers.*

9.3 PROPOSED APPLICATIONS OF FABRY-PEROT MODULATORS IN COMPOSITE DEVICES

In this section we present some novel ideas where the FP quantum well structure is incorporated in composite devices.

Waveguide-to-Vertical (and vice-versa) SEED

We have already introduced the self-electro-optic effect device (SEED) in Chapter 1 and discussed details of its operation in Chapter 8. That type of arrangement may be implemented to perform a conversion from in-plane waveguide operation to free-space and vice-versa. For this purpose, a waveguide modulator may be connected in series with a surface-normal modulator in a vertical integration arrangement as is schematically shown in Fig.9.3.1. With a constant beam incident on the vertical modulator, a digital signal will be imprinted on the reflected signal as imposed by the input to the waveguide. Alternatively, a signal incident on the vertical device can be imprinted on the beam leaving the waveguide. The two devices used may be operated either in their normally-on or their normally-off mode, where when at least one of the two shows negative differential resistance bistability may be obtained from the composite structure. This is, however, not necessary as the proposed element is aimed

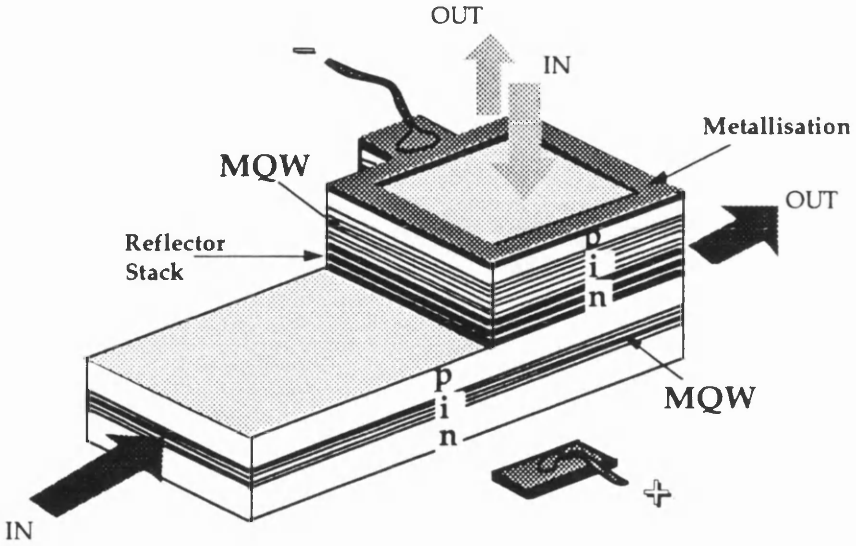

Fig.9.3.1 *A schematic of the combination of a waveguide with a surface-normal reflection modulator to produce a converter from the in-plane to the surface-normal mode and vice-versa. Care is needed that the performance of the waveguide is not affected by the presence of the top layers, which may imply differing lateral positions for the two components.*

at a mode conversion rather than the realisation of a logic function (at this stage it is difficult to forsee an application for a logic element in this form).

The wavelengths of the light in the two modes can be different from one other. Also the powers may be unequal to allow for control of a large power beam by a lower power one, provided careful design has been performed. The vertical modulator may be realised by a double-pass reflection structure (Chapter 1). However, the use of an AFPM will be advantageous not only because of the superior performance of that device (Chapter 2) but also because the low voltages of operation make it easier to match those of a waveguide structure (Chapter 1).

FP T-SEED

As mentioned in Chapter 1, the connection in series of a transistor with a modulator results in a composite device where the input to the transistor and the output from the (pumped with a constant beam) modulator show a characteristic with two well defined on- and off- states. This device may be used to perform optical logic and in general take part in a complex node or smart pixel [Taylor, 1990].

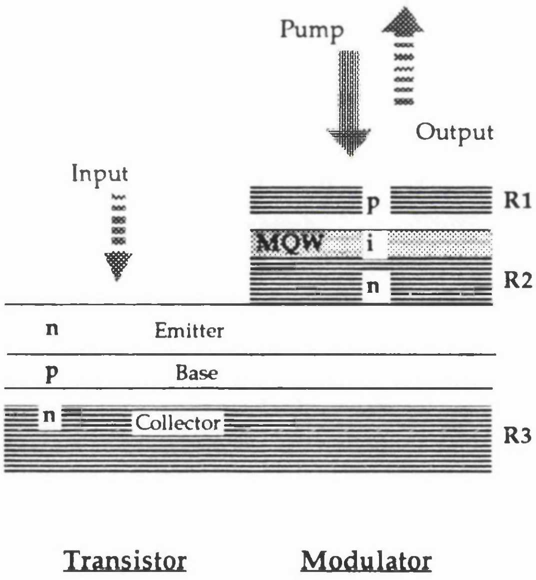

Fig.9.3.2 *A schematic of the proposed configuration for a T-SEED. The modulator part is an AFPM and the transistor part is also a resonant structure. R1, R2, and R3 are the reflectivities of the corresponding Bragg stacks.*

Taylor [1990] had proposed the use of an AFPM to comprise the modulator element in such an arrangement, thereby obtaining better contrast. In that proposal the layers from top to the substrate are as follows: a p-type reflector stack followed by a pi(MQW)-n modulator, and finally an n-p-n transistor. Subsequently, this would be flip-chip bonded to a host supporting block (such as sapphire) and the substrate etched off thereby yielding an AFPM window at places where the transistor layers are etched off or a transistor window otherwise. This device has an inherent inflexibility in terms of the AFPM design, involves a certain difficulty concerning the quality of the top surface of the AFPM after the long etching process, and also requires an AR coating at the transistor surface.

Kurokawa *et al.* [1992] have demonstrated a T-SEED where they use a Bragg mirror between the modulator and transistor elements to achieve optical isolation between the two. The modulator and the transistor are addressed from the top and the substrate respectively. AR coatings are used to avoid Fabry-Perot effects.

Here we propose an arrangement where both elements are addressed from the top surface, making the device much more flexible in terms of addressing and integrating, and they are mutually optically isolated by a reflector stack. The modulator is an AFPM with a front mirror (R1) that can be designed as required to optimise the performance (Fig.9.3.2). The transistor also takes advantage of the FP effects so as to absorb all the incident light thereby increasing its efficiency [Ünlü *et al.*, 1990]. In this design we are actually making use of the finite length and the phase change introduced from a Bragg reflector stack (Chapter 8) to produce this structure where the cavity that corresponds to the final transistor element (on the left in Fig.9.3.2), thus without a front mirror, is at a resonance whereas the cavity formed between the two lower mirrors (R2 and R3) is at an antiresonance. This latter cavity acts then as a highly reflecting back mirror for the modulator part. In that way the optical pump beam to the modulator will have only a negligible direct effect on the transistor. The etching step required to reveal the transistor must be done using some in-situ monitoring and control of the etching process (Chapter 5) so as to accurately stop directly after the second reflector stack (R2). It should be noted, however, that a slight error would not have a tremendous effect on the operation of the transistor since the resonance will be reasonably broad (low finesse).

Thus, in this design we manage to both increase the transistor efficiency, by making use of the FP effects, and achieve an improved modulator performance using the AFPM. This device is expected to outperform any previous such structure (i.e. T-SEED) and thus be a very efficient high contrast switch with inherent gain that may lend itself to an array of optical systems (Chapter 1).

Integrated externally modulated surface emitting laser diode

Chirp in directly modulated lasers [Surbo, 1986] has promoted external modulation, especially so in telecommunications links where it limits the bandwidth and the speed of operation [Ribot *et al.*, 1989]. Here we propose a vertically integrated device where a surface emitting laser is externally modulated using a FP MQW modulator.

The structure is shown in Fig.9.3.3. The modulator constitutes in effect an electrically controlled mirror that will promote lasing when at its high-reflection state, and will prevent lasing when at its low-reflection state. Indeed, if the laser is injected at just above the threshold current corresponding to the highly reflecting state of the modulator, a decrease of the reflectivity by a sufficient amount will destroy the carrier balances and pull the laser to a non-lasing state since the threshold current will then be increased (decreased cavity efficiency). However, since the carrier build-up continues taking place in the laser, chirping will be diminished.

The mirrors for surface emitting lasers are required to be quite high so as to achieve low threshold currents [Coldren *et al.*, 1992; Hasnain *et al.*, 1992]. Thus the modulator is required to have a characteristic with a very low insertion loss as the mirrors for the surface emitting lasers must be very high to achieve lasing at reasonable current densities. Thus the on-state reflectivity of the modulator ought to be preferably $R_{on}>99\%$ while a relatively small reflection change (estimated <20%) ought to suffice allowing at the same time for a certain tolerance in the injection levels (Cai Bo, private communications). This modulator performance may be realised by a double-pass reflection modulator operated very far from the exciton (implying a high operating voltage). Alternatively, a normally-on AFPM may be used where only a fraction of the critical amount of absorber is incorporated in the cavity and the back reflector is as highly reflecting as may be realised (Chapter 6). Another option is to use a SCEM with a very high front mirror and a lower back mirror so as to obtain the required large on-state reflectivity (Chapter 8). In either case the quantum wells in the

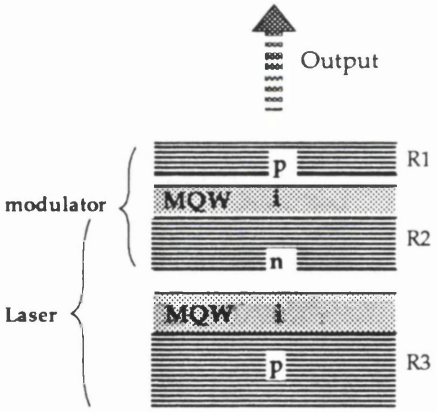

Fig.9.3.3 *The double cavity arrangement to realise an integrated externally modulated surface emitting diode. See text for details.*

modulator would have to be narrower than those in the laser structure since the laser operates at best at the vicinity of the heavy-hole exciton peak, while all the modulator structures mentioned above operate at wavelengths longer than the zero-bias exciton.

This structure is realisable in this form thanks to the decoupled double cavity configuration discussed in Chapter 8. Thus with correct design, there is no coupling between the top and the bottom cavity. The cavity formed between R1 and R2 as well as that formed between R2 and R3 may be at a resonance without the longer cavity being formed between R1 and R3 being at a resonance. The problem of this configuration is, however, that it is very demanding on the epitaxial growth and it is not very tolerant to any deviations from the designed structure or from the optimum operational conditions. Worse, deviations from the optimum conditions could cause the device to cease to operate altogether.

Fritz *et al.* [1989] have demonstrated an electrically modulated mirror in GaAs/AlGaAs and Blum *et al.* [1991] have realised such a mirror in the InGaAs/InP material system, both using similar complex Bragg stacks where one of the $\lambda/4$ layers in the stack is in fact a MQW region. Modulation is achieved mainly by means of the electroabsorptive effects, which, however, limits the maximum reflectivity of the mirror while the attained changes in transmission are quite low (≈14%). The use of a modulator is by far preferable in terms of the flexibility, and the optimisation, of the performance characteristics. Our proposed structure is an efficient compact form of an externally modulated laser that would be quite valuable in optical communications and optical processing applications.

Tunable detector/ add-drop filter, demultiplexer

In Chapter 8 we saw that the SCEM is an inherently highly wavelength selective device which is a disadvantage for a modulator, while at the same time it denotes the low tolerances of that structure. However, this very characteristic may be actually exploited to produce devices where wavelength selectivity is desired. Furthermore, a combination of a) IFVD (section 9.2.1), to shift the excitonic features to shorter wavelengths, b) dielectric front mirrors, to leave the cavity exposed, and c) etching back, to tune the cavity length to the wavelength required for each individual device [Ünlü *et al.*, 1990], may produce a composite device that consists of many SCEMs that operate at distinct wavelengths. The control of the amount of intermixing by the different oxide thicknesses enables the realisation of a fully integrated such device as discussed earlier. The composite device is schematically shown in Fig.9.3.4.

A large number of wells needs to be incorporated in this structure so as to compensate for the loss in absorption and the broadening of the excitonic peaks that follows the IFVD process. The consequent broadening in particular, requires operation at increasingly larger distances from the zero bias exciton peak for the more diffused wells. In total, a good SCEM performance has been calculated to be attainable by different, (i.e. in differing degrees intermixed) devices.

Eventually thus, the SCEM modulation characteristic can be obtained at different wavelengths from individual devices in close proximity to one other. The spacing of the channels can be very small by using long cavity lengths, however, a reasonable spacing may be estimated to about 1-2nm. The trade-off involved here is brought about by the fact that as the resonance becomes sharper, allowing thus for dense channel spacing, the tolerances of the structure are increasingly diminished.

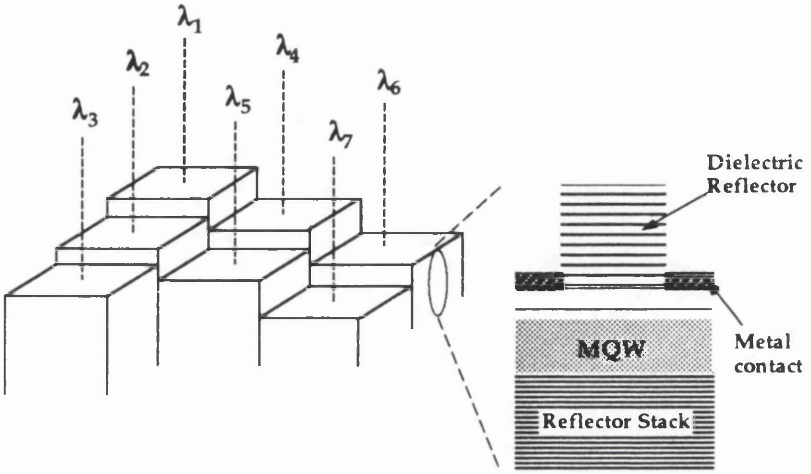

Fig.9.3.4 *SCEM operation may be obtained at different wavelengths from adjacent devices on the same wafer. The QW effects are post-growth shifted using IFVD, the resonant wavelength is tailored by etching, and a (common design) dielectric mirror is deposited to realise the SCEM configuration.*

With all devices biased bar one, only that one of the wavelengths incident on the composite device will be absorbed and thus a tunable detector is realised. With the multiple wavelengths going through the devices in sequence of increasing wavelength (by means of an hologram or a mirror in the simple case), any wavelengths may be chosen to be picked out thereby realising a drop-out filter in both the reflection and the photocurrent mode. This action is complementary simultaneously in the two modes. Finally, this arrangement may act as a demultiplexer in free-space links.

In the case of the tunable detector and the filter configurations, there is a restriction in the overall range of wavelengths that may be used. This is imposed by the resonance that lies at shorter wavelengths (lower order) than that of operation and which will cause the devices to absorb the corresponding wavelengths, in addition to their prime wavelength of operation and obviously regardless of the voltage applied to the terminals of the device. A typical range is ≈30nm as obtained for a high-finesse device of typical cavity length. There is no such restriction of range for the straight demultiplexer where the devices are addressed in sequence of increasing wavelength, provided of course the absorptance of the devices at their operating wavelengths is sufficiently high.

The problems encountered with this structure are brought about firstly by its low tolerance that requires a good design, to yield reasonable operation by all devices, and also requires stable operating conditions, mainly a control of the ambient temperature. The IFVD process is potentially controllable and reproducible [Ghisoni, 1992] and the etching back step may be carried out very accurately using in-situ optical monitoring (Chapter 5). One serious consideration is the accuracy in the deposition of the front mirror which, unlike other steps of the overall fabrication process, may only be corrected by a repeat. This front mirror (one single for all devices) also poses difficulties in designing the structure as the phase-change introduced by it is wavelength dependent. Note that the phase-change modifies the cavity length required to obtain the resonance at a certain position and therefore it may result in a severe alteration of the device performance.

Tunable detection, add-drop filtering and demultiplexing are valuable functions [see for example Ragdale *et al.*, 1992]. The composite device proposed here would be a very useful element for systems where the capacity of the links has been extended by the implementation of wavelength division multiplexing.

9.4 SUMMARY.

In this final Chapter we have examined the FP modulator in terms of its potential to take part in complex integrated optoelectronic modules. Firstly, we have explained the role of integration and the means by which the modulator may be integrated with other optoelectronic devices as well as with electronic circuitry. We have subsequently focussed on the versatility of the FP structure and have pointed out how it may lend itself to efficient integrated modules of complex functionality. The large range of ultimately integrable devices that may be realised by the same basic structure opens up a broad area of applications and establishes an increased scope for novel configurations. We have raised the main issues involved in the matching of the various components and have pointed out how the work presented in this thesis may be employed to yield an optimisation of the overall performance.

Finally, we have proposed some novel composite devices where the FP modulator plays a key role. These and other possible configurations may be implemented in a range of applications in optical communications and processing.

CONCLUSION

The work described in this thesis started with the asymmetric Fabry-Perot modulator (AFPM), a device that had been demonstrated to exhibit contrast over 20dB, reflection change of 45%, at operating voltages of 9V. It appeared that there was scope for a thorough investigation and performance optimisation of this type of structure which we decided would be directed towards an examination of the achievable characteristics under real operating conditions.

The work carried out for this thesis includes a number of distinct contributions which have advanced the field in the following ways:-

We have shown that the AFPM can exhibit very high contrast and large reflection changes with low operating voltages. Specifically, we have demonstrated 13dB contrast, 52% change in reflectivity, with 3.4V. The result is significant because it opens up the possibility of driving modulators from standard electronic circuitry thereby enhancing the attraction of the implementation of AFPMs as interface elements between optics and electronics.

We have developed a number of design procedures which allow optimum design of AFPMs for a variety of specifications, involving both quantum well optimisation and micro-resonator optimisation. Realistic modelling has predicted that contrasts in excess of 20dB, reflection changes over 90%, may be attained at operating voltages below 3V. A detailed investigation has highlighted the flexibility of the AFPM showing quantitatively how various performance characteristics can be traded-off in different designs. Our procedures permit tailored design to predefined specifications.

The structures used are inherently sensitive to variations in thickness and composition of the layers during fabrication, temperature changes, and operational conditions such as operating voltage and optical wavelength as well as the angle of incidence when optically addressing them. We have studied these sensitivities in detail and developed designs which are least sensitive to these problems. Specifically, we have shown that it is possible to obtain good device performance over a temperature range of ≈20°C which is encouraging because this degree of tolerance can be coped with in many applications by unsophisticated control systems. Additionally, several ways of improving this sensitivity have been examined experimentally. Variations in layer thickness during growth are probably the most restrictive of all parameters involved in the AFPM. Indeed, whilst individual devices can be produced and small arrays can be fabricated, the stringent imposed requirements cannot be fully provided in current growth systems if high yields are demanded. We have suggested various ways of dealing with this among which is our proposed use of a new double-cavity arrangement that results in an improvement of the overall tolerances in applications where large reflection changes are required. Nevertheless, a satisfactory solution of this problem requires further advancements in epitaxial growth systems.

We have proposed, demonstrated, and investigated in detail the Symmetric Cavity Electroabsorption Modulator (SCEM). The work was developed independently but the idea was first published by others. We showed that the device is suitable for normally-off operation, demonstrated a record reflection-change in that mode, and for the first time switching using a symmetric self-electro-optic effect device (S-SEED) configuration.

We have attempted to evaluate critically the role micro-resonator modulator devices may play in future optoelectronic systems where versatility and integrability are particularly important. The course of this work generated some ideas that we maintain further enhance the attraction of such modulators in that respect, and we proposed a number of new integrated configurations and novel composite device structures.

The AFPM has been realised in III-V materials other than GaAs/AlGaAs. The insights gained from our work in this thesis may be implemented in the optimisation of these as well as yield efficient operation in other III-Vs such as the GaInP/AlInP and InGaAlP/GaAs systems. Furthermore, resonant devices may also be attempted in materials that are currently at a less developed stage, such as II-VIs that have received a lot of attention in the last couple of years, or Si/Ge.

The course of this work has highlighted various aspects of the modulator that need further investigation. In most applications it is desirable that the device can handle large optical powers and therefore it is important to examine the impact of saturation effects upon the performance. Another area of particular practical interest is the optical addressing by a highly converging beam, as is required for high-speed operation where the device features are scaled down to a few microns. This may lead to diminished modulation depth.

But at this stage of development it is particularly important that applications-oriented prototype systems are demonstrated and future work should progressively head in that direction. Hence steps towards narrowing the evident gap between component-building and systems-architecture are required that will ultimately facilitate a sober evaluation of the potential of actual implementations. This asks for advancements in the purely technological side of assembled miniature optics, a closer link with the inevitable hosting electronics, and efficient sophisticated integration.

ACKNOWLEDGEMENTS

First of all I would like to thank my supervisor, Gareth Parry, whose breadth and depth of knowledge has been an indispensable source of guidance. I greatly appreciate his and John Midwinter's efforts that have provided, in many respects, a high calibre environment to work in.

This work would not have been completed were it not for the contributions of various individuals. I am indebted to John Roberts of the University of Sheffield for the growth of often demanding structures. Tony Rivers' expert processing ensured the devices materialised and I am also grateful to him for hours of cleanroom coaching. Peter Stevens developed the theory for the model used in this work (which he patiently explained...) and Mark Whitehead's pioneering work on the AFPM gave me a well-founded and interesting project to work on. I am thankful to Mark Abbott, the computer guru, not only for his actual assistance but also because at solo moments of panic over my inconsistent programming his potential assistance has been a great consolation. Many thanks go to all former members of the Digital Optics Group, especially Craig Tombling, Mark Whitehead, Peter Stevens, David Atkinson and Mic Taylor, for the background work they have done for the group. Also Kevin Lee, Fred Stride, Tony Overbury, Chris Carey and Pask Visocchi have provided technical assistance, and many others in the department have always been ready to help.

But I am especially grateful to my near-colleagues and companions in the DOG, whose parallel efforts have certainly benefited mine. I would like to thank Marco Ghisoni and Paul Barnes who shared the very same four-year-long journey, and (in sequence of appearance) Mic Taylor, David Atkinson, Robert Grindle, and Paul Stavrinou, as well as new-comers, who shared part of it. Alas, some follow the doctrine 'the cause justifies the means'.

I am indeed indebted to the Greek State Scholarships Foundation not only for financially supporting me through the major part of my studies, but mainly for giving me the opportunity to come here in the first place. Support for the final year was provided by the European programme FOCUS and the project was funded by the UK SERC.

APPENDIX

DETAILS ON MODELLING

A.1 Evaluation of the sub-band energies

As mentioned in Chapter 3, the sub-band energies and overlap integrals were obtained using the model developed by Peter Stevens that uses the tunneling resonance technique. In Chapter 3 we gave a brief outline of that technique. The parameters used for those calculations are listed below.

There are two approaches to account for the non-parabolic bands, where the effective masses are either assumed velocity-dependent or energy-dependent. These have been presented by Hiroshima and Lang [1986] and Nelson *et al.* [1987a]. An energy dependent effective mass has been employed in the calculations of Stevens [1989] that we use when the modelling the absorption spectra. Thus the effective mass $m_\perp^*(E)$ of the particles in the direction perpendicular to the layers, is given by

$$m_\perp^*(E) = m_\perp^* \cdot \left[1 + (E - V)/E_{np}\right]$$
$$\text{where} \quad E_{np} = \hbar^2 / m_\perp^* \gamma$$

where E is the energy of the respective particle, V is the potential at the position of interest (be it in the well or in the barrier material) and γ is the band non-parabolicity. This expression for the mass refers to both the electron in the conduction band and the hole in valence band.

The effective masses [Miller R C *et al.*, 1984], bandgaps [Casey and Panish], band offset ratios [Duggen *et al.*, 1985], and non-parabolicity parameters [Nelson *et al.*, 1987a] used for the modelled GaAs/AlGaAs system are shown in the Table below, where x is the Al concentration.

Parameter	**Value**
Electron mass (m_0)	*0.0667+0.0835 x*
Heavy hole mass (m_0)	*0.34+0.412 x*
Light hole mass (m_0)	*0.094+0.066 x*
Bandgap Energy (eV)	*1.4247+1.247 x*
Band offset ratio (%)	*65*
Electron non-parabolicity (m^2)	*4.9×10^{-19}*
Light hole non-parabolicity (m^2)	*7.35×10^{-19}*

A.2 Evaluation of the absorption spectra

The binding energies required in order to obtain the position of the final transition have been assumed field-independent and well width dependent, as mentioned in Chapter 3. The values used in our model have been obtained by a polynomial fit to those reported by Ekenberg and Altarelli [1987], and are finally given by

$$\begin{aligned} E_b^{hh} &= 25.135337 - 0.63813686 \cdot L_w + 1.0720868 \cdot 10^{-2} \cdot L_w^2 \\ &- 9.1849721 \cdot 10^{-5} \cdot L_w^3 + 3.8235542 \cdot 10^{-7} \cdot L_w^4 \\ &- 6.1557315 \cdot 10^{-10} \cdot L_w^5 \end{aligned}$$

$$\begin{aligned} E_b^{lh} &= 25.422539 - 0.56194801 \cdot L_w + 9.6858652 \cdot 10^{-3} \cdot L_w^2 \\ &- 8.6270938 \cdot 10^{-5} \cdot L_w^3 + 3.7064877 \cdot 10^{-7} \cdot L_w^4 \\ &- 6.1224895 \cdot 10^{-10} \cdot L_w^5 \end{aligned}$$

where hh denotes the heavy hole and lh denotes the light hole, L_w is the well width in Å, and the obtained binding energy values are in meV.

The masses used in the calculation of the absorption spectra refer to the motion of the particles within the plane of the wells. The heavy and light hole masses in the direction parallel to the layers differ from their values in the perpendicular direction and are given by [Chemla and Miller, 1985]

$$m_{hh}^* = \frac{4 \cdot m_{\perp hh}^* \cdot m_{\perp lh}^*}{3 \cdot m_{\perp hh}^* + m_{\perp lh}^*}$$

$$m_{lh}^* = \frac{4 \cdot m_{\perp hh}^* \cdot m_{\perp lh}^*}{m_{\perp hh}^* + 3 \cdot m_{\perp lh}^*}$$

where $m_{\perp hh}^*$ and $m_{\perp lh}^*$ are the heavy and light hole masses, respectively, in the direction perpendicular to the layers (see above). The exciton reduced mass is given by

$$\mu = \frac{m_c^* \cdot m_v^*}{m_c^* + m_v^*}$$

where m_c^* is the mass of the electron in the conduction band and m_v^* is the mass of the particle in the valence band, i.e. the mass of either the heavy or the light hole as expressed by the preceding equations. The Rydberg is then given by (in eV)

$$R_y = \frac{e^4 \mu}{8 \varepsilon^2 h}$$

where ε is the material permittivity, and h is Planck's constant. Depending on whether the reduced mass μ of the heavy-hole associated or the light-hole associated exciton is used in this equation, the corresponding Rydberg is found. This value is subsequently used to calculate the exciton area relative to the continuum level (Chapter 3).

The Sommerfeld factor, that is included in the continuum of states when evaluating the absorption spectra, varies with photon energy E as given by

$$S(E) = \frac{2}{1 + e^{-2\pi\sqrt{R_y / \left(E - E_{cv}^{ij}\right)}}}$$

where S(E) above starts at the corresponding band-edge E_{cv}^{ij} and R_y is the corresponding Rydberg constant.

Broadening

The thermal lineshape employed in our model is a Lorentzian with exponential tails. We give details of the empirically derived exponential roll-off in Chapter 3. The Lorentzian used is the one used by Peter Stevens.

The Lorentzian lineshape centred at the exciton position E_{ex} is given by

$$L(E) = \frac{\Gamma_T}{2\pi \cdot \left[(E - E_{ex})^2 + (\Gamma_T / 2)^2 \right]}$$

$$\Gamma_T = \frac{\Gamma_{ph}}{e^{(h\Omega/kT)} - 1}$$

where Γ_{ph} is clearly an important parameter the empirical derivation of which is explained below, Γ_T is the FWHM of the Lorentzian, k is Boltzman's constant, T is the temperature (K), and Ω is the LO phonon energy (37meV) [see Chemla *et al.*, 1984]

The FWHM of this lineshape was derived by a fit to experimental data. Specifically, the heavy-hole exciton linewidth was measured as a function of temperature. Then the linewidth Γ_{ph} employed in the Lorentzian above was estimated as that which provided the best fit to the obtained data after a convolution with a Gaussian that corresponded to one monolayer fluctuation of the well thickness and a square lineshape to account for broadening due to field non-uniformities. The details of this are given in Peter Stevens' Ph.D. thesis [1989].

Finally, let us refer to the field-induced broadening. We have given a description of the technique employed to account for field-induced broadening in Chapter 3. It is useful to note here that in the field-versus-distance diagram (see Chapter 3), the area underneath the curve within the intrinsic region is equal to the total voltage, i.e. $\text{Area} = V + V_{bi}$ where V is the applied voltage and V_{bi} is the built-in field. The slope of that curve is a function of the doping concentration N_b and is given by $\text{slope} = N_b \cdot |e| / \varepsilon$. These allow the calculation of the field seen by individual wells.

REFERENCES

Acklin B, Bagnoud C, Dupertuis M A, Wuethrich C : "*Design and investigation of a nonlinear Fabry-Perot device with GaAs spacer layer*", 6th Workshop on 'Optical Functions in Computers', SFO , Strassbourg 1990.

Amano C, Matsuo S, Kurokawa T: "*Novel photonic switching arrays consisting of vertically integrated multiple quantum well reflection modulators and phototransistors: Exciton absorptive reflection switch*", Phot. Tech. Lett, 3(8), pp 736-738, 1991.

Amano C, Matsuo S, Kurokawa T, Iwamura H: "*20dB contrast GaAs/AlGaAs multiple quantum well non-resonator modulators*", Phot. Tech. Lett, 4(1), pp 31-33, 1992.

Aoki M, Takahashi M, Susuki M, Sano H, Uomi K, Kawano T, Takai A: "*High-excitation-ratio MQW electroabsorption modulator integrated DFB laser fabricated by in-plane bandgap energy control technique*", IEEE Phot. Tech. Lett., 4 (6), pp 580-582, June 1992.

Asada M, Kameyama A, Suemune Y: "*Gain and intervalence band absorption in quantum well laser*", IEEE J. Quant. Elect., QE-20, pp 745-753, 1984.

Atkinson D, Parry G, Austin E J: "*Modelling of electroabsorption in coupled quantum wells with applications to low-voltage optical modulation*", Semicond. Sci. Tech., 5, pp 516-524, 1990.

Atkinson D: Ph.D. thesis, University of London, 1990.

Babic D I, Corzine S W: "*Analytic expressions for the reflection delay, penetration depth, and absorptance of quarter-wave dielectric mirrors*", IEEE J. Quantm. Elect., 28(2), pp 514-524, 1992.

Ballance J W, Roberts P H, Halls M F: "*ATM access through a passive optical network*", Elect. Lett., 26 (9), pp 558-560, April 1990.

Barnes N, Healey P, Rejman-Greene M A Z, Scott E G, Webb R P: "*16-channel parallel optical interconnect demonstration with an InGaAs/InP MQW modulator array*", Elect. Lett., 26 (15), pp 1126-1127, July 1990a.

Barnes N, Healey P, McKee P, O'Neil A W, Rejman-Greene M A Z, Scott E G, Webb R P, Wood D: "*High speed optoelectronic neural network*", Elect. Lett. 26 (15), pp 1110-1112, July 1990b.

Barnes P, Stride A A, Parry G, Roberts J S, Button C: "*Low voltage GaAs on Si reflection modulators with 51% reflection change*", Elect. Lett., 27 (24), pp 2283-2284, Nov 1991.

Barnes P, Woodbridge K, Roberts C, Stride A A, Rivers A W, Whitehead M, Parry G, Zhang X, Staton-Bevan A, Roberts J S, Button C C: "*GaAs multiple quantum well microresonator modulators grown on Silicon substrates*", Optcl. Quantm. Elect., 24 (2), pp 5177-5192, 1992.

Barron C C, Whitehead M, Law K K, Scott J W, Heimbuch M E, Coldren L A: "*K-band operation of asymmetric Fabry-Perot modulators*", IEEE Phot. Tech. Lett., 4 (5), pp 459-461, May 1992.

Berger P R, Dutta N K, Choquette K D, Hasnain G, Chand N: "*Monolithically Peltier-cooled vertical-cavity surface-emitting lasers*", Appl. Phys. Lett., 59 (1), pp 117-119, July 1991a.

Berger P R, Dutta N K, Sivco D L, Cho A Y: "*GaAs quantum well laser and heterojunction transistor integration using molecular beam epitaxial regrowth*", Appl. Phys. Lett. 59 (22), pp 2826-2828, Nov 1991b.

Bertolotti M, Bogdanov V, Ferrari A, Jascow A, Nazorova N, Pikhtin A, Schirone L: "*Temperature dependence of the refractive index in semiconductors*", J. Opt. Soc. Amer., B/ 7(6), June 1990.

Beyette F P, Geib K M, Feld S A, An X, Hafich M J, Robinson G Y, Wilmsen C W: "*Integrated optical NOR gate*", IEEE Phot. Tech. Lett., 4 (4), April 1992.

Beyler C A, Hummel S G, Frateschi N, Dapkus P D: "Small dimension Bragg reflectors formed by air-isolated GaAs layers", Elect. Lett., 27 (7), pp 588-590, 1991.

Blakemore, J.S.: "*Semiconductor and other major properties of Gallium Arsenide*", J. Appl. Phys., 53(10), pp. R123-R181, 1982.

Blum O, Zucker J E, Chiu T H, Divino M D, Jones K L, Chu S N G, Gustafson T K: "*InGaAs/InP multiple quantum well tunable Bragg reflector*", Appl. Phys. Lett., 59 (23), pp 2971-2973, Dec. 1991.

Boyd G D, Miller D A B, Chemla D S, McCall S L, Gossard A C, English J H: "*Multiple quantum well reflection modulator*", Appl. Phys. Lett 50 (17), pp 1119-1121, April 1987.

Boyd G D, Fox A M, Miller D A B, Chirovsky L M F, D' Asaro L A, Kuo J M, Kopf R F: "*33ps optical switching of symmetric self-electrooptic effect devices*", Appl. Phys. Lett. 57 (18), pp 1843-1845, Oct 1990.

Boyd G D, Livescu G: "*Electroabsorption and refraction in Fabry-Perot quantum well modulators: A general discussion*", Optcl. Quantm. Electr., 24 (2), S147-S166, 1992.

Buydens L, Demmester P, Yu Z, Van Daele P: "*High-contrast/low-voltage normally on InGaAs/AlGaAs asymmetric Fabry-Perot modulator*", Phot. Tech. Lett., 3(12), pp 1104-1106, 1991.

Buydens L, Demeester P, Van Daelle P: "*Asymmetric Fabry-Perot modulators with InGaAs/ AlGaAs active region*", Optcl. Quantm. Elect., 24 (2), S167-S176, 1992.

Casey H C, Panish M B: "Heterostructure lasers", Academic Press, 1978.

Chan W K, Harbison J P, Von Lehmen A C, Florez L T, Nguyen C K, Schwarz S A: "*Optically controlled surface emitting lasers*", Appl. Phys. Lett., 58 , pp 2342-4, 1991.

Chand N, Chu S N G : "*Origin and improvement of interface roughness in AlGaAs/GaAs heterostructures grown by molecular beam epitaxy*", Appl. Phys. Lett., 57 (17), pp 1796-1798, Oct. 1990.

Chemla D S, Damen T C, Miller D A B, Gossard A C, Wiegmann W: "*Electroabsorption by Starck effect on room-temperature excitons in GaAs/AlGaAs multiple quantum well structures*", Appl. Phys. Lett., 42, pp 864-6, 1983.

Chemla, D S, Miller D A B, Smith P W, Gossard A C, Weigmann W: "*Room temperature excitonic nonlinear absorption and refraction in GaAs/AlGaAs multiple quantum well structures*", IEEE J. Quantm. Elect., QE-20, pp 265-275, 1984.

Chen L, Kappe R M, Hu K, Madhukai A: *"High-contrast optically bistable optoelectronic switch based on InGaAs/GaAs (100) asymmetric Fabry-Perot modulator, detector, amd resonant tunneling diode"*, Appl. Phys. Lett., 59 (13), pp 1523-1525, Sept. 1991.

Chirovsky L M F, Focht M W, Freund J M, Guth G D, Leibenguth R E, Przybylek G J, Smith L E, D'Asaro L A, Lentine A L, Novotny R A, Buchholz D B: "*Large arrays of Symmetric-Self-Electro-optic-Effect devices*", IEEE/OSA Proc. on 'Photonics Switching',pp 56-59, Salt Lake City, Utah, March 1991.

Choa F S, Tai K, Tsang W T, Chu N G: *"High reflectivity 1.55mm InP/InGaAsP Bragg mirror grown by chemical beam epitaxy"*, Appl. Phys. Lett., 59 (22), pp 2820-2822, Nov. 1991.

Chong T C, Fonstad C G: *"Low threshold operation of AlGaAs/GaAs multiple quantum well lasers on Si substrates by molecular beam epitaxy"*, Appl. Phys. Lett., 51 (4), pp 221-223, July 1987.

Coldren L A, Geels R S, Corzine S W, Scott J W: "*Efficient vertical cavity lasers*", Optcl. Quantm. Elect., 24 (2), S105-S120, 1992.

Corzine S W, ˇYan R H, Goldren L A: ˇ"*A tanh substitution technique for the abrupt and graded interface multilayer dielectric stacks*", IEEE J. Quantm. Elect., 27(9), pp 2086-2090, 1991.

Coudenys G, Moerman I, Zhu Y, Van Daele P, Demeester P: *"Multiwavelength InGaAs/InGaAsP strained-layer MQW-laser array using shadow-masked growth"*, IEEE Phot. Tech. Lett., 4 (6), pp 524-526, June 1992.

Dagata J A, Tseng W, Bennett J, Evans C J, Schneir, Harary H H: *"Selective-area epitaxial growth of gallium arsenide on silicon substrates patterned using a scanning tunneling microscope operating in air"*, Appl. Phys. Lett. 57 (23), pp 2437-2439, Dec. 1990.

Dagenais M, Leheny R F, Temkin H, Bhattacharya P: *"Applications and challenges of OEIC technology: A report on the 1989 Hilton head workshop"*, IEEE J. Lightwv. Tech., 8 (6), pp 846-861, June 1990.

Deppe D G, Holonyak N Jr: *"Atom diffusion and impurity layer disordering in quantum well III-V semiconductor heterostructures"*, J. Appl. Phys., 64 (12), R93-R113, Dec. 1988.

Dhoebt B, De Dobbelaere P, Baets R, Houssay B: *"Micro-optic imaging systems for optical board-to-board interconnect: a comparison of lens systems"*, OSA 'Gradient-Index Optical Systems' topical meeting, Monterey, April 1991.

Duggan G, Ralph H I, Moore K J: *"Reappraisal of band-edge discontinuities at the AlGaAs-GaAs haterojunction"*, Phys. Rev. B, 32, pp 8395-8397, 1985.

Ekenberg U, Altarelli M: *"Exciton binding energy in a quantum well with inclusion of valence band coupling and non-parabolicity"*, Phys. Rev. B, Vol. 35, pp 7585-7595, 1987.

Facanha H S, Selviah D R, Steptoe K, Zhi-Qiang M: "Design of Fresnel holograms for optical interconnections of VLSI", 2nd IEEE Int. Conf. on' Holographic Systems Components and Applications' No 311, pp 213-217, 1989.

Feldman M R, Guest C C: *"Interconnected desnity capabilities of computer generated holograms for optical interconnection of very large scale integrated citcuits"*, Appl. Optcs., 28 (15), 3134-3137, Aug. 1989.

Feldmann J, Goossen K W, Miller D A B, Fox A M, Cunningham J E, Jan W Y: *"Fast escape of photocreated carriers out of shallow quantum wells"*, Appl. Phys. Lett., 59(1), pp 66-68, July 1991.

Fox A M, Miller D A B, Livescu G, Cunningham J E, Henry J E, Jan W Y: *"Exciton saturation biased quantum wells"*, Appl. Phys. Lett., 57 (22), pp 2315-2317, Nov 1990.

Fox A M, Miller D A B. Livescu G, Cunningham J E, Jan W Y: *"Quantum well carrier sweep-out: Relation to electroabsorption and exciton saturation"*, IEEE J. Quantm. Elect., 27 (10), pp 2281-2295, Oct 1991.

Fritz I J, Gourley P L, Drummond T J: *"Electric field response of a semiconductor superlattice optical mirror from electroreflectance spectra"*, Appl. Phys Lett., 55 (13), Sept.

1989.

Fritz I J, Myers D R, Vawter G A, Brennan T M, Hammons B E: "*Novel reflectance modulator employing an InGaAs/AlGaAs strained-layer superlattice Fabry-Perot cavity with unstrained InGaAs/InAlAs mirrors*", Appl. Phys. Lett., 58 (15), pp 175- 176, April 1991.

Fujita S, Suzaki T, Matsuoka A, Miyazaki S, Torikai T, Nakata T, Shikata M: "*High sensitivity 5Gbit/s optical receiver module using Si IC and GaInAs APD*", Elect. Lett., 26 (3), Feb. 1990.

Fujiwara K, Tsukada T, Nakayama T: "*Observation of free exciton in room-temperature photoluminescence of GaAs/AlGaAs single quantum wells*", Appl. Phys. Lett., 53(8), pp. 675-677, 1988.

Fukui T, Ando S, Tokura Y: "*GaAs tetrahedral quantum dot structures fabricated using selective area metalorganic chemical vapor deposition*", Appl. Phys. Lett., 58 (18), pp 2018-2020, May 1991.

Gaihanou M, Labourie C, Lievin J L, Perales A, Lambert M, Poingt F, Sigogne D: "*Chemical beam epitaxial selective growth of InP for laser fabrication*", Appl. Phys. Lett. 58 (8), pp 796-798, Feb. 1991.

Geels R S, Corzine S W, Scott J W, Young D B: "*Low threshold planarised vertical-cavity surface-emitting lasers*", IEEE Phot. Tech. Lett, 2, p 234, 1990.

Ghisoni M, Parry P, Pate M, Hill G, Roberts J: "*Post growth fabrication of GaAs/AlGaAs reflection modulators via impurity free disordering*", Jap. J. Appl. Phys., 30 (6A), L-1018-L1020, June 1991.

Ghisoni M U P: Ph.D. thesis, University of London, 1992.

Giugni S. Tansley T L, Green F, Shwe C, Gal M: "*Optical transitions in symmetric compositionally graded triangulat AlGaAs quantum wells grown by molecular beam epitaxy*", J. Appl. Phys., 71 (7), pp 3486-3491, April 1992.

Goodfellow R C: "*Applications and materials for semiconductor optoelectronic devices*", Sym Proc.: 'Materials for optoelectronic devices OEICs and Photonics', E-MRS, Holland, 1991.

Goodman J W, Leonberger F I, Kung S Y, Athale R A : "*Optical interconnects for VLSI systems*", IEEE Proc., 72 (7), pp 850- 866, July 1984.

Goossen K W, Cunningham J E, Jan W Y : "*Excitonic electroabsorption in extremely shallow quantum wells*", Appl. Phys. Lett. 57 (24), pp 2582-2584, Dec 1990.

Goossen K W, Yan R H, Cunningham J E, Jan W Y: "*AlGaAs-AlAs quantum well surface-normal electroabsorption modulators operating at visible wavelengths*", Appl. Phys. Lett., 59(15), pp 1829-1831, 1991.

Goossen K W, Cunningham J E, White A E, Short K T, Jan W Y, Walker J A: "*GaAs on Si modulator using a buried siliside reflector*", Phot. Tech. Lett, 4(2), pp 140-142, 1992a.

Goossen K W, Cunningham J E, Jan W Y: "*Monolithic integration of normally-on and normally-off asymmetric Fabry-Perot modulators by selective antireflection coating*", Appl. Phys. Lett., 60 (24), pp 2966-2968, June 1992.

Goswami S, Hong S-C, Biswas D, Bhattacharya P K, Singh J: "*Low power exciton based heterojunction bipolar transistor for thresholding logic applications*", IEEE J. Quantm. Elect., 27 (3), pp 760-768, March 1991.

Grande W J, Johnson J E, Tang C L: "*GaAs/AlGaAs photonic integrated circuits fabricated using chemically assisted ion beam etching*", Appl. Phys. Lett., 57 (24), pp 2537-2539, Dec. 1990.

Grindle R J, Midwinter J E, Roberts J S: "*High contrast low voltage symmetric selfelectro-optic effect device (S-SEED)*", Elect. Lett., pp 2327-2329, 27 (25), 1991.

Grindle R J, Midwinter J E: "*A self-configuring optical fibre-tap/photodetector-modulator with very high photo-detection efficiency and high extinction ratio*", Elect. Lett., 27 (23), pp 2170-2172, 1991.

Grindle R J, Midwinter J E: "*A high contrast symmetric self-electro-optic effect device (S-SEED) and its potential use in a distributed control, all optical packet switch*", SPIE Con. Proc., Vol 1843, ICO topical meeting on 'Photonic Switching', Minsk, July 1992.

Guha A, Bristow J, Sullivan C, Husain A: "*Optical interconnections for massively parallel* *architectures*", Applied Optics, 29 (8), pp 1077-1093, March 1990.

Guy D R P, Apsley N, Taylor L L, Bass S J, Klipstein P C: "*Theory of an electro-optic modulator based on quantum wells in a semiconductor etalon*", SPIE, 'Advances in semiconductors and semiconductor structures', Bay Point, Florida, March 1987.

Haigh D, Everard J: "GaAs`technology and its impact on circuits and systems", IEE Circuits and Systems, Series 1, Peter Peregrinus Ltd., 1989.

Hamamoto K, Anan T, Komatsu K, Sugimoto M, Mito I: "*First 8x8 semiconductor optical matrix switches using GaAs/AlGaAs electro-optic guided-wave directional couplers*", Elect. Lett., 28 (5), Feb. 1992.

Haruna M, Takahashi M, Wakahayashi K, Nishihara H: "*Laser beam lithographed micro-Fresnel lenses*", Appl. Optics, 29(34), pp 5120-5126, 1990.

Harwit A, Harris J S, Kapitulnic A: "*Calculated quasi-eigenstates and quasi-eigenenergies of quantum well superlattices in an applied electric field*", J. Appl. Phys., pp 3211-3213, 1986.

Hashimoto M, Fukui M, Kitayama K-I: "*Self-routing optical crossbar switch*", IEEE Phot. Tech. Lett., 2 (7), pp 522-524, July 1990.

Hasnain G, Tai K, Wynn J D, Wang Y H, Fisher R J, Hong M, Weir B E, Zydzik G J, Mannaerts J P, Gamelin J, Cho A Y: "*Continuous wave top surface emitting quantum well lasers using hybrid metal/semiconductor reflectors*", Elect. Lett. ,26 (19), pp 1590-1591, Sept. 1990.

Hasnain G, Wiesenfeld J M, Damen T C, Shah J, Wynn J D, Wang Y H, Cho A Y: "*Electrically gain-switched vertical cavity surface emitting lasers*", Phot. Tech. Lett., 4(1), pp 6-9, 1992.

Hayashi H, Yano H, Aga k, Kamai H, Sasaki G: "*Giga-bit rate receiver OEICs grown by OMVPE for long-wavelength optical communications*", IEE Proc. J., 138 (2), pp 164-170, April 1991.

Herman M A, Bimberg D, Christen J: "*Heterointerfaces in quantum wells and epitaxial* *growth processes: Evaluation by luminescence techniques*", J. Appl. Phys. 70 (2), R1-R52, July 1991.

Hiroshima T, Lang R: "*Effect of conduction band nonparabolicity on the quantised energy levels of a quantum well*", Appl. Phys. Lett, 49(8), pp 456-457, 1986.

Hsu T Y, Wu W Y, Efron U: "*Amplitude and phase modulation in a 4μm-thick GaAs/AlGaAs multiple quantum well modulator*", Elect. Lett., 24 , pp 603-4, 1988.

Hu K, Chen L, Madhukar A, Chen P, Rajkumar K C, Kaviani K, Karim Z, Tanguay A R Jr.: *"High contrast ratio asymmetric Fabry-Perot reflection light modulator based on GaAs/InGaAs multiple quantum wells"*, Appl. Phys. Lett., 59 (9), Aug. 1991a.

Hu K, Chen L, Madhukar A, Chen P, Kyriakidis C, Karim Z, Tanguay A R Jr.: *"Inverted cavity GaAs/InGaAs asymmetric Fabry-Perot reflection modulator"*, Appl. Phys. Lett., 59 (14), pp 1664-1666, Sept. 1991b.

Ikegami T, Kawaguchi H: "*Semiconductor devices in photonic switching*", IEEE J. Selected areas in Communctns., 6 (7), pp 1131-1140, Aug. 1988.

Ishikawa T, Nishimura S, Tada K: "*Quantum-confinemened Stark effect in a parabolic potential quantum well*", Jap. J. Appl. Phys., 29 (8), pp 1466-1473, Aug. 1990.

Ismail K, Burkhardt M, Smith H I, Karam N H, Sekula-Moise P A: "*Patterning and characterisation of large-area quantum wire arrays*", Appl. Phys. Lett 58 (14), pp 1539-1541, April 1991.

Jahns J, Shreibl N, Walker S J: "*Multilevel phase structures for array generation*", SPIE 1052 Holographic Optics: Optically and Computer Generated, pp 198-203, 1989.

Jelley K W, Alavi K, Engelman R W H :"*Experimental determination of electroabsorption in GaAs/*$Al_{0.32}Ga_{0.68}As$ *multiple quantum well structures as a function of well width*", Elect. Lett., 24 (25), pp 1555-1557, Dec. 1988.

Jelley K W, Engelmann R W H, Alavi K, Lee H :"*Well size related limitations on maximum electroabsorption in GaAs/AlGaAs multiple quantum well structures*", Appl. Phys. Lett. 55 (1), pp 70-72, July 1989.

Ketterson A A, Tong M, Seo J W, Nummila K, Morikuni J J, Kang S-M, Adesida I: "*A high performance AlGaAs/InGaAs/GaAs pseudomorphic MODFET-based monolithic optoelectronic receiver*", IEEE Phot. Tech. Lett., 14 (1), pp 73-76, Jan. 1992.

Kiamilev F E, Marchand P, Krishnamoorthy A V, Esener S C, Lee S H: "*Performance comparison between optoelectronic and VLSI multistage interconnection networks*", J. Lightwave Tech., 9 (12), p 1674, Dec. 1991.

Kim Y, Ourmazd A, Bode M, Feldman R D: "*Nonlinear diffusion in multilayered semiconductor systems*", Phys. Rev. Lett., 63(6), pp 636-639, 1989.

Kishi N, Carter J N, Mottahedeh R, Morkel P R, Smart R G, Seeds A J Roberts J S, Burton C C, Payne D N, Tropper A C, Hanna D N: "*Actively mode-locked and passively Q-switched operation of Thulium-doped fibre laser using multiquantum well asymmetric Fabry-Perot modulator*", Elect. Lett. 28 (2), pp 175-177, Jan. 1992.

Kishino K, Kikuchi A, Kaneko Y, Nomura I: "*Enhanced carrier confinement effect by the multiquantum barrier in 660nm GaInP/AlInP lasers*", Appl. Phys. Lett., 58 (17), pp 1822-1824, April 1991.

Kisting S R, Bohn P W, Andideh E, Adesida I, Cunningham B T, Stillman G E, Harris T D: "*High precision temperature- and energy-dependent refractive index of GaAs determined from excitation of optical waveguide eigenmodes*", Appl. Phys. Lett., 57 (13), pp 1328-1330, Sep 1990.

Klipstein P C, Apsley N: "*A theory for the electroreflectance spectra of quantum well structures*", J. Phys. C: Solid State Phys., 19, pp 6461-6478, 1986.

Koch T L, Koren U: "*Photonic integrated circuits: Research curiocity or packaging common sense?*", IEEE LCS, pp 50-56, Nov 1990.

Koch T L, Koren U: "*InP-based photonic integrated circuits*", IEE Proc. J., 138 (2), pp 139-147, April 1991.

Kopf R F, Herman M H, Ohring M: "*Band offset determination in analog graded parabolic and triangular quantum wells of GaAs/AlGaAs and GaInAs/AlInAs*", J. Appl. Phys. 71 (10), pp 5004-5011, May 1992.

Kostuk R K, Goodman J W, Hesselink L: "*Optical imaging applied to microelectronic chip-to-chip interconnection*", Appl. Optcs., 24 (17), pp 2851-2858, Sept. 1985.

Kurata H, Tsuchiya M, Sasaki H: "*A novel optical bistability device consisting of resonant tunnelling diode and quantum Stark modulator: experimental demonstration*", Surface Scien., 228, pp 468-471, 1990.

Kurokawa T, Matsuo S, Amano C: "*Banishing the electron*", IEEE Lightwave Comm. Systms., Feb. 1992.

Law K K, Whitehead M, Merz J L, Coldren L A: "*Simultaneous achievement of low insertion loss high contrast and low voltage in asymmetric Fabry-Perot reflection modulator*", Elect. Lett., 27 (20), pp 1863-1865, Sep 1991.

Lee J, Vassell M O, Koteles E S, Elman B: "*Excitonic spectra of asymmetric couple double quantum wells in electric fields*", Phys. Rev. B, 39 (14), pp 10133-10143, May 1989.

Lee Y H, Tell B, Brown-Goebeler K, Jewell J L, Hore J V: "*Top surface emitting GaAs four-quantum-well lasers emitting at 0.85μm*", Elect. Lett., 26 (11), pp 710-711, May 1990.

Lei C, Rogers T J, Deppe D G, Streetman B G: "*InGaAs-GaAs quantum well vertical cavity surface-emitting laser using molecular beam epitaxial regrowth*", Appl. Phys. Lett., 58 (11), pp 1122-1124, March 1991.

Lengyel G, Jelley K W, Engelmann R W H: "*A semi-empirical model for electroabsorption in GaAs/AlGaAs multiple quantum well structures*", IEEE J. Quantm. Elect., 26 (2), pp 296-304, Feb. 1990.

Lentine A L, Hinton H S, Miller D A B, Henry J E, Cunningham J E, Chirovsky L M F: "*Symmetric self electro-optic effect device: optical set-reset latch*", Appl. Phys. Lett., 52, pp 1419-1421, 1988.

Lentine A L, Miller D A B, Henry J E, Cunningham J E, Chirovsky L M F: "*Optical logic using electrically connected quantum well pin diode modulators and detectors*", Appl. Optics, 29 (14), pp 2153-2163, May 1990.

Lentine A L, Miller D A B, Chirovsky L M F, D'Assaro L A: "*Optimisation of absorption* *in symmetric self-electro-optic effect devices: A systems perspective"*, IEEE J. Quantm. Elect., 27 (11), pp 2431-2439, Nov 1991.

Lindgren S, Oeberg M G, Andre J, Nilson S, Broberg B, Holmberg B, Bäckbom L: "*Loss-compensated optical Y-branch switch in InGaAsP-InP*", J. Lightwave Tech., 8 (10), pp 1591-1595, Oct. 1990.

Livescu G, Boyd G D, Morgan R A, Chirovsky L M F, Fox A M, Leibenguth R E, Asom M T, Focht M W: *"Role of electrorefraction in quantum well Fabry-Perot modulators"*, Appl. Phys. Lett., 60 (12), pp 1418-1420, March 1992.

Lloyd A D: "*High contrast submilliwatt switches in an optically bistable liquid-crystal etalon utilising absorption of reflection signal*", Optcs. Lett., 13, p 227, March 1988.

Macleod H A, "Thin film optical filters", Adam Higler, London (1969).

Matsuda K, Shibata J: *"Optical interconnections and optical digital computing based on the photonic parallel memory (PPM)"*, IEE Proc. J., 138 (2), pp 67-74, April 1991.

Matsumoto Y, Matsuura M, Tarucha S, Okamoto H: "*Direct observation of two dimensional shrinkage of exciton wave function in quantum wells*", Phys. Rev. B, 32, pp 4275-4278, 1985.

McCormick F B, Tooley F A P, Cloonan T J, Sasian J M, Hinton H S: "*Microbeam interconnections using microlens arrays for free space photonic systems*", IEEE/OSA topical meeting on Photonics Switching, Conf. Proc. pp 90-96, Salt Lake City, Utah, March 1991a.

McCormick F B, Tooley F A P, Sasian J M, Bribaker J L, Lentine A L, Cloonan T J, Morrison R L, Walker S L, Crisci R J: "*Parallel interconnection of two 64x32 symmetric self-electro-optic-effect device arrays*", Electr. Lett. 27 (20), pp 1869-1871, Sept. 1991b.

Mendoza-Alvarez J G, Coldren L A, Apling A, Yan R H, Hausken T, Lee K, Pedrotti K: *"Analysis of depletion edge translation lightwave modulators"*, J. Lightwv. Tech., 6, pp 793-807, 1988.

Midwinter, J E : "*'Light' electronics, myth or reality?*", IEE Proc., Vol 132, Pt. J., pp 371-383, Dec 1985.

Midwinter J E: "*Novel approach to the design of optically activated wideband matrices*", IEE Proc., Pt. J., 134 (5), pp 261-268, Oct 1987.

Midwinter J E: "*Photonic switching technology: component characteristics versus network requirements*", J. Lightwave Tech., 6(10), Oct. 1988.

Midwinter J E: "*Digital optics, smart interconnection or optical logic?*", Phys. Tech., 19, pp 101-108 (part 1) and 153-165 (part 2), 1988.

Miller D A B, Chemla D S, Damen T C, Gossard A C, Wiegmann W, Wood T H, Burrus C A: *"Novel hybrid optically bistable switch: The quantum well self-electro-optic effect device"*, Appl. Phys. Lett. 45 (1), pp 13-15, July 1984.

Miller, D.A.B., Chemla, D.S., Damen, T.C., Gossard, A.C., Wiegmann, W., Wood, T.H., and Burrus, C.A.: *"Electric field dependence of optical absorption near the band-gap of quantum well structures*", Phys. Rev. B, 32, pp. 1043-1060, 1985a.

Miller D A B, Chemla D S, Damen T C, Wood T S, Burrus C A, Gossard A C, Wiegmann W: "*The quantum well self-electrooptic effect device: optoelectronic bistability and oscillation, and self-linearised modulation*", IEEE J. Quantm. Elect., QE-21 (9), pp 1462-1476, Sept. 1985b.

Miller D A B, Weiner J S, Chemla D S: "*Electric field dependence of linear optical properties in multiple quantum well structures: Waveguide electroabsorption and sum rules*": IEEE J. Quantm. Elect., QE-22, pp 1816-1830, 1986.

Miller D A B: *"Optical bistability in self-electro-optic effect devices with asymmetric quantum wells"*, Appl. Phys. Lett., 54 (3), pp 202-204, Jan 1989.

Miller D A B: *"Quantum well self-electro-optic effect devices"*, Opt. Quantm. Elect., 22, S61-S98, 1990.

Moretti A L, Vezzetti D J, Chambers F A, Stair K A, Devane G P: "*GaAs/AlGaAs superlattice waveguide absorption modulators with very low drive voltage*", IEEE Phot. Tech. Lett, 4 (6), pp 576-579, June 1992.

Moseley A J, Thompson J, Kearley M Q, Robbins D J, Goodwin M J: "*Low voltage*

InGaAs/InP multiple quantum well reflective Fabry-Perot modulator", Elect. Lett., 26 (13), pp 913-915, June 1990.

Moseley A J, Kearley M Q, Morris R C, Urquhart J, Goodwin M J, Harris G: *"8x8 flipchip assembled InGaAs detector arrays for optical interconnect"*, Elect. Lett., 27 (17), Aug. 1991.

Nakagawa K, Shimada S: "*Optical Amplifiers in future optical communications systems*", Lightwave Communc. Systms., pp 57-62, Nov 1990.

Nelson D F, Miller R C, Kleinman D A: "*Band non-parabolicity effects in semiconductor quantum wells*", Phys. Rev B, 35, pp 7770-7773, 1987a.

Nelson D F, Miller R C, Tu C W, Sputz S K: "*Exciton binding energies from an envelope function analysis of data on narrow quantum wells of integral monolayer widths in* $Al_{0.4}Ga_{0.6}As/GaAs$": Phys. Rev. B, 36(15), pp 8063-8071, 1987b.

Nozawa K, Horikoshi Y: *"Low-threading dislocations density GaAs on Si (100) with InGaAs/GaAs strained layer superlattices grown by migration enhanced epitaxy"*, Jap. J. Appl. Phys., Part 2, 30 (4B), April 1991.

Nussbaum E: "*Communication network needs and technologies- A place for photonic switching?*", IEEE J. Selected Areas Commnctns., 6 (7), pp 1036-1043, Aug. 1988.

Ohnaka K, Inone K, Uno T, Hasegawa K, Hase N, Serizawa H: *"A planar InGaAs PIN/JFET fibre-optic detector"*, IEEE J. Quantm. Elect., QE-21, pp 1236-1240, 1985.

Ogura I, Numai T, Kosaka H, Sugimoto M, Kasahara K: "*Surface emitting laser operation and optical switching characteristics in vertical to surface transmission electro-photonic devices with a vertical cavity (VC-VSTEP)*", IEEE/OSA topical meeting on 'Quantum Optoelectronics', pp 96-98, Salt Lake City, March 1991.

Orenstein M, Von Lehnman A C, Chang-Hasnain C, Stoffel N G,Harbison J P, Florez L T: "*Matrix addressable vertical cavity surface emitting laser array*", Elect. Lett., 27 (5), pp 437-438, Feb. 1991.

Orenstein M, Kapon E, Stoffel N G, Harbison J P, Florez L T, Wullert J: "*Two-dimensional phase-locked arrays of vertical-cavity semiconductor lasers by mirror* *modulation*", Appl. Phys. Lett., 58 (8), pp 804-806, Feb 1991.

Ourmazd A: "*Chemical interfaces: structure properties relaxation*", MRS Bulletin, XV(9), pp 58-64, 1990.

Pankove J I: "Optical processes in semiconductors", Dover Publication Inc., NY, 1971.

Parker J W: "*Progress in optical interconnection technology and demonstrators under ESPRIT II OLIVES program*", IEEE/OSA topical meeting on 'Photonic Switching', Salt Lake City, March 1991.

Panish M B, Sumski S: "*Gas source molecular beam epitaxy of* $Ga_xIn_{1-x}P_yAs_{1-y}$", J. Appl. Phys., 55, pp 3571-3576, 1984.

Pessa M, Jylha O: "*Growth of* $Cd_{1-x}Mn_xTe$ *film with* $o<x<0.9$ *by atomic layer epitaxy*", Appl. Phys. Lett., 45, pp 646-648, 1984.

Pezeshki B, Thomas D, Harris J S: "*Optimisation of modulation ratio and insertion loss in reflective electroabsorptive modulators*", Appl. Phys. Lett, 57 (15), pp 1491-1492, Oct 1990.

Pezeshki B, Thomas D, Harris J S Jr: "*Novel cavity design for high reflectivity changes in a normally off electroabsorption modulator*", Appl. Phys. Lett., 58 (8), pp 813-815, Feb 1991.

Pezeshki B, Thomas D, Harris J S Jr: "*Optimisation of reflection electroabsorption modulators*", preprint from SPIE meeting, 1991b.

Pezeshki B, Lord S M, Boukin T B, Harris J S Jr.: "*GaAs/AlAs quantum wells for electroabsorption modulators*", Appl. Phys. Lett. 60 (22), pp 2779-2781, June 1992a.

Pezeshki B, Liu D, Lord S M, Harris J S Jr: "*Visible wavelength Fabry-Perot reflection modulator using indirect-gap AlGaAs/AlAs*", Elect. Lett., 28 (12), pp 1170-1171, June 1992.

Pollentier I, Demeester P, Ackaert A, Buydens L, Van Daele P, Baets R: "*Epitaxial lift-off GaAs LEDs to Si for fabrication of opto-electronic integrated circuits*", Elect. Lett., 26 (3), pp 193-194, Feb. 1990.

Prucnal P R, Perrier P A: "*Opticall processed routing for fast packet switching*", IEEE Lightwave Comm. Systms., May 1990.

Pütz N: "*InP based optoelectronics*", J. Crystal Growth, 107, pp 806-821, 1991.

Qingyou Z, Yushu Z, Dingsan G: "*Mode-selection characteristic of the symmetrical three-section composite-cavity InGaAsP/InP semiconductor laser*", Opt. Quantm. Elect., 22, pp 77-81, 1990.

Ragdale C M, Reid T J, Reid D C J, Carter A C, Williams P J: "*Integrated laser and add-drop optical multiplexer for narrowband wavelength division multiplexing*", Elect. Lett., 28 (8), pp 712-714, April 1992.

Ribot H, Lee K W, Simes R J, Yan RH, Coldren L A: "*Disordering of GaAs/AlGaAs multiple quantum well structures by thermal annealing for monolithic integration of laser and phase modulator*", Appl. Phys. Lett., 55 (7), pp 672-674, Aug. 1989.

Roberts J S, Pate M A, Mistry P, David J P R, Franks R B, Whitehead M, and Parry G: "*MOVPE grown MQW p-i-n diodes for electro-optic modulators and photodiodes with enhanced electron ionisation coefficient*", J. Crystal Growth, 93, pp. 877-884, 1988.

Rudin S, Reinecke T L, Segall B: "*Temperature dependent exciton linewidths in semiconductors*", Phys. Rev. B, 42 (17), pp 11218-11231, Dec. 1990.

Ryvkin B S: "*Falling current-voltage characteristic and optical bistability of a resonator photocell in the Franz-Keldysh effect*", Sov. Phys. Scien., 15, pp 796-798, 1981.

Schmitt-Rink S, Chemla D S, Miller D A B: "*Linear and nonlinear optical properties of semiconductor quantum wells*", Advances in Physcs., 38(2), pp 89-188, 1989.

Schiff L I: "Quantum Mechanics", MacGraw Hill, Tokyo (1981).

Sedra A S, Smith K C: "Microelectronic Circuits", third edition, Saunders College Publishing, 1990.

Sell D D, Casey H C Jr, Wecht K W: "*Concentration dependence of the refractive index for n- and p-type GaAs between 1.2 and 1.8 eV*", J. Appl. Phys., 45 (6), pp 2650-2657, June 1974.

Sfez B G, Oudar J L, Michel J C, Kuszelewicz R, Azoulay R: "*High contrast multiple quantum optical bistable device with integrated Bragg reflectors*", Appl. Phys. Lett., 57 (4), July 1990.

Shibata J, Nakao I, Sasai Y, Kimur S, Hase N, Serizawa H: "*Monolithic integration of an InGaAsP/InP laser diode with heterojunction bipolar transistor*", Appl. Phys. Lett., 45, pp.191-193, 1984.

Shimomura K, Tanaka N, Aizawa T, Arai S: "*2V drive-voltage switching operation in 1.55μm GaInAs/InP MQW intersectional waveguide optical switch*", Elect. Lett., 28 (10), pp 955-957, May 1992.

Shoop B L, Pezeshki B, Goodman J W, Harris J S Jr.: "*Laser-power stabilisation using a quantum well modulator*", Phot. Tech. Lett., 4(2), pp 136-139, 1992.

Simes R J, Yan R H, Geels R S, Coldren L A, English J H, Gossard A C, Lishan D G : "*Electrically tunable Fabry-Perot mirror using multiple quantum well index modulation*", Appl. Phys. Lett., 53 (8), pp 637-639, Aug. 1988.

Sonek G J, Chen Y J : "*Effect of temperature variations on optical waveguiding in GaAs multiple quantum wells*", J. Lightwave Techn. 7 (7), pp 1130-1135, July 1989.

Stevens P J, Whitehead M, Parry G, Woodbridge K: "*Computer modelling of the electric field dependent absorption spectrum of multiple quantum well material*", IEEE J. Quantm. Elect., QE-24 (10), pp 2007-2016, 1988.

Stevens P J, Parry G :"*Limits to normal incidence electroabsorption modulation in GaAs/GaAlAs multiple quantum well diodes*", IEEE J. Lightwave Tech., 7 (7), pp 1101-1108, July 1989.

Stevens P J: Ph.D. thesis, University of London, 1989.

Sturge M D : "*Optical absorption of Gallium Arsenide between 0.6 and 2.75 eV*", Phys. Rev., 127 (3), pp 768-773, Aug. 1962.

Sudbo A S: "*The frequency chirp of current modulated semiconductor diode lasers*", IEEE J. Quantm. Electr., QE-22 (7), pp 1006-1008, July 1986.

Sugimoto M, Numai T, Ogura J, Kosaka H, Kurihara K, Kasahara K: "*Vertical to surface transmission electrophotonic device with pnpn structure and vertical cavity*", Opt. Quantm. Elect., 24 (2), S121-S132, 1992.

Tell B, Lee Y H, Brown-Goebeler K, Jwell J L, Leibenguth R E, Asom M T, Livescu G, Luther L, Mattera V D : "*High power cw vertical cavity top surface emitting GaAs quantum well lasers*", Appl. Phys. Lett. 57 (18), pp 1855-1857, Oct. 1990.

Taylor M G: PhD thesis, University of London, Oct 1990.

Taylor M G, Midwinter J E: "*Optically interconnected switching networks*", J. Lightwave Tech., 9 (6), June 1991.

Tombling C, Saitoh T, Susuki Y, Tanaka H: "*Experimental gain and saturation performance of GaAs/AlGaAs SCH quantum well travelling wave optical amplifier*", Elect. Lett., 27, pp 1374-1376, 1991.

Tooley F A P: "*Design issues in free-space optical interconnection of switching systems*", IEEE/OSA topical meeting on 'Photonic Switching', Salt Lake City, Utah, 1991.

Topham D: "*Implications for interconnect*", IEE Collqm on 'Advances in interconnection technology', London, April 1991.

Tsai C S, Zang D Y, Le P: "*A novel scheme for efficient excitation of high density channel-waveguide array using ion-milled planar microlens array*", 'Optoelectronics'-Devices & Technologies, 5(2), pp 317-324, Dec 1990.

Tsang W T: "*Chemical beam epitaxy of InP and GaAs*", Appl. Phys. Lett., 45, pp 1234-1236, 1984.

Tucker R S : "*High speed modulation of semiconductor lasers*", J. Lightwave Tech., LT-3, p 1180, 1985.

Ünlü M S, Kishino K, Chyi J I, Reed J, Arsenault L, Morkoc: "*Wavelength demultiplexing heterojunction phototransistor*", Elect. Lett., 26(22), pp 1857-1858, Oct 1990.

Ünlü M S, Demirel A L, Strite S, Tasiran S, Salvador A, Morcoc H: *"Wavelength demultiplexing optical switch"*, Appl. Phys. Lett., 60 (15), pp April 1992.

Van der Ziel J P, Ilegems M: "*Multilayer GaAs/*$Al_{0.3}Ga_{0.7}As$ *dielectric quarter wave stacks grown by molecular beam epitaxy*", Appl. Optics, 14 (11), pp 2627-2630, Nov 1975.

Wada O, Furuya A, Makiushi M: *"Planar compatible OEICs based on multiquantum well structures"*, IEEE Phot. Tech. Lett., 1 (1). pp 16-18, Jan. 1989.

Wada O: *"GaAs in integrated optoelectronics"*, from 'Properties of Gallium Arsenide', INSPEC, 2nd Edtn., pp 732-744, 1990.

Wada O, Kumai T, Hamaguchi H, Makiushi M, Kuramata A, Mikawa T: *"High-reliability flip-chip GaInAs/InP pin photodiode"*, Elect. Lett., 26 (18), Aug. 1990.

Walker R G: *"High speed III-V semiconductor intensity modulators"*, IEEE J. Quantm. Elect., 27 (3), pp 654-667, March 1991.

Walther M, Ebeling K J: *"Gigabit operation of an MQW modulator with integrated Fabry-Perot resonator"*, ECOC, Conf. Proc. pp225-228, Amsterdam, Sept 1990.

Wang Y H, Tai K, Hsieh Y F, Chu S N G, Wynn J D, Cho A Y: "*Observation of reduced current thresholds in GaAs/AlGaAs vertical cavity surface-emitting lasers grown on 4° off-orientation (001) GaAs substrates*", Appl. Phys. Lett. 57 (16), pp 1613-1615, Oct. 1990.

Weiner J S, Chemla D S, Miller D A B, Gossard A C, Wiegmann, Burrus C A: "*Highly anisotropic optival properties of single quantum well waveguides*", Appl. Phys. Lett. 47(7), pp 664-667, Oct 1985.

Weiner J S, Miller D A B, Chemla D S, Damn T C, Burrus C A, Wood T H, Gossard A C, Wiegmann W: "*Strong polarisation sensitive electroabsorption in GaAs/AlGaAs quantum well waveguides*", Appl. Phys. Lett., 47 (11), pp 1148-1150, Dec 1985.

Weisbuch C: "*Fundamental properties of III-V semiconductor two-dimensional quantised structures: The basis for optical and electronic device applications*", Semiconductors & Semimetals, Vol. 24 , Academic Press, 1986.

Weisbuch C ,and Vinter B: "Quantum semiconductor structures", Academic Press,

1991.

Wheatley P, Bradley P J, Whitehead M, Parry G, Midwinter J E, Mistry P, Pate M A, Roberts J S: *"Novel non-resonant optoelectronic logic device"*, Elect. Lett., 23, pp 92-93, 1987.

Wherrett B S, Chow Y T, Hutchings D C, Lloyd A D, Janossy I: *"All-optical logic elements for optical processing"*, SPIE Vol.800, Novel Optoelectronic Devices, 1987.

Whitehead M, Stevens P J, Parry G, Roberts J S, Mistry P, Pate M, Hill G: *"Effects of well width on the characteristics of GaAs/AlGaAs multiple quantum well electroabsorption modulators"*, Appl. Phys. Lett., 53 (11), pp 956, 958, Sept. 1988.

Whitehead M, Parry G, Wheatley P: *"Investigation of etalon effects in GaAs/AlGaAs multiple quantum well modulators"*, IEEE Proc. J., 136(1), pp 52-58, 1989a.

Whitehead M, Rivers A, Parry G, Roberts J S, and Button C: *"Low voltage Multiple Quantum Well reflection Modulator with on:off ratio >100:1"*,Elect. Lett., 25, pp. 984-985, 1989b.

Whitehead M, Parry G: *"Modelling the limits of low voltage operation for the GaAs multiple quantum well asymmetric Fabry-Perot cavity modulators"*, IEE Colloqium on 'Optoelectronic device modelling', Feb. 1990a.

Whitehead M, Rivers A, Parry G, Roberts J S: *"Very low voltage, normally-off asymmetric Fabry-Perot reflection modulator"*, Elect. Lett., 26 (19), pp 1588-1590, Sept. 1990b.

Wood T H, Burrus C A, Miller D A B, Chemla D S, Damen T S, Gossard A C, Wiegmann W: *"High speed optical modulation with GaAs/GaAlAs quantum wells in a p-i-n diode structure"*, Appl. Phys. Lett., 44, pp 16-18, 1984.

Wood T H, Burrus C A, Miller D A B, Chemla D S, Damen T C, Gossard A C, Wiegmann W : *"131 ps optical modulation in semiconductor multiple quantum wells (MQWs)"*, IEEE J. Quantm. Electr., QE-21 (2), pp 117-118, Feb. 1985.

Woodbridge K, Barnes P, Murray R, Roberts C, Parry G: *"GaAs/AlGaAs pin MQW structures grown on patterned Si substrates"*, 7th Int. Conf. on MBE, Schwäbisch Gmünd, Germany, Aug 1992.

Woodward T K, Chirovsky L M F, Lentine A L, D'Asaro L A, Laskowski E J, Focht M, Guth G, Pei S S, Ren F, Przybylek G J, Smith L E, Leibenguth R E, Asom M T, Kopf R F, Kuo J M, Feuer M D: *"Operation of a fully integrated GaAs-AlGaAs FET-SEED: A basic optically addressed integrated circuit"*, IEEE Phot. Tech. Lett., 4 (6), pp 614-617, June 1992.

Wüthrich C, James J H, Ganiere J D, Reinhart F K: *"Room temperature vertical cavity GaAs/AlGaAs surface emitting injection laser"*, Elect. Lett., 26 (19), Sep 1990.

Yamanishi M, Suemune I: *"Comment on polarization dependent momentum matrix elements in a quantum welllaser"*, Jap. J. Appl. Phys., 23, pp 135-136, 1984.

Yamaguchi M, Sugo M, Hoh Y: *"Misfit stress-dependence of dislocation density reduction in GaAs film on Si substrates grown by strained layer superlattices"*, Appl. Phys. Lett., 54 (25), June 1989.

Yan R H, Simes R J, Coldren L A: *"Electroabsorptive Fabry-Perot reflection modulators with asymmetric mirrors"*, IEEE Phot. Tech. Lett. 1 (9), pp 273-275, Sept 1989.

Yan R H, Simes R J, Coldren L A: *"Analysis and design of surface normal Fabry-Perot electro-optic modulators"*, IEEE J. Quantm. Elect., 25 (11), pp 2272-2280, Nov 1989b.

Yan R H, Simes R J, Coldren L A: *"Extremely low-voltage Fabry-Perot reflection modulators"*, IEEE Phot. Tech. Lett., Vol 2, pp 118-119, 1990.

Yan R H, Simes R J, Coldren L A, Gossard A C: *"Transverse modulators with a record refelction change of >20% using asymmetric Fabry-Perot structures"*, Appl. Phys. Lett. 56 (17), pp 1626-1628, April 1990a.

Yan R H, Law K K, Coldren L A, Merz J L: *"Asymmetric Fabry-Perot modulators using red- and blue-shifted electroabsorption effects"*, J. Appl. Phys. 66 (2), pp 875-877, July 1990b.

Yan R H, Simes R J, Coldren L A: *"Surface normal electroabsorption reflection modulators using asymmetric Fabry-Perot structures"*, IEEE J. Quantm. Elect, 27(7), pp 1922-1931, July 1991.

Yoffe C N, Dell J M: *"Multiple quantum well reflection modulator using a lifted-off GaAs/AlGaAs film bonded to gold on Si"*, Elect. Lett, 27 (7), pp 557-558, 1991.

Yoo H, Scherer A, Harbison J P, Florez L T, Paek E G, Van der Gaag B P, Hayes J R, Von Lehmen A, Kapon E, Kwon Y S: *"Fabrication of a two dimensional phased array of vertical cavity surface emitting lasers"*, Appl. Phys. Lett., 56 (13), pp 1198-1200, March 1990.

Yoo H J, Hayes J R, Paek E G, Harbison J P, Florez L T: *"Phase locked two-dimensional arrays of implant isolated vertical cavity surface emitting lasers"*, Elect. Lett., 26 (23), pp 1944-1946, Nov 1990.

Zinckiewicz L M, Roth T J, Mawst L J, Tran D, Botez D: *"High power vertical cavity surface emitting AlGaAs/GaAs diode lasers"*, Appl. Phys. Lett., 54 (20), pp 1959-1961, May 1989.

Zhou P, Cheng J, Schaus C F, Sun S Z, Hains C, Armour E, Myers D R, Vawter G A: *"Inverting and latching optical logic gates based on the integrationof vertical-cavity surface - emitting lasers and photothyristors"*, Phot. Tech. Lett., 4(2), pp 157-162, 1992.

Zucker J E, Wegener M, Jones K L, Chang T Y, Sauer N, Chemla D S: *"Optical waveguide intensity modulators based on a tunable electron density multiple quantum well structure"*, Appl. Phys. Lett., 56 (20), pp 1951-1953, May 1990.

PUBLICATIONS

First Author

"Temperature sensitivity of Asymmetric Fabry-Perot Modulators". P. Zouganeli, M. Whitehead, P.J. Stevens, A. Rivers, G. Parry, J.S. Roberts, C. Button. *Elect. Lett.*, 26 (17), pp 1384-6, Aug 1990.

"The temperature sensitivity of asymmetric Fabry-Perot modulators". P. Zouganeli, M. Whitehead, P.J. Stevens, A. Rivers, G. Parry, J.S. Roberts, C. Button. *IEE Colloqium* on 'Applications of quantum wells in Optoelectronics', London, June 1990.

"A high-contrast, low insertion loss, asymmetric Fabry-Perot modulator operating at 4.1V". P. Zouganeli, M. Whitehead, P. J.Stevens, A. Rivers, G. Parry, J.S. Roberts. Presented at the *OSA/ IEEE* topical meeting on 'Quantum Optoelectronics', Salt Lake City, USA, March 1991.

"High tolerances for a low voltage, high contrast, low insertion loss asymmetric Fabry-Perot modulator". P. Zouganeli, M. Whitehead, P. J.Stevens, A. Rivers, G. Parry, J.S. Roberts. *Phot. Tech. Lett.*, Vol 3 (8), pp 733-5, Aug 1991.

Contributing Author

"GaAs/AlGaAs multiple quantum well optical modulator using multilayer reflector stacks, grown on Si substrates". P. Barnes, P.Zouganeli, M. Whitehead, A. Rivers, G. Parry, K. Woodbridge. *Elect. Lett.*, 25 (15), pp 995-6, July 1989.

"Quantum well modulators as interface elements for optical interconnection of electronic circuits". G. Parry , M. Whitehead, P. Barnes, P.J.Stevens, D. Atkinson, P. Zouganeli, J.S. Roberts, C. Button. IoP Electronics Group Meeting. London, March 1990.

"Some practical issues associated with the design and fabrication of high contrast quantum well modulator arrays". G. Parry, M. Whitehead, P. Zouganeli, A. Rivers, K. Woodbridge, J.S. Roberts, C. Button. Invited paper presented at the *OSA/IEEE* 'Optical Computing' topical meeting , Salt Lake City, USA, March 1991.

"Micro-Resonator Modulators: Design, Fabrication and Fine-Tuning the Performance". G. Parry, M. Ghisoni, P. Zouganeli, P. Barnes, A. Rivers, J. S. Roberts, C. Button. Invited paper at *SPIE* meeting on "Quantum Well and Superlattice Physics", New Jersey, 1992.

"High performance microcavity resonator devices grown by atmospheric pressure MOVPE". J S Roberts, C Button, T.Sale, G. Parry, P.Barnes, R. Grindle, P. Zouganeli. The sixth international conference on *Metalorganic Vapor Phase Epitaxy.* Cambridge Massachusetts, June 1992